Fermilab FERMILAB-THESIS-2003-14

A MEASUREMENT OF THE DIRECT CHARM MESON PRODUCTION CROSS SECTION AT CDF II

Chunhui Chen

A DISSERTATION

in

PHYSICS AND ASTRONOMY

Presented to the Graduate Faculty of the University of
Pennsylvania in Partial Fulfillment of the Requirement for
the Degree of Doctor of Philosophy

March 2003

Supervisor of Dissertation ____________________

Graduate Group Chairman ____________________

Dedication

This thesis is dedicated to my family, who have always been there for me.

ACKNOWLEDGMENTS

I would like to thank my advisor Joseph Kroll for his guidance and support. His sharp intuition and advices influenced many of my decisions and will certainly benefit my career in years to come. I also deeply appreciate the numerous discussions and helps from Dr. Rolf Oldeman during my stay at Fermilab. His enthusiasm for high energy physics, kindness and patience impressed me so much. It is such a great pleasure working with you and sharing the same office.

I am very grateful to Professor Nigel Lockyer, Professor Hugh H. Williams and Dr. Joel Heinrich for their guidance during my stay at Penn and Fermilab. I also want to say thanks to Professor Marjorie Shapiro of University of California at Berkeley for her helps.

Many thanks to Dr. Matthew Jones, Rick P. Van Berg and Mitch Newcomer for always answering my naive electronics questions while I worked on the Time of Flight project at Penn.

I would like to thank Tianjie Gao, Shin-Shan Yu, Nemes Norbert Marcel, Walter Kononenko, Isamu Nakamura, Peter Wittich, Denys Usynin and Andrew Kovalev for many conversations and fun we had. Finally, I would like to thank all the people who taught me an immense amount and who helped me get through my time in graduate school again!

ABSTRACT

A MEASUREMENT OF THE DIRECT CHARM MESON PRODUCTION CROSS SECTION AT CDF II

Chunhui Chen

Joseph Kroll

We present a measurement of the cross section of direct charm meson production in $p\overline{p}$ collisions at $\sqrt{s} = 1.96\,\text{TeV}$ using the CDF II detector at the Fermilab Tevatron. We use $5.8\,\text{pb}^{-1}$ of early 2002 data collected with a trigger that is sensitive to the long lifetime of particles containing heavy flavor. We use fully reconstructed candidates in the following modes: $D^0 \to K^-\pi^+$, $D^{*+} \to D^0(K^-\pi^+)\pi^+$, $D^+ \to K^-\pi^+\pi^+$, $D_s^+ \to \phi(K^+K^-)\pi^+$ and their charge conjugates. We subtract the contribution of secondary charm originating from B decay, and we correct for trigger and reconstruction efficiencies. We report the differential cross section $d\sigma/dp_T$ and the total cross section above a minimum transverse momentum p_T for the rapidity range $|y| \leq 1.0$. We find $\sigma(D^0, p_T \geq 5.5\,\text{GeV}/c) = 13.3 \pm 0.2 \pm 1.5\,\mu\text{b}$, $\sigma(D^{*+}, p_T \geq 6.0\,\text{GeV}/c) = 5.2 \pm 0.1 \pm 0.8\,\mu\text{b}$, $\sigma(D^+, p_T \geq 6.0\,\text{GeV}/c) = 4.3 \pm 0.1 \pm 0.7\,\mu\text{b}$ and $\sigma(D_s^+, p_T \geq 8.0\,\text{GeV}/c) = 0.75 \pm 0.05 \pm 0.22\,\mu\text{b}$, where the first error is statistical and the second systematic. The measured cross-sections are found to be larger than, but compatible with, the theoretical expectation.

Contents

1 Introduction **1**

1.1 Bottom Physics at CDF 5

1.1.1 B_s Flavor Oscillation 6

1.1.2 The Importance of B_s^0 Mixing in the Standard Model 8

1.1.3 B_s mixing measurement in Hadronic Decay Channels at CDF 11

1.2 Charm Physics at CDF 12

1.2.1 $D^0 \leftrightarrow \overline{D}^0$ Mixing 15

1.2.2 CP violation 18

1.2.3 Rare and Forbidden Decays of charm 20

2 Theoretical Background **22**

2.1 The Gauge Invariance 22

2.2 Gauge Theories and Spontaneous Symmetry Breaking 25

2.3 Standard model 25

  2.3.1 Quantum Chromodynamics 26

  2.3.2 Electroweak Interaction 28

  2.3.3 Fermion Mass Term 30

  2.3.4 The CKM Matrix 32

  2.3.5 The Electroweak Lagrangian 34

2.4 Heavy Quark Production 34

2.5 Heavy Quark Fragmentation 39

3 CDF Detector **43**

3.1 Overview 43

3.2 Tracking System 45

  3.2.1 Helix Parameters at CDF 45

  3.2.2 The Central Outer Tracker 47

  3.2.3 Silicon Vertex Detector 48

3.3 Time of Flight System 51

3.4 Calorimeter and Muon Systems 54

3.5 CDF Cherenkov Luminosity Monitor 56

3.6 CDF Trigger System 59

4 The Data Sample **62**

4.1 Introduction 62

4.2 Trigger Path 63

4.2.1 Two Track Hadronic Trigger 63

4.2.2 Two Track L1 Auto Accept Trigger 64

4.2.3 Minimum Bias Trigger 65

4.3 Track Quality Selection Criteria and Trigger Confirmation 65

5 Charm Meson Reconstruction **68**

5.1 Reconstruction of $D^0 \to K^-\pi^+$ 68

5.2 Reconstruction of $D^{*+} \to D^0\pi^+, D^0 \to K^-\pi^+$ 72

5.3 Reconstruction of $D^+ \to K^-\pi^+\pi^+$ 74

5.4 Reconstruction of $D_s^+ \to \phi\pi^+, \phi \to K^+K^-$ 79

5.5 OIZ Tracking v.s. OI Tracking 85

6 Direct Charm Fraction 89

6.1 Description of method 89

6.2 Two Track Trigger Bias 91

6.3 Predicted Impact Parameter Distribution of Secondary Charm Mesons 96

6.4 Direct Charm Impact Parameter Resolution 98

6.4.1 K_S^0 Reconstruction 99

6.4.2 K_S^0 Impact Parameter Distribution 100

6.4.3 Expected Impact Parameter Resolution for Charm 103

6.5 The Direct Charm Fraction 103

6.6 Discussion of the Measured Fraction 105

7 Single-Track Detector Efficiency 114

7.1 COT Efficiency 115

7.2 COT efficiency from track embedding 117

7.3 XFT Efficiency 120

7.4 SVT Efficiency 121

7.5 SVX Efficiency for Single SVT-matched Tracks 130

7.6 SVX Efficiency for Single Tracks without the SVT Matching Requirement 132

7.7 Effect of Track Multiplicity on Single-Track Efficiencies 134

8 Single-Track Detector Resolution 137

8.1 XFT and SVT Curvature Resolution 137

8.2 Impact Parameter Distribution for Offline Tracks 138

8.3 Impact Parameter Resolution for SVT-matched Tracks 142

9 Detector Monte Carlo Simulation 147

9.1 Transverse Beam Spot Size 148

9.2 Shape of the Luminous Region 152

9.3 Level-1 Simulation 154

9.4 Level-2 Simulation 155

9.5 Level-3 Simulation 156

9.6 Energy Loss Simulation 156

9.7 Offline Reconstruction 157

9.8 Decay and Hadronic Interaction 158

10 Data and Monte Carlo Comparison for the Detector Simulation 161

10.1 MC and Data Comparison for XFT and SVT Curvature Resolution Effects 162

10.2 Two-Track XFT Efficiency 163

10.3 Two-Track SVT Efficiency 164

10.4 SVX Efficiency of the Third Track in Three-Track Systems 167

10.5 K_S^0 Impact Parameter Distribution 170

11 Charm Meson Trigger and Reconstruction Efficiency 176

11.1 Monte Carlo Generation of Prompt Charm Mesons 176

11.2 Monte Carlo Generation of Secondary Charm Mesons 178

11.3 Dalitz Structure of the $D^+ \to K^-\pi^+\pi^+$ Decay 178

11.4 Correction of the D Meson p_T Distribution in the MC Simulation . . 180

11.5 Correction of the D Meson Rapidity Distribution in the MC Simulation185

11.6 *D* Meson Trigger and Reconstruction Efficiency 185

11.7 Discussion 188

11.8 Data and Monte Carlo Comparison 202

11.9 Systematic Uncertainties 210

12 Cross Section Results 212

12.1 Integrated Cross Section 212

12.2 Differential Cross Section 214

12.3 Comparison with the Theory 215

12.3.1 *D* meson Production Ratio 215

12.3.2 Differential Cross Section 222

13 Conclusion 225

A Run List 227

B General Relations of Helix Parameter 233

C Vertex Fit Package and Two Dimensional Vertex Constraints 236

D Test of the B Fraction Fit Procedure 238

List of Tables

1.1 Present status of D^0 lifetime difference measurements. 16

1.2 Present status of wrong-sign hadronic D^0 decays 18

1.3 Present status of direct CP violation searches in neutral charm decays 19

1.4 Present status of direct CP violation searches in charged charm decays 19

3.1 Some features of the COT 49

3.2 Some features of the SVX II 57

5.1 Summary of the charm meson yields and the associated uncertainties. The total systematic error is calculated by adding all contributions in quadrature. 86

6.1 The fraction of D mesons with negative and positive impact parameter products predicted by the Monte Carlo simulation described in the text. In this Table, d_{01} and d_{02} are the signed impact parameters of the two tracks forming the SVT-pair. Directly produced D^0 and D^{*+} only have $d_{01} \cdot d_{02} < 0$. Three-body decays have two possible SVT-pairs and there can be more than one SVT-pair per decay. . . . 95

6.2 Summary of the measured direct charm fraction for the two track hadronic data and the corresponding uncertainties. 113

11.1 Resonances contributing to the $D^+ \to K^-\pi^+\pi^+$ decay from E691. . . 179

11.2 The D^0 meson trigger and reconstruction efficiencies and systematic uncertainties. The total systematic error is calculated by adding all individual components in quadrature. 189

11.3 The D^0 meson trigger and reconstruction efficiencies and systematic uncertainties. The total systematic error is calculated by adding all individual components in quadrature. 190

11.4 The D^{*+} meson trigger and reconstruction efficiencies and systematic uncertainties. The total systematic error is calculated by adding all individual components in quadrature. 191

11.5 The D^{*+} meson trigger and reconstruction efficiencies and systematic uncertainties. The total systematic error is calculated by adding all individual components in quadrature. 192

11.6 The D^{+} meson trigger and reconstruction efficiencies and systematic uncertainties. The total systematic error is calculated by adding all individual components in quadrature. 193

11.7 The D^{+} meson trigger and reconstruction efficiencies and systematic uncertainties. The total systematic error is calculated by adding all individual components in quadrature. 194

11.8 The D_s^{+} meson trigger and reconstruction efficiencies and systematic uncertainties. The total systematic error is calculated by adding all individual components in quadrature. 195

11.9 The D_s^{+} meson trigger and reconstruction efficiencies and systematic uncertainties. The total systematic error is calculated by adding all individual components in quadrature. 196

12.1 Summary of the measured direct charm meson cross sections and their uncertainties in different p_T bins. The first error is statistical and the second systematic. 216

12.2 Summary of the measured direct charm meson differential cross sections and their uncertainties at the center of each p_T bin. The first error is statistical and the second systematic. 217

12.3 calculated values of the bin center correction for D mesons in different p_T bins. For the uncertainties, the number between parentheses is the relative uncertainty in %. 220

List of Figures

1.1 The box diagrams for $B_s^0/\bar{B}_s^0$ mixing. 7

1.2 The unitarity triangle with the sides renormalized in a convenient way. 9

2.1 The leading order $\mathcal{O}(\alpha_s^2)$ Feynman diagrams of the heavy quark production. The left one is the quark-antiquark annihilation. The center and right diagrams are gluon fusion. 35

2.2 The next-to-leading order $\mathcal{O}(\alpha_s^3)$ Feynman diagrams of the heavy quark production. The first row is the hard gluon radiation, the second row is the gluon splitting, and the third row is flavor excitation. 35

2.3 The fragmentation of a heavy quark Q into a meson $H(Q\bar{q})$. 40

3.1 An overview of the Collider Detector of Fermilab in its Run II configuration. 46

3.2 A cut-away view of one quadrant of the inner portion of the CDF II detector showing the tracking region surrounded by the solenoid and end-cap calorimeters. 46

3.3 A helix in the transverse plane with the impact parameter d_0 and ϕ_0 labeled. The radius of the helix is $1/2C$, where C is the curvature. . . 47

3.4 1/6 section of the COT end plate. For each super layer is given the average radius. 49

3.5 An end view of the CDF II silicon system 52

3.6 A side view of half of the CDF Run II silicon system on a scale in which the z coordinate is highly compressed. 52

3.7 Time difference as a function of momentum between K/π, p/K and p/π traversing a distance of 140 cm, expressed in ps and separation power, assuming a resolution of 100 ps. The dashed line shows the K/π separation power from the dE/dx measurement in the COT. . . 55

3.8 The block diagram of the electronics processing chain for the signal of one phototube in the TOF system. 55

3.9 The average number of interactions ($\bar{N}$) for various conditions at CDF. 36 bunches is equivalent to 396 ns crossings, 108 bunches is equivalent to 132 ns crossings. 57

3.10 The functional block diagram of the CDF II data flow. 61

3.11 The block diagram the CDF II trigger system 61

5.1 The $K\pi$ invariant mass distribution of $D^0 \to K^-\pi^+$ candidates in different p_T bins. The lowest p_T bin has been split into two bins to improve the description of the signal and the background. The results of the fit are indicated in the upper right corner. The last number, FR, indicates the ratio between the width of the signal and the auto-reflection. It is not a free parameter in the fit; it has been determined from a study of tagged D^0's from D^{*+} as discussed in the text. 71

5.2 The $m(K\pi\pi) - m(K\pi)$ distribution for $D^{*+} \to D^0\pi^+, D^0 \to K^-\pi^+$ candidates in different p_T bins. The fit results are indicated in the upper right box. The parameters a and c determine the shape of the background, according to Equation 5.1. The variable f_1 indicates the fraction of the signal in the narrow Gaussian. 75

5.3 Difference between the histogram entries and the fitted curve that describes the signal and background in the Δm histogram of D^{*+} candidates in different p_T bins. 76

5.4 The D^+ and D_s^+ yield as a function of the vertex χ^2 requirement. The errors are statistical only. 78

5.5 The $K\pi\pi$ invariant mass distribution for $D^+ \to K^-\pi^+\pi^+$ candidates with different criteria on $\Delta m \equiv |m(K\pi\pi) - m(K\pi)|$. 80

5.6 The $K\pi\pi$ invariant mass distribution for $D^+ \to K^-\pi^+\pi^+$ candidates in different p_T bins. The fraction of the signal described by the narrow Gaussian indicated by f_1. 81

5.7 The $KK\pi$ invariant mass distribution for $D^+ \to \phi\pi^+$ and $D_s^+ \to \phi\pi^+, \phi \to K^+K^-$ candidates in different p_T bins. 82

5.8 The reconstructed mass distribution of D meson candidates. The curve is the superposition of the fitted D mass distributions in different P_T bins, and is used to calculate the χ^2 for the summed distributions. We obtain $\chi^2/\mathrm{NDF} = 1.88$ for D^0, 1.11 for D^{*+}, 1.32 for D^+, and 0.87 for D_s^+. 83

6.1 The impact parameter of direct and secondary charm in the $r - \phi$ plane. 90

6.2 The topology of the two track trigger bias for $D^0 \to K^-\pi^+$. 92

6.3 The impact parameter distribution predicted by the generator level Monte Carlo simulation described in the text of secondary D^0, D^{*+}, D^+ and D_s^+ after the SVT trigger requirements are satisfied. 94

6.4 The Monte Carlo prediction of the true impact parameter distributions for secondary D^0, D^{*+}, D^+ and D_s^+ after trigger and offline selection requirements 98

6.5 The $K^0_{\mathrm{S}} \to \pi^+\pi^-$ invariant mass, p_T and L_{xy} distributions. The left hand mass distribution is for K^0_{S} candidates with $d_0(\pi^+) \cdot d_0(\pi^-) < 0$, and the right hand mass distribution is for $d_0(\pi^+) \cdot d_0(\pi^-) < 0$. There is no signal apparent in this right hand mass distribution, which indicates a lack of secondary K^0_{S}. The p_T and L_{xy} distributions are for candidates in the 2σ signal region, which is defined in the text. No sideband subtraction has been performed. 101

6.6 The impact parameter distribution of K^0_{S} in the signal region (left) and sideband region (right) defined in the text. 101

6.7 The impact parameter distribution of K^0_S after side band subtraction. 107

6.8 The comparison between ct distributions of the prompt and secondary D mesons predicted by the Monte Carlo simulation and the distribution from data after side band subtraction. The distributions are normalized to one. 107

6.9 The impact parameter distribution for the signal region of the D^0 after side band subtraction. 108

6.10 The impact parameter distribution for the signal region of the D^{*+} after side band subtraction. 109

6.11 The impact parameter distribution for the signal region of the D^{+} after side band subtraction. 110

6.12 The impact parameter distribution for the signal region of the D_s^{+} after side band subtraction. 111

6.13 The impact parameter distribution of the D meson in signal region after side band subtraction. The black curve is the superposition of the fitted D meson impact parameter distributions in different P_T bins, and is used to calculate the χ^2 for the summed distributions. We obtain χ^2/NDF = 1.32 for D^0, 0.92 for D^{*+}, 1.05 for D^+, and 1.15 for D_s^+. The red curve is the fitted impact parameter distribution from the secondary charm mesons. The prompt D meson fractions f_D including all p_T bins are calculated using the event number and B fraction in each p_T bins. We obtain $f_D(D^0) = 86.5 \pm 0.4 \pm 3.5\%$, $f_D(D^{*+}) = 88.1 \pm 1.1 \pm 3.9\%$, $f_D(D^+) = 89.1 \pm 0.4 \pm 2.8\%$, and $f_D(D_s^+) = 76.0 \pm 3.2 \pm 2.1\%$, where the first error is statistical, and the second one is the systematic uncertainty. We also fit the D meson impact parameter distribution all together instead of in different p_T bins, and yield similar results: $f_D(D^0) = 86.5 \pm 0.4\%$, $f_D(D^{*+}) = 87.6 \pm 1.1\%$, $f_D(D^+) = 89.1 \pm 0.4\%$, and $f_D(D_s^+) = 72.4 \pm 3.4\%$, where the error is statistical only. Since we measure the D_s^+ cross section with minimum $p_T \geq 8\,\mathrm{GeV/c}$, the calculation shows that $f_D(D_s^+) = 77.3 \pm 3.8 \pm 2.1\%$, with χ^2/NDF = 1.15 in this case. 112

7.1 The COT efficiency as a function of $p_T(D)$ for charm meson reconstruction as determined from the track embedding study. The three different values of minimum merge criteria are described in the text. We use the values corresponding to 20 ns as our central value of efficiency. 118

7.2 Single-track XFT efficiency as a function of p_T, z_0, ϕ_0, and $\cot\theta$. The last plot is the XFT efficiency as a function of z_0 and $\cot\theta$ together. . 122

7.3 SVT efficiency dependence on the impact parameter d_0, as measured from J/Ψ data. Tracks are required to have 4 SVX hits, which explains the high SVT efficiency. Therefore, we use only the shape, not the absolute value. Note that the data used in our analysis correspond to the blue points (old patterns). 124

7.4 Single-track SVT efficiency as a function of p_T, z_0, ϕ_0, and $\cot\theta$ before excluding mechanical barrel-crossers. The last two plots are the SVT efficiency as a function of z_0 and ϕ_0 together for the data from two different beam stores, which shows the difference between their SVT configuration. 125

7.5 Single-track SVT efficiency as a function of p_T, z_0, ϕ_0, and $\cot\theta$ when excluding mechanical barrel-crossers. The last four plots are the SVT efficiency as a function of (z_0,$\cot\theta$) and (ϕ_0,$\cot\theta$) with and without excluding mechanical barrel-crossers. 126

7.6 The impact parameter distribution of tracks from the Level-1 two-track trigger. All tracks have $p_T \geq 2.0\,\mathrm{GeV}/c$ and 3 or more SVX ϕ-side hits in different layers. The fraction of tracks with an impact parameter $\geq 1\,\mathrm{mm}$, which fall outside the SVT acceptance, is 1.92%. 129

7.7 The efficiency for an offline track to have 3 or more SVX ϕ-side hits when the offline track is an SVT-matched track with $p_T(\mathrm{SVT}) \geq 2\,\mathrm{GeV}/c$. 131

7.8 Single-track SVX efficiency as a function of p_T, z_0, ϕ_0, and $\cot\theta$. The last two plots are the SVX efficiency as a function of z_0 and ϕ_0 together for the data from two different beam stores, which shows the difference between their SVX configurations. 133

7.9 XFT and SVT efficiency dependence on the number of tracks with $p_T \geq 2\,\mathrm{GeV}/c$ and $|\Delta\phi_0| \leq 0.6$; both efficiencies are measured using minimum bias data. 134

7.10 Left plots: The difference in angle between charm daughters with $p_T \geq 2\,\mathrm{GeV}/c$ (MC) after trigger and offline selection requirements. Middle plots: the MC multiplicity of tracks with $p_T \geq 2\mathrm{GeV}/c$ and $|\Delta\phi| \leq 0.6$. The generator used for the MC is HeavyQuarkGen: one charm meson per event is generated; no fragmentation tracks are simulated. Right plots: the same multiplicity distribution for data. . 136

8.1 XFT and SVT curvature resolution and their correlation measured from minimum bias data. The XFT resolution is not centered at zero, due to the bias in the XFT system, which was introduced intentionally to increase the XFT efficiency at a given p_T(XFT) threshold. 139

8.2 The results of the study of the d_0 distribution for offline tracks with 3 or more ϕ side SVX hits in minimum bias data (no XFT or SVT requirement). The quantities f_1, σ_1, and σ_2, and their corresponding parameterizations are described in the text. 141

8.3 SVT-matched track offline d_0 and online d_0(SVT) distributions in different p_T bins. The quantities f_1, σ_1, and σ_2 are described in the text. 143

8.4 The correlation of track impact parameters measured by SVT and offline SVX from data (minimum bias) and parameterization. 144

9.1 The block diagram of the detector Monte Carlo Simulation. 149

9.2 Upper plots: Using the correlation between the average impact parameter product of track pairs and their opening angle to determine the beam spot size. Lower plots: Beam spot size dependence on z. The low p_T threshold plots on the left are from minimum-bias data, the right-hand plots with the higher p_T threshold are from Level-1 accepts of the two-track trigger. 151

9.3 Shape of the luminous z-profile from minimum-bias data; the dashed lines indicate the size of the SVX detector, and the quoted efficiency refers to the $|z| \leq 47.25\,\mathrm{cm}$ requirement. The lower-right plot shows the run-dependence of the average z-position. 153

9.4 The top two plots are the COT reconstruction probabilities of kaons and pions that decay at the radius R inside COT. The other four plots are the hadronic interaction probabilities of kaons and pions as a function of various track parameters. 159

10.1 Comparison between measured two-track XFT efficiency and the Monte Carlo simulation, where we specifically require that both tracks to have opposite charge, and their offline qualities satisfy $p_{T1} \geq 2\,\mathrm{GeV}/c$, $p_{T2} \geq 2\,\mathrm{GeV}/c$, $p_{T1} + p_{T2} \geq 5.5\,\mathrm{GeV}/c$, and $2^\circ \leq |\Delta\phi_0| \leq 90^\circ$. 165

10.2 Comparison between measured two-track SVT efficiency from Level-1 auto-accepts of the two-track trigger and the parameterized two-track efficiency using the data as input. The tracks are required to have opposite charge, with $p_{T1} \geq 2\,\mathrm{GeV}/c$, $p_{T2} \geq 2\,\mathrm{GeV}/c$, $p_{T1} + p_{T2} \geq 5.5\,\mathrm{GeV}/c$, $2^\circ \leq |\Delta\phi_0| \leq 90^\circ$. Shown in green is the two-track efficiency without the additional 0.10 correlation for tracks in the same SVT wedge. 168

10.3 Plots (a),(b),(c) and (d) are comparisons between measured two-track SVT efficiency from Level-1 auto-accepts of the two-track trigger and the parameterized two-track efficiency of D^0 events from MC. The tracks are required to have opposite charge, with $p_{T1} \geq 2\,\mathrm{GeV}/c$, $p_{T2} \geq 2\,\mathrm{GeV}/c$, $p_{T1} + p_{T2} \geq 5.5\,\mathrm{GeV}/c$, $2^\circ \leq |\Delta\phi_0| \leq 90^\circ$. The deviation of the two track efficiencies between data and D^0 MC at low p_T bins is due to the different opening angle distribution between the two tracks, as illustrated in plot (e). In plot (f), the two tracks in Level-1 auto-accept data are required to have $K\pi$ invariant mass $|m(K\pi) - m(D^0)| \leq 400\,\mathrm{MeV}/c^2$, the deviation becomes less and is well covered by the systematic uncertainties. 169

10.4 Comparison between measured SVX efficiency for the third track and the Monte Carlo simulation. 171

10.5 Comparison between measured and simulated single-track XFT and SVT efficiency with minimum p_T requirement. 174

10.6 The p_T and L_{xy} distribution of K_S^0 after trigger and analysis requirements from Monte Carlo simulation and data. 174

10.7 Comparison between the K_s impact parameter distribution measured from two-track data and the Monte Carlo simulation. The black and red curve are the fit results of the K_S^0 impact parameter from data and MC respectively. The histogram is the d_0 distribution from data. All of them are normalized to one. 175

11.1 Dalitz distribution for $D^+ \to K^-\pi^+\pi^+$ with the amplitudes of the contributing resonances. 181

11.2 Comparison of normalized D^0, D^{*+} p_T distribution from data and Monte Carlo, and their ratios. 183

11.3 Comparison of normalized D^+, D_s^+ p_T distribution from data and Monte Carlo, and their ratios. 184

11.4 Comparison of normalized D^0, D^{*+} rapidity distribution from data and Monte Carlo, and their ratios. 186

11.5 Comparison of normalized D^+, D_s^+ rapidity distribution from data and Monte Carlo, and their ratios. 187

11.6 The D^0 trigger and reconstruction efficiency after various selections from Monte Carlo simulation. 198

11.7 The D^{*+} trigger and reconstruction efficiency after various selections from Monte Carlo simulation. 199

11.8 The D^+ trigger and reconstruction efficiency after various selections from Monte Carlo simulation. 200

11.9 The D_s^+ trigger and reconstruction efficiency after various selections from Monte Carlo simulation. 201

11.10 Comparison of normalized D meson p_T and z_0 distribution from data and Monte Carlo simulation, where we assume that the secondary D fractions are: $f_B(D^0) = 14\%$, $f_B(D^{*+}) = 12\%$, $f_B(D^+) = 12\%$, and $f_B(D_s^+) = 30\%$. 204

11.11 Comparison of normalized D meson L_{xy} and ct distribution from data and Monte Carlo simulation, where we assume that the secondary D fractions are: $f_B(D^0) = 14\%$, $f_B(D^{*+}) = 12\%$, $f_B(D^+) = 12\%$, and $f_B(D_s^+) = 30\%$. 205

11.12 The ratio between the D meson yields with and without offline d_0 requirements from Monte Carlo simulation (prompt D only) and data. 206

11.13 The ratio between the D meson yields with tight offline impact parameter requirements ($150\,\mu$m in the upper four plots and $200\,\mu$m in the lower four plots) and no offline impact parameter requirement for MC (prompt D only) and data. 207

11.14 Data/MC comparison of the angle between the D^{*+} flight direction and the direction of the π_s^+ in the D^{*+} center of mass frame. Here we assume the secondary D^{*+} fraction is $f_B(D^{*+}) = 12\%$. 208

11.15 Data/MC comparison of the angle between the D^0 flight direction and the direction of the K^- in the D^0 center of mass frame. For this plot we only used D^0's from D^{*+} decay for which there is no ambiguity of the mass assignment. Here we assume the secondary D^{*+} fraction is $f_B(D^{*+}) = 12\%$. 208

11.16 Dalitz-plot of the $D^+ \to K^-\pi^+\pi^+$ decay in MC (left) and data (right). No background subtraction has been applied to data. The lower plot shows the non-uniformity of the trigger and reconstruction efficiency over the allowed Dalitz-space. 209

12.1 D^0 meson differential cross section. The inner error bar represents the statistical uncertainty, the outer error bar the quadratic sum of the statistical and systematic uncertainty. 218

12.2 D^{*+} meson differential cross section. The inner error bar represents the statistical uncertainty, the outer error bar the quadratic sum of the statistical and systematic uncertainty. 218

12.3 D^+ meson differential cross section. The inner error bar represents the statistical uncertainty, the outer error bar the quadratic sum of the statistical and systematic uncertainty. 219

12.4 D_s^+ meson differential cross section. The inner error bar represents the statistical uncertainty, the outer error bar the quadratic sum of the statistical and systematic uncertainty. 219

12.5 Ratio of the measured cross sections to the theoretical calculation from Cacciari and Nason. The inner error bar represents the statistical uncertainty, the outer error bar the quadratic sum of the statistical and systematic uncertainty. The yellow line represents the uncertainty from varying the renormalization and factorization scale. 224

C.1 The pull distributions for the invariant mass (upper left), the decay length (upper right), and the impact parameter (lower left) for Monte Carlo generated $D^+ \to K^-\pi^+\pi^+$ decays. The lower right plot shows the probability distribution of the vertex χ^2. 237

D.1 The distributions of B fraction f_B determined by the fit for 100 toy experiments for each of the various f_b and signal N. 240

D.2 The pull distribution of B fraction f_B determined by the fit for 100 toy experiments for each of the various f_b and signal N. 241

Chapter 1

Introduction

Ever since the beginning of the twentieth century, it has been a long journey for particle physicists to search for the answers to two questions: what are the basic building blocks of matter? What are the interactions between those building blocks? Decades of experimental and theoretical work on those two questions have led to the "Standard Model" [1, 2, 3] of particle physics: a picture of the high energy physics. In the Standard Model, the fundamental building blocks of matter are spin-1/2 fermions contained in three generations of quarks and leptons. They are the down-type quarks (d, s, b), up-type quarks (u, c, t), charged leptons (e, μ, τ), and neutrinos (ν_e, ν_μ, ν_τ). These particles interact through the exchange of gauge bosons with integer spins: the weak intermediate vector bosons, $W^\pm$, Z^0 and the photon for electroweak interaction, and the eight gluons for the strong interaction. In order for the quarks and leptons to acquire mass while preserving local gauge invariance, a spontaneous symmetry breaking mechanism is invoked with an addition of spin zero neutral gauge boson field: the Higgs boson. This approach also naturally introduces a way to couple the charge 2/3 quarks (u,c,t) and the charge $-1/3$ quarks (d,s,b) through a 3×3 unitary matrix in the weak interaction,

$$V = \begin{pmatrix} V_{ud} & V_{us} & V_{ub} \\ V_{cd} & V_{cs} & V_{cb} \\ V_{td} & V_{ts} & V_{tb} \end{pmatrix}, \tag{1.1}$$

which is called the *Cabibbo-Kobayashi-Maskawa* (CKM) matrix [4, 5]. Although the Standard Model has been tremendously successful and has survived numerous severe tests during last a few decades, there are still many mysteries left for us to solve. These mysteries includes the existence of Higgs Boson, why there are three families? Why the masses are so different and why matter dominate antimatter in Universe? Studies of the production and decays of heavy flavor (beauty and charm) hadrons provide a powerful way to test Standard Model fermion sector, to understand the strong interaction theory, Quantum Chromodynamics (QCD), and to search the physics beyond Standard Model through virtual processes.

The Fermilab Tevatron is a proton-antiproton collider that provides a unique laboratory for us to test QCD, an essential piece of the Standard Model. During Run I data taken period from 1992 to 1996, bottom quark production was measured by both CDF [6, 7, 8] and D0 [9] at the center of mass energy of 1.8 TeV and found to be a factor of two or more larger than the next-to-leading order (NLO) QCD prediction [10, 11, 12, 13, 14]. The most recent publication of the B^+ meson production cross section by CDF [15] found an excess over the QCD predictions by about a factor of 3. However, recent theoretical developments [16] show that part of discrepancy may be due to incorrect implementation of fragmentation function. Since the Peterson fragmentation parameter [17] ϵ has been determined using leading-log calculations that are commonly used in shower Monte Carlo programs, the Peterson fragmentation function with an $\epsilon = 0.006 \pm 0.002$ is not appropriate to use in conjunction with the NLO calculation. After correctly using the fragmentation function combined with the NLO QCD calculation, the measured B^+ cross section is only 1.7 higher than the predicted value.

Given this discrepancy between measured and expected b quark production, it is of interest to compare the direct charm production cross section measurement with the theoretical prediction. At CDF Run I, the direct charm production measurement is not trivial since there was no dedicated trigger to collect large statistics of direct charm hadrons. Using the inclusive muon trigger, the direct D^{*+} production cross section was measured in the CDF Run I data [18] where the D^{*+} is reconstructed from the decay chain $D^{*+} \rightarrow D^0\pi^+, D^0 \rightarrow K^-\mu^+X$. The integrated D^{*+} cross section with $p_T(D^{*+}) \geq 10\,\mathrm{GeV}$ and $|y(D^{*+})| \leq 1$ has been found about 50 % higher than the NLO calculation [19]. However, this result was not published.

After Run I, the Tevatron beam energy was increased from $\sqrt{s} = 1.8\,\text{TeV}$ to $1.98\,\text{TeV}$, the CDF detector also underwent a major upgrade from 1992 to 2001. For the newly rebuilt CDF detector, which is refer to CDF II, a Silicon Vertex Tracker (SVT) [20] has been designed and implemented to trigger on displaced tracks, which is primarily motivated to enhance the CDF B physics potential by collecting a high statistics B hadron sample in fully hadronic final states. Using this trigger , large samples of fully reconstructed charm hadrons are also collected. In $1\,\text{pb}^{-1}$ data, we reconstructed [1] about 6000 $D^0 \to K^-\pi^+$, 1500 $D^{*+} \to D^0\pi^+, D^0 \to K^-\pi^+$, 5000 $D^+ \to K^-\pi^+\pi^+$, and 250 $D_s^+ \to \phi\pi^+, \phi \to K^-K^+$. Since most of them are directly produced by $p\bar{p}$ collision instead of originating from B hadron decays [21], all four kinds of charm meson direct production cross section can be measured even with limited CDF Run II data.

From the experimental point of view, the measurement of the charm meson direct production cross section is also very appealing for the CDF heavy flavor physics program (B physics and charm physics). The CDF II detector is almost completely rebuilt; a cross section measurement provides an opportunity to understand the new trigger and tracking systems, as well as the corresponding detector Monte Carlo simulation. The knowledge we obtained through this analysis will be valuable for future heavy flavor analyses at CDF. In next two sections, I will give a brief review on some

---

[1] The D meson yield depends on the reconstruction selection criteria. Unless state explicitly, the charge conjugate mode is implied.

highlights of heavy flavor physics program at CDF II, in addition to the heavy quark production.

1.1 Bottom Physics at CDF

The elements of the CKM matrix are fundamental parameters in the Standard Model and must be measured. The study of the decay of hadrons containing b quarks is important since these decays are sensitive to five of the nine elements of the CKM matrix. One way to test the consistency of the Standard Model, as well as to search for physics beyond the Standard Model [22, 23], is to explicitly test the unitarity of the CKM matrix through experimental measurements. In addition, the CP symmetry is broken naturally if the CKM matrix has a complex phase. This is of great interest because this violation is required to produce the large matter-antimatter asymmetry of the universe observed in cosmology.

For the last decade, the CDF B physics program has achieved tremendous success. At Tevatron, the $b\bar{b}$ cross section is much higher than the production cross section at e^+e^- machines. Despite the higher background rates, large statistics sample of B hadrons with good signal-to-noise ratio can be obtained using selective trigger. Furthermore, unlike the e^+e^- machines operating at $\Upsilon(4S)$ resonance that only produce B^+ and B_d^0, all b flavor hadrons are produced at Tevatron including

B_s, Λ_b, B_c. The CDF II upgrade has greatly enhanced the existing CDF B programs to test the Standard Model CKM mechanism and probe for non-CKM sources of CP and flavor violation. This enhanced program includes the measurement of the B_s^0 oscillation with high sensitivity, and CP asymmetry determinations in $B_s \to \psi\phi$, $B_d \to \psi K_S$, as well as $B_{d,s} \to h_1^+ h_2^-, h_i = K, \pi$. Moreover, the large statistics of B hadron sample gives us an opportunity to test QCD in great precision though measurement of lifetimes and production. As the result, the CDF B physics program provides many interesting and essential measurements, it is a good complement of the e^+e^- B factory.

The B physics program at Tevatron has been reviewed in depth in reference [24]. In the next section, I will only present a brief discussion on the B_s^0 mixing analysis at CDF Run II.

1.1.1 B_s Flavor Oscillation

For the neutral B_s^0 meson system, B_s mesons can oscillate between their particle and anti-particle state via the box diagrams shown in Figure 1.1. The box diagram calculation [22, 25] yields:

$$M_{12} = \frac{G_F^2 m_W^2}{12\pi^2} \eta_B f_B^2 B_B m_B S(\bar{m}_t/m_W)(V_{ts}^* V_{tb})^2, \tag{1.2}$$

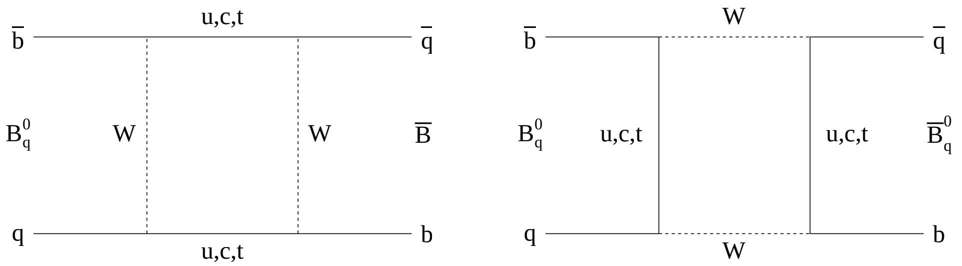

Figure 1.1: The box diagrams for $B_s^0/\bar{B}_s^0$ mixing.

where $S(\bar{m}_t/m_W) = 0.784(\bar{m}_t/m_W)^{2\times 0.76}$, $\eta_B = 0.55$ is a QCD correction, and $B_B f_B^2$ parameterizes the hadronic matrix element. Approximately we have

$$\Delta M_s \approx 2M_{12}. \tag{1.3}$$

The probability that a B_s^0 meson decays at proper time t in the same state or has mixed to the $\bar{B}_s^0$ state is given by

$$\begin{aligned} P_{unmix}(t) &= \tfrac{1}{2}\Gamma_s e^{-\Gamma_s t}(1+\cos\Delta M_s t), \\ P_{mix}(t) &= \tfrac{1}{2}\Gamma_s e^{-\Gamma_s t}(1-\cos\Delta M_s t), \end{aligned} \tag{1.4}$$

where Γ is the average decay rate of $B_s^0/\bar{B}_s^0$ mesons. For flavor-specific final states, we define the time dependent asymmetry and time-integrated mixing probability as the following:

$$A_{mix}(t) = \frac{N_{unmix}(t) - N_{mix}(t)}{N_{unmix}(t) + N_{mix}(t)} = \cos\Delta M_s t; \tag{1.5}$$

$$\chi_s = \frac{\int_0^{+\infty} P_{mix}(t)dt}{\int_0^{+\infty} P_{mix}(t)dt + \int_0^{+\infty} P_{unmix}(t)dt} = \frac{x_s^2}{2(1+x_s^2)}. \tag{1.6}$$

Where $x_s = \Delta M_s/\Gamma$ is the dimensionless mixing parameter.

At experiments in which both B_d^0 and B_s^0 are produced, the time integrated measurements determine the average mixing parameter $\bar{\chi} = f_d\chi_d + f_s\chi_s$, where

$f_d \approx 40\%$ is the B_d^0 fraction in the b sample, and $f_s \approx 11\%$ is the B_s^0 fraction. Since $\chi_d = 0.174 \pm 0.009$ [26] and $\bar{\chi} = 0.118 \pm 0.006$ [27], a large value for χ_s is required, indicating that B_s^0 mesons do oscillate. The B_s^0 mesons oscillate at very high frequency, $\chi_s \approx 0.5$. The time dependent asymmetry measurement is the only way to resolve the ΔM_s, since χ_s has no power to derive ΔM_s. So far several experiments have searched for the B_s^0 mixing; the searches are based either on inclusive lepton samples with high statistics but low B_s^0 purity, or on the low statistics exclusive semileptonic samples in which the D_s daughter of the B_s^0 has been reconstructed. Unfortunately no one has yet succeeded in directly measuring ΔM_s, only lower limits have been determined [26]:

$$\Delta M_s > 14.3\,\mathrm{ps}^{-1} \quad \text{at } 95\% \text{ C.L.} \tag{1.7}$$

Based on the CKM matrix parameters determined from the experimental data and theoretical evaluation, the limits on ΔM_S has been estimated in the Standard Model framework. ΔM_S is expected to be between [12.0 - 17.6] ps^{-1} within 68% C.L. and $< 20\,\mathrm{ps}^{-1}$ within 95% C.L. [28].

1.1.2 The Importance of B_s^0 Mixing in the Standard Model

Unlike the experiments operating on the $\Upsilon(4S)$, at CDF the B_s^0 are produced in large quantities. One of the particular strength of the CDF B physics program is the ability to measure B_s^0 mixing parameter ΔM_s directly. The unitarity of CKM matrix leads to nine unitarity relationship, one of which is particularly interesting:

$$V_{ud}V_{ub}^{*} + V_{cd}V_{cb}^{*} + V_{td}V_{tb}^{*} = 0. \tag{1.8}$$

In principle, some of these CKM matrix elements can be directly determined from observable physical qualities. For example, we can compute $|V_{td}|$ by measuring the oscillation frequency ΔM_d of the $B_d^0/\bar{B}_d^0$ mixing. However, these determinations are often limited by the large theoretical uncertainties. Therefore we approach the problem by doing the following approximation: $V_{ud} \approx V_{tb}^{*} \approx 1$, $V_{cb}^{*} \approx -V_{ts}$ and $V_{cd} = -\lambda$, where the parameter λ is the sine of the Cabibbo angle θ_C ($\sin\theta_C \approx 0.22$). Equation (1.8) is now simplified as

$$1 + \frac{V_{td}}{\lambda V_{ts}} - \frac{V_{ub}^{*}}{\lambda V_{cb}^{*}} = 0. \tag{1.9}$$

which is shown as the sum of three vectors in the complex plane in Figure 1.2.

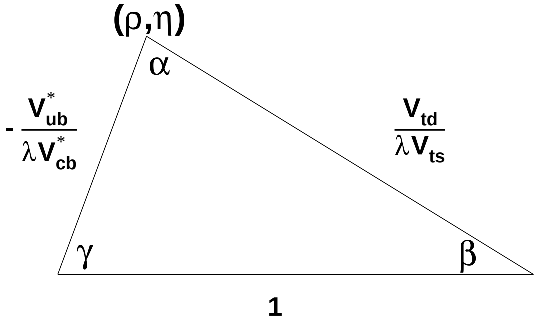

Figure 1.2: The unitarity triangle with the sides renormalized in a convenient way.

The Cabibbo angle is already measured with better than 1% precision: $\lambda =$

0.2196 ± 0.0023 [26]. The ratio $|V_{ub}/V_{cb}| = 0.090 \pm 0.025$ [26] was determined from the combined results from CLEO and LEP. The angle β has been measured by the CDF, Belle and BaBar collaborations, [29, 30, 31] from the asymmetry in $B_d^0/\bar{B}_d^0 \to J/\psi K_S^0$. The current combined results give a world average $\sin 2\beta = 0.734 \pm 0.055$, a more precise measurement is expected while more experimental data is accumulated in both Belle and BaBar.

As for $|V_{td}/V_{ts}|$, it can be determined by comparing ΔM_s to the already well measured oscillation frequency ΔM_d of $B_d^0/\bar{B}_d^0$ mixing [25]:

$$\frac{\Delta M_s}{\Delta M_d} = \frac{m_{B_s}}{m_{B_d}} \xi^2 \left| \frac{V_{ts}}{V_{td}} \right|^2 , \tag{1.10}$$

where $\xi = (f_{B_s}\sqrt{B_{B_s}})/(f_{B_d}\sqrt{B_{B_d}})$, B_{B_i} are the B meson bag parameters ($i = d, s$), and f_{B_i} are the B meson weak decay constants. ξ is of order unity and has been estimated theoretically as [27]:

$$\xi = 1.36 \pm 0.14. \tag{1.11}$$

Although Belle and BaBar do not have the ability to produce B_s^0 because of energy limitations at this moment, they do have the ability to determine $|V_{td}/V_{ts}|$ by measuring the ratio of decay rates of radiative B_d^0 decays $B(B_d^0 \to \rho\gamma)/B(B_d^0 \to K^*\gamma)$. However, the small branching fractions and potentially large long-distance contributions make the measurement and extraction of $|V_{td}/V_{ts}|$ difficult.

1.1.3 B_s mixing measurement in Hadronic Decay Channels at CDF

The basic analysis steps for any time-dependent $B_s^0/\bar{B}_s^0$ flavor oscillation measurement are as follows:

1. Reconstruct the B_s^0 meson in the appropriate flavor specific final states so that the B_s meson flavor at the time of decay can be determined. For example: the semileptonic decay mode $B_s^0 \to D_s^- l^+ \nu_l X$ or the hadronic mode $B_s^0 \to D_s^- \pi^+ (\pi^- \pi^+)$.

2. Measure the proper time $t = m_{B_s} L/P$ at which the decay occurred, where L is the decay length and P is the B_s momentum. The uncertainty on the proper time is given by
$$\sigma_t = t\sqrt{\left(\frac{\sigma_L}{L}\right)^2 + \left(\frac{\sigma_P}{P}\right)^2}. \tag{1.12}$$

3. Determine the flavor of the B_s meson at the production in order to classify whether the decay was mixed or unmixed at the time of decay. This determination is referred to as “b flavor tagging”.

4. Fit the measured time-dependent asymmetry with respect to the proper time to get the mixing frequency.

Unlike the $B_d^0/\bar{B}_d^0$ mixing, in which the dominant factor affecting the measurement is the effective tagging efficiency, the resolution of the proper time measurement in the $B_s^0/\bar{B}_s^0$ mixing measurement becomes another crucial factor because of its large mixing parameter. In general we require the proper time resolution not to be significantly larger than the period of oscillation. The partially reconstructed semileptonic B_s decays have much worse proper time resolution than the fully hadronic decays, such as $B_s^0 \to D_s^- \pi^+(\pi^-\pi^+)$, because of the large momentum uncertainty due to the undetected neutrino. Therefore fully hadronic decay modes are much more desirable for the $B_s^0/\bar{B}_s^0$ mixing measurement.

A hadronic SVT trigger has been added in CDF Run II. For the first time in the world, we are able to collect a large sample of B_s events fully reconstructed in hadronic final states that will have much smaller proper time resolution than the expected oscillation period. Furthermore, the momentum uncertainty is so small ($\leq 0.4\%$) that we can neglect its contribution to the overall proper time resolution in our analysis.

1.2 Charm Physics at CDF

Similar to the B-system, charm offers many opportunities to search for new physics. In the B-system, loop diagrams are often dominated by the heavy top-quark, resulting in large amplitudes for mixing, CP violation and penguin decays, all of which have by now been observed.

Since the charm is an up-type quark, loop diagrams do not involve the heavy top-quark and the Standard Model prediction for these processes is smaller by many orders of magnitude. Intermediate meson-states are expected to contribute at the 10^{-3} level and thus overshadow the short-distance contributions. While it will be more difficult to observe loop-mediated processes, new physics may enhance them and actually leave more distinct signatures in the charm system than in the bottom system.

Experimentally, charm has some distinct advantages compared to the B-system: Branching fractions into fully reconstructed modes are at the 10% level, while the product of branching ratios to fully reconstruct a B-decay is typically at the 10^{-4} level. About one third of the D^0's comes from a $D^{*+} \rightarrow D^0\pi^+$ decay, where the slow pion tags the D^0 flavor at production with an efficiency of almost 100%.

Charm physics has long been dominated by fixed target experiments such as SELEX, E791 and E687/FOCUS. B-factories running at the $\Upsilon(4S)$ get free charm from the continuum, with a cross-section similar to the B-cross-section. CLEO results are now competitive with the best fixed-target experiments. Many of the world best charm measurement are now coming from BaBar and Belle, which continue data taking at ever higher rates. CLEO is planning a 3-year special run (CLEO-C) at various thresholds to measure for example absolute branching ratios. However, they will not be able to compete in terms of statistics with BaBar or Belle. On the long term, LHC-B and BTeV will collect huge charm samples as well.

Charm physics has not yet been done at the $p\bar{p}$ collider, and it was not considered part of the CDF Run II physics program. Because of the large production cross section and the SVT trigger, CDF has the ability to collect a huge sample of charm hadrons, opening a completely new window of opportunities for CDF. By the end of 2002, CDF Run II recorded about $70\,\mathrm{pb}^{-1}$ data with silicon hit information, in which more than 1 million hadronic decayed D meson were reconstructed. This data set is already much larger than the statistics available from FOCUS, E791, CLEO, and is compatible with those of BABAR and Belle [32]. By the end of Run IIa, CDF will have more than 2×10^7 fully reconstructed D hadrons in $2\,\mathrm{fb}^{-1}$ data, which is more than 10 times of statistics from Belle and BaBar at this time [32]. Along with Dr. Rolf Oldeman and Professor Joseph Kroll, we were the first people to propose a charm physics program at CDF [33]. Since then, interest within the collaborations has grown and a new research program in the charm sector has been established at CDF.

In summary, given large amount of charm meson sample, CDF II is a natural charm factory and will play a major role in the future charm physics. In the following sections, we review some aspects of charm physics and a few measurements that the

CDF can be competitive.

1.2.1 $D^0 \leftrightarrow \overline{D}^0$ Mixing

Just like in the Kaon and B systems, mixing of neutral mesons can occur in the charm system through box-diagrams. Since the charm-quark is of the up-type, box-diagrams involve the relatively light d, s and b quark, and lack the large contributions from the heavy top-quark. The box-diagram prediction for $x = \frac{\Delta M}{\Gamma}$ and $y = \frac{\Delta\Gamma}{2\Gamma}$ are at the 10^{-5} level [34]. Hadronic intermediate states can bring this to the 10^{-3} level. New physics has little effect on $\Delta\Gamma$, but may have significant contributions to ΔM up to values of x at the 1% level. Contributions from non-perturbative QCD tend to increase $\Delta\Gamma$, but do little to ΔM. An observation of x at the percent level together with a strong limit on y at the 10^{-3} level would be a strong indication for new physics. No evidence for D^0 mixing has been found yet. Present limits on x and y are at the percent level.

There are three common ways to measure D^0 mixing:

- Measure the lifetime difference between CP-mixed and CP-specific states like $D^0 \to K^-\pi^+$ versus $D^0 \to K^-K^+$ or $D^0 \to \pi^-\pi^+$. This is directly sensitive to the value of y
- Measure wrong-sign hadronic decays like $D^0 \to K^+\pi^-$. The interpretation

of this measurement is complicated by Doubly-Cabibbo-Suppressed (DCS) decays without mixing. A time-dependent study is needed to disentangle y' and $(x'^2 + y'^2)$ from the DCS decay. Here $x' \equiv x \cos\delta + y \sin\delta$, $y' \equiv y \cos\delta - x \sin\delta$ where δ is the (as yet unknown) strong phase difference between the $D^0 \to K^-\pi^+$ and $D^0 \to K^+\pi^-$ decay.

- Measure wrong-sign semileptonic decays such as $D^0 \to K^+\mu^-\overline{\nu}_\mu$. This is sensitive to $(x^2 + y^2)$.

D^0 Mixing through lifetime differences

The most powerful method for measuring $\Delta\Gamma$ is comparing the lifetime of $D^0 \to K^-\pi^+$ (CP mixed) with $D^0 \to K^-K^+$ (CP even). The experimental situation for D^0 lifetime difference measurements is summarized in Table 1.1.

	$K^-\pi^+$	K^-K^+	y	reference
E791	35K	3.2K	$(0.8 \pm 2.9 \pm 1.0)\%$	[35]
FOCUS	120K	10K	$(3.4 \pm 1.4 \pm 0.7)\%$	[36]
CLEO	20K	2.5K	$(-1.2 \pm 2.5 \pm 1.4)\%$	[37]
BaBar	45K	4K	$(-1.0 \pm 2.2 \pm 1.7)\%$	[38]
Belle	214K	18K	$(-0.5 \pm 1.0 \pm 0.8)\%$	[39]

Table 1.1: Present status of D^0 lifetime difference measurements.

Particle identification is not mandatory for this measurement. The reflection from $D^0 \to K^-\pi^+$, where the kaon mass is attributed to the pion, has a reconstructed mass well above the D^0-mass. However, backgrounds from partially reconstructed charged charm are expected to affect the K^-K^+ channel stronger than the $K^-\pi^+$ channel and must be fully understood and corrected for, Alternatively, one can select a low-background sample of D^0 by requiring an accompanied slow π^+ from $D^{*+} \to D^0\pi^+$ decay, at the cost of a factor ≥ 3 loss in event sample. The trigger bias in lifetime due to impact-parameter cuts, cancels to first order the ratio of the two lifetimes. Further studies are needed to evaluate residual effects. For a precision measurement of $\Delta\Gamma$, the effect of secondary charm from B-decays needs to be studied.

D^0 Mixing through wrong-sign hadronic decays

In order to measure wrong sign decays of the D^0, one needs to identify the charm flavor both at production and decay. The most common method is to use the decay chain

$$D^{*+} \to D^0\pi^+, \quad D^0 \to \bar{D}^0 \to K^+\pi^-, K^+\pi^+\pi^-\pi^-$$

The charge of the soft pion from a $D^{*\pm}$ identifies the flavor of neutral D meson at production. The subsequent decay of D into final states with "wrong sign" kaon can be caused by mixing, Doubly Cabibbo Suppressed (DCS) decay or the interference between both. The three contributions can be disentangled from a time dependent analysis of r_{WS}, the ratio between wrong sign and right sign events [40]:

$$r_{WS} = r_{DCS} + y't\sqrt{r_{DCS}} + \frac{x'^2 + y'^2}{4}t^2 \tag{1.13}$$

The experimental status of wrong sign decays is summarized in Table 1.2. The experiments are only starting to extract limits on y' and x' from the time-dependence of this decay. Typically, the limits on x' and y' are at the few percent level.

	$D^{*+} \to K^-\pi^+$	$D^0 \to K^+\pi^-$	r_{WS}	reference
E791	5.6K	not quoted	$(0.68 \pm 0.34 \pm 0.07)\%$	[41]
FOCUS	37K	150	$(0.40 \pm 0.09 \pm 0.03)\%$	[42]
CLEO	13.5K	45	$(0.33 \pm 0.06 \pm 0.04)\%$	[43]
BaBar	120K	440	$(0.357 \pm 0.022 \pm 0.027)\%$	[44]
Belle	120K	450	$(0.372 \pm 0.025^{+0.009}_{-0.014})\%$	[45]

Table 1.2: Present status of wrong-sign hadronic D^0 decays

1.2.2 CP violation

Searches for CP violation in charm decays have concentrated on direct CP violation, since mixing in the charm system is known to be small. Direct CP violation can be observed as an asymmetry A_{CP} in the partial decays widths between $D \to f$ and its CP conjugate decay mode $\bar{D} \to \bar{f}$:

$$A_{CP} = \frac{\Gamma(D \to f) - \Gamma(\bar{D} \to \bar{f})}{\Gamma(D \to f) + \Gamma(\bar{D} \to \bar{f})}. \qquad (1.14)$$

Non-zero values of A_{CP} occur when the decay amplitude is the sum of two contribution, with differing weak and strong phases. For the CP-conjugate process, the weak phase changes sign, but the strong phase does not.

For singly Cabibbo suppressed decays, such as $D^0 \to K^+K^-$ or $D^+ \to K^+K^-\pi^+$, interference with Cabibbo favored penguin contributions are expected to result in values of A_CP at the 10^{-3} level.

The present experimental situation is summarized in Tables 1.2.2 and 1.2.2.

	$D^0 \to K^+K^-$	A_{CP}	reference
E791	600	$(-1.0 \pm 4.9 \pm 1.2)\%$	[46]
FOCUS	3.3K	$(-0.1 \pm 2.2 \pm 1.5)\%$	[47]
CLEO	3K	$(0.0 \pm 2.2 \pm 0.8)\%$	[37]

	$D^0 \to \pi^+\pi^-$	A_{CP}	reference
E791	350	$(-4.9 \pm 7.8 \pm 3.0)\%$	[46]
FOCUS	1.2K	$(4.8 \pm 3.9 \pm 2.5)\%$	[47]
CLEO	1.1K	$(1.9 \pm 3.2 \pm 0.8)\%$	[37]

Table 1.3: Present status of direct CP violation searches in neutral charm decays

	$D^+ \to K^+K^-\pi^+$	A_{CP}	reference
E791	2.3K	$(-1.4 \pm 2.9)\%$	[48]
FOCUS	14K	$(0.6 \pm 1.1 \pm 0.5)\%$	[47]

	$D^+ \to \pi^+\pi^-\pi^+$	A_{CP}	reference
E791	1.5K	$(-1.7 \pm 4.2)\%$	[48]

Table 1.4: Present status of direct CP violation searches in charged charm decays

For neutral charm, the flavor of the decaying D^0 has to be tagged. Thus one needs the D^0's that come from the $D^{*+} \to D^0\pi^+$ decay chain and have the charge of the slow pion reconstructed. Charged D-meson decays are self-tagging.

For fixed target experiments, production asymmetries complicate the measurement. Therefore, CP asymmetries are measured with respect to a Cabibbo-favored decay with a similar topology, for which no CP asymmetry is assumed. At the Tevatron, the total charm production is symmetric (small left-right asymmetries can be handled by choosing a symmetric acceptance in pseudo-rapidity). However, our tracking has highly asymmetric efficiencies for low-momentum particles, and we expected that CP asymmetries in CDF will need to be related to a Cabibbo-favored decay as well.

1.2.3 Rare and Forbidden Decays of charm

In the Standard Model, Flavor Changing Neutral Currents (FCNC) such as $c \rightarrow u\ell^+\ell^-$ are not allowed at tree-level, but can occur though box and penguin diagrams. The amplitudes are strongly suppressed and branching ratios from short distance physics are at the 10^{-8} level. Long distance contributions can bring this to the 10^{-6} level [49], mostly though an intermediate ϕ state. Analysis of the invariant mass distribution of the lepton pair allows to separate the short-distance from the long-distance contribution. In particular, the invariant mass region above the ϕ is dominated by short-distance contributions. New physics may increase the branching ratio and change the dilepton invariant-mass distribution.

The best limits on rare and forbidden charm decays with leptons in the final state come from two searches by E791. In a first paper [50] they set 21 limits on 3-body FCNC and forbidden decays, and 3 limits on 2-body fully leptonic decays of the D^0. Examples are $Br(D^+ \rightarrow \pi^+\mu^+\mu^-) < 1.5 \times 10^{-5}$, $Br(D_s^+ \rightarrow K^+\mu^+\mu^-) < 1.4 \times 10^{-4}$ and $Br(D^0 \rightarrow \mu^+\mu^-) < 5.2 \times 10^{-6}$. In a second paper [51] they set 18 limits on 4-

body decays of the D^0, and 9 limits on submodes that involve a resonance. Examples are $Br(D^0 \to \pi^+\pi^-\mu^+\mu^-) < 3.0 \times 10^{-5}$, $Br(D^0 \to \overline{K}^{*+}\mu^+\mu^-) < 2.4 \times 10^{-5}$.

Chapter 2

Theoretical Background

2.1 The Gauge Invariance

To our best knowledge, there are four fundamental forces in the universe. They are the gravitational, electromagnetic, weak and strong interaction. The Quantum Electrodynamics (QED) was formulated during 1940's [52, 53, 54, 55], and has achieved tremendous success with many precise experimental confirmation. The Lagrangian of QED is invariant under a local (position-dependent) phase rotation. The invariance is the famous *gauge symmetry* of QED. From the modern viewpoint, the gauge symmetry is a fundamental principle that determines the form of all the Lagrangian.

For a complex-valued Dirac field $\psi(x)$, under the gauge transformation

$$\psi(x) \to e^{-\alpha(x)}\psi(x), \tag{2.1}$$

its fermion mass term $m\bar{\psi}\psi(x)$ is invariant. However as for the kinematic term with derivative, we must compensate the difference in phase transformation in different space points. One simplest way is to define a scalar quantity $U(y, x)$ that depends on the two points and has the transformation law

$$U(y, x) \to e^{\alpha(y)}U(y, x)e^{-\alpha(x)} \tag{2.2}$$

simultaneously with (2.1). At zero separation, we set $U(y, y) = 1$. This defined an *covariant derivative* in the direction of the vector n^μ as follow:

$$n^\mu D_\mu \psi = \lim_{\epsilon \to 0} \frac{1}{\epsilon}[\psi(x + \epsilon n) - U(x + \epsilon n, x)\psi(x)]. \tag{2.3}$$

If the phase of $U(y, x)$ is a continuous function of the position y and x, then $U(y, x)$ can be expanded in the separation of the two points:

$$U(x + \epsilon n, x) = 1 - ie\epsilon n^\mu A_\mu(x) + \mathcal{O}(\epsilon^2). \tag{2.4}$$

Here we have an arbitrary constraint e and a new vector field $A_\mu(x)$. The covariant derivative then takes the form

$$D_\mu \psi(x) = \partial_\mu \psi(x) + ieA_\mu \psi(x). \tag{2.5}$$

The A_μ transforms under this local gauge transformation as

$$A_\mu(x) \to A_\mu(x) - \frac{1}{e}\partial_\mu \alpha(x). \tag{2.6}$$

The gauge invariant Lagrangian then has the form

$$\mathcal{L} = \bar{\psi}(i \not{D})\psi - \frac{1}{4}(F_{\mu\nu})^2 - m\bar{\psi}\psi. \tag{2.7}$$

Where

$$F_{\mu\nu} = \frac{1}{ie}[D_\mu, D_\nu] = \partial_\mu A_\nu - \partial_\nu A_\mu. \tag{2.8}$$

The previous discussion can be generalized to any continuous group of transformation, represented by a set of $n \times n$ unitary matrices V. Then the basic $\psi(x)$ will form an n-plet, and transform according to

$$\psi(x) \to V(x)\psi(x) = e^{i\alpha^a(x)t^a}\psi(x). \tag{2.9}$$

The corresponding Lagrangian is

$$\mathcal{L} = \bar{\psi}(i \not{D})\psi - \frac{1}{4}(F^i_{\mu\nu})^2 - m\bar{\psi}\psi. \tag{2.10}$$

Where

$$D_\mu = \partial_\mu - igA^a_\mu t^a, \tag{2.11}$$

$$[D_\mu, D_\nu] = -igF^a_{\mu\nu}t^a, \tag{2.12}$$

or more explicitly,

$$F^a_{\mu\nu} = \partial_\mu A^a_\nu - \partial_\nu A^a_\mu + gf^{abc}A^b_\mu A^c_\nu, \tag{2.13}$$

$$[t^a, t^b] = if^{abc}t^c. \tag{2.14}$$

2.2 Gauge Theories and Spontaneous Symmetry Breaking

Under the gauge invariance, the gauge boson must be massless since a mass term $\frac{1}{2}m_{ab}^2 A_\mu^a A^{b\mu}$ is incompatible with the local gauge invariance. In order to generate a mass for a gauge boson, a set of gauge invariant scalar fields have been introduced, which Lagrangian has the form as

$$\mathcal{L} = \frac{1}{2}|D_\mu \phi|^2 - V(\phi) = |(\partial_\mu - igA_\mu^a t^a)\phi|^2 - [-\frac{1}{2}\mu^2\phi^+\phi + \frac{\lambda}{4}(\phi^+\phi)^2]. \qquad (2.15)$$

Now let the ϕ_i acquire non-zero vacuum expectation values $\langle\phi_i\rangle = (\phi_0)_i$, and expand the ϕ_i about these values, the Lagrangian then contains a term with the structure of a gauge boson mass,

$$\Delta\mathcal{L} = \frac{1}{2}m_{ab}^2 A_\mu^a A^{b\mu}, \qquad (2.16)$$

with the mass matrix

$$m_{ab}^2 = g^2(t^a\phi)^+(t^b\phi). \qquad (2.17)$$

2.3 Standard model

In the Standard Model [1, 2, 3], there are three generations of quarks and leptons. They are the down-type quarks (d, s, b), up-type quarks (u, c, t), charged leptons (e, μ, τ), and neutrinos (ν_e, ν_μ, ν_τ). The up-type quark has electric charge $q = \frac{2}{3}e$ and the down-type quark has electric charge $q = -\frac{1}{3}e$, where e is the magnitude of the electron's electric charge. All the quarks and leptons are spin-half particles called fermions. They interact through the exchange of gauge bosons: the weak boson $W^\pm$ and Z^0, the photon, and the gluons, which have integer spins. These interactions are dictated by local gauge invariance, with gauge group $SU(3) \times SU(2) \times U(1)_Y$.

2.3.1 Quantum Chromodynamics

Quantum Chromodynamics (QCD) is the gauge theory which describes the strong interactions of the colored quarks and gluons, is one of the components of the $SU(3) \times SU(2) \times U(1)_Y$ Standard Model. Quarks have three colors, gluons have eight colors. A hadron is a color-singlet combinations of quarks, anti-quarks and gluons. The QCD Lagrangian is

$$\mathcal{L}_{QCD} = -\frac{1}{4}(F^a_{\mu\nu})^2 + i\sum_q \bar{\psi}^i_q \gamma^\mu (D_\mu)_{ij} \psi^j_q - \sum_q m_q \bar{\psi}^i_q \psi_{qj}, \tag{2.18}$$

$$F^a_{\mu\nu} = \partial_\mu A^a_\nu - \partial_\nu A^a_\mu + g_s f^{abc} A^b_\mu A^c_\nu, \tag{2.19}$$

$$(D_\mu)_{ij} = \delta_{ij}\partial_\mu - ig_s \sum_a \frac{\lambda^a_{ij}}{2} A^a_\mu, \tag{2.20}$$

where g_s is the QCD coupling constant, and the f_{abc} is the structure constants of the $SU(3)$ algebra. The $\psi^i_q(x)$ are the 4-component Dirac spinors associated with each quark field of color i and flavor q. The $A^a_\mu(x)$ are the 8 Yang-Mills gluon fields.

So far, no free quarks have been observed in nature. Although it has not been proved, it is generally believed that the QCD is a color confining theory, which means that colored objects cannot be liberated.

Like QED, the QCD coupling constant $\alpha_s = g_s^2/4\pi$ evolves as an function of the virtual gluon's momentum Q^2:

$$\alpha_s(Q^2) = \frac{\alpha_s(\mu^2)}{1 + \frac{\alpha_s(\mu^2)}{12\pi}(33 - 2n_f)\log(Q^2/\mu^2)}, \tag{2.21}$$

where n_f is the number of the quark flavors, μ^2 is an arbitrary scale. Since the number of quark flavor is six, α_s decreases as the Q^2 increases (short distance), which leads to the asymptotic freedom. It is customary to denote the Q^2 scale at which the coupling constant be come large by Λ

$$\Lambda = \mu^2 \exp\left[\frac{-12\pi}{(32 - 2n_f)\alpha_s(\mu^2)}\right]. \tag{2.22}$$

Thus the running coupling constant can be written as

$$\alpha_s(Q^2) = \frac{12\pi}{(33 - 2n_f)\log(Q^2/\Lambda^2)} \tag{2.23}$$

The QCD scaling factor $\Lambda = \Lambda_{\text{QCD}}$ is about the order of 200 MeV [26], for the heavy quark production $p\bar{p} \to q\bar{q}$ at Tevatron, the momentum transfer is high, therefore the QCD perturbation theory is a good approximation to calculate the quark production cross section.

2.3.2 Electroweak Interaction

In the standard electroweak model, the left-handed leptons and quarks forms the $SU(2)$ weak isospin doublets as

$$\begin{aligned} L_L &= \begin{pmatrix} \nu_L^i \\ l_L^i \end{pmatrix} = \left(\begin{pmatrix} \nu_e \\ e \end{pmatrix}_L, \begin{pmatrix} \nu_\mu \\ \mu \end{pmatrix}_L, \begin{pmatrix} \nu_\tau \\ \tau \end{pmatrix}_L \right), \quad Y = -\tfrac{1}{2}; \\ Q_L &= \begin{pmatrix} u_L^i \\ d_L^i \end{pmatrix} = \left(\begin{pmatrix} u \\ d \end{pmatrix}_L, \begin{pmatrix} c \\ s \end{pmatrix}_L, \begin{pmatrix} t \\ b \end{pmatrix}_L \right), \quad Y = +\tfrac{1}{6}. \end{aligned} \tag{2.24}$$

The right-handed fermion fields make singlet under this group.

$$\begin{aligned} L_R &= (l_R^i) = (e_R, \mu_R, \tau_R), \quad Y = -1; \\ U_R &= (u_R^i) = (u_R, c_R, t_R), \quad Y = +\tfrac{2}{3}; \\ D_R &= (d_R^i) = (d_R, s_R, b_R), \quad Y = -\tfrac{1}{3}. \end{aligned} \tag{2.25}$$

Where the Y is the hypercharge and the electric charge quantum number can be identified as $Q = T^3 + Y$. In the minimal model that there are three fermion families and a single complex Higgs doublet $\phi \equiv \begin{pmatrix} \phi^+ \\ \phi^0 \end{pmatrix}$, $Y = \frac{1}{2}$. The Lagrangian for $G = 3$ generation theory may be written as

$$\begin{aligned} \mathcal{L} &= \mathcal{L}_{scalar} + \mathcal{L}_{gauge} + \mathcal{L}_{leptons} + \mathcal{L}_{quarks} \\ &= \tfrac{1}{2}|D_\mu \phi|^2 - V(\phi) - \tfrac{1}{4}F^l_{\mu\nu}F^{l\mu\nu} - \tfrac{1}{4}f_{\mu\nu}f^{\mu\nu} \\ &\quad + \textstyle\sum_i \bar{L}_L^i (i\not{D}) L_L^i + \sum_i \bar{L}_R^i (i\not{D}) L_R^i \\ &\quad + \textstyle\sum_i \bar{Q}_L^i (i\not{D}) Q_L^i + \sum_i \bar{U}_R^i (i\not{D}) U_R^i + \sum_i \bar{D}_R^i (i\not{D}) D_R^i. \end{aligned} \tag{2.26}$$

Where the covariant derivative is

$$D_\mu = \partial_\mu - igA_\mu^a \tau^a - ig^{'} Y B_\mu . \tag{2.27}$$

The A_μ^a and B_μ are the $SU(2)$ and $U(1)$ gauge bosons respectively. (Here $\tau^a = \sigma^a/2$.) Through the gauge transformation, the scalar field can be expanded around the vacuum expectation value as

$$\phi(x) = U(x)\frac{1}{\sqrt{2}} \begin{pmatrix} 0 \\ v + h(x) \end{pmatrix} = U(x)\frac{1}{\sqrt{2}} \begin{pmatrix} 0 \\ \sqrt{\mu^2/\lambda} + h(x) \end{pmatrix} . \tag{2.28}$$

The two-component spinor of the right has an arbitrary real-valued lower component, given by the vacuum expectation value of ϕ and a fluctuating real-valued field $h(x)$ with $\langle h(x) \rangle = 0$. Here $U(x)$ is a general $SU(2)$ gauge transformation which can produces the general complex-valued two column spinor. We can make a gauge transformation to eliminate the $U(x)$ in the Lagrangian so that we work in the *unitarity gauge*. This reduces ϕ to a field to with only one physical degree of freedom, which is corresponding to a scalar particle with mass $m_h = \sqrt{2}\mu = \sqrt{2\lambda}v$. This particle is known as the Higgs boson. As for the gauge fields, the spontaneous symmetry breaking leads them to three massive vector bosons:

$$\begin{aligned} W_\mu^\pm &= \tfrac{1}{2}(A_\mu^1 \mp iA_\mu^2) \qquad &&\text{with mass } \ m_W = g\tfrac{v}{2}; \\ Z_\mu^0 &= gA_\mu^3 \cos\theta_W - g^{'} B_\mu \sin\theta_W \qquad &&\text{with mass } \ m_Z = m_W/\cos\theta_W . \end{aligned} \tag{2.29}$$

The fourth vector field, orthogonal to Z_μ^0 is the massless photon field:

$$A_\mu = g^{'} A_\mu^3 \sin\theta_W + gB_\mu \cos\theta_W \quad e = g\sin\theta_W . \tag{2.30}$$

Where

$$\cos\theta_W = \frac{g}{\sqrt{g^2 + g^{'2}}}, \quad \sin\theta_W = \frac{g^{'}}{\sqrt{g^2 + g^{'2}}}. \tag{2.31}$$

2.3.3 Fermion Mass Term

Notice that one cannot put the ordinary mass terms into the Electroweak Lagrangian because the left and right handed components of the fermion fields have different gauge quantum number so that the simple mass terms violate gauge invariance. To give the quarks and leptons masses, again we invoke the mechanism of spontaneous symmetry breaking. For the leptons, the gauge invariant coupling with the higgs field can be written as:

$$\mathcal{L}_{M,leptons} = -\sum_i \lambda_i \bar{L}^i_L \cdot \phi L^i_R + \text{h.c.} \tag{2.32}$$

If we expand the ϕ around its vacuum expectation value, we obtain the mass terms for leptons and also the coupling terms between leptons and the higgs field.

$$\mathcal{L}_{M,leptons} = -m_e \bar{e}_L e_R - m_\mu \bar{\mu}_L \mu_R - m_\tau \bar{\tau}_L \tau_R + \text{h.c.} + \cdots \tag{2.33}$$

Where the masses are: $m_e = \lambda_e \upsilon/\sqrt{2}$, $m_\mu = \lambda_\mu \upsilon/\sqrt{2}$, and $m_\tau = \lambda_\tau \upsilon/\sqrt{2}$. As for the Higgs field couplings to the quarks, if we don't impose any additional symmetries on the theory, we can write the most general renormalizable gauge invariant coupling terms as:

$$\mathcal{L}_{M,Quarks} = -\sum_{ij} \lambda^{ij}_d \bar{Q}^i_L \cdot \phi d^j_R - \sum_{ij} \lambda^{ij}_u \epsilon^{ab} \bar{Q}^i_{La} \phi^+_b u^j_R + \text{h.c.}, \tag{2.34}$$

where λ_d^{ij} and λ_u^{ij} are general complex-valued matrices. We can define the unitary matrices U_u and W_u by

$$\begin{aligned}\lambda_u\lambda_u^+ = U_u D_u^2 U_u^+, \quad \lambda_u^+\lambda_u = W_u D_u^2 W_u^+;\\ \lambda_d\lambda_d^+ = U_d D_d^2 U_d^+, \quad \lambda_d^+\lambda_d = W_d D_d^2 W_d^+,\end{aligned} \tag{2.35}$$

where D_u^2 and D_d^2 are two diagonal matrices with positive eigenvalues. Then we can obtain

$$\lambda_u = U_u D_u W_u^+, \quad \lambda_d = U_d D_d W_d^+, \tag{2.36}$$

where D_u and D_d are diagonal matrices with positive element values. Now we can expand the (2.34) around the vacuum expectation value and also make the change of variables

$$u_R^i \to W_u^{ij} u_R^j, \quad d_R^i \to W_d^{ij} d_R^j, \tag{2.37}$$

$$u_L^i \to U_u^{ij} u_L^j, \quad d_L^i \to U_d^{ij} d_L^j. \tag{2.38}$$

The (2.34) becomes

$$\mathcal{L}_{M,Quarks} = -\sum_i m_d^i \bar{d}_L^i d_R^i \left(\frac{h}{\upsilon}\right) - \sum_i m_u^i \bar{u}_L^i u_R^i \left(1 + \frac{h}{\upsilon}\right) + \text{h.c.} \tag{2.39}$$

Here we can express the quark masses as:

$$m_u^i = \frac{1}{\sqrt{2}} D_u^{ii} \upsilon, \quad m_d^i \frac{1}{\sqrt{2}} D_d^{ii} \upsilon. \tag{2.40}$$

Since each of the three u_R^i and each of the three d_R^i have the same coupling to the QCD and gauge field, W_u and W_d commute with the corresponding covariant derivative and the transformation (2.37) don't change the form of the QCD and

Electroweak Lagrangian. For the same token, the matrices U_u , U_d and their corresponding transformation (2.38) also keep the QCD Lagrangian invariant. However, u_L and d_L are mixed by the weak interaction. In the current that couples to the W boson field, we find

$$J^{\mu+} = \frac{1}{\sqrt{2}} \bar{u}^i_L \gamma^\mu d^i_L \rightarrow \frac{1}{\sqrt{2}} \bar{u}^i_L \gamma^\mu (U^+_u U_d)^{ij} d^j_L. \tag{2.41}$$

Here the unitary matrix

$$V = U^+_u U_d \tag{2.42}$$

is known as the *Cabibbo-Kobayashi-Maskawa* (CKM) mixing matrix [4, 5].

2.3.4 The CKM Matrix

In the Standard Model, the quarks and leptons are coupled to the W bosons field via the charged current J^μ_{cc}. The Charge-current interaction Lagrangian is given by

$$\mathcal{L}_{cc} = -\frac{g}{\sqrt{2}} \left(J^\mu_{cc} W^+_\mu + J^{\mu+}_{cc} W^-_\mu \right), \tag{2.43}$$

where the weak charge current is

$$J^\mu_{cc} = \sum_k \bar{\nu}^k_l \gamma_\mu \frac{1}{2}(1-\gamma_5) l^k + \sum_{ij} \bar{u}^i \gamma_\mu \frac{1}{2}(1-\gamma_5) V_{ij} d^j. \tag{2.44}$$

Here the sum (i, j, k) are over the 3 generations. The 3×3 unitary matrix V is the CKM matrix which describes the coupling of the charge 2/3 quarks and the charge

$-1/3$ quarks.

$$V = \begin{pmatrix} V_{ud} & V_{us} & V_{ub} \\ V_{cd} & V_{cs} & V_{cb} \\ V_{td} & V_{ts} & V_{tb} \end{pmatrix} \tag{2.45}$$

An unitary 3×3 matrix depends on nine parameters: three real angle and six phases. We can remove these phases by making the phase rotations of the quark fields as

$$u_L^i \rightarrow \exp[i\alpha_u^i]u_L^i \quad d_L^i \rightarrow \exp[i\alpha_d^i]d_L^i \quad \text{(no sum)}, \tag{2.46}$$

since this global phase rotation has no effect on any term of the Lagrangian except for the weak charge current (2.44). Notice that a equal phase rotation for all 6 quark fields cancels out of the (2.44), so we can remove only 5 of those phases. The final form of CKM matrix therefore can be written in terms of four independent real parameters, in which one of them is a phase factor. Inspired by the 2 generation matrix introduced by Cabibbo [4], Wolfenstein [56] has written the CKM matrix in a form as following:

$$V = \begin{pmatrix} 1-\lambda^2/2 & \lambda & A\lambda^3(\rho - i\eta) \\ -\lambda & 1-\lambda^2/2 & A\lambda^2 \\ A\lambda^3(1-\rho-i\eta) & -A\lambda^2 & 1 \end{pmatrix} \tag{2.47}$$

The parameter λ is the sin of the Cabibbo angle θ_C ($\sin\theta_C \approx 0.22$). Based on current measurement of CKM matrix elements, the values of the Wolfenstein parameters are [26]:

$$\lambda = 0.2196 \pm 0.0023,\ A = 0.819 \pm 0.035,\ (\rho^2 + \nu^2)^{1/2} = 0.36 \pm 0.09 \tag{2.48}$$

2.3.5 The Electroweak Lagrangian

After spontaneous symmetry breaking the complete Electroweak Lagrangian can be expressed as

$$\mathcal{L}_{EW} = \mathcal{L}_{kin} + \mathcal{L}_{int} \tag{2.49}$$

Where the interaction term for fermion fields is:

$$\begin{aligned}
\mathcal{L}_F = \;& \mathcal{L}_{HIGGS} + \mathcal{L}_{EM} + \mathcal{L}_{NC} + \mathcal{L}_{CC} \\
= \;& -\textstyle\sum_i \left(m_l^i \bar{l}^i l^i + m_u^i \bar{u}^i u^i + m_d^i \bar{d}^i d^i\right) \frac{h}{v} \\
& -e \textstyle\sum_i \left[-\bar{l}^i \gamma_\mu l^i + \frac{2}{3} \bar{u}^i \gamma_\mu u^i - \frac{1}{3} \bar{d}^i \gamma_\mu d^i\right] A^\mu - \frac{g}{4\cos\theta_W} \sum_i \bar{\nu}^i \gamma_\mu (1-\gamma_5) \nu^i Z^\mu \\
& -\tfrac{g}{4\cos\theta_W} \textstyle\sum_i \bar{l}^i \gamma_\mu \left[2\sin^2\theta_W (1+\gamma_5) + (2\sin^2\theta_W - 1)(1-\gamma_5)\right] l^i Z^\mu \\
& -\tfrac{g}{4\cos\theta_W} \textstyle\sum_i \bar{u}^i \gamma_\mu \left[-\frac{4}{3}\sin^2\theta_W (1+\gamma_5) + (1 - \frac{4}{3}\sin^2\theta_W)(1-\gamma_5)\right] u^i Z^\mu \\
& -\tfrac{g}{4\cos\theta_W} \textstyle\sum_i \bar{d}^i \gamma_\mu \left[\frac{2}{3}\sin^2\theta_W (1+\gamma_5) + (-1 + \frac{2}{3}\sin^2\theta_W)(1-\gamma_5)\right] d^i Z^\mu \\
& -\tfrac{g}{\sqrt{2}} \left[\textstyle\sum_k \bar{\nu}^k \gamma_\mu \frac{1}{2}(1-\gamma_5) l^k + \sum_{ij} \bar{u}^i \gamma_\mu \frac{1}{2}(1-\gamma_5) V_{ij} d^j\right] W_\mu^+ \\
& -\tfrac{g}{\sqrt{2}} \left[\textstyle\sum_k \bar{l}^k \gamma_\mu \frac{1}{2}(1-\gamma_5) \nu^k + \sum_{ij} \bar{d}^i V_{ij}^+ \gamma_\mu \frac{1}{2}(1-\gamma_5) u^j\right] W_\mu^- .
\end{aligned} \tag{2.50}$$

Here the summation is over the 3 generations and the V is the CKM matrix.

2.4 Heavy Quark Production

For the heavy quark $Q = (c, b, t)$ production in the $p\bar{p}$ hadron collider, the $Q\bar{Q}$ pairs are produced by the hard collision of a parton from each hadron. There are two

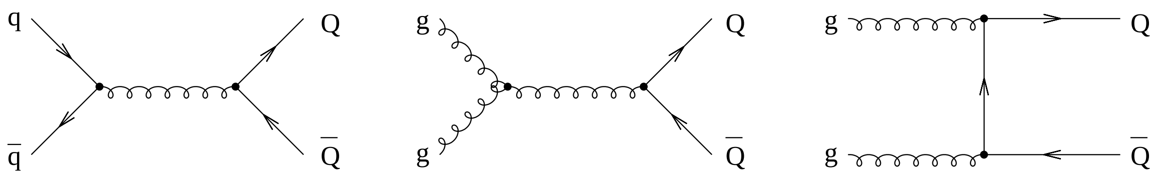

Figure 2.1: The leading order $\mathcal{O}(\alpha_s^2)$ Feynman diagrams of the heavy quark production. The left one is the quark-antiquark annihilation. The center and right diagrams are gluon fusion.

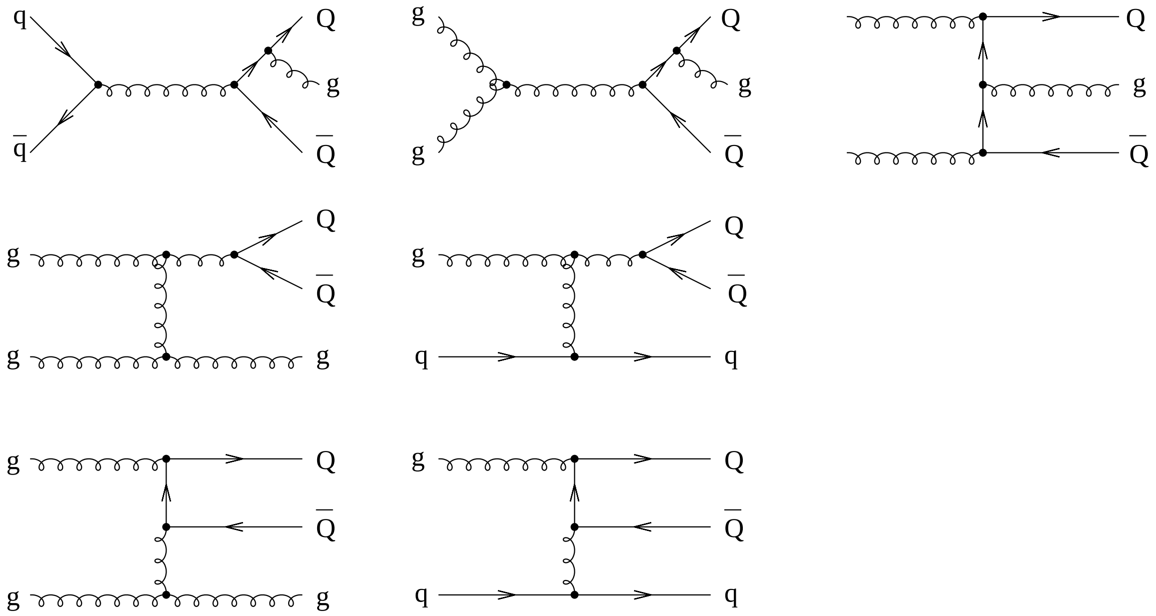

Figure 2.2: The next-to-leading order $\mathcal{O}(\alpha_s^3)$ Feynman diagrams of the heavy quark production. The first row is the hard gluon radiation, the second row is the gluon splitting, and the third row is flavor excitation.

contributions for the leading order (LO) calculation:

$$q + \bar{q} \to Q + \bar{Q} \text{ and } g + g \to Q + \bar{Q}, \tag{2.51}$$

as shown in Figure 2.1. For the s-channel diagram, it is obviously that the minimum transverse momentum exchange $\sqrt{\hat{s}}$ is $4m_Q$, where the m_Q is the heavy quark mass. As for the t-channel, it can be easily shown that the $\sqrt{\hat{s}} = m_Q$ is the minimum virtual momentum exchanged. Since the heavy quark mass is much larger than the Λ_{QCD}, perturbative QCD can be applied to calculate the heavy quark production. On the other hand, this is not the case for the light quarks due to their small masses.

At the $p\bar{p}$ collisions, the final quark production cross sections are convoluted with the parton distribution functions $f(x)$, which is the probability for a parton to carry a fraction x of the hadron momentum $\sqrt{s}$. If we neglect the intrinsic transverse momentum and know the transverse momenta p_T and rapidity of the outgoing heavy quarks, the momentum fraction x_1 and x_2 of the partons will be fixed. their four momentum in the center-of-mass frame of the incoming hadrons can be written as:

$$\begin{aligned} p_1 &= \tfrac{1}{2}\sqrt{s}(x_1, 0, 0, x_1), \\ p_2 &= \tfrac{1}{2}\sqrt{s}(x_2, 0, 0, -x_2), \\ p_Q &= (m_T \cosh y, p_T, 0, m_T \sinh y), \\ p_{\bar{Q}} &= (m_T \cosh \bar{y}, -p_T, 0, m_T \sinh \bar{y}). \end{aligned} \tag{2.52}$$

The y and $\bar{y}$ are the produced quark and anti-quark rapidity, and the $m_T =$

$\sqrt{p_T^2 + m_Q^2}$ is the transverse momentum. They are defined by

$$y = \frac{1}{2} \ln \left(\frac{E + p_z}{E - p_z} \right), \quad \hat{s} = 2m_T[1 + \cosh(y - \bar{y})]. \tag{2.53}$$

The final hadron-production quark cross section is then expressed

$$\frac{d\sigma}{dy d\bar{y} dp_T^2} = \frac{1}{16\pi^2 \hat{s}^2} \sum_{i,j} x_1 f_i(x_1) x_2 f_i(x_2) \bar{\sum} |M_{ij \to Q\bar{Q}}|^2. \tag{2.54}$$

For a fixed value of p_T, the production rate is heavily suppressed when $|y - \bar{y}|$ becomes large, thus the Q and $\bar{Q}$ tend to be created with the same rapidity. Heavy quark production cross section is dependent of the quark mass, which becomes less when the transverse momentum transfer $\sqrt{\hat{s}}$ gets larger. At the Tevatron Run I energy $\sqrt{s} = 1.8\,\mathrm{TeV}$, the $\sigma(p\bar{p} \to c\bar{c}) \gg \sigma(p\bar{p} \to b\bar{b})$ at low p_T, and becomes almost equal when $p_T \geq 40\,\mathrm{GeV}$, which is equivalent to $\sqrt{\hat{s}} \geq 80\,\mathrm{GeV}$. In case of the top, the production rate is a lot less than b and c until we go out to $p_T \geq 400\,\mathrm{GeV}$ because of the much heavier top mass.

The hadron parton distribution function is determined by the lepton hadron deep inelastic scattering. In the limit of large momentum transfer q^2 (Bjorken limit), the parton inside the hadron behaves like pointlike particles, the interaction between partons are negligible. The parton distribution function depend only on the dimensionless variable x, which is called scaling law. However, a quark or gluon carrying a momentum fraction x could do so either because it intrinsically has that momentum fraction or because it originally had a larger momentum fraction but radiates a gluon and drops to x. There is more phase space available to radiate gluons at larger q^2, so the parton distribution functions show a greater probability to small x if q^2 is larger. As the result, the parton distribution function is also a function of q^2. This variation is called "scaling violation". For large q^2, since the gluon radiation can be calculated in perturbative QCD, the structure function can be inferred at q^2 and x given a known measured value at certain q^2 and x. Consequently in Equation 2.54, the parton distribution function used is defined at a factorization scale μ_f. Since the majority momentum of proton is carried by the gluons, the $b\bar{b}$ and $c\bar{c}$ are dominated by the gluon gluon interaction. However, as for the top quark, large momentum fractions x are needed to pass the kinematic threshold ($\hat{s} \sim x_1 x_2 s \geq m_t^2$), the $t\bar{t}$ is produced predominantly by $q\bar{q}$ annihilation due to steeply falling gluon distribution function at larger x.

Figure 2.2 shows some of the NLO Feynman diagrams of the heavy quark production, they are corresponding to the following process:

$$\begin{aligned} q + \bar{q} &\rightarrow Q + \bar{Q} + g \\ g + \bar{g} &\rightarrow Q + \bar{Q} + g \\ g + q &\rightarrow Q + \bar{Q} + q \\ g + \bar{q} &\rightarrow Q + \bar{Q} + \bar{q} \end{aligned} \tag{2.55}$$

The complete calculation of the next-to-leading (NLO) order calculation were done in reference [10, 11, 12, 13, 14]. It has been found that the NLO contribution terms have similar magnitudes as the LO contributions for $b\bar{b}$ production, which implies that the high order correction may not negligible. Although a full calculation of next-to-next-to-leading (NNLO) QCD contributions are beyond current ability, one may hope that the resumed large logarithms due to collinear gluon emission capture all the essential features of the higher-order corrections, so that a complete NNLO QCD is not necessary. In the calculation of bottom and charm production, people often set the default factorization scale μ_F and the renormalization scale μ_R at:

$$\mu_F = \mu_R = \mu = \sqrt{m_Q^2 + p_T^2}. \tag{2.56}$$

Detail discussion on the heavy quark production can be found in reference [57, 58, 59, 60].

2.5 Heavy Quark Fragmentation

When a heavy quark $Q = c, b$ is produced by a hard collision between partons, it pulls a light quark-antiquark pair $q\bar{q}$ from the vacuum, and one of them is then picked up to form a heavy meson $H = Q\bar{q}$, as shown in Figure 2.3. This soft hadronization (fragmentation) process is non-perturbative, and can not be calculated reliably from the first principle. Since the energy scale of the fragmentation is much softer than that of the initial heavy quark creation, it is generally considered that these two processes are decoupled. Therefore the hadron-level cross section for $H(Q\bar{q})$ can

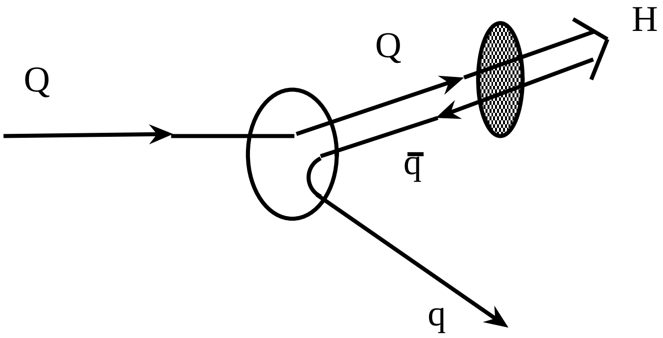

Figure 2.3: The fragmentation of a heavy quark Q into a meson $H(Q\bar{q})$.

be written as

$$\frac{d\sigma}{dp} = \int dp_Q dz \frac{d\sigma^Q}{dp_Q} D(z)\delta(p - zp_Q) = \int dz(\frac{1}{z}D(z)\frac{d\sigma^Q}{dp_Q}(p/z), \tag{2.57}$$

where the P_Q is the momentum of the heavy quark, z is the fraction of the available momentum carried by the heavy hadron, and the fragmentation function $D_Q^H(z) = D(z)/z$ is then the probability density to find the meson $H(Q\bar{q})$ with momentum $p = zp_Q$.

Inclusion of non-perturbative effects in the calculation of the heavy quark fragmentation is done in practice by convolving the perturbative results with a phenomenological non-perturbative form. Among several parameterization [61], one of the most popular ones is the Peterson parameterization [17]. When a light antiquark $\bar{q}$ is attached to a heavy quark Q, the heavy quark Q only slightly decelerates and its momentum is almost the same as the heavy meson $H(Q\bar{q})$. The corresponding transition amplitude [62]: is approximately inversely proportional to the energy transfer: $\Delta E = E_H + E_q - E_Q$. Assuming $m_H \approx m_Q$ for simplicity, we have

$$\begin{aligned}\Delta E &= (m_Q^2 + z^2 p_Q^2)^{1/2} + (m_q^2 + (1-z)^2 p_Q^2)^{1/2} - (m_Q^2 + p_Q^2)^{1/2} \\ &\propto 1 - 1/z - \epsilon/(1-z),\end{aligned} \tag{2.58}$$

therefore the Peterson fragmentation function can be written as

$$D_Q^H(z) = \frac{N}{z[1 - 1/z - \epsilon/(1-z)]^2}, \tag{2.59}$$

where the N is the normalization factor that is fixed by summing over all hadrons containing Q,

$$\Sigma \int dz D_Q^H(z) = 1\,. \tag{2.60}$$

The Peterson parameter $\epsilon \sim m_q^2/m_Q^2$ is a non-perturbative parameter that dependent on the Q and meson $H(Q\bar{q})$. It is determined experimentally and the typical values for charm and bottom quarks are $\epsilon_c \sim 0.02$ and $\epsilon_b \sim 0.006$ depending on the model of hard radiation [61]. The fragmentation reduce the meson momentum with respect to that of the Q quark. This effect is roughly the order of $\Lambda_{\mathrm{QCD}}/m_Q$, as the result, the charm fragmentation is much softer than the bottom quark's.

The fragmentation function $D(z)$ is often extracted from the fits to e^+e^- data. One can easily show that

$$\langle x_H^{N-1} \rangle = \langle x_Q^{N-1} \rangle D_N \tag{2.61}$$

where

$$x_H = \frac{p}{p_{\max}}, \quad x_Q = \frac{p_Q}{p_{Q\max}}, \quad D_N = \int dz z^{N-1} D(z). \tag{2.62}$$

It has been noted that for the hadronic cross section computation, only the first a few moments of the fragmentation function are important. This can be easily seen from the fact that heavy quark hadroproduction cross section is a steeply falling function of the transverse momentum, following roughly a power law. Assuming the form $d\sigma/dp_Q = Ap_Q^{-n}$, one can obtain that

$$\frac{d\sigma}{dp_T} = \frac{A}{p_T^n} D_n. \tag{2.63}$$

The measurement data of heavy quark spectra in e^+e^- machines is mostly sensitive to the first moment, as for the hadronic collision, the exponent n ranges from 3 to 5.

Chapter 3

CDF Detector

3.1 Overview

The Collider Detector at Fermilab (CDF) is a general purpose experiment to study the $p\bar{p}$ collision at the Fermilab Tevatron Collider. Since the first collision in October of 1985, at the center-of-mass energy at $\sqrt{s} = 1.8\,\mathrm{TeV}$, the Tevatron and CDF performance have steadily improved and yield large sample of data. The analysis of the experimental data resulted in more than 100 published papers ranging over the entire state of the hadron collider physics.

Since the shutdown of 1996, the Tevatron and CDF detector had underdone major upgrades [20]. The modest increase in the Tevatron energy from $\sqrt{s} = 1.8\,\mathrm{TeV}$

to $\sqrt{s} = 2.0\,\mathrm{TeV}$ has a major impact on physics. (For example it increases the $t\bar{t}$ yield by 40 %.) The dramatically increases of the luminosity provided by the Main Injector also give us the capability of precision hadron collider physics. Assuming that the proton and antiproton beams collide head-on without a crossing angle and with optimal alignment, the Tevatron's luminosity can be written as

$$\mathcal{L} = \frac{f_{\mathrm{BC}} N_p N_{\bar{p}}}{2\pi T(\sigma_p^2 + \sigma_{\bar{p}}^2)} F(\frac{\sigma_l}{\beta^*}) \tag{3.1}$$

where $T \approx 21\,\mu\mathrm{s}$ is the revolution period, f_{BC} is the number of bunches in each beam, N_p and $N_{\bar{p}}$ are the number of protons and antiprotons per bunch, σ_p and $\sigma_{\bar{p}}$ are the transverse beam sizes (RMS) at the interaction point, and F is a form factor that depends on the ratio between the bunch longitudinal RMS size σ_l, and the beta function β^* at the interaction point. At Run II, the Tevatron luminosity will be increased most significantly by increasing the number of bunches per beam from 6 to 36, while keeping similar or even higher N_p and $N_{\bar{p}}$ than Run I figures. The goal of accumulated integrated luminosity at Tevatron Run II is $2\,\mathrm{fb}^{-1}$, using the luminosity as high as $2 \times 10^{32}\,\mathrm{cm}^{-2}\mathrm{s}^{-1}$.

In order to accommodate the higher collision rate, and to best utilize the CDF physics program capabilities, most of the existing CDF detector have been rebuilt or upgraded. This chapter gives a general description of the CDF II detector with an emphasis on the elements relevant to this analysis. Figure 3.1 is an overview of the detector, and Figure 3.2 shows a 1/4 slice of the detector with more detailed labeling of the components.

3.2 Tracking System

3.2.1 Helix Parameters at CDF

In the standard CDF coordinate system, the proton direction is defined as the $\hat{z}$ or longitudinal axis, which is opposite to the magnetic field direction. In the transverse plane looking in the proton direction, the 9'clock position defines the $\hat{x}$ axis and the 12 o'clock position is the $\hat{y}$ axis. The polar angle θ is measured starting from the positive $\hat{z}$ direction, and the pseudorapidity is defined as

$$\eta = -\log(\tan\frac{\theta}{2}) \tag{3.2}$$

In a homogeneous magnetic field the trajectory of a charged particle is a helix which axis is parallel to the magnetic field, as shown in Figure 3.3. At CDF the 5 tracking parameters [63] used to describe the helix of the charged particle are:

$$\vec{\alpha} = (\lambda, C, z_0, d_0, \phi_0) \tag{3.3}$$

where λ=cot θ, θ is the polar angle at the minimum approach. C is the half curvature and has the same sign as the particle charge. z_0 and ϕ_0 are the z position and direction at the point of minimum approach to origin of helix respectively. d_0 is the signed impact parameter, its magnitude is equal to the distance between helix and

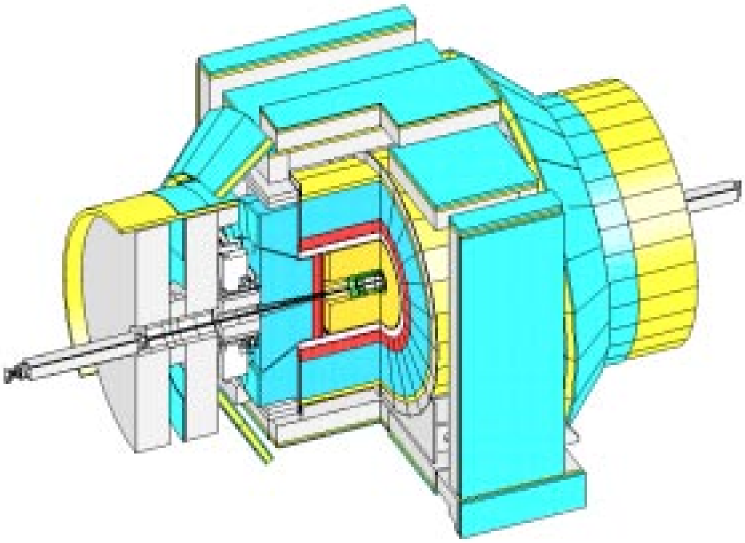

Figure 3.1: An overview of the Collider Detector of Fermilab in its Run II configuration.

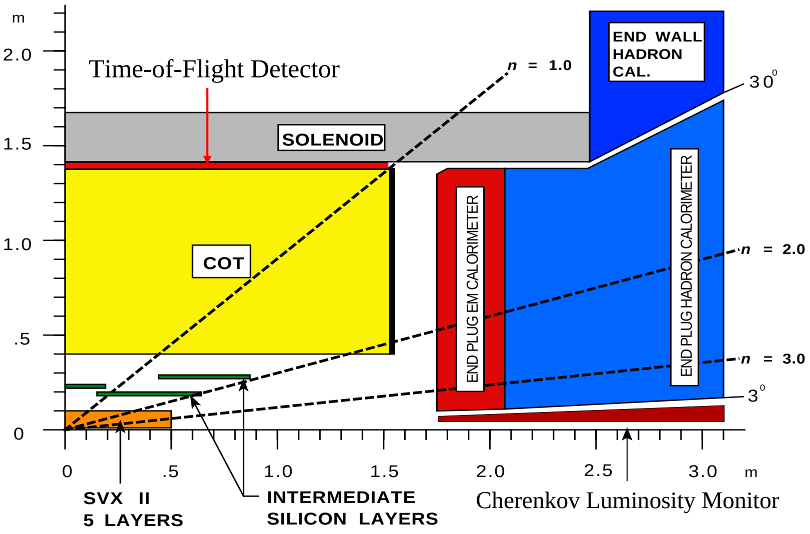

Figure 3.2: A cut-away view of one quadrant of the inner portion of the CDF II detector showing the tracking region surrounded by the solenoid and end-cap calorimeters.

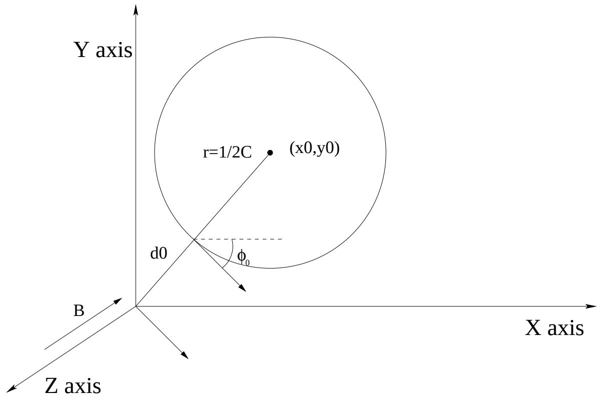

Figure 3.3: A helix in the transverse plane with the impact parameter d_0 and ϕ_0 labeled. The radius of the helix is $1/2C$, where C is the curvature.

origin at minimum approach. The impact parameter of a track has a sign that is defined by the following formula:

$$d_0 = \frac{\hat{z} \cdot (\vec{r} \times \vec{P}_T)}{|\vec{P}_T|}, \tag{3.4}$$

where $\vec{p}_T$ is the transverse momentum vector of the particle, $\vec{r}$ is the vector pointing from the primary vertex to the reconstructed particle trajectory at the point of closest approach to the primary in the $r - \phi$ plane and $\hat{z}$ is the unit vector along the z axis.

3.2.2 The Central Outer Tracker

The Central Outer Tracker (COT) is an open-cell drift chamber [20, 64]. The COT begins at a radius of 40 cm from the beam axis and ends at 137 cm. It has eight superlayers, each one is divided in ϕ into “super cells”. There are 12 sense wires in each super cell with approximated same maximum drift distance, therefore the number of super cells in a given super layers is roughly proportional to the radius of the super layer. The super cell is tilted by 35° with respect to the radial direction, as illustrated in Figure 3.4. The super layer alternates between axial (parallel to the beam direction) alignmnet and small ±3° stereo alignment, where the tilt angle is a rotation about an axis in the radial direction. Table 3.1 gives some feature of the COT.

For a charged particle travelling trough the entire COT radially, the 4 axial and stereo super layers will provide 96 measurements. The drift time of ionization electrons in the gas is used to measure the spatial charged particle position. The total collected charge is encoded in the output discriminator pulse height, which is corresponding to the measurement of the energy loss through ionization of the gas per unit length (dE/dx). The dE/dx of a charged particle is a function of partcile velocity that can be used to infer the particle mass combining the imformation of the particle momentum.

3.2.3 Silicon Vertex Detector

CDF II has three silicon detectors [65]: Layer 00 (L00), the Silicon Vertex Detector (SVX II), and the Intermdiate Silicon Layer (ISL). Figure 3.5 and 3.6 show the end

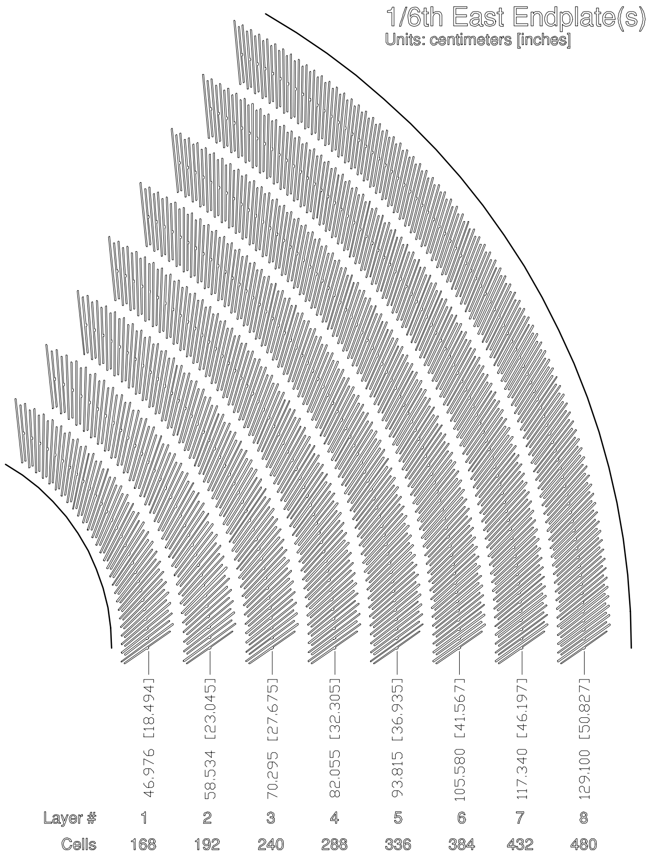

Figure 3.4: 1/6 section of the COT end plate. For each super layer is given the average radius.

COT	
Number of superlayers	8
Measurements per superlayer	12
Stereo Angle	+3 0 -3 +3 0 -3 0°
Cell/Layer	168 192 240 288 336 384 432 480
Radius at Cener of SL	46 58 70 82 94 106 119 131 cm
Tilt Angle	35°
Length of Active Region	310 cm
Number of channels	30,240
Material thickness	1.3% X_0

Table 3.1: Some features of the COT

view and the side view of half of the CDF Run II silicon system.

SVX II is the CDF Run II baseline detector, it is built in three cylindral assemblies called "barrels". Each barrel is 29 cm long, they are positioned end-to-end along the beam axis and centered longitudially with the detector. There are 12 wedges in ϕ per barrel, each has five layers of silicon staggered in radius numbered from 0 to 4. One layer consists of wire-bonded pair of double-sided silicon microstrip detectors. On the side facing the beamline, the strips are spaced in $r\phi$ by approximately 60 μm, and have implant widths of 14-15 μm. On the other side, both 90° and small angle stereo sensors are used, in the pattern (90 90 -1.2 90 +1.2) degresss from the innermost to the outmost SVX II layers. They are spaced by (141, 125.5, 60, 141, 65) μm, and have implant widths of 2- μm for the 90° strips and 15 μm for the small-angle stereo layers. The readout electronics chips are mounted on an electrical hybrid on the surface of the silicon detectors. Table 3.2 shows some of the SVX II features.

The ISL consists of a double-sided silicon layer, similar to the SVX II, placed at a radius of 22 cm in the central region. In the plug region, $1.0 \leq |\eta| \leq 2.0$, two layers of silicon are placed at the radii of 20 cm and 28 cm. Together with the SVX II, the ISL provides a stand-alone silicon tracking and b-tagging over the full region $|\eta| \leq 2.0$.

The Layer 00 is the most recent addition to CDF II tracking system. It is a single sided, radiation hard silicon layer placed immediately outside the beam pipe ($r \approx 1.5\,\mathrm{cm}$), which greatly improves the track impact parameter resolution.

3.3 Time of Flight System

During CDF Run II upgrade, a new Time of Flight (TOF) system [66, 67] is added to improve the identification of kaon and pion with low transverse momentum. The major movivation is to improve the b flavor tagging power, which is essential for B mixing and CP violation analysis. Particle identification with the TOF is done by measuring the difference (time-of-flight) in the time of arrival of the particle at the scintillator with the collision time t_0. The particle mass m can be determined from the momentum p, the path-length L from the beam collision point to scintillator bar, and the time-of-flight t:

$$m = \frac{p}{c}\sqrt{\frac{c^2t^2}{L^2} - 1}, \tag{3.5}$$

where p and L are measured by the tracking system. Figure 3.7 shows the time-of-flight difference between K/π, p/K and p/π. For comparison, the separation provided by the specific ionization energy loss dE/dx measured by the central drift chamber is shown too. The TOF improves substantially K/π separation in the momentum region $p \leq 1.6\,\mathrm{Gev}/c$.

The TOF consists of 216 bars of $4 \times 4 \times 279\,\mathrm{cm}$ Bicron BC-408 scintillator located

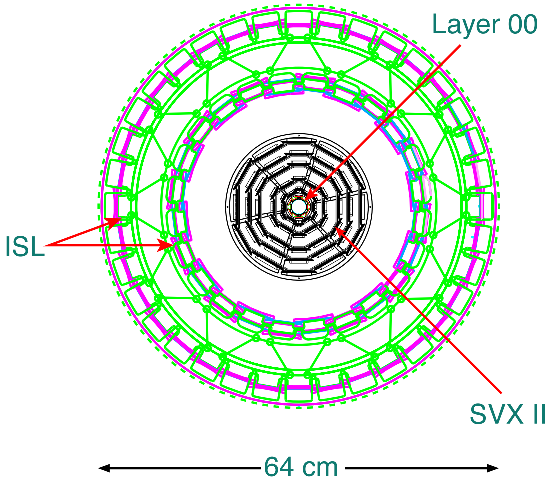

Figure 3.5: An end view of the CDF II silicon system

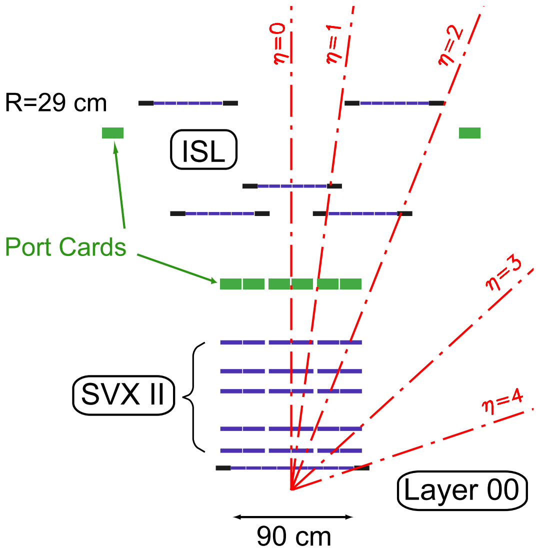

Figure 3.6: A side view of half of the CDF Run II silicon system on a scale in which the z coordinate is highly compressed.

at a radius of 138 cm from the beam line in 4.7 cm of radial space between the Central Outer Tracker and the cryostat of the superconducting solenoid, as shown in Figure 3.2. A Hamamatsu R7761 nineteen-stage fine-mesh photomultiplier tube (PMT) is attached to each end of each bar. The tube can operate in the 1.4T magnetic field of the CDF solenoid with an average gain reduction factor of 500 from the nominal gain of 10^6. For each phototube we measure the pulse arrival time and charge giving a total of $432 \times 2 = 864$ electronics channels. The expected time-of-flight resolution of our system is 100 ps, which is dominated by photo statistics. The electronics contribution [68] to this overall resolution is less than 15 ps.

Figures 3.8 shows the signal path and the timing diagram for a single phototube channel. A custom designed high voltage base is attached to the PMT. A differential signal is formed from the anode and the last dynode stage. A minimum ionizing particle passing through 4 cm of scintillator at the face of the phototube yields a differential signal of about 100 mV when the anode and dynode are terminated into 50Ω and PMT high voltage is set to the expected operating gain. The differential signal is then fed into a preamplifier that drives the signal through 13 m twisted pair signal cable to the VME based TOF Transition Board. The TOF transition board consists of a 9U high 160 mm wide main transition board (TOMAIN) and three analog daughter boards (TOAD), each of which processes three phototube channels. The PMT signal cable is directly connected to the TOAD, which contains the analog electronics for pulse shaping, baseline restoration, discrimination, gate generation, time to amplitude conversion (TAC), self-calibration, and charge measurement. The TOMAIN distributes power and provides digital services, programmable voltages, clock fanout, and remote monitoring functions. In addition, the TOMAIN feeds the analog time and charge signals to a CDF ADMEM board, which has CDF CAFE daughter cards to read the charge and TOF specific DECAF cards to read the TAC voltage.

3.4 Calorimeter and Muon Systems

Outside the solenoid, scintillator based calorimetry covers the region $|\eta| \leq 3.0$ with seperate electromegnatic and hadronic measurements. By matching the tracks found in the tracking system too the corresponding calorimetry towers, it provides us a powerful analysis and calibration framework, including an understanding of the absolute jet energy with a $2.5\,\%$ accuracy.

The outmost component of the CDF II is a set of scintillators, proportional chambers and steel absorbers. They are used to detect the muon over the region $|\eta| \leq 2.0$.

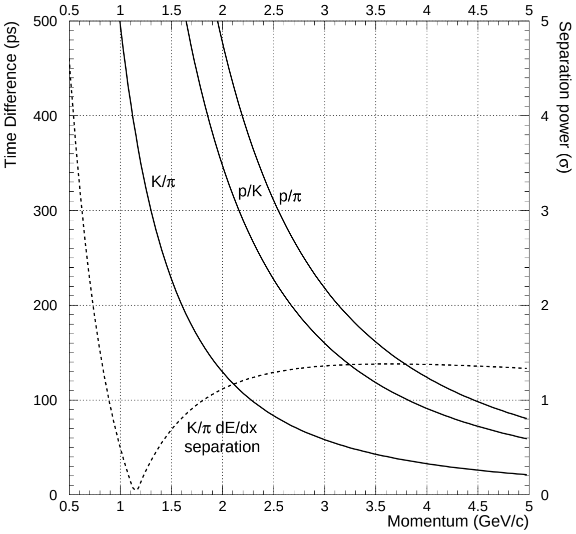

Figure 3.7: Time difference as a function of momentum between K/π, p/K and p/π traversing a distance of 140 cm, expressed in ps and separation power, assuming a resolution of 100 ps. The dashed line shows the K/π separation power from the dE/dx measurement in the COT.

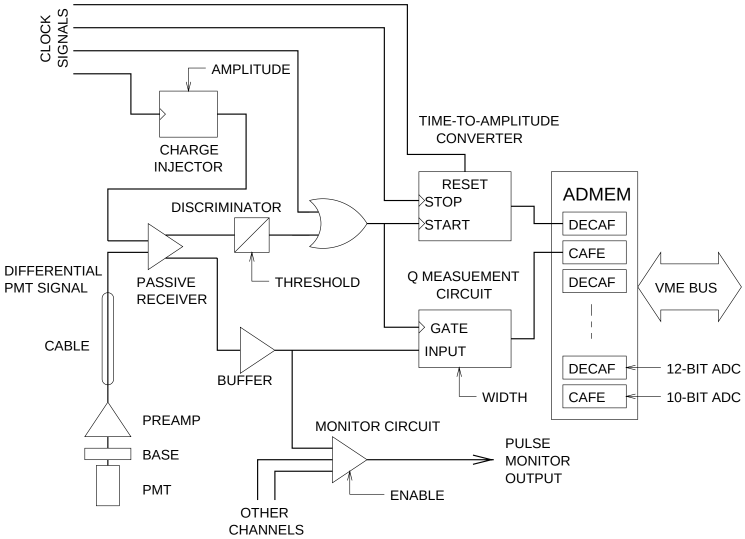

Figure 3.8: The block diagram of the electronics processing chain for the signal of one phototube in the TOF system.

3.5 CDF Cherenkov Luminosity Monitor

The luminosity $\mathcal{L}$ of hadron collider is often determined from the rate of inelastic $p\bar{p}$ interaction using the fomula

$$\bar{N} f_{\mathrm{BC}} = \sigma_{\mathrm{in}} \mathcal{L} \tag{3.6}$$

where the $\bar{N}$ is the average number of interactions per beam crossing. The inelastic cross section $\sigma_{\mathrm{in}} \sim 60\,\mathrm{mb}$ at the center of mass energy 1.8 TeV at Tevatron was measured by CDF [69], E710 and E811 experiments with about 3 % uncertainty.

At CDF Run II, a Cherenkov Luminosity Counter (CLC) [70, 71, 72] has been implemented to measure $\bar{N}$ within a few percent uncertainty for Tevatron luminosity determination. There are two CLC detector modules in the CDF detector installed in a "3-degree holes" inside the CDF end-plug calorimeter as illustrated in Figure 3.2, which covers the pseudorapidity range $3.7 \leq |\eta| \leq 4.7$. Each CLC module consists of 48 thin, long, conical, gas-filled, Cherenkov conters. These counters are arranged around beam pipe in three concentric layers with 16 counters each, and pointing to the interaction region. The counters in the outer two layers are 180 cm long, and the inner layer's are 110 cm long due to geometrical constraints. The conter cross sections ranges between 2 and 6 cm in diameter. A photomultiplier tube is attached to the far end of each conter to collect the light of relativistic particle traveling through the CLC. A primary particle from $p\bar{p}$ interactions will transverse the full

SVX II	
Readout coordinates	$r-\phi$; $r-z$
Number of barrels	3
Number of layers per barrel	5
Number of wedges per barrel	12
Ladder length	29.0 cm
Combined barrel length	87.0 cm
Radius at axial layers	2.545 4.120 6.520 8.220 10.095 cm
Radius at stereo layers	2.995 4.570 7.020 8.720 10.645 cm
number of ϕ strips	256 384 640 768 896
number of Z strips	256 576 640 512 896
ϕ strip pitch	60 62 60 60 65 μm
Z strip pitch	141 125.5 60 141 65 μm
Cell/Layer	168 192 240 288 336 384 432 480
Number of channels	405,504
Material thickness	3.5% X_0

Table 3.2: Some features of the SVX II

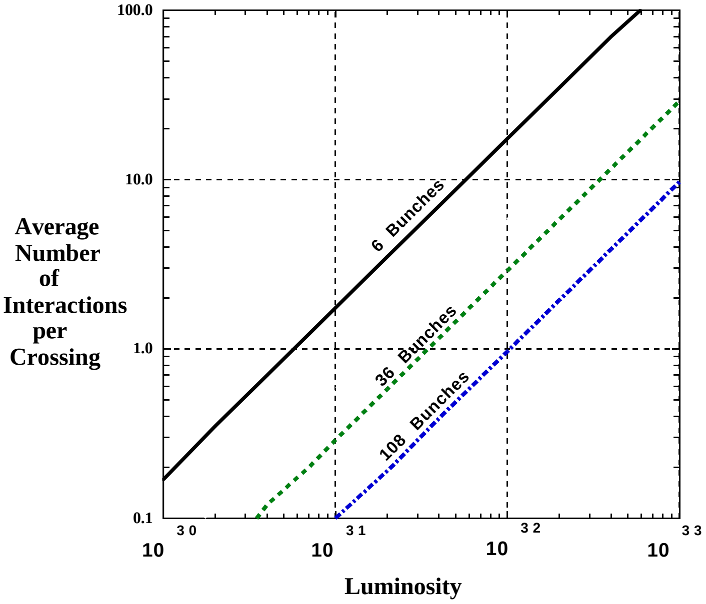

Figure 3.9: The average number of interactions ($\bar{N}$) for various conditions at CDF. 36 bunches is equivalent to 396 ns crossings, 108 bunches is equivalent to 132 ns crossings.

length of the counter and generate a large PMT signal, while the secondary particle produced in the beam pipe and materials surrounding the CLC cross the counter at different angles and yield much smaller signals. In addition, the Cherenkov counter is not sensitive to low momentum particles because of its momentum thresholds (2.6 GeV/c for pions), as well as the beam halo interaction.

The number of interactions in a bunch crossing follows Poisson statistics with mean $\bar{N}$. For traditional scintillator counter based luminosity measurement, by measuring the fraction of empty crossings we can calculate the $\bar{N}$. However, this approach fails at very high luminosity, where the average interactrion numbers becomes too large to determine the no interaction crossing fraction with a small relative uncertainty. At CDF Run II, the expected $\bar{N}$ can reach as high as 6, as shown in Figure 3.9. As for the CLC, since the PMT signal amplitude collected by Cherenkov counter is proportional to the primary particle number, it allows us to directly measure the $\bar{N}$ with high precision even at high luminosity. Moreover, collision data from zero biased and minimum biased triggers at CDF are continuously recorded through each run ($\sim 1\,Hz$), they are then analyzed in detail offline to produce the final luminosity measurement.

3.6 CDF Trigger System

At the Tevatron the $p\bar{p}$ collision rate is much higher than the rate at which the data can be recorded, and the cross section of the interesting physics events is only a small fraction of the total inelastic cross section. In CDF a three level architecture trigger system has been implemented to select the most interesting events and reject large number of inelastic background. Each trigger level provides a rate reduction sufficient to allow for processing in the next level with minimal deadtime.

The first level uses custom designed hardware to find physics objects such as clusters in the electromagnetic calorimeter or track-segments in the muon chambers. An eXtremely Fast Tracker (XFT) was added to Level-1 at CDF II, which allows tracks to be reconstructed on the transverse plane of the COT. An extrapolation unit (XTRP) matchs a track to an electromagnetic calorimeter energy cluster for improved electron identification or to a stub in the muon system for better muon identification and momentum resolution. It can be also used alone for triggering. The Level-1 trigger will make a decision within $4\,\mu s$, while the event's data is still in the pipeline. The rejection factor is expected to be about 150, thus decreasing the event rate from 7.6 MHz to about 50 KHz.

The events accepted by the Level-1 system are processed by the Level-2 hardware, which has four asynchronous event buffers and a maximum input rate at

50 KHz. The Level-2 system has improved momentum resolution for tracks, finer angular matching between muon stubs and central tracks, and data from the central shower-max detector (CES) for improved identification of electrons and photons. The data from the silicon tracker (SVX II) will also be available at Level-2; it can be associated with XFT tracks by the Silicon Vertex Trigger (SVT) [73, 74] to provide precise measurements of track impact parameter d_0, which is defined as the minimum distance between the origin and the track trajectory. The Level-2 accept rate will be around 300 Hz, with a rejection of about 150.

The Level-3 trigger consists of a farm of PCs running Linux. It uses the full detector to reconstruct and filter events with a maximum 75 Hz written rate to permanent storage.

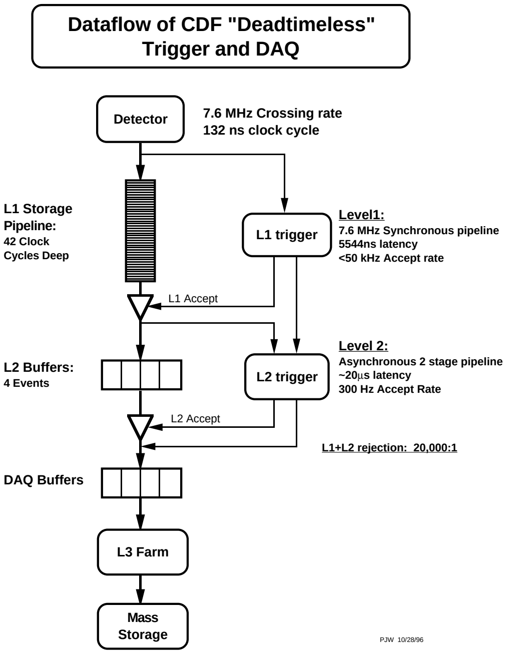

Figure 3.10: The functional block diagram of the CDF II data flow.

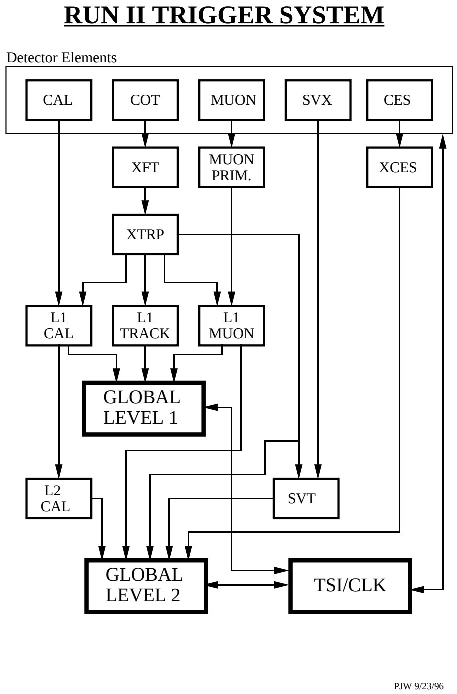

Figure 3.11: The block diagram the CDF II trigger system

Chapter 4

The Data Sample

4.1 Introduction

The data used in this analysis cover run 138809 to 142206, which have been collected by CDF in February and March 2002. The data were produced with version 4.3.1 of the CDF offline reconstruction program (dataset hbhd01 and gcrs01). We exclude the runs with less than 1 nb^{-1} live luminosity and those marked bad for either known detector problems (*e.g.* COT HV) or trigger problems. The complete good run list is listed in Appendix A. The total number of minimum-bias events used is 9.6×10^5; the number of L1 auto-accepts of the two-track trigger is 1.9×10^5. The corresponding integrated luminosity is 5.693 pb^{-1}.

4.2 Trigger Path

4.2.1 Two Track Hadronic Trigger

The charm meson signal is reconstructed in the data collected by he two track hadronic trigger [75, 76, 77, 78, 79], it is a combination of the following requests:

- Level 1:
  - 2 XFT track with $P_T \geq 2\,\mathrm{GeV/c}$;
  - Opposite charge;
  - $P_{T1}(\mathrm{XFT}) + P_{T2}(\mathrm{XFT}) \geq 5.5\,\mathrm{GeV/c}$;
  - $|\Delta\phi_0| \leq 135°$.
- Level 2:
  - 2 SVT track with $P_T \geq 2\,\mathrm{GeV/c}$;
  - Each SVT track has $120\,\mu\mathrm{m} \leq |d_0(\mathrm{SVT})| \leq 1\mathrm{mm}$
  - Opposite charge;
  - $P_{T1}(\mathrm{SVT}) + P_{T2}(\mathrm{SVT}) \geq 5.5\,\mathrm{GeV/c}$;
  - $|\Delta\phi_0| \leq 135°$.
- Level 3:

L3 matched an SVT tracks with a COT track by requiring the difference between their curvatures and track azimuthal angles at COT super-layer 6 to satisfy $|\Delta C| = |C(\mathrm{COT}) - C(\mathrm{SVT})| \leq 2.0 \cdot 10^{-4}\,\mathrm{cm}^{-1}$ and $|\Delta\phi_6| = |\phi_6(\mathrm{COT}) - \phi_6(\mathrm{SVT})| \leq 15\,\mathrm{mrad}$.

  - 2 COT track with $P_T \geq 2\,\mathrm{GeV/c}$;
  - Opposite charge;
  - $P_{T1}(\mathrm{COT}) + P_{T2}(\mathrm{COT}) \geq 5.5\,\mathrm{GeV/c}$;
  - $2^\circ \leq |\Delta\phi_0| \leq 90^\circ$.

4.2.2 Two Track L1 Auto Accept Trigger

The events collected with the two track L1 auto accept trigger are used to study the SVT efficiency and resolution. The trigger selection criteria is the same as the L1 requirement of the two track hadronic trigger.

- Level 1:
  - 2 XFT track with $P_T \geq 2\,\mathrm{GeV/c}$;
  - Opposite charge;
  - $P_{T1}(\mathrm{XFT}) + P_{T2}(\mathrm{XFT}) \geq 5.5\,\mathrm{GeV/c}$;
  - $|\Delta\phi_0| \leq 135^\circ$.

4.2.3 Minimum Bias Trigger

The minimum bias data sample is used to understand the detector efficiency and resolution. This trigger [80] requires loose coincident hits in CLC scintillator counts, that is at least one counter on each side of the CLC is above the threshold.

4.3 Track Quality Selection Criteria and Trigger Confirmation

Unless stated otherwise, the following offline track quality selection criteria are applied:

- the number of axial COT hits is ≥ 25
- the number of stereo COT hits is ≥ 25
- the number of SVX phi-side hits on different layers is ≥ 3
- the minimum offline transverse momentum $\geq 0.5\,\mathrm{GeV/c}$
- the track has $|z_0| \leq 47.25\,\mathrm{cm}$
- The track must pass through the whole SVX detector: we extrapolate the helix to R=10.645 cm and demand that $|z| \leq 47.25\,\mathrm{cm}$

- The track must pass through all 4 COT axial super-layers: we extrapolate the helix to R=133 cm and demand that $|z| \leq 155$ cm

An offline track is matched with an SVT track by requiring the difference between their curvatures and track azimuthal angles at COT super-layer 6 to satisfy $|\Delta C| = |C(\text{offline}) - C(\text{SVT})| \leq 2.0 \cdot 10^{-4}\,\text{cm}^{-1}$ and $|\Delta\phi_6| = |\phi_6(\text{offline}) - \phi_6(\text{SVT})| \leq 15\,\text{mrad}$. An offline track is called a trigger track if it satisfies:

- Track has offline $p_T \geq 2.0\,\text{GeV/c}$
- Track has offline $120\,\mu\text{m} \leq |d_0| \leq 1\text{mm}$
- Track is matched with an SVT track
- The matched SVT track has $p_T(\text{SVT}) \geq 2.0\,\text{GeV/c}$
- The matched SVT track has $120\,\mu\text{m} \leq |d_0(\text{SVT})| \leq 1\text{mm}$
- Track enters and leaves the same mechanical SVX barrel

For this last requirement we increase the size of each SVX barrel by 2 cm to allow for finite resolution in z:

- SVX barrel 0 extends from -47.25 cm to -14.75 cm in the z direction
- SVX barrel 1 extends from -16.75 cm to 16.75 cm in the z direction

- SVX barrel 2 extends from 14.75 cm to 47.25 cm in the z direction

Two trigger tracks are called a "trigger pair" if they satisfy:

- The two tracks have opposite charge
- The offline tracks have $p_{T1} + p_{T2} \geq 5.5\,\mathrm{GeV/c}$
- The offline tracks have $2^\circ \leq |\Delta\phi_0| \leq 90^\circ$.
- The matched SVT tracks have $p_{T1}(\mathrm{SVT}) + p_{T2}(\mathrm{SVT}) \geq 5.5\,\mathrm{GeV/c}$

Chapter 5

Charm Meson Reconstruction

All charm reconstruction criteria also apply to the charge conjugate of the decay mode under investigation. For example, when we say we reconstruct $D^+ \to K^-\pi^+\pi^+$, we imply also $D^- \to K^+\pi^-\pi^-$ decays.

5.1 Reconstruction of $D^0 \to K^-\pi^+$

The selection criteria for $D^0 \to K^-\pi^+$ are the following:

- the $K^-\pi^+$ pair is a trigger pair;
- $p_T(D^0) \geq 5.5\,\mathrm{GeV}/c$;
- $L_{xy}(D^0) \geq 500\,\mu\mathrm{m}$;

- $d_0(K^-) \cdot d_0(\pi^+) < 0$;
- $|z_0(K^-) - z_0(\pi^+)| \leq 5\,\mathrm{cm}$.

Since we do not use particle identification to distinguish kaons from pions, for each $D^0 \to K^-\pi^+$ candidate, there is a $\bar{D}^0 \to K^+\pi^-$ candidate as well. This auto-reflection of the true signal has a much broader invariant mass distribution for the majority of the range of $p_T(D^0)$ selected by the SVT trigger and has been studied in detail elsewhere [81]. To extract the signal number, the signal is modeled as a single Gaussian, and we use a first order polynomial to model the combinatorial background. A wide Gaussian is also added to account for the auto-reflection background. The auto-reflected D^0 mass distribution centers at the same mean value as the D^0 signal Gaussian, and the number of events is constrained to be equal to the D^0 event number. The ratio of the widths of the auto-reflection and the signal are determined using the mass distribution of D^0 decayed from D^{*+} in each p_T bin [81] (the charge of the bachelor pion can be used to remove the auto-reflection background). The reconstructed signals are shown in Figure 5.1. The signal numbers are extracted with a binned maximum likelihood fit.

Since every D^0 candidate is entered twice, and because we constrain the number of events in the signal peak to be equal to the number of events in the auto-reflection peak, the statistical uncertainty is underestimated by up to a factor $\sqrt{2}$, depending on what fraction of the auto-reflection background is covered by the fit. We conservatively correct for this by multiplying by the statistical uncertainty obtained from the fit by $\sqrt{2}$.

To estimate the systematic uncertainties related to the shape of the auto-reflection, we repeat the fitting procedure by varying the ratio between wrong sign and right sign widths measured from the D^{*+} sample with $\pm 1\sigma$ [81]. We observe a 1.1% variation of the extracted D^0 signal numbers without significant p_T dependence. and we treat this number as a systematic uncertainty.

To estimate the uncertainty from the the background model, we used a second order polynomial instead of a linear function. We find a difference of 2.6% in the event yield, without significant difference between the p_T bins, and treat this difference a systematic uncertainty.

We checked the occurrence of multiple candidates per event, and find in fewer than 0.1% of the events more than one candidate in the 2σ window around the D^0 peak.

The D^0 yield, with the corresponding statistical and systematic uncertainties are summarized in Table 5.1.

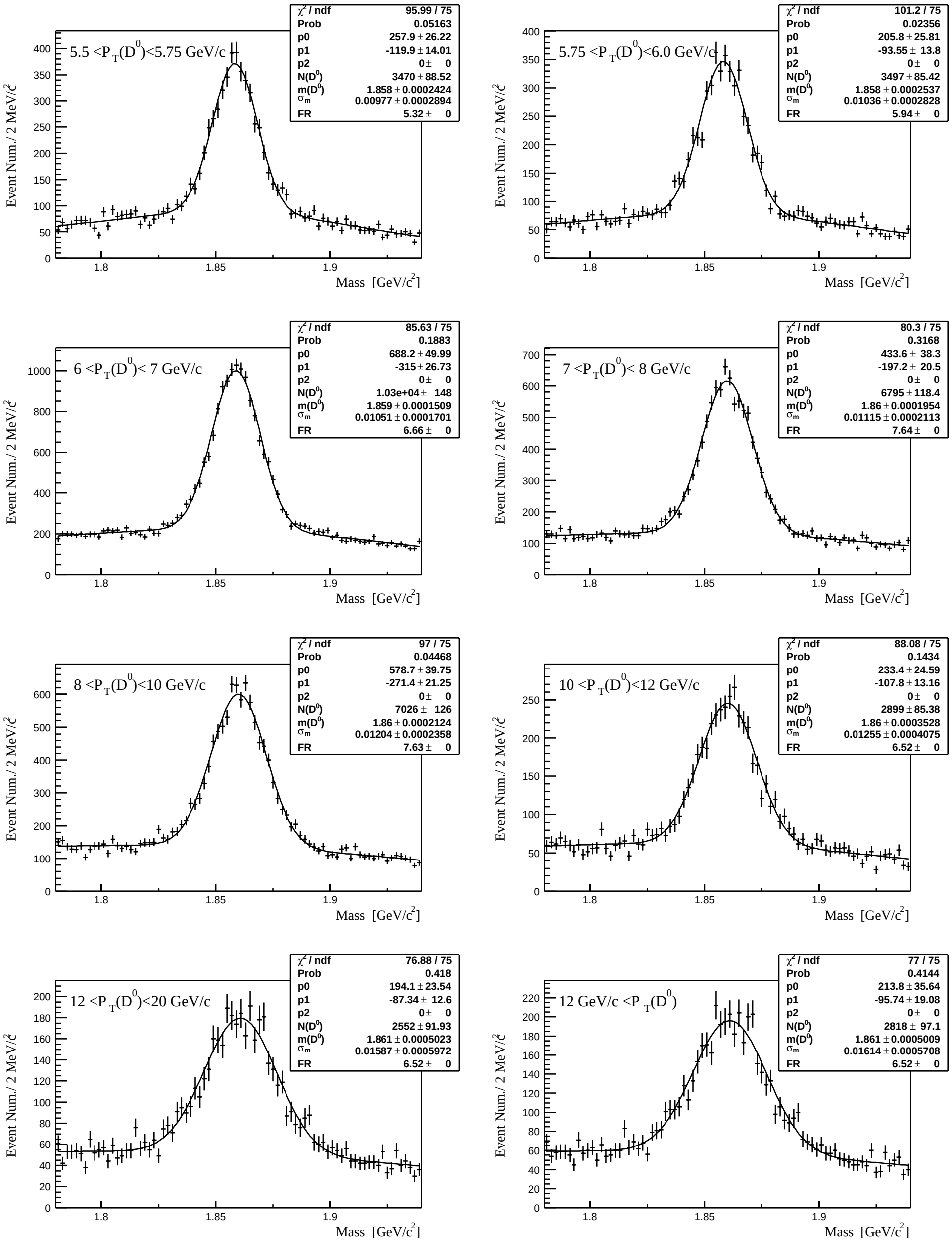

Figure 5.1: The $K\pi$ invariant mass distribution of $D^0 \to K^-\pi^+$ candidates in different p_T bins. The lowest p_T bin has been split into two bins to improve the description of the signal and the background. The results of the fit are indicated in the upper right corner. The last number, FR, indicates the ratio between the width of the signal and the auto-reflection. It is not a free parameter in the fit; it has been determined from a study of tagged D^0's from D^{*+} as discussed in the text.

5.2 Reconstruction of $D^{*+} \to D^0\pi^+, D^0 \to K^-\pi^+$

To extract the D^{*+} yield, we examine the mass difference $\Delta m = m(K\pi\pi) - m(K\pi)$. We apply the following selection criteria:

- the $K^-\pi^+$ pair is a trigger pair;
- $p_T(D^{*+}) \geq 6.0\,\mathrm{GeV}/c$;
- $L_{xy}(D^0) \geq 500\,\mu\mathrm{m}$;
- $d_0(K^-) \cdot d_0(\pi^+) < 0$;
- $|\Delta z_0| \leq 5\,\mathrm{cm}$ between any two tracks;
- $|m(K\pi) - m(D^0)| \leq 3\sigma_m(D^0)$;
- no SVX requirement for the soft pion;
- the soft pion π and the kaon have opposite charge (right sign correlation).

For $m(D^0)$ and $\sigma_m(D^0)$ we use the measured D^0 mass and width per bin as obtained in Section 5.1. We do not require the soft pion from the D^{*+} decay to be a trigger track, since its momentum is very small for the kinematic range we consider. As shown in Figure 5.2, clean signals of D^{*+} are obtained for the right sign Δm distribution. In our analysis, the D^{*+} signal is modeled as a double Gaussian with the same mean. We parameterize the background with the following shape:

$$a(\Delta m - m_\pi)^b \exp(c(\Delta m - m_\pi)). \tag{5.1}$$

We fix the value of b to 0.5, which corresponds to the shape expected from phase space for the background from random combinations of D^0 with pions. To have a strong constraint on the shape of the background, we use a long lever arm, up to $\Delta m = 0.18\,\mathrm{GeV}/c^2$.

Since we require the D^0 from D^{*+} decay to be inside a 3σ mass window of the D^0, we lose 0.27% of the D^{*+} signal as they fall outside the D^0 mass window, and we correct for this inefficiency. As a cross check, we applied a 2σ mass window around the D^0 and find the yield consistent with the expected 5% decrease from the Gaussian shape.

To investigate the fit to the signal and background shapes, we plot the difference between the histogram and the fit in Figure 5.3. We find no large deviations. As a further test of the signal extraction, we count the number of events in 2σ and 3σ (of the wide Gaussian) mass windows around the measured peak in Δm, and find less than 0.2% and 0.5% difference with the integral of the fit. We assign a systematic uncertainty of 0.5% to the signal model.

To account for systematic uncertainties due to the background shape, we vary the background model in two different ways and use the method that gives the largest variation to estimate the systematic uncertainty. First, we allow b to be a free parameter in the fit, which has a negligible effect on the signal yield ($\leq 1\%$). When we use a second order polynomial function to model the shape of the background, the variation of the signal yield is about 1.2%, without significant p_T dependence. We conclude that the background is so small that the signal extraction is very robust for different background models, and we assign a systematic uncertainty of 1.2% on the D^{*+} yield.

We checked for the occurrence of multiple candidates and find that in fewer than 0.5% of the events more than one D^{*+} candidate exists in the 2σ signal region in Δm.

5.3 Reconstruction of $D^+ \to K^-\pi^+\pi^+$

The following criteria have been applied for D^+ signal reconstruction:

- a trigger pair amongst the D^+ decay daughters;
- $p_T(D^+) \geq 6.0\,\mathrm{GeV}/c$;
- $L_{xy}(D^+) \geq 800\,\mu m$;
- $|\Delta z_0| \leq 5\,\mathrm{cm}$ between any two tracks;
- $\chi^2 \leq 30$ for the three track vertex fit;

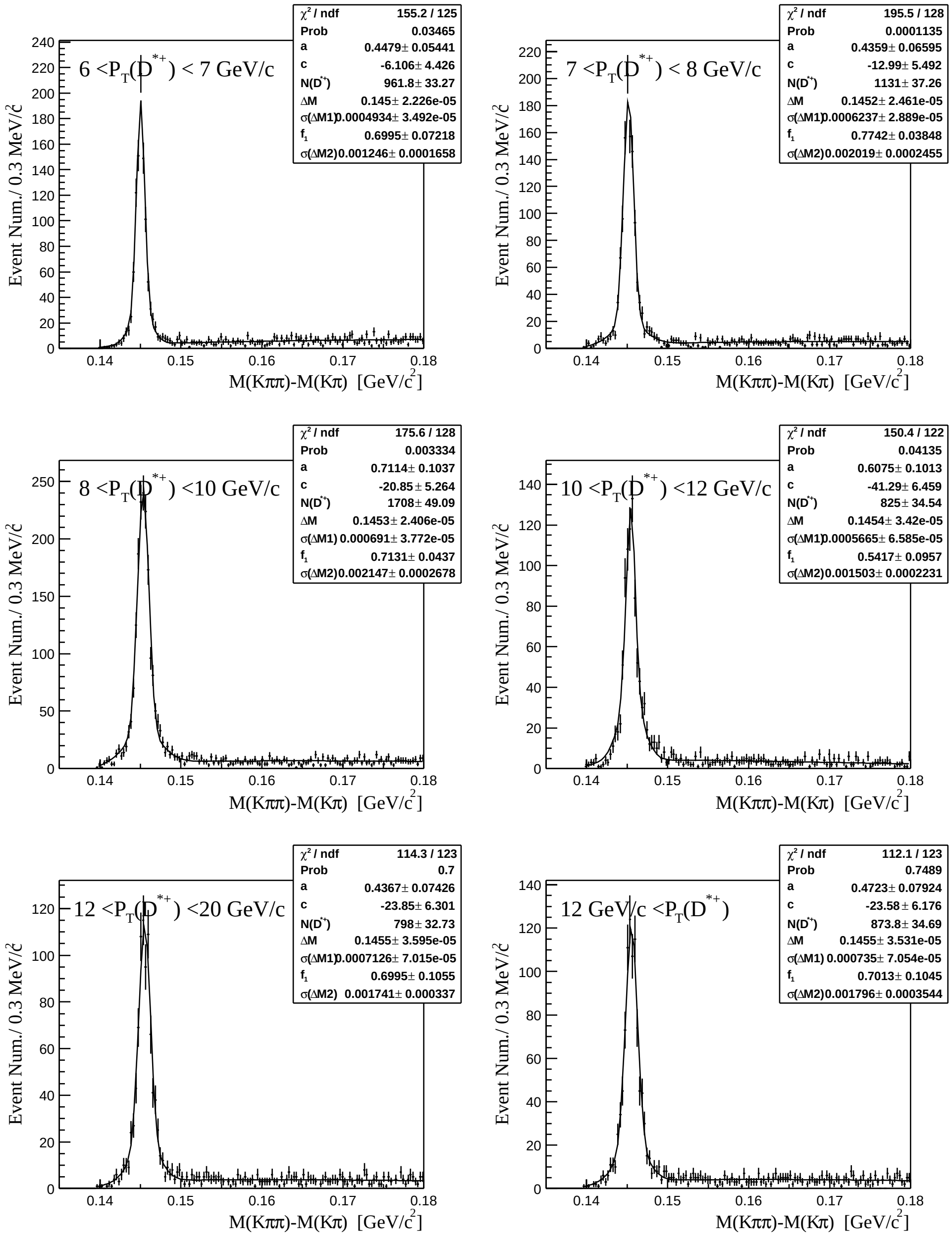

Figure 5.2: The $m(K\pi\pi) - m(K\pi)$ distribution for $D^{*+} \to D^0\pi^+, D^0 \to K^-\pi^+$ candidates in different p_T bins. The fit results are indicated in the upper right box. The parameters a and c determine the shape of the background, according to Equation 5.1. The variable f_1 indicates the fraction of the signal in the narrow Gaussian.

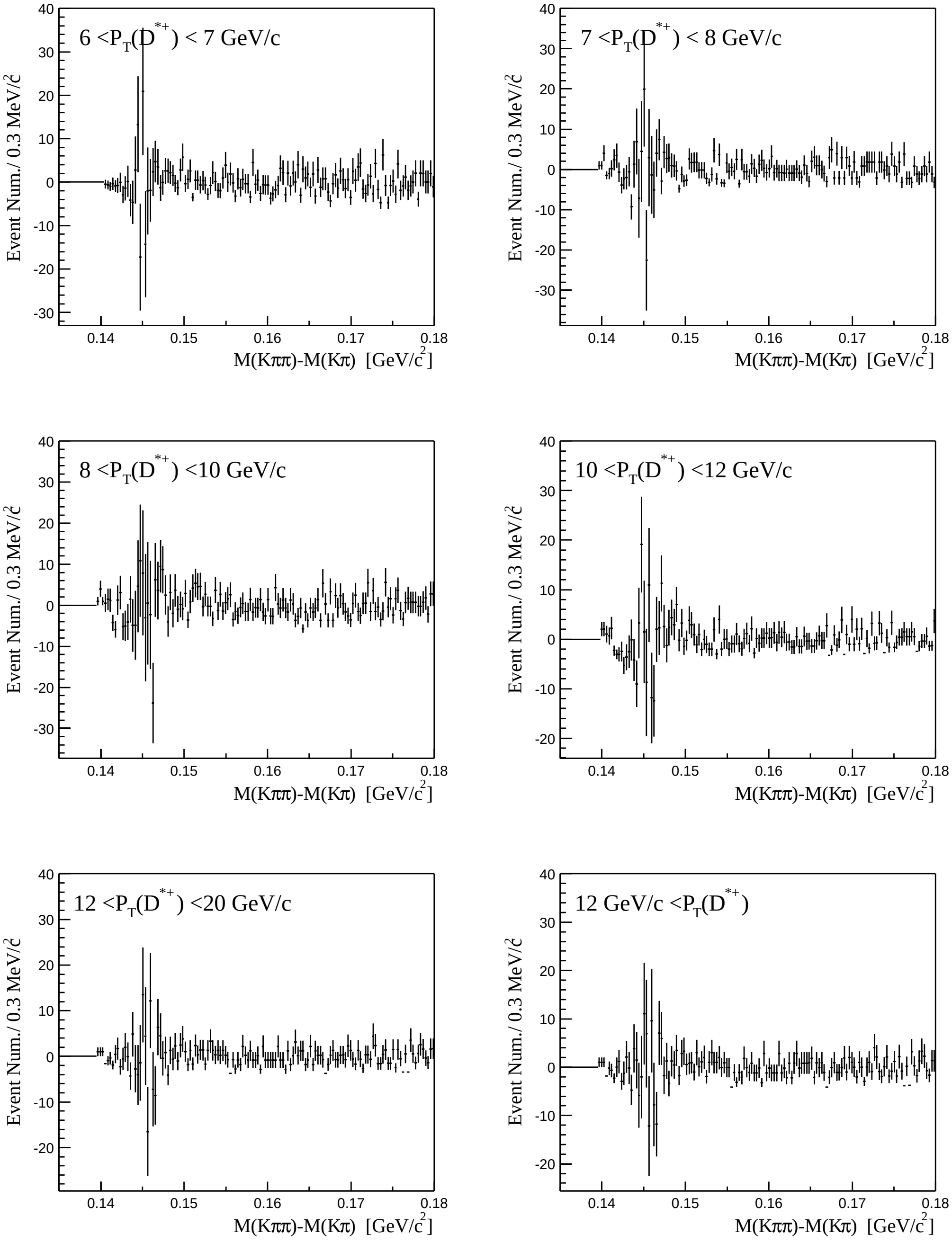

Figure 5.3: Difference between the histogram entries and the fitted curve that describes the signal and background in the Δm histogram of D^{*+} candidates in different p_T bins.

- $\Delta m \equiv |m(K\pi\pi) - m(K\pi)| \geq 0.18\,\mathrm{GeV}/c^2$, where $m(K\pi)$ is the invariant mass of the trigger pair.

Since we apply a very loose χ^2 requirement, the D^{*+} with a partially reconstructed D^0 forms a wide peak underneath the D^+ mass distribution, which results in a background with a complicated shape. As shown in Figure 5.5a, two peaks are evident; when no Δm requirement is made; one corresponds to the D^+ and one to the D^{*+}. After imposing the requirement on Δm, the fully reconstructed D^{*+} peak has disappeared in Figure 5.5b, and the background looks more flat. Figure 5.5c shows the invariant mass distribution of the events that have been removed. The fully reconstructed D^{*+} are clearly visible, but also the complicated shape of the D^{*+} with partially reconstructed D^0, such as $D^0 \to K^-\pi^+\pi^0$. The fraction of D^+ rejected by this selection is small ($\approx 2\%$), and has been accounted for the the efficiency calculation.

We extract the number of D^+ mesons using a double Gaussian for the signal and a linear function for the background.

Since we would need a detailed understanding of the track parameter covariance matrix to predict the efficiency of a tight vertex χ^2 requirement, we have chosen instead to make the χ^2 requirement loose enough that it has no significant inefficiency. Figure 5.4 shows the event yield as a function of the vertex χ^2 requirement. The reconstructed D^+ signal number varies by less than 1% when we vary the χ^2

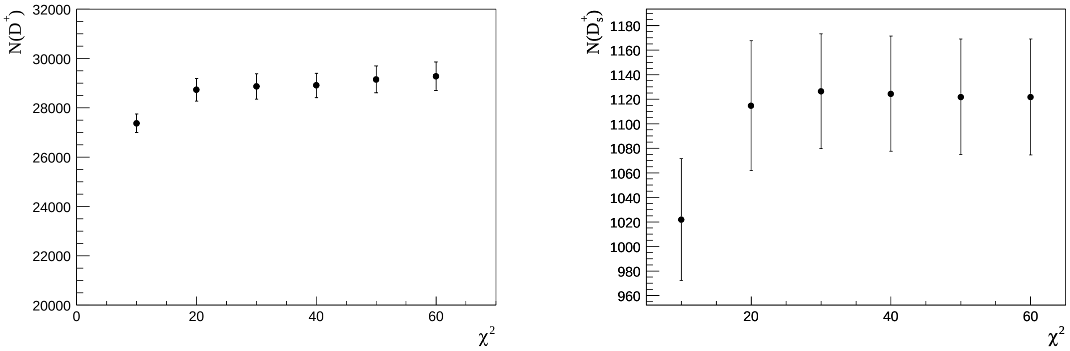

Figure 5.4: The D^+ and D_s^+ yield as a function of the vertex χ^2 requirement. The errors are statistical only.

requirement between 20 and 60.

To account for the uncertainty in the shape of the background, we change the background model to a second order polynomial function, and observe a 3.6% variation without significant p_T dependence. To evaluate the systematic uncertainty for the signal shape, we repeat the above analysis using a single Gaussian with a linear background. The yield difference does not differ significantly between the p_T bins, so we use the averaged yield difference of 5.1% for all p_T bins as a systematic uncertainty.

Unlike the D^0 and D^{*+}, the chance to have in one event more than one D^+ candidate in the 2σ mass window is not negligible(2-4%). We find that most D^+ candidates in one event share the same trigger pair. Due to the loose χ^2 requirement in the D^+ reconstruction, a trigger pair can combine with several other tracks to form a good vertex, which results in several candidates per event. For events with at least one candidate in the signal region, we verified the invariant mass distribution of other candidates, and found no particular structure that would significantly bias the signal extraction.

5.4 Reconstruction of $D_s^+ \to \phi\pi^+, \phi \to K^+K^-$

The selection criteria for $D_s^+ \to \phi\pi^+, \phi \to K^+K^-$ are as follows:

- the $K^-\pi^+$ pair form a trigger pair;
- $1.0\,\mathrm{GeV}/c^2 \leq m(K^+K^-) \leq 1.04\,\mathrm{GeV}/c^2$;
- $p_T(D_s^+) \geq 6.0\,\mathrm{GeV}/c$;
- $L_{xy}(D_s^+) \geq 500\,\mu\mathrm{m}$;
- $|\Delta z_0| \leq 5\,\mathrm{cm}$ between any two tracks;
- $\chi^2 \leq 30$ for the three track vertex fit.

The D_s^+ daughters contain two charged tracks of opposite charge that form a trigger pair: the K^+K^- pair from the ϕ decay and the $K^-\pi^+$ pair. The mass difference between a ϕ and two charged kaons is very small, resulting in an opening angle between the two kaons of a few degrees. Therefore the trigger requirement of $|\Delta\phi_0| \geq 2^\circ$ results in a poor efficiency for triggering on the kaons from the ϕ, which

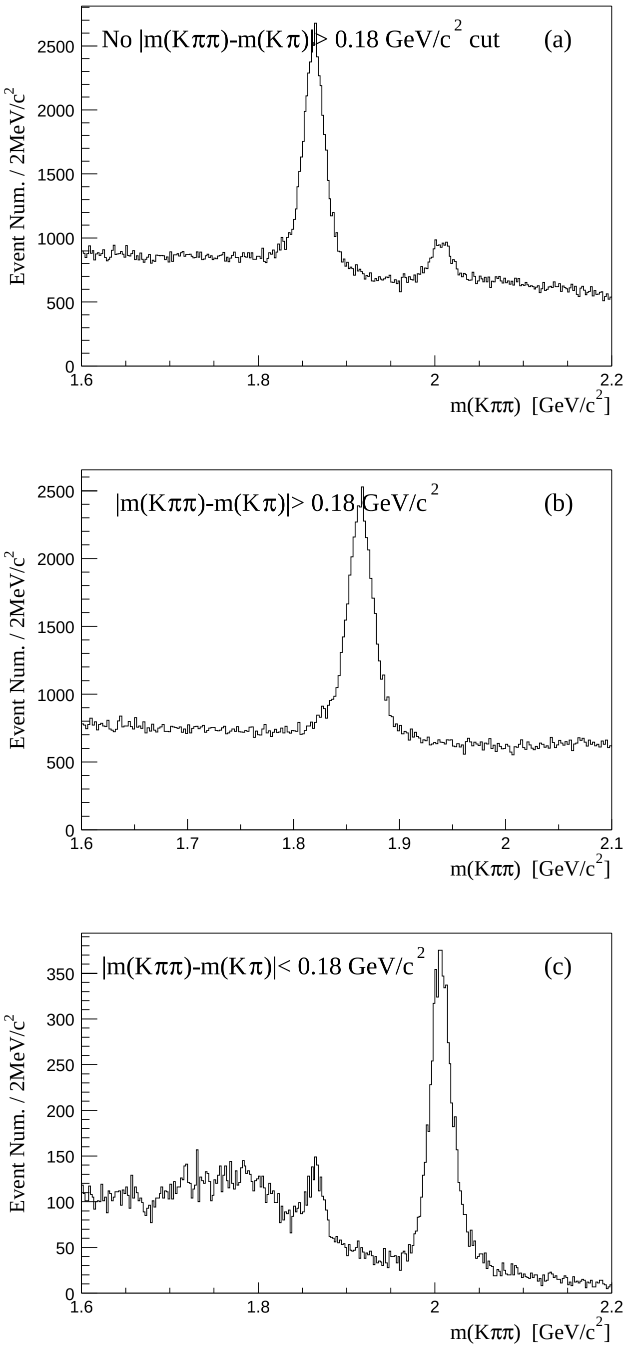

Figure 5.5: The $K\pi\pi$ invariant mass distribution for $D^+ \to K^-\pi^+\pi^+$ candidates with different criteria on $\Delta m \equiv |m(K\pi\pi) - m(K\pi)|$.

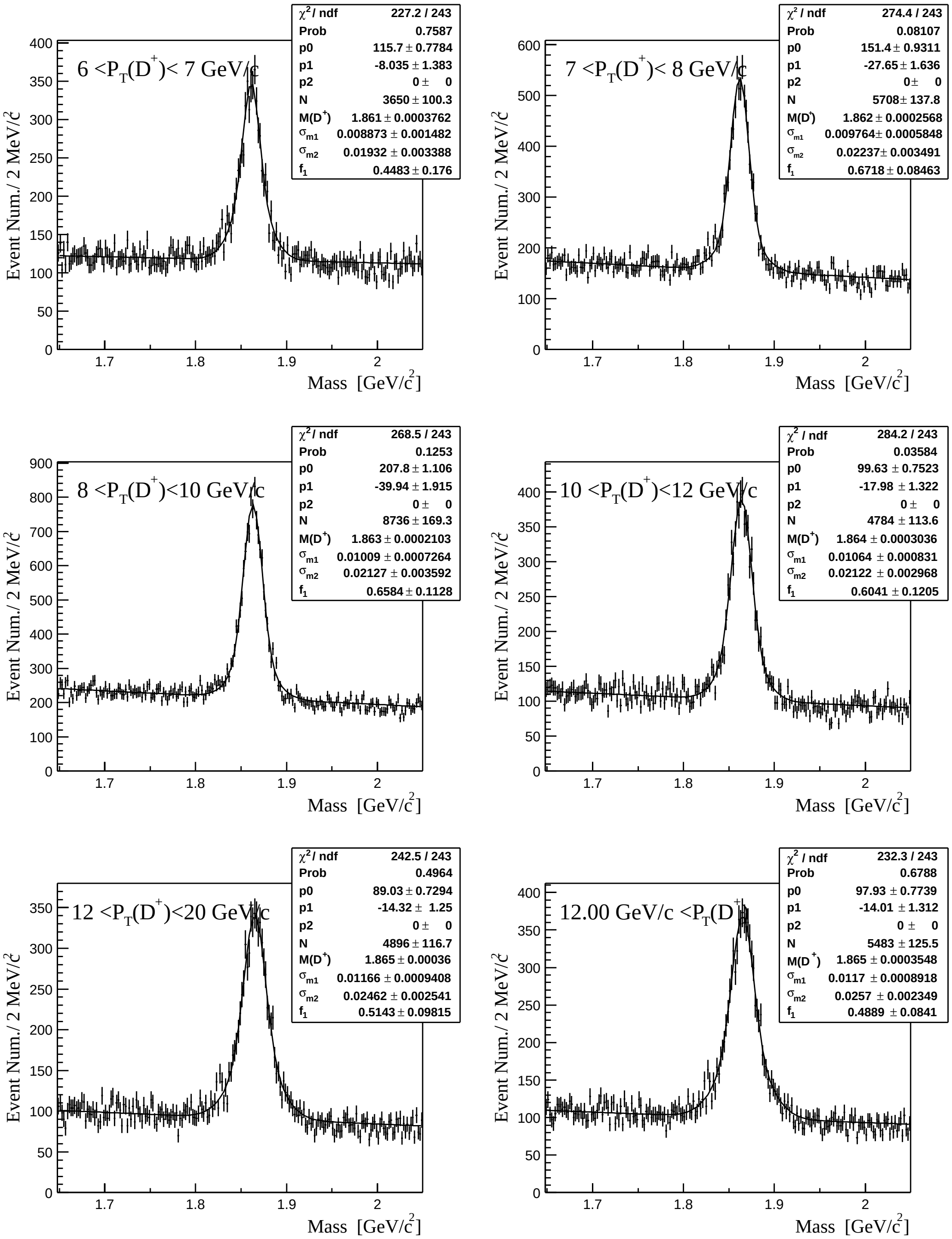

Figure 5.6: The $K\pi\pi$ invariant mass distribution for $D^+ \rightarrow K^-\pi^+\pi^+$ candidates in different p_T bins. The fraction of the signal described by the narrow Gaussian indicated by f_1.

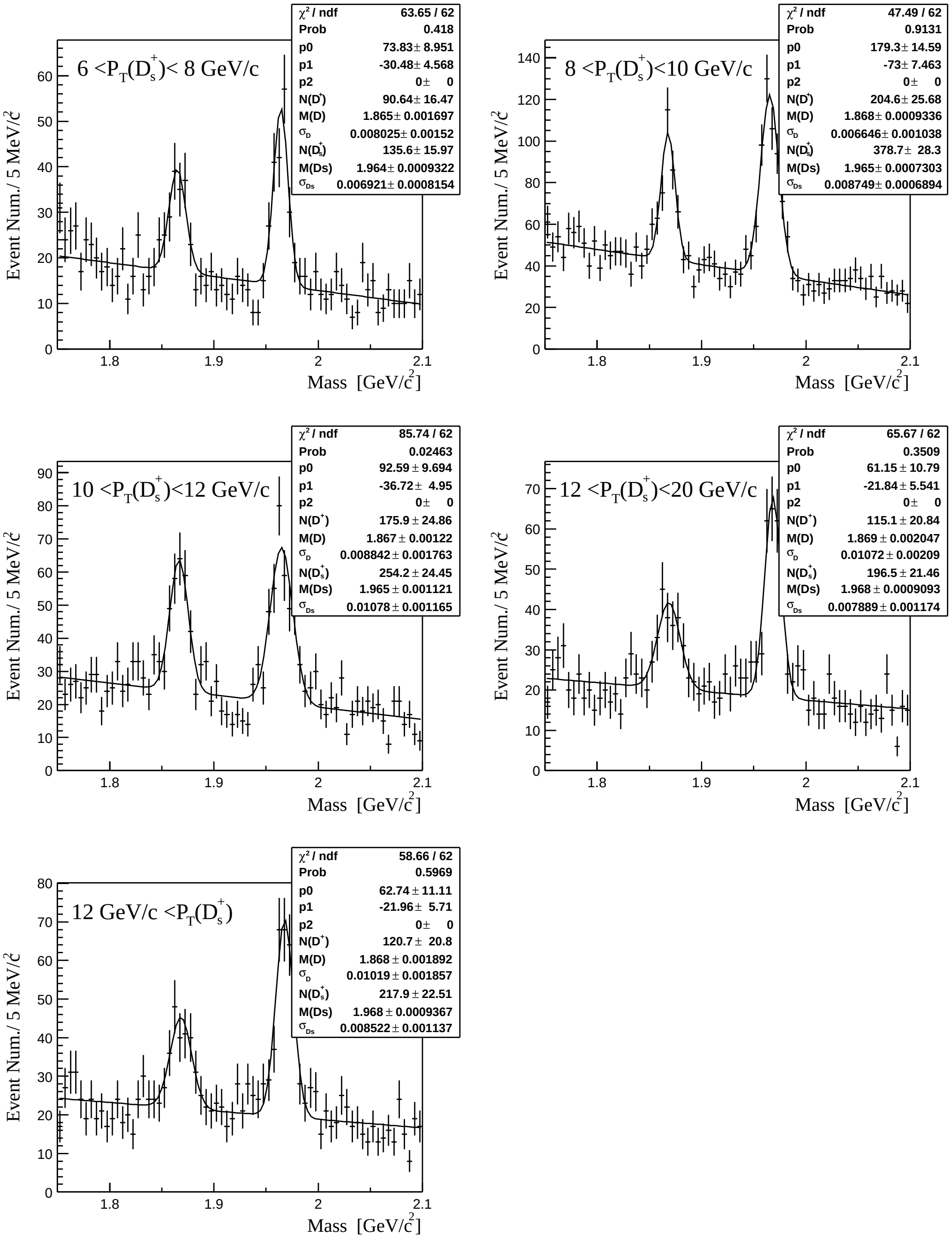

Figure 5.7: The $KK\pi$ invariant mass distribution for $D^+ \rightarrow \phi\pi^+$ and $D_s^+ \rightarrow \phi\pi^+, \phi \rightarrow K^+K^-$ candidates in different p_T bins.

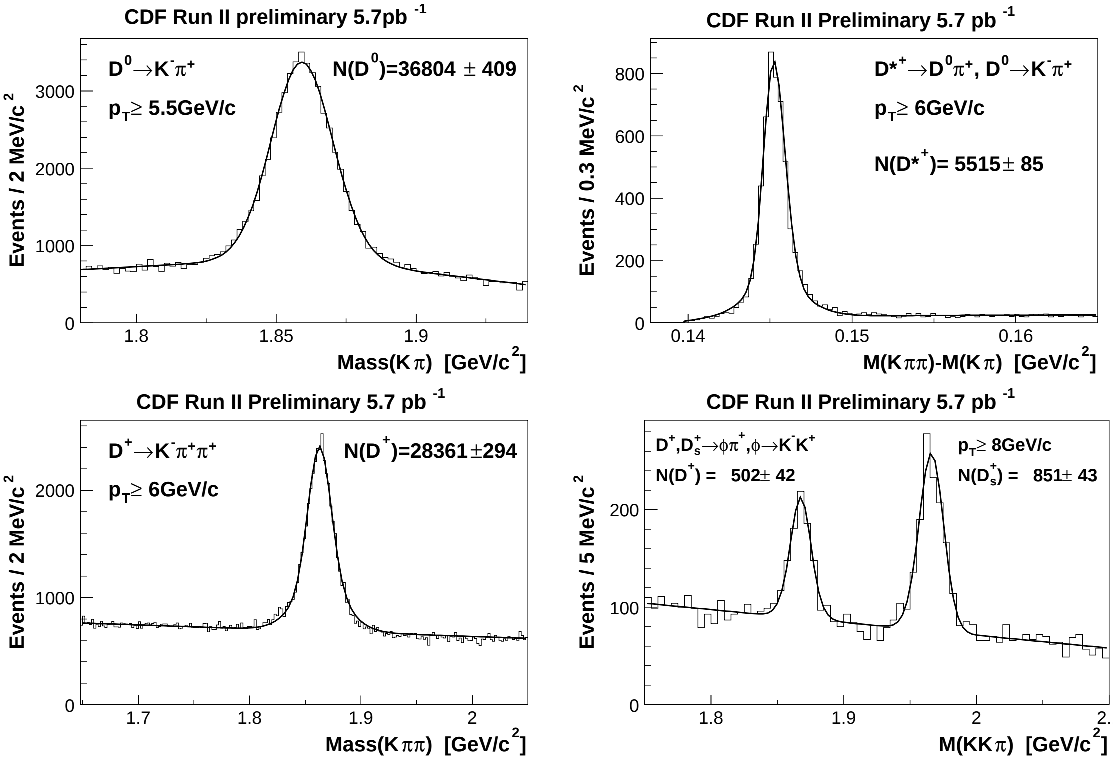

Figure 5.8: The reconstructed mass distribution of D meson candidates. The curve is the superposition of the fitted D mass distributions in different P_T bins, and is used to calculate the χ^2 for the summed distributions. We obtain $\chi^2/\mathrm{NDF} = 1.88$ for D^0, 1.11 for D^{*+}, 1.32 for D^+, and 0.87 for D_s^+.

depends strongly on the angular resolution of the trigger. By specifically requiring that the $K^-\pi^+$ pair form a trigger pair, we avoid a strong the dependence on the angular resolution of the trigger.

To extract the signal number, we use two Gaussian functions, one for the D^+ and the other for the D_s^+, plus a linear background, as shown in Figure 5.7.

The background model has been studied in detail elsewhere [82]. The mass distribution in the data is fit with two Gaussians over a linear combination of Legendre polynomials for the mass region. The values of Legendre polynomials of order 2 and higher were found to be consistent with zero. This indicated that a linear function is sufficient to describe the background under the D_s^+ signal. We also use an exponential background model to evaluate the systematic uncertainties due to the background shape, and observe no significant difference.

For the signal model, we compare the D_s^+ signal number from the histogram and the fitter in 2σ mass window, and find the deviation is negligible. As the result, we don't assign any systematic uncertainty to the D_s^+ signal extraction.

Since we apply a vertex χ^2 requirement during our reconstruction, we studied the reconstructed signal number as a function of different χ^2 values. As shown in Figure 5.4, the variation is negligible. We also study multiple D_s^+ candidate per event and find the probability to have a second D_s^+ candidate is small ($\leq 0.5\%$). The D_s^+ signal number and its corresponding statistical and systematic uncertainties are summarized in Table 5.1.

5.5 OIZ Tracking v.s. OI Tracking

For this analysis, we use data produced in pass 1, reconstructed with CDF offline version 4.3.1 of. It has been know that this pass of the production did not have a good SVX alignment, in particular for the SVX z coordinate.

A commonly used vertex fitting package in CDF is CTVMFT [83], which fits vertices in three dimensions. Using CTVMFT with the 4.3.1 data has the danger of introducing an inefficiency due to the alignment problems in the z coordinate. Therefore we did not use CTVMFT, but a similar vertex fitter that can fit in either two or three dimensions [21], and we restrict ourselves to two dimensional vertex fits. For a two-body decay, the vertex is simply the position where the two track trajectories intersect in the $r - \phi$ plane, therefore the number of degrees of freedom is zero. For three body D decays, there is one degree of freedom.

Although no SVX z information are used for the vertex constraint, there is still concern that there could be inefficiencies due to the incorrect SVX z hit assignment during offline production. To investigate a potential bias, we repeat the signal reconstruction with the same offline selection criteria but using OI tracks instead of OIZ tracks.

$D^0 \to K^-\pi^+$							
p_T [GeV/c]	5.5-6.0	6.0-7.0	7.0-8.0	8.0-10	10-12	12-20	≥ 12
N	6967	10296	6795	7026	2899	2552	2818
Statistical error	±174	±209	±167	±178	±121	±130	±137
Relative stat. error [%]	±2.5	±2.0	±2.5	±2.5	±4.2	±5.1	±4.9
Systematic sources							
Reflection model [%]	±1.1	±1.1	±1.1	±1.1	±1.1	±1.1	±1.1
Background model [%]	±2.6	±2.6	±2.6	±2.6	±2.6	±2.6	±2.6
Total sys. error [%]	±2.8	±2.8	±2.8	±2.8	±2.8	±2.8	±2.8

$D^{*+} \to D^0\pi^+, D^0 \to K^-\pi^+$						
p_T [GeV/c]	6.0-7.0	7.0-8.0	8.0-10	10-12	12-20	≥ 12
N	965	1134	1713	827	800	876
Statistical error	±33	±37	±49	±35	±33	35
Relative statistical error [%]	±3.4	±3.3	±2.9	±4.2	±4.1	±4.0
Systematic sources						
Signal model [%]	±0.5	±0.5	±0.5	±0.5	±0.5	±0.5
Background model [%]	±1.2	±1.2	±1.2	±1.2	±1.2	±1.2
Total systematic error [%]	±1.3	±1.3	±1.3	±1.3	±1.3	±1.3

$D^+ \to K^-\pi^+\pi^+$						
p_T [GeV/c]	6.0-7.0	7.0-8.0	8.0-10	10-12	12-20	$\geq$12
N	3650	5708	8736	4784	4896	5483
Statistical error	±96	±133	±164	±112	±114	±122
Relative statistical error [%]	±2.6	±2.3	±1.9	±2.3	±2.3	±2.2
Systematic sources						
Signal model [%]	±5.1	±5.1	±5.1	±5.1	±5.1	±5.1
Background model [%]	±3.6	±3.6	±3.6	±3.6	±3.6	±3.6
Total systematic error [%]	±6.2	±6.2	±6.2	±6.2	±6.2	±6.2

$D_s^+ \to \phi\pi^+, \phi \to K^-K^+$					
p_T [GeV/c]	6.0-8.0	8.0-10	10-12	12-20	≥ 12
N	136	379	254	197	218
Statistical error	±16	±28	±24	±21	±23
Relative statistical error [%]	±11.8	±7.4	±9.4	±10.7	±10.6
Systematic sources					
Signal & background model [%]	-	-	-	-	-

Table 5.1: Summary of the charm meson yields and the associated uncertainties. The total systematic error is calculated by adding all contributions in quadrature.

For $D^0 \to K^-\pi^+$ decay, we find that the yield from OI tracks is about 1.7% more than from OIZ tracks. We have two explanations for this difference which are not related to tracking efficiencies:

- From minimum bias events, we find that the SVT and offline d_0 correlation is slightly higher for OI tracks (~ 0.77) than for OIZ tracks (~ 0.75). Since we require an impact parameter larger than $120\,\mu$m both offline and from the SVT, a higher correlation means a smaller inefficiency from "double cutting". Indeed, when we compare the D^0 yield without applying impact parameter requirement on the offline tracks, the difference becomes smaller (0.7%).
- The width of the D^0 peak using OI tracks is roughly 10% wider compared to using OIZ tracks because of the relatively poor track $\cot\theta$ measurement. When fixing the ratio between the width of the signal and the width of the autoreflection to the values found in [81], we over estimate the width of the autoreflection. After correcting the ratio of the widths, we find that OIZ tracking yields more D^0's than OI tracking. (2.3% more with the offline track d_0 requirement and 3.1% more without the requirement.)

For three body $D^+ \to K^-\pi^+\pi^+$ decays, we find that OI tracking yields about 1.3% more events that OIZ tracks, which can be attributed to the higher correlation between the offline and SVT measurement of the impact parameter.

Since we measure the single track SVT, SVX efficiencies and resolutions from data [84], we conclude that we find no significant reconstruction inefficiency loss for OIZ tracks with respect to OI tracks, that has not been accounted for in the efficiency study.

Chapter 6

Direct Charm Fraction

6.1 Description of method

The basis of the method is illustrated in Fig. 6.1. The left hand sketch illustrates direct charm production, which produces charmed mesons at the primary vertex (PV). Weakly decaying charmed particles will propagate from the primary vertex and decay. The decay products are then detected by the SVT and the event is selected. Since all of the decay products of the charm hadron are found, the charm hadron is completely reconstructed, and the line of flight of the charm hadron from the decay point can be extrapolated back to the primary vertex. With perfect detector resolution, the impact parameter of the charm hadron, which is the distance of closest approach of the line of flight to the primary vertex measured in the plane transverse to the beamline ($r - \phi$ plane), is zero. Due to finite tracking resolution and the finite resolution on the position of the primary vertex, the distribution of impact parameters of directly produced charm will be a Gaussian centered at zero with a width dominated by the resolution of the Silicon Vertex Detector (SVX). This distribution may have non-Gaussian tails due to assigning incorrect silicon hits to the charm daughter tracks or due to alignment errors in the SVX.

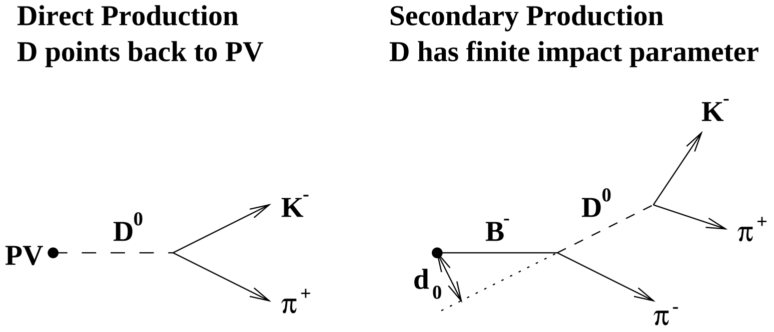

Figure 6.1: The impact parameter of direct and secondary charm in the $r - \phi$ plane.

In the case of secondary charm production, the charm hadron may have a nonzero impact parameter d_0, as illustrated in the right hand sketch in Fig. 6.1. The actual impact parameter distribution of secondary charm after the two track trigger may be obtained from Monte Carlo simulation. The uncertainty introduced by the Monte Carlo is small as long as the simulation describes correctly the B hadron production properties (transverse momentum p_T and rapidity y distributions) and decay kinematics. The impact parameter of secondary charm will be smeared by the same resolution effects as direct charm.

The expected impact parameter distribution for charm hadrons is

$$F(d_0) = (1 - f_D) \int F_B(x) F_D(d_0 - x) dx + f_D F_D(d_0), \tag{6.1}$$

where f_D is the fraction of prompt charm hadrons, F_B is the true impact parameter distribution for secondary charm obtained from Monte Carlo and F_D is the detector impact parameter resolution function. The secondary charm fraction is therefore $f_B = 1 - f_D$. We use combinations of exponentials and Gaussians to describe F_B and F_D so that the integral in Eq. 6.1 can be performed analytically. By fitting the observed charm hadron impact parameter distribution from the data, we can determine simultaneously the fraction of direct charm f_D in the data sample and the parameters that describe the detector resolution function $F_D(d_0)$.

6.2 Two Track Trigger Bias

For a given decay topology, the impact parameter requirements imposed by the trigger define three regions in the $r - \phi$ plane. These three regions are shown in Fig. 6.2 for a specific $D^0 \to K^-\pi^+$ decay. The impact parameter of a track has a sign that is defined by the following formula:

$$d_0 = \frac{\hat{z} \cdot (\vec{r} \times \vec{P}_T)}{|\vec{P}_T|}, \tag{6.2}$$

where $\vec{p}_T$ is the transverse momentum vector of the particle, where $\vec{p}_T$ is the transverse momentum vector of the particle, $\vec{r}$ is the vector pointing from the primary vertex to the reconstructed particle trajectory at the point of closest approach to the primary in the $r - \phi$ plane and $\hat{z}$ is the unit vector along the z axis. Using the example of $D^0 \to K^-\pi^+$ shown in Fig. 6.2, the product of the impact parameters of the two tracks is $d_0(K^-) \cdot d_0(\pi^+) < 0$ in Region I and $d_0(K^-) \cdot d_0(\pi^+) > 0$ in Region II. The trigger excludes decays in Region III. A D^0 from direct production can only populate Region I with positive L_{xy}. Secondary D^0's may populate Region I or Region II. Because the forbidden region is $240\,\mu m$ wide, which is significantly larger than the resolution on the impact parameter from the SVT, the decays in Region I are cleanly separated from the decays in Region II. The distinction between Region I and Region II plays an important role in determining the impact parameter resolution and in checking the fraction of direct and secondary D's [21].

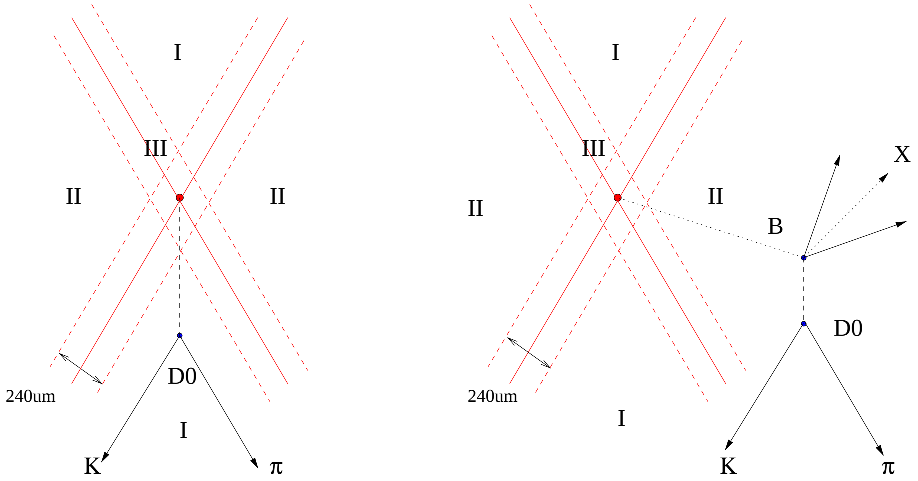

Figure 6.2: The topology of the two track trigger bias for $D^0 \to K^-\pi^+$.

A generator-level Monte Carlo study is used to illustrate the two track trigger bias on the D meson decays, The production and fragmentation of b quarks is simulated with the Monte Carlo generator BGENERATOR, and the resulting B hadrons are decayed using the QQ package. The decays of the B mesons are inclusive, but the secondary charm mesons are forced to decay in the following modes:

- $D^0 \to K^-\pi^+$,
- $D^{*+} \to D^0\pi^+, D^0 \to K^-\pi^+$,
- $D^+ \to K^-\pi^+\pi^+$, and
- $D_s^+ \to \phi\pi^+, \phi \to K^+K^-$.

SVT-like selection criteria [1] are applied to the D decay daughters. The impact parameter distributions for secondary D^0, D^{*+}, D^+, and D_s^+ for Region I and Region II defined by the trigger are shown in Fig. 6.3. The trigger bias sculpts the shape of the impact parameter distribution. Since for two body D decays only secondary charm contributes to Region II, we only need to determine the fraction of direct charm in Region I. Therefore for the D^0, we require $d_0(K^-) \cdot d_0(\pi^+) < 0$.

The trigger also affects the impact parameter distribution of three-body D^+ and D_s^+ decays, as shown in Fig. 6.3. A small fraction of direct D^+ have a positive impact parameter product for the two decay products that form an SVT-pair. This

---

[1] We require two tracks with opposite charge, each one satisfies $p_T \geq 2.0\,\mathrm{GeV/c}$, $120\,\mu m \leq |d_0| \leq 1\,\mathrm{mm}$, $p_{T1} + p_{T2} \geq 5.5\,\mathrm{GeV/c}$, $2^\circ \leq |\Delta\phi_0| \leq 90^\circ$, and $L_{xy} \geq 200\mu m$.

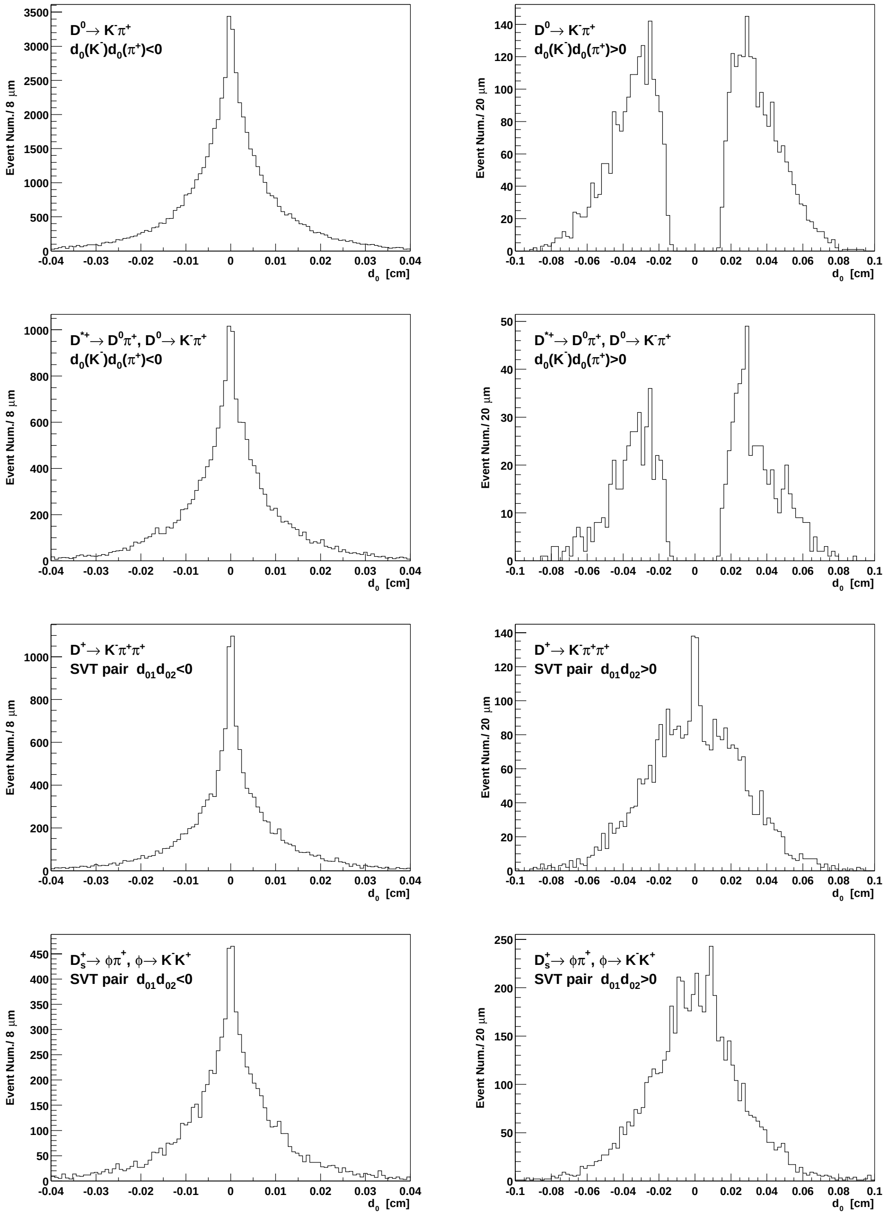

Figure 6.3: The impact parameter distribution predicted by the generator level Monte Carlo simulation described in the text of secondary D^0, D^{*+}, D^+ and D_s^+ after the SVT trigger requirements are satisfied.

	$d_{01} \cdot d_{02} < 0$	$d_{01} \cdot d_{02} > 0$
Secondary D^0	93.56%	6.44%
Secondary D^{*+}	94.14%	5.86%
Prompt D^+	96.74%	5.47%
Secondary D^+	85.84%	18.93%
Prompt D_s^+	94.21%	18.33%
Secondary D_s^+	65.86%	48.22%

Table 6.1: The fraction of D mesons with negative and positive impact parameter products predicted by the Monte Carlo simulation described in the text. In this Table, d_{01} and d_{02} are the signed impact parameters of the two tracks forming the SVT-pair. Directly produced D^0 and D^{*+} only have $d_{01} \cdot d_{02} < 0$. Three-body decays have two possible SVT-pairs and there can be more than one SVT-pair per decay.

fraction is slightly higher for secondary D^+. In the case of D_s^+ decays, the mass difference of the ϕ and its decays daughters is very small, so the kaons tend to have similar momentum and a small opening angle. At least one of the kaons must be an SVT-like track, and, therefore, there is a high probability that the other kaon is a SVT-like track. In this case, the impact parameter product $d_0(K^-) \cdot d_0(K^+)$ is almost always positive. Often all three decay products of the D_s^+ are SVT-like tracks, resulting in two SVT-pairs, one with a positive impact parameter product and one with a negative impact parameter product. The fractions of D mesons with positive and negative impact parameter products predicted by the Monte Carlo are listed in Table 6.1. We do not apply a requirement on the impact parameter product of the SVT-pairs in D^+ and D_s^+ decays.

6.3 Predicted Impact Parameter Distribution of Secondary Charm Mesons

The impact parameter distributions of secondary D mesons ($d_0(D)$) predicted by the Monte Carlo simulation are shown in Fig. 6.3. There is a large spike at at zero impact parameter in the $d_0(D)$ distribution. At least two phenomena contribute to this spike. First, D mesons from B hadrons that decay close to the primary vertex will appear prompt. Second, as a result of the trigger requirements, the secondary D meson often follows the parent B line-of-flight, which again results in $d_0(D)$ being close to zero. Nevertheless, the $d_0(D)$ distribution from secondary charm has a long tail that is absent in the direct charm production. This long tail is used to separate statistically secondary charm from direct charm.

A more detail Monte Carlo study was performed to find the true impact parameter distribution of secondary charm. The production and fragmentation of b quarks is simulated with the Monte Carlo generator BGENERATOR, and the resulting B hadrons are decayed using the QQ package. The decays of the B mesons are inclusive, but the secondary charm mesons are forced to decay in the following modes:

- $D^0 \to K^- \pi^+$;

- $D^+ \to K^-\pi^+\pi^+$;
- $D_s^+ \to \phi\pi^+, \phi \to K^+K^-$.

More than 5×10^8 $b\bar{b}$ events are generated and the trigger and offline reconstruction simulation are subsequently performed, as described in section 9. Note that we apply the trigger and analysis requirements on the smeared variables, but evaluate the true impact parameter distribution of secondary D^0, D^{*+}, D^+, and D_s^+. We then fit this with a double exponential for each p_T bin:

$$F_B(d_0) = \frac{\epsilon_1}{2\lambda_1} e^{-|d_0|/\lambda_1} + \frac{1-\epsilon_1}{2\lambda_2} e^{-|d_0|/\lambda_2}. \tag{6.3}$$

The fitter parameters ϵ_1, λ_1, λ_2 are slightly p_T dependent. For all four types of D mesons considered here, λ_2 varies from $15\,\mu m$ to $25\,\mu m$, with a rather small contribution to the overall d_0 distribution ($\sim$ 20%). A much longer exponential function ($\lambda_1 \sim 100\,\mu m$) makes up the rest as illustrated in Figure 6.4. As we will see later, because the detector resolution is characterized by a Gaussian resolution that is smaller[2] than λ_1, the observed secondary $d_0(D)$ distribution after detector smearing has a small central peak similar to the detector resolution function, with a distinctive long tail that is mostly unaffected by detector resolution effects.

As a cross check, we applied the trigger and reconstruction requirements on the unsmeared variables and found no significant difference.

---

[2] A Gaussian falls off much faster than an exponential as well.

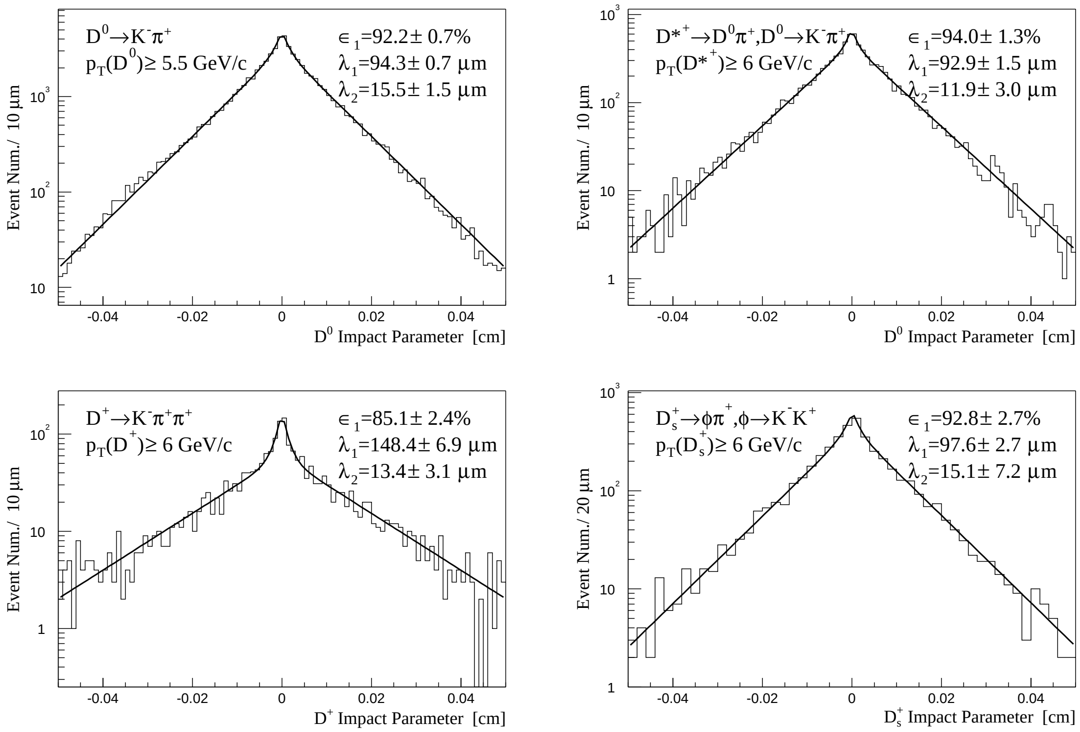

Figure 6.4: The Monte Carlo prediction of the true impact parameter distributions for secondary D^0, D^{*+}, D^+ and D_s^+ after trigger and offline selection requirements

6.4 Direct Charm Impact Parameter Resolution

Knowledge of the direct charm impact parameter resolution is essential to make a reliable measurement of the direct and secondary charm fraction. In this section, we study the impact parameter distribution of $K_S^0 \to \pi^+\pi^-$ decays collected with the two-track trigger. Because of the 1 mm upper limit on the impact parameter for SVT tracks, the trigger selects K_S^0 that have decayed close to the beam spot.

6.4.1 K^0_S Reconstruction

To extract a $K^0_{\mathrm{S}} \to \pi^+\pi^-$ signal, we use the selection criteria itemized below. We use similar criteria for $D^0 \to K^-\pi^+$ reconstruction. We correct for the beam offset and slope when calculating impact parameter d_0 and decay length L_{xy}.

- the $\pi^-\pi^+$ pair is a trigger pair;
- $p_T(K^0_S) \geq 5.5\,\mathrm{GeV}/c$;
- $L_{xy}(K^0_S) \geq 500\,\mu\mathrm{m}$;
- $d_0(\pi^-) \cdot d_0(\pi^+) < 0$;
- $|z_0(\pi^-) - z_0(\pi^+)| \leq 5\,\mathrm{cm}$.

The invariant mass distribution for $K^0_{\mathrm{S}} \to \pi^+\pi^-$ candidates is shown in Fig. 6.5. The signal is about 95 000. No K^0_{S} mass peak is observed when applying the same selection criteria outlined above *except* reversing the requirement on the product of the impact parameters of the pions to $d_0(\pi^+) \cdot d_0(\pi^-) > 0$. The opening angle between two pions from K^0_{S} is small. If a significant fraction of the K^0_{S} are not prompt, some of these secondary kaons would satisfy the SVT-like requirements and would have $d_0(\pi^+) \cdot d_0(\pi^-) > 0$. The absence of a peak after requiring $d_0(\pi^+) \cdot d_0(\pi^-) > 0$ indicates that a large fraction of the K^0_{S} are prompt, making this a good sample of SVT-pairs to study the resolution of the impact parameter distribution.

This sample is an inclusive $K^0_{\rm S}$ sample. Since the $K^0_{\rm S}$ lifetime is so much longer than the lifetime of D hadrons and B hadrons, the lifetime aspect of the two displaced track trigger does not enhance the fraction of $K^0_{\rm S}$ from heavy flavor (the p_T requirements do enhance this fraction by a modest amount). Although this inclusive $K^0_{\rm S}$ selection might somewhat enhance the c and b fraction of inelastic collisions, it is our prejudice that the fraction of non-prompt $K^0_{\rm S}$ will remain small. A detail study [21] has shown that the secondary $K^0_{\rm S}$ fraction is small ($\sim 5\,\%$).

In Fig. 6.5 the $\pi^+\pi^-$ invariant mass distribution for $K^0_{\rm S}$ candidates is fit with a Gaussian to describe the signal and a linear term to describe the combinatorial background. The wings of the mass peak are poorly described using a single Gaussian because the signal width varies with $p_T(K^0_{\rm S})$. No corrections have been made for energy loss, so the measured $K^0_{\rm S}$ mass is smaller than the world average and increases with $p_T(K^0_{\rm S})$.

6.4.2 K^0_S Impact Parameter Distribution

The impact parameter distributions of $K^0_{\rm S}$ in the signal region and sideband region are shown in Fig. 6.6. The distribution has a much longer tail in the sideband region than in the signal region. After correcting the signal distribution for background using a sideband subtraction, the resulting distribution is not described well by a single Gaussian. Instead, it can be modeled very well with the combination of a

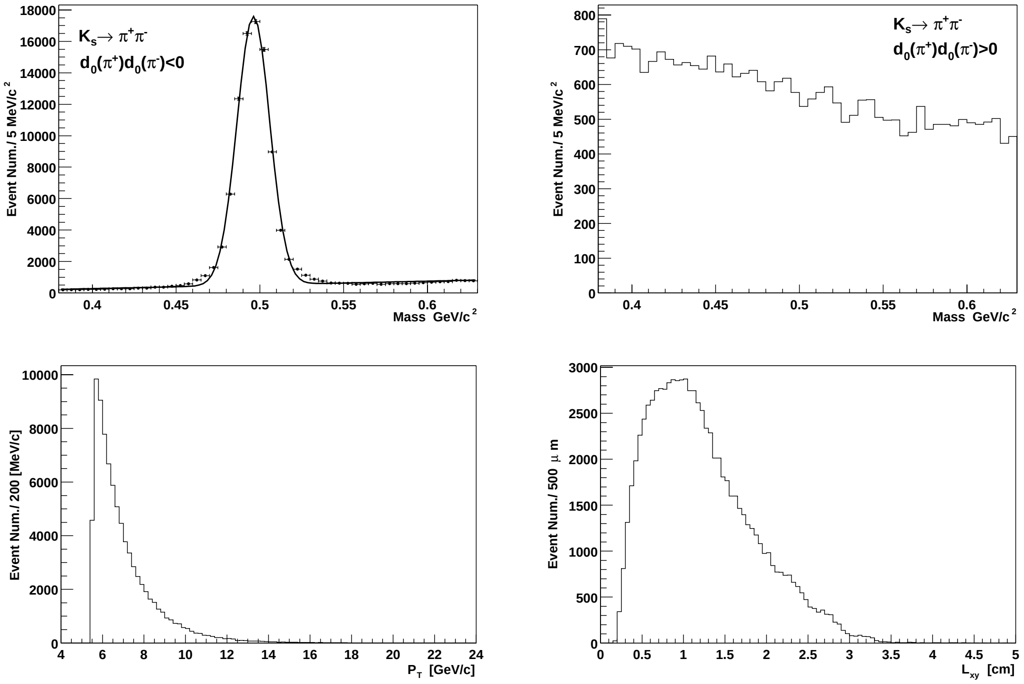

Figure 6.5: The $K^0_{\mathrm{S}} \to \pi^+\pi^-$ invariant mass, p_T and L_{xy} distributions. The left hand mass distribution is for K^0_{S} candidates with $d_0(\pi^+) \cdot d_0(\pi^-) < 0$, and the right hand mass distribution is for $d_0(\pi^+) \cdot d_0(\pi^-) < 0$. There is no signal apparent in this right hand mass distribution, which indicates a lack of secondary K^0_{S}. The p_T and L_{xy} distributions are for candidates in the 2σ signal region, which is defined in the text. No sideband subtraction has been performed.

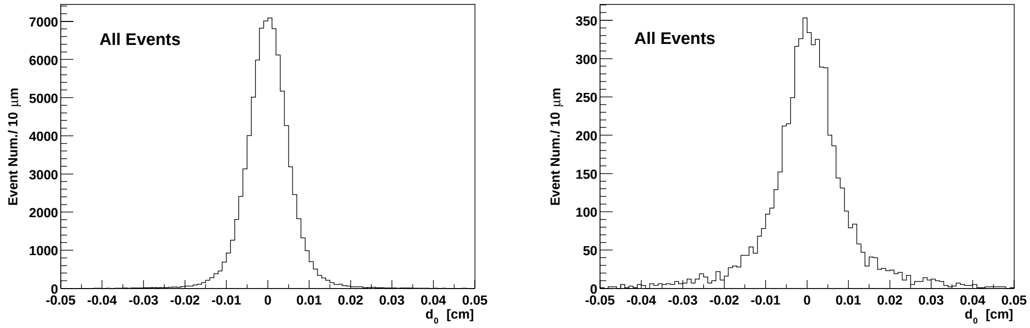

Figure 6.6: The impact parameter distribution of K^0_{S} in the signal region (left) and sideband region (right) defined in the text.

Gaussian distribution and an exponential distribution:

$$F_{K_s}(d_0) = \frac{1-\alpha_0}{2\lambda_{K_s}} e^{-|d_0|/\lambda_{K_s}} + \frac{\alpha_0}{\sqrt{2\pi}\sigma_{K_s}} e^{-d_0^2/2\sigma_{K_s}^2}, \qquad (6.4)$$

where the free parameters are the exponential tail λ_{K_s}, the Gaussian resolution σ_{K_s}, and the fraction of the area of the impact parameter distribution that is described by the Gaussian α_0. The results of fitting this function to the impact parameter distribution measured in the signal region K_S^0 after sideband subtraction are shown in Fig. 6.7. About 80% of K_s impact parameter distribution is accounted for by a single Gaussian with a width of $40\mu m$; the other 20% is accounted for by the exponential function with a decay length around 45μm. Although the d_0 distribution of prompt K_S^0 has a significant (non-Gaussian) component from the exponential tail, the tails of secondary D mesons are two to three times longer and still provide a means to separate secondary charm from direct charm.

Since the K_S^0 has a much longer lifetime than charm and B mesons, the decay length L_{xy} distribution of the K_S^0 extends significantly beyond 1 cm, as shown in Fig. 6.5. The value of L_{xy} for direct charm rarely exceeds 1 cm. The L_{xy} distribution of secondary charm extends to slightly larger values than direct charm because of the long B hadron lifetime. Since the pointing resolution degrades as L_{xy} increases, the non-Gaussian tails of the impact parameter resolution function may increase with increasing L_{xy} as well. To check this, we measure the impact parameter resolution of the K_S^0 as a function of L_{xy}. We perform the fits in bins of p_T as well and observe no strong p_T and L_{xy} dependence [21].

6.4.3 Expected Impact Parameter Resolution for Charm

We expect the impact parameter resolution function for charm $F_D(d_0)$ to be similar to $F_{K_s}(d_0)$:

$$F_D(d_0) = \frac{1-\alpha_0}{2\lambda_D} e^{-|d_0|/\lambda_D} + \frac{\alpha_0}{\sqrt{2\pi}\sigma_D} e^{-d_0^2/2\sigma_D^2}. \tag{6.5}$$

However, since the K_S^0 and D mesons have different p_T and L_{xy} distributions, we do not expect that the parameters of the resolution functions will have same values. In the fits of the D meson impact parameter distributions described in the following section, we assume that the percentage of the Gaussian term in Equation 6.5 for charm is the same as this percentage in $F_{K_s}(d_0)$ and that the ratio between the width of Gaussian term and the decay length of the exponential term is the same for D mesons and K_s. Furthermore, for simplicity, variations of the resolution function with p_T and L_{xy} are ignored. We fix $\alpha_0 = 82.0\%$ and the ratio $\lambda_D/\sigma_D = 1.11$ to the values determined in the fit to the inclusive K_S^0. Only σ_D is kept as a free parameter.

6.5 The Direct Charm Fraction

The impact parameter distributions for D^0, D^{*+}, D^+ and D_s^+ after side band subtraction are shown in Figures 6.9, 6.10, 6.11, and 6.12. The signal regions are defined as $|m - \bar{m}| \leq 2\sigma$ and the side band regions are defined as $3\sigma \leq |m - \bar{m}| \leq 5\sigma$, where $\bar{m}$ and σ are the measured charm meson mass and width quoted in Section 5. When the signal is modeled with a double Gaussian, the width of the wide Gaussian is used.

To fit the D meson impact parameter distribution, the parameters of the true impact parameter distribution $F_B(d_0)$ for secondary charm are fixed to the values obtained from the Monte Carlo. For the impact parameter resolution function $F_D(d_0)$, we use the value of α_0 and the ratio between λ_D and σ_D obtained from the K_S^0 study. There are only two free parameters left in the final fit function: the detector resolution σ_D and the fraction of direct charm mesons f_D. A binned likelihood technique is used and the fit results are listed in Table 6.2.

As discussed in reference [21], the dominant systematic uncertainty for the direct charm fraction measurement comes from the impact parameter resolution function. To estimate the systematic uncertainty, we repeat the above analysis with a pure Gaussian impact parameter resolution function. Since the deviation has no significant p_T dependence, we assigned the averaged variation as the systematic uncertainty.

6.6 Discussion of the Measured Fraction

As shown in Figure 6.13, the B fractions measured for the four different D mesons are different, especially in the case of the D_s^+, in which the secondary contribution is more than twice as much as the other three D mesons. This is due to the facts that the relative production of D_s^+ from B decays is larger than for the other three D mesons because B^0 and B^+ mesons as well as B_s^0 mesons contribute to D_s^+ production [21], and the secondary D_s^+ also has relatively larger acceptance.

Since we measure both the length of the flight path L_{xy} in the plane transverse to the beamline and the p_T of the D mesons, we can measure the proper decay time t:

$$ct = \frac{m_D L_{xy}}{p_T}, \tag{6.6}$$

where c is the speed of light in cm/s, and the mass m_D and transverse momentum are in units of GeV/c^2 and GeV/c, respectively. In the case of direct charm production, this is the true decay time in the rest frame of the charm meson. In the case of secondary charm, this is an overestimate of the decay time, because L_{xy} includes a significant contribution due to the initial displacement of the parent B hadron. As a result, the ct distribution for secondary charm has a smaller slope and longer tail than the ct distribution for direct charm.

The expected ct distribution for direct and secondary charm for the four types of

D mesons are shown in Fig 6.8, as well as the background subtracted ct distribution from data. The distribution for secondary charm is distinctly different from the distribution for direct charm., clearly these do not describe the observed distributions in the data. In contrast, the combination of direct and secondary charm based on the fractions measured with the D meson impact parameter describe the data well as shown in Figure 11.11 at section 11.8.

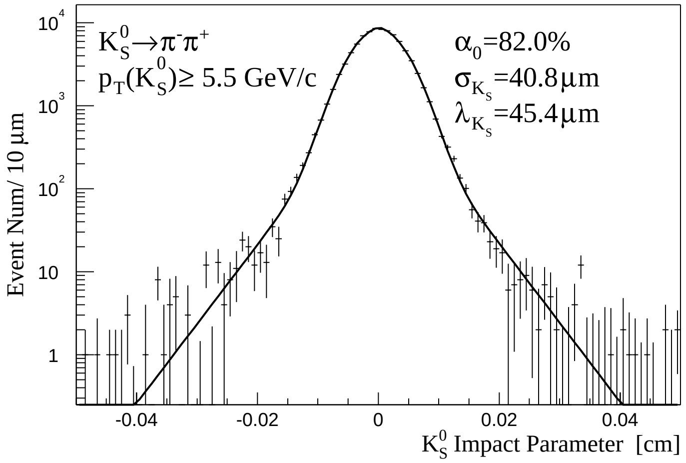

Figure 6.7: The impact parameter distribution of K_S^0 after side band subtraction.

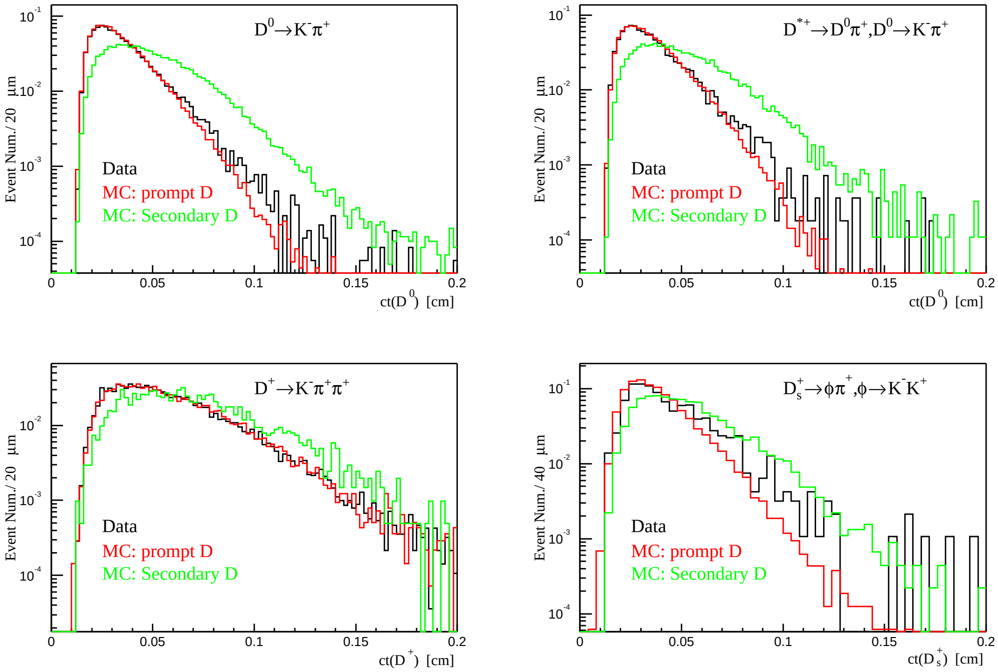

Figure 6.8: The comparison between ct distributions of the prompt and secondary D mesons predicted by the Monte Carlo simulation and the distribution from data after side band subtraction. The distributions are normalized to one.

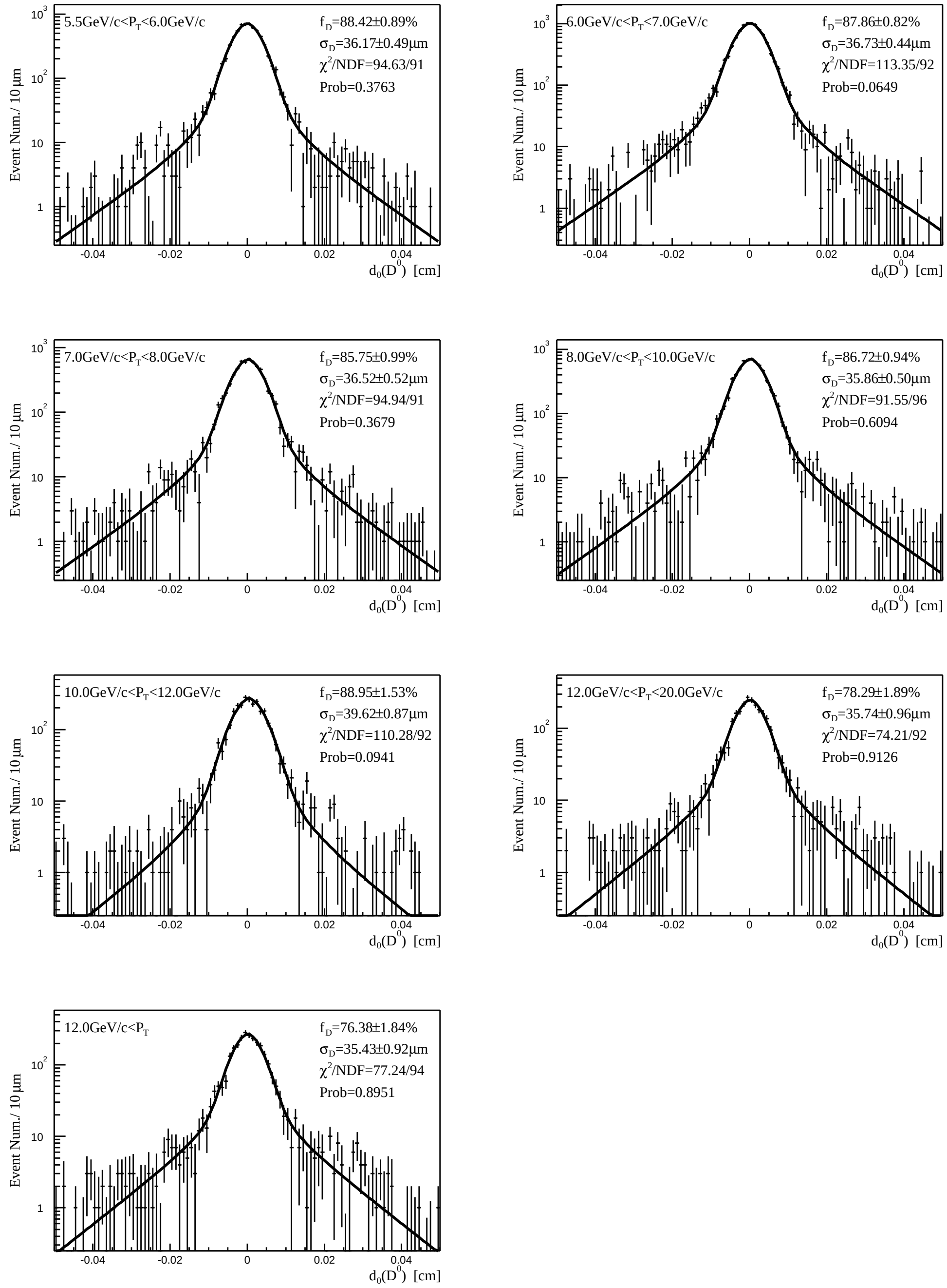

Figure 6.9: The impact parameter distribution for the signal region of the D^0 after side band subtraction.

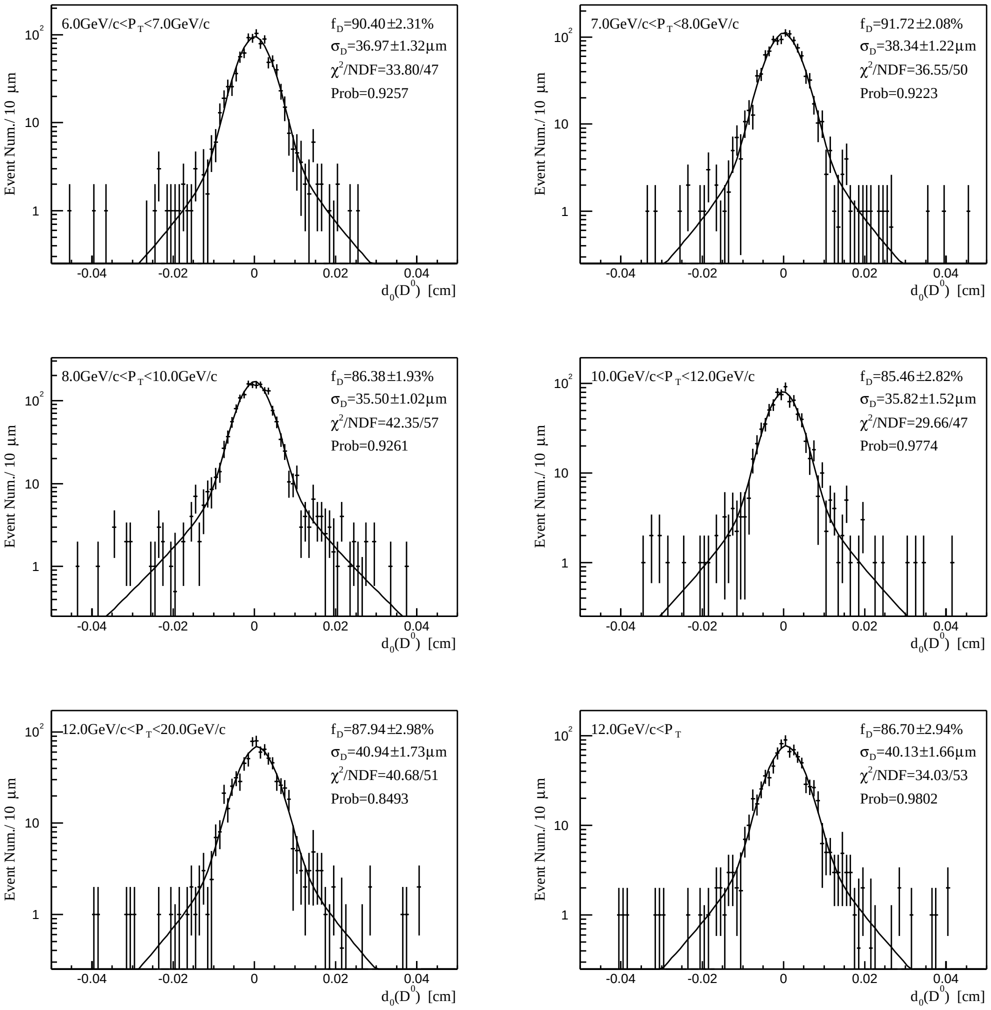

Figure 6.10: The impact parameter distribution for the signal region of the D^{*+} after side band subtraction.

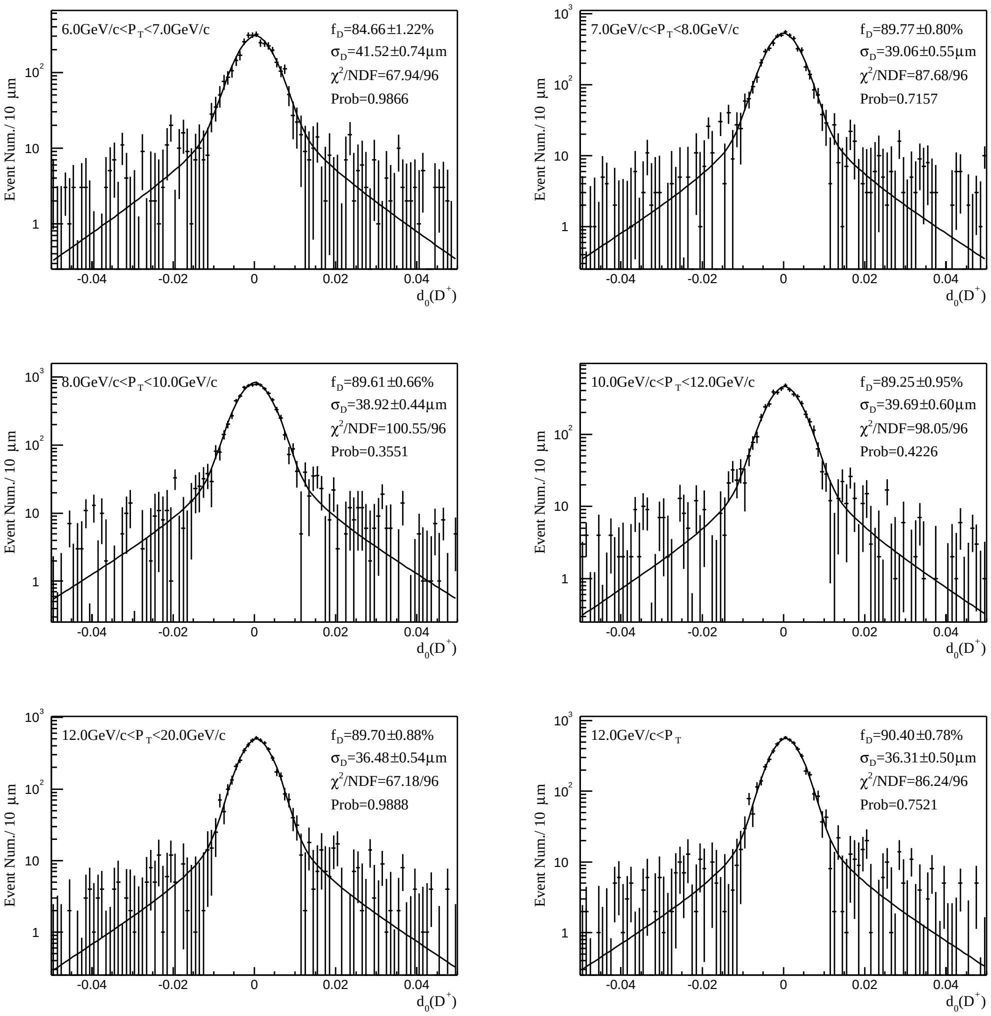

Figure 6.11: The impact parameter distribution for the signal region of the D^+ after side band subtraction.

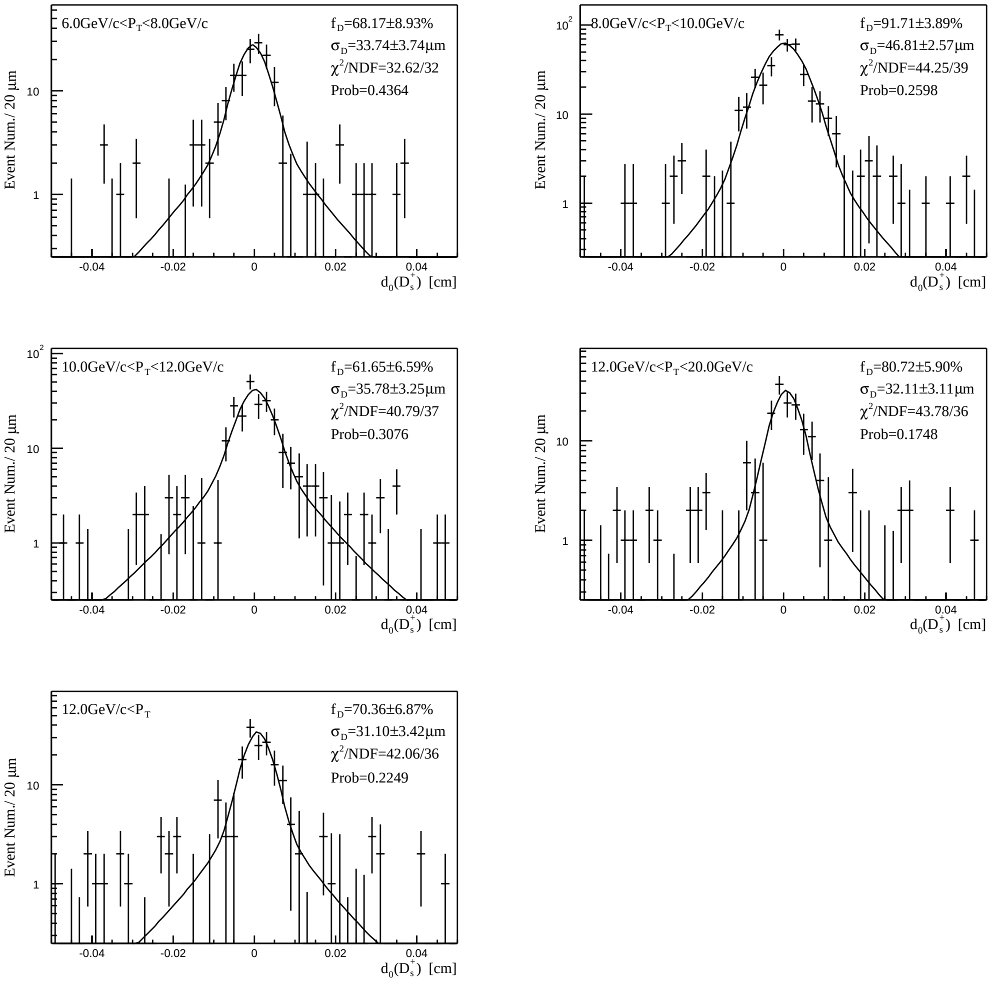

Figure 6.12: The impact parameter distribution for the signal region of the D_s^+ after side band subtraction.

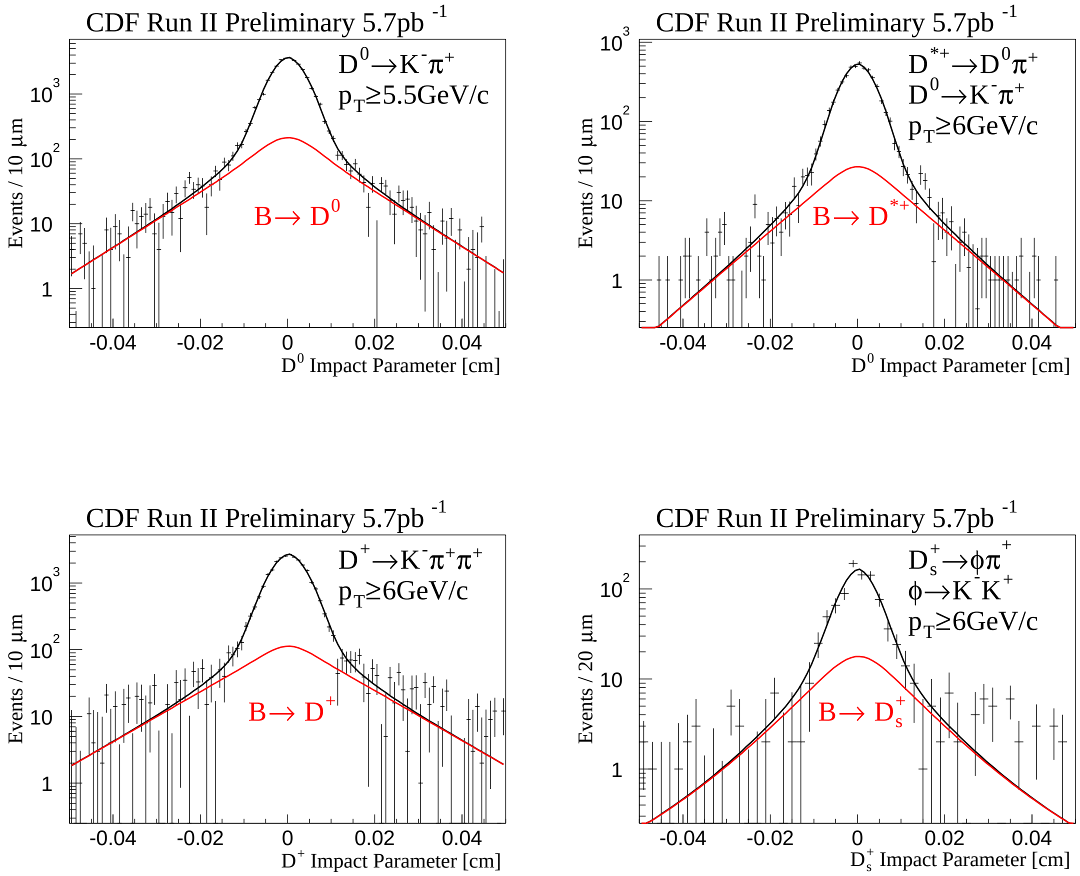

Figure 6.13: The impact parameter distribution of the D meson in signal region after side band subtraction. The black curve is the superposition of the fitted D meson impact parameter distributions in different P_T bins, and is used to calculate the χ^2 for the summed distributions. We obtain $\chi^2/\mathrm{NDF} = 1.32$ for D^0, 0.92 for D^{*+}, 1.05 for D^+, and 1.15 for D_s^+. The red curve is the fitted impact parameter distribution from the secondary charm mesons. The prompt D meson fractions f_D including all p_T bins are calculated using the event number and B fraction in each p_T bins. We obtain $f_D(D^0) = 86.5 \pm 0.4 \pm 3.5\%$, $f_D(D^{*+}) = 88.1 \pm 1.1 \pm 3.9\%$, $f_D(D^+) = 89.1 \pm 0.4 \pm 2.8\%$, and $f_D(D_s^+) = 76.0 \pm 3.2 \pm 2.1\%$, where the first error is statistical, and the second one is the systematic uncertainty. We also fit the D meson impact parameter distribution all together instead of in different p_T bins, and yield similar results: $f_D(D^0) = 86.5 \pm 0.4\%$, $f_D(D^{*+}) = 87.6 \pm 1.1\%$, $f_D(D^+) = 89.1 \pm 0.4\%$, and $f_D(D_s^+) = 72.4 \pm 3.4\%$, where the error is statistical only. Since we measure the D_s^+ cross section with minimum $p_T \geq 8\,\mathrm{GeV/c}$, the calculation shows that $f_D(D_s^+) = 77.3 \pm 3.8 \pm 2.1\%$, with $\chi^2/\mathrm{NDF} = 1.15$ in this case.

$D^0 \to K^-\pi^+$							
p_T [GeV/c]	5.5-6.0	6.0-7.0	7.0-8.0	8.0-10	10-12	12-20	≥ 12
f_D [10^{-2}]	88.4	87.9	85.8	86.7	89.0	78.3	76.4
Relative stat. error [%]	±1.0	±0.9	±1.2	±1.1	±1.7	±2.4	±2.4
Relative sys. error [%]	±4.1	±4.1	±4.1	±4.1	±4.1	±4.1	±4.1

$D^{*+} \to D^0\pi^+, D^0 \to K^-\pi^+$						
p_T [GeV/c]	6.0-7.0	7.0-8.0	8.0-10	10-12	12-20	≥ 12
f_D [10^{-2}]	90.4	91.7	86.4	85.5	87.9	86.7
Relative stat. error [%]	±2.6	±2.3	±2.2	±3.3	±3.4	±3.4
Relative sys. error [%]	±4.4	±4.4	±4.4	±4.4	±4.4	±4.4

$D^+ \to K^-\pi^+\pi^+$						
p_T [GeV/c]	6.0-7.0	7.0-8.0	8.0-10	10-12	12-20	≥ 12
f_D [10^{-2}]	84.7	89.8	89.6	89.3	89.7	90.4
Relative stat. error [%]	±1.4	±0.9	±0.8	±1.1	±1.0	±0.9
Relative sys. error [%]	±3.2	±3.2	±3.2	±3.2	±3.2	±3.2

$D_s^+ \to \phi\pi^+, \phi \to K^-K^+$					
p_T [GeV/c]	6.0-8.0	8.0-10	10-12	12-20	≥ 12
f_D [10^{-2}]	68.2	91.7	61.7	80.7	70.4
Relative stat. error [%]	±13.1	±4.2	±10.7	±7.3	±9.8
Relative sys. error [%]	±2.7	±2.7	±2.7	±2.7	±2.7

Table 6.2: Summary of the measured direct charm fraction for the two track hadronic data and the corresponding uncertainties.

Chapter 7

Single-Track Detector Efficiency

Thanks to the high efficiency and purity of COT tracking at CDF, we can use the measured COT tracks as a denominator to measure the efficiency of trigger tracks reconstructed by the XFT and SVT, and to measure the efficiency of finding hits in the silicon detector.

We use the following requirements to select COT tracks of high quality:

- the number of axial COT hits is ≥ 25;
- the number of stereo COT hits is ≥ 25;
- the track has $|z_0| \leq 47.25\,\mathrm{cm}$;
- the track must pass through the whole SVX detector: we extrapolate the helix

to R=10.645 cm and demand that $|z| \leq$47.25 cm;

- the track must pass through all 4 COT axial superlayers: we extrapolate the helix to R=133 cm and demand that $|z| \leq$155 cm;

- the absolute value of the impact parameter, $|d_0| < 1$ cm.

Since we use COT tracks as a denominator for all other efficiencies, the final efficiency calculation relies on the absolute COT tracking efficiency, which is described in the next sections.

7.1 COT Efficiency

Two tracking algorithms are used for tracking in the COT, one based on Segment Linking (SL) and the other based on Histogram Linking (HL). For offline reconstruction, both tracking methods are used, and the results are merged. In Level-3 of the trigger, tracking is based on Histogram Linking only, and the calibration constants used in the online tracking are less refined than the constants used in the offline reconstruction.

The relative tracking efficiency between offline tracking and Level-3 tracking was measured and found to be $(99.7 \pm 0.1 \pm 0.2)\%$ for muons with $p_T \geq 1.35\,\mathrm{GeV}/c$ and $(99.8 \pm 0.1 \pm 0.2)\%$ for tracks with $p_T \geq 1.5\,\mathrm{GeV}/c$. Because this efficiency is so high, effectively 100%, and the systematic error associated with this efficiency is small compared to the systematics associated with the offline tracking efficiency, we have ignored this efficiency in the calculation of the D meson trigger efficiency.

The offline COT tracking efficiency has been measured to be $99.63^{+0.35}_{-0.40}\%$ using high-p_T electrons from W decay collected from the W-notrack trigger [85]. While the measurement of the tracking efficiency for these high p_T isolated electrons gives confidence that pattern recognition can be fully efficient, it is not necessarily applicable to lower momentum non-isolated decay products from D meson decay. In the two-track data samples, larger track multiplicities may result in lower tracking efficiencies due to confusion of the pattern recognition from a dense hit environment or due to the loss of hits on tracks because they are obscured by hits from other tracks. The Monte Carlo does not reproduce the occupancy of hits in the COT found in the data, nor has it been demonstrated that the Monte Carlo reproduces the local charged particle environment around directly produced D mesons, so a pure Monte Carlo simulation cannot be used to determine a reliable estimate of the COT tracking efficiency. Instead we use a technique known as "track embedding." We embed Monte Carlo D meson decays in real data events that have been collected with the B_CHARM trigger, and calculate the efficiency of finding these embedded D mesons.

7.2 COT efficiency from track embedding

The track embedding technique and the efficiencies determined with track embedding for this analysis are described in reference [86]. There are two adjustable parameters in the track embedding Monte Carlo: the scale factor for the hit resolution and the minimum merge distance, which is the minimum difference in nanoseconds between the trailing edge of a hit from one track and the leading edge of the hit from a second track. If this difference is less than the minimum merge distance, the second hit is merged with the first hit and is *lost* for the purposes of pattern recognition. Values of 0.8 for the resolution scale factor and 20 nsec for the minimum merge distance were found to reproduce the hit residual and hit usage patterns distributions for tracks in the data. Details of these comparisons and tuning can be found in reference [86].

Figure 7.1 shows the COT efficiency as a function of $p_T(D)$ found using track embedding for the four types of charm mesons. The three sets of points in each plot correspond to minimum merge distances of 0 ns, 20 ns, and 40 ns. We use the values obtained for 20 ns merge distance as the central efficiency values, and we assign half the difference between 0 ns and 40 ns as an estimate of the systematic uncertainty on these efficiencies. The statistical uncertainty on the central efficiency value is also treated as a systematic error. To study variations in tracking efficiency with local track environment, we evaluated the efficiency of finding the embedded D meson as

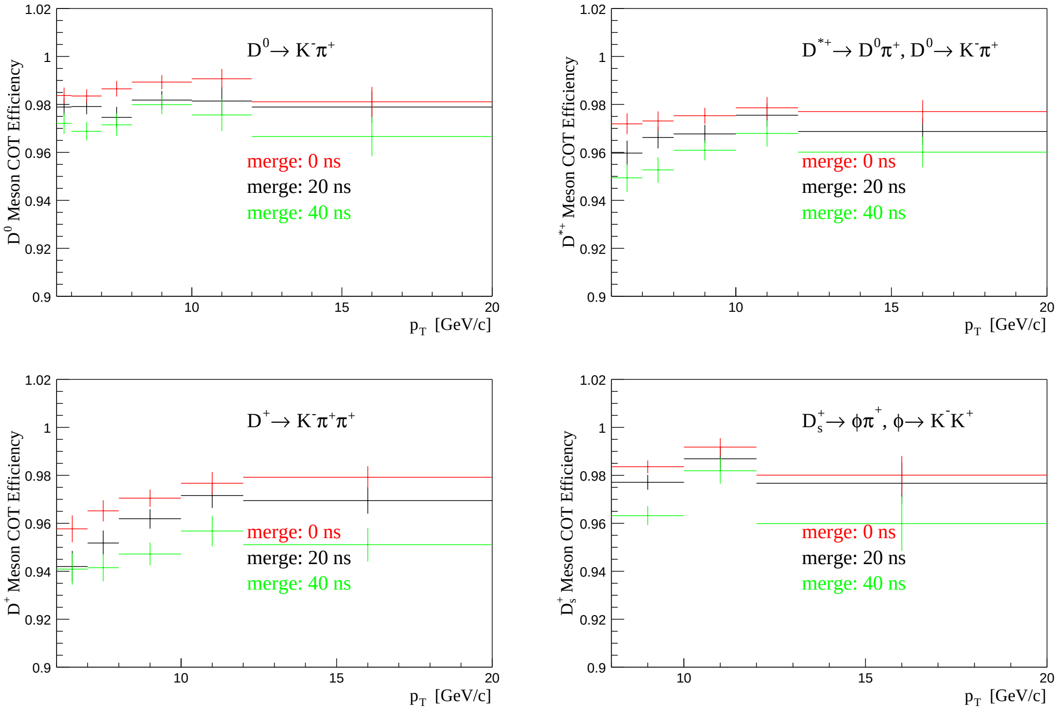

Figure 7.1: The COT efficiency as a function of $p_T(D)$ for charm meson reconstruction as determined from the track embedding study. The three different values of minimum merge criteria are described in the text. We use the values corresponding to 20 ns as our central value of efficiency.

a function of the separation (in ΔR) of this embedded meson with the the SVT pair that triggered the event (the relevant figures can be found in reference [86]). As a result of this study, an additional systematic error of 0.9% to 1.3% of the tracking efficiency has been added.

The track embedding study has measured the efficiency of finding the charm mesons with loose hit selection criteria on the COT tracks ($\geq$ 20 axial and $\leq$ 16 stereo hits), while throughout this analysis we apply stronger requirements ($\geq$ 25 axial and $\geq$ 25 stereo hits). We have evaluated the effect of these tighter COT hit selection criteria using the $D^+ \rightarrow K\pi\pi$ sample. For each $D^+ \rightarrow K\pi\pi$ candidate, we use the one track without a trigger bias to evaluate the relative efficiency between the tight and the loose COT hit requirements. We find a relative efficiency of 97.8%. The same relative hit selection criteria on embedded Monte Carlo tracks is 97.1%. We therefore attribute a per-track efficiency of $97.8 \pm 0.7\%$ to the additional inefficiency from cutting on $\geq$ 25 axial and $\geq$ 25 stereo hits. The difference in signal found in the data for D mesons selected with the tight and loose COT hit requirements is found to be consistent within statistics with this 97.8% per-track efficiency.

7.3 XFT Efficiency

The single-track XFT efficiency is defined as the probability for a COT track to be matched with an XFT track:

$$\epsilon_{\mathrm{XFT}} = \mathcal{P}(\mathrm{XFT}|\mathrm{COT}), \tag{7.1}$$

The offline track is matched with an XFT track by requiring the difference between their curvatures and track azimuthal angles at COT super layer 6 to satisfy $|\Delta C| = |C(\text{offline}) - C(\text{XFT})| \leq 2.0 \times 10^{-4}\,\text{cm}^{-1}$ and $|\Delta\phi_6| = |\phi_6(\text{offline}) - \phi_6(\text{XFT})| \leq 15\,\text{mrad}$.

The single-track XFT efficiency is measured using the minimum bias data. It is a function of various track parameters as shown in Figure 7.2. As expected, the XFT efficiency is high, well above 90%. No strong p_T, ϕ_0 or z_0 dependence is observed. However, the XFT efficiency varies significantly with $\cot\theta$, and the effect of the COT wire spacers is evident in the 2 dimensional $(\cot\theta, z_0)$ efficiency plots. We parameterize the single-track XFT efficiency as:

$$\epsilon_{\mathrm{XFT}}(p_T, \cot\theta, z_0, \phi_0) \approx \epsilon(p_T) \cdot \epsilon(z_0, \cot\theta)/\epsilon_0; \tag{7.2}$$

where the $\epsilon(p_T)$ and $\epsilon(z_0, \cot\theta)$ are the measured XFT efficiency in Figure 7.2. We divide by ϵ_0 the integrated efficiency, to get the correct normalization.

To account for systematic uncertainty due to possible fake matches in the matching window, we enlarge the size of the matching window to $|\Delta\phi_6| \leq 20\,\text{mrad}$ and

$|\Delta C| \leq 2.5 \times 10^{-4}$ and treat the difference in efficiency as a systematic uncertainty. For the larger matching window, we find an overall efficiency of 95.2%, compared to 94.9% for the default matching window, a relative difference of 0.3% per track.

7.4 SVT Efficiency

The single-track SVT efficiency is defined as the probability for a COT track that satisfies the XFT matching requirement to be matched with an SVT track:

$$\epsilon_{\mathrm{svt}} = \mathcal{P}(\mathrm{SVT}|\mathrm{XFT},\mathrm{COT}). \tag{7.3}$$

Factorizing the XFT efficiency in this way allows us to use the L1 auto-accept data, which has larger statistics of $p_T \geq 2.0\,\mathrm{GeV}/c$ tracks than the minimum bias sample. The matching is done by comparing the difference in track curvature and azimuthal angle between the SVT track and the COT track. The same matching criteria as used in reference [87] are applied here, namely $|\Delta C| = |C(\mathrm{offline}) - C(\mathrm{SVT})| \leq 1.5 \times 10^{-4}\,\mathrm{cm}^{-1}$ and $|\Delta\phi_0| = |\phi_0(\mathrm{offline}) - \phi_0(\mathrm{SVT})| \leq 15\,\mathrm{mrad}$. The SVT track χ^2 is required to be smaller than or equal to 25. In the rare case of multiple matches, we use the SVT track with the smallest χ^2. An offline track that can be matched with an SVT track is referred to as an “SVT-matched track” in this analysis.

The SVT efficiency measured from L1 auto-accept data is dominated by tracks

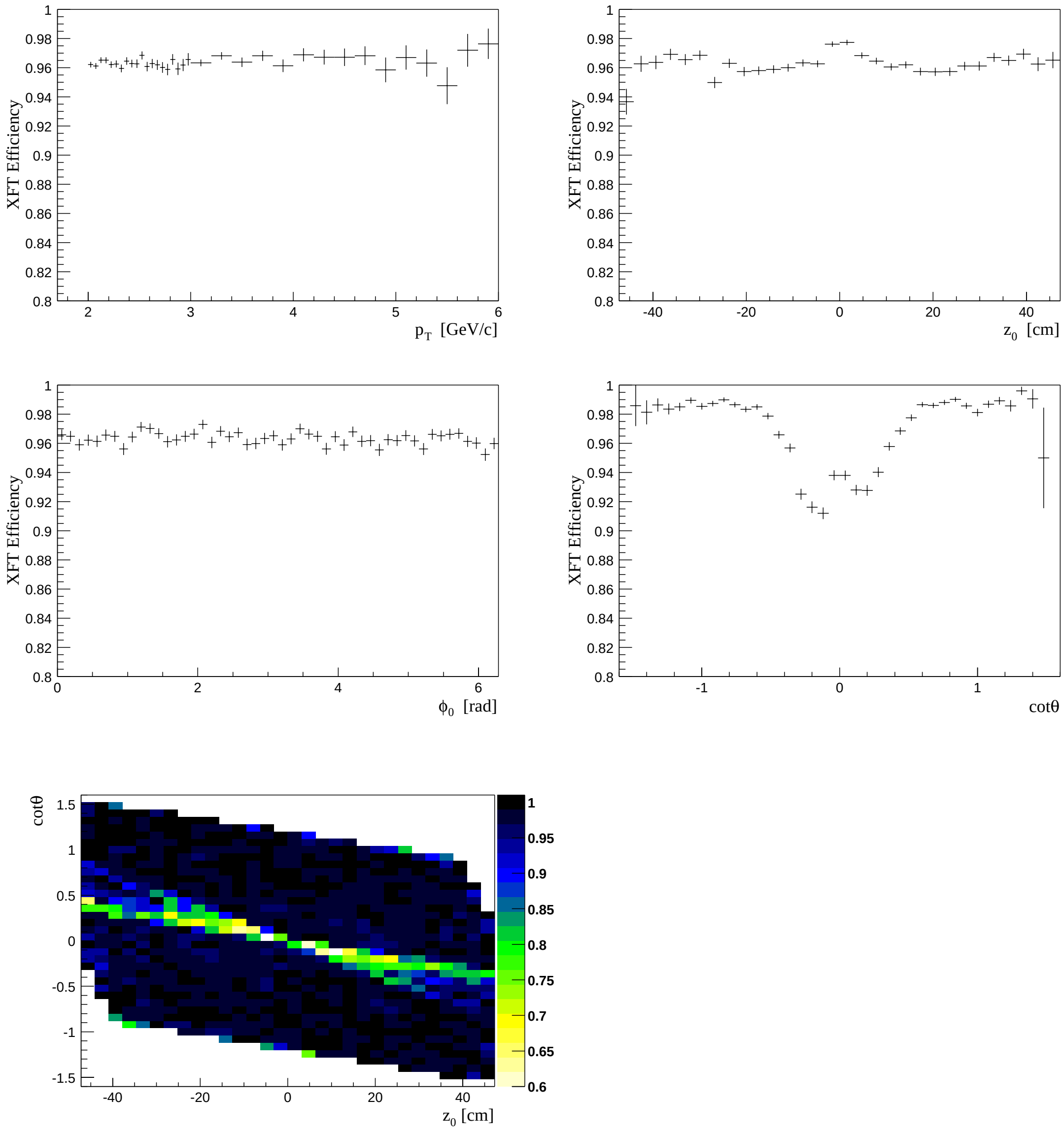

Figure 7.2: Single-track XFT efficiency as a function of p_T, z_0, ϕ_0, and $\cot\theta$. The last plot is the XFT efficiency as a function of z_0 and $\cot\theta$ together.

with small impact parameter, while the charm signals are triggered by tracks with an impact parameter between 0.12 and 1.0 mm. The SVT efficiency dependence on the impact parameter has been studied in $J/\Psi \rightarrow \mu^+\mu^-$ data, which is rich in displaced tracks from B-decay. Figure 7.3 illustrates that the SVT efficiency may not be fully efficient all the way up to the nominal value of 1 mm on d_0 [88].

We apply the parameterization shown in Figure 7.3 to take into account the shape of the d_0 dependence of the SVT efficiency:

$$\epsilon_{SVT}(d_0) = \epsilon_{SVT}(0) \cdot \Big(1 - \exp(-180.09\mathrm{cm}^{-2} \cdot (0.18799\mathrm{cm} - \mathrm{d}_0)^2)\Big) \tag{7.4}$$

where d_0 is the impact parameter of the track, expressed in cm. We use the curve of Figure 7.3 for calculating the central value of the efficiency and use the difference with a flat efficiency as a measure of the systematic uncertainty.

Unlike the XFT efficiency, the SVT efficiency is not close to unity and is a complicated function of various track parameters, as shown in Figure 7.4. This is no surprise. Not all of the 72 SVX wedges were fully functioning during this data taking period and also not all of them were used by the SVT, because the SVT online reconstruction requires 4 ϕ-side hits in 4 different SVX layers including a hit in layer 0. The SVT configuration (*i.e.* the patter coverage, the super-strip size, etc.) strongly affects the SVT efficiency, and its dependence on the track geometrical parameters ϕ_0, $\cot\theta$, and z_0. Moreover, the intrinsic SVT efficiency depends on the track-p_T, and the track efficiency is also significantly lower around the SVX barrel

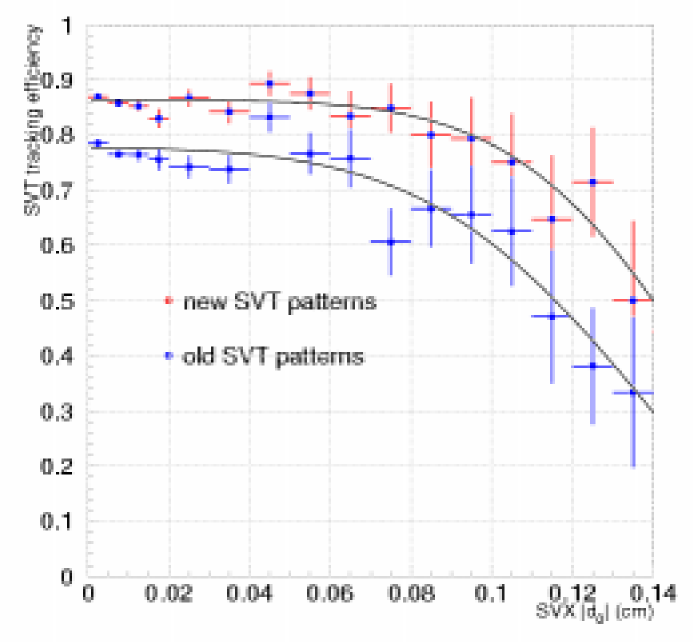

Figure 7.3: SVT efficiency dependence on the impact parameter d_0, as measured from J/Ψ data. Tracks are required to have 4 SVX hits, which explains the high SVT efficiency. Therefore, we use only the shape, not the absolute value. Note that the data used in our analysis correspond to the blue points (old patterns).

joints due to the loss of tracks that cross mechanical barrels.

To calculate the efficiency for two SVT tracks, we cannot simply take the square of the single-track efficiency. We need to understand the single-track SVT efficiency as a function of all track parameters, since the track parameters of two trigger tracks from a charm meson are strongly correlated. The limited statistics, however, does not allow us to bin the data in 5 dimensions, and we try to account for the strongest correlations with 2-dimensional histograms and factorize whenever possible. Section 10 describes how we compare calculated two-track efficiencies with measured

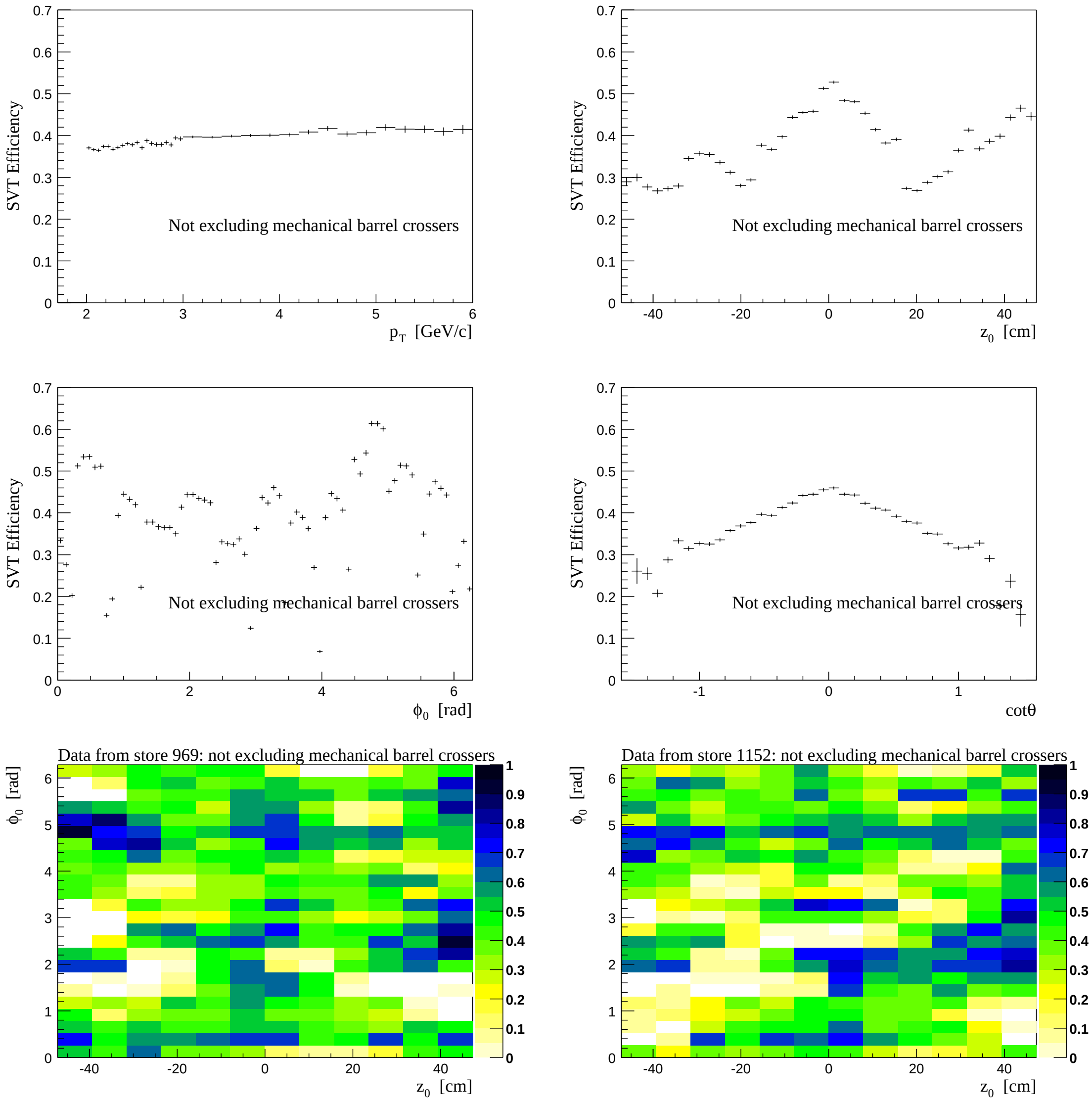

Figure 7.4: Single-track SVT efficiency as a function of p_T, z_0, ϕ_0, and $\cot\theta$ before excluding mechanical barrel-crossers. The last two plots are the SVT efficiency as a function of z_0 and ϕ_0 together for the data from two different beam stores, which shows the difference between their SVT configuration.

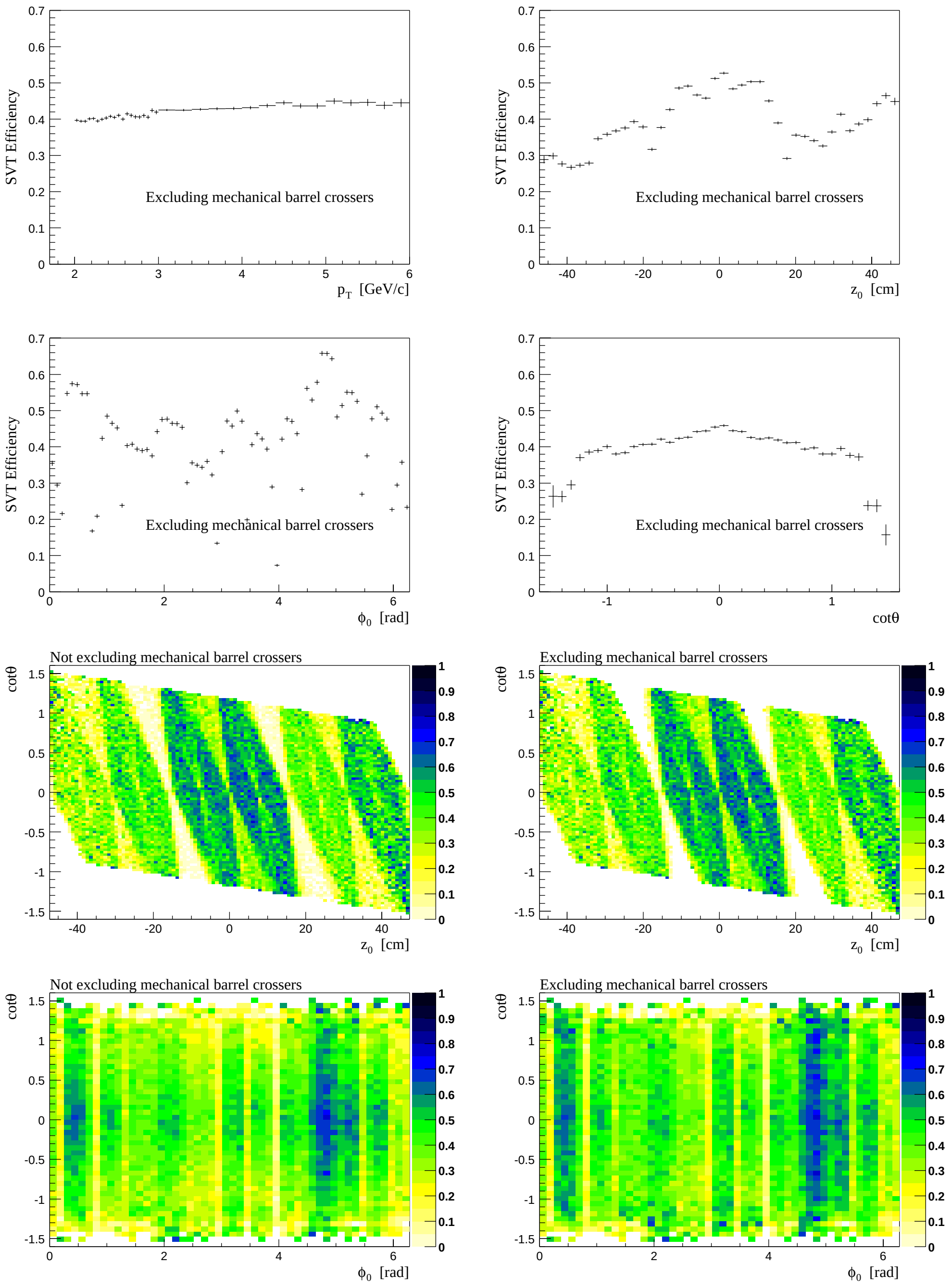

Figure 7.5: Single-track SVT efficiency as a function of p_T, z_0, ϕ_0, and $\cot\theta$ when excluding mechanical barrel-crossers. The last four plots are the SVT efficiency as a function of (z_0,$\cot\theta$) and (ϕ_0,$\cot\theta$) with and without excluding mechanical barrel-crossers.

two-track efficiencies to validate this method. We tried the following two forms for the SVT single-track efficiency:

$$\epsilon_{\mathrm{SVT}}(p_T, \cot\theta, z_0, \phi_0) \approx \epsilon(p_T) \cdot (\epsilon(z_0, \phi_0)/\epsilon_0) \cdot (\epsilon(\cot\theta)/\epsilon_0); \tag{7.5}$$

$$\epsilon_{\mathrm{SVT}}(p_T, \cot\theta, z_0, \phi_0) \approx \epsilon(p_T) \cdot (\epsilon(z_0, \phi_0)/\epsilon_0) \cdot (\epsilon(z_0, \cot\theta)/\epsilon(z_0)). \tag{7.6}$$

In the first case, the efficiency correlation between z_0 and $\cot\theta$ is ignored, while in the second case, the efficiency correlation between z_0 and $\cot\theta$ is explicitly modeled. The difference between the two methods is small, since we explicitly set the efficiency for mechanical barrel crossers to zero (described later in this section). Some residual $(z_0, \cot\theta)$ correlation remains due to the smaller efficiency for electrical barrel crossers, compared to tracks that do not cross barrels, as can be seen in the $\epsilon(z_0, \cot\theta)$ plots in Figure 7.5. Indeed we found no large difference between using parameterization 7.5 and 7.6. Since the latter gives a more detailed description, we use it as a default. We verified that the SVT efficiency has no strong correlation between $\cot\theta$ and ϕ_0 (see Figure 7.5).

The SVT configuration was not stable during the data taking period. It went through several changes which affected the efficiency. Therefore, we determine the SVT efficiency on a store-by-store basis and we weight the efficiency calculation accordingly.

The SVT does not reconstruct tracks that cross the boundary between mechanical SVX barrels. In order to account for this inefficiency, we explicitly exclude the tracks that cross barrels for the SVT efficiency measurement. We calculate the z positions for the track at the point of entry and exit in the SVX by extrapolating the helix of the track to R=2.545 cm and R=10.645 cm respectively, and demand that these points are in the same mechanical SVX barrel.

The explicit rejection of barrel-crossers increases the SVT efficiency by a few percent, and reduces its dependence on $\cot\theta$ and z, as can be seen by comparing Figures 7.4 and 7.5.

To prevent loss of SVT tracks from finite resolution in z, we use coordinates of the SVX barrels that extend 1 cm beyond their physical boundaries:

- SVX barrel 0 extends from -47.25 cm to -14.75 cm in the z direction;
- SVX barrel 1 extends from -16.75 cm to 16.75 cm in the z direction;
- SVX barrel 2 extends from 14.75 cm to 47.25 cm in the z direction.

To account for a systematic uncertainty due to possible fake matches in the matching window, we enlarge the size of the matching window to $|\Delta\phi_6| \leq 20\,\mathrm{mrad}$ and $|\Delta C| \leq 2.0 \times 10^{-4}\,\mathrm{cm}^{-1}$ and treat the difference in matching efficiency as a systematic uncertainty. For the larger matching window, we find a relative difference of 0.5% per track.

A small fraction of the COT tracks used in the denominator for the present efficiency measurement are tracks that have an impact parameter larger than 1 mm, and fall outside the acceptance of the SVT. We correct for this small fraction using the impact parameter distribution of tracks that have at least 3 silicon R, ϕ hits on different layers. This distribution is shown in Figure 7.6. We find that 1.92% of the tracks have a large impact parameter, which implies we have underestimated the single track SVT efficiency by 1.92%. We correct for this by applying a correction factor to the charm trigger efficiency of $(1 - 0.0192)^{-2} = 1.040$. We attribute the full size of this correction as a systematic uncertainty.

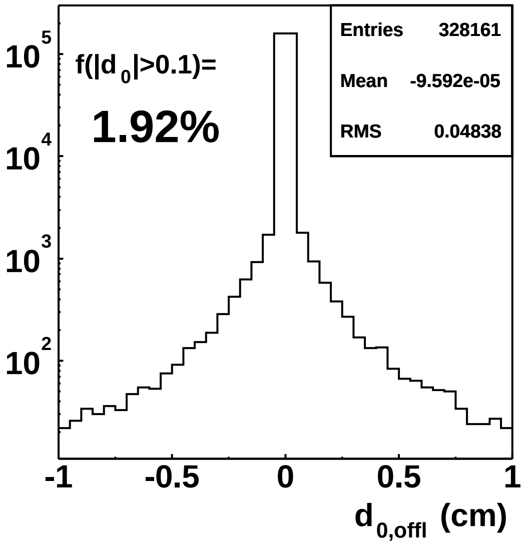

Figure 7.6: The impact parameter distribution of tracks from the Level-1 two-track trigger. All tracks have $p_T \geq 2.0\,\mathrm{GeV}/c$ and 3 or more SVX ϕ-side hits in different layers. The fraction of tracks with an impact parameter ≥ 1 mm, which fall outside the SVT acceptance, is 1.92%.

7.5 SVX Efficiency for Single SVT-matched Tracks

During the offline charm signal reconstruction, we require that an SVT track matches with an offline track with a certain of minimum number of SVX hits.

Although the SVT requires a minimum of 4 SVX ϕ-side hits during the online reconstruction, the actual SVX hit number associated with the offline SVT-matched track can be smaller due to differences in the clustering and pattern recognition between the SVT and the offline tracking. The SVX efficiency for an SVT-matched track is defined as the probability for an offline SVT-matched track to have ≥ 3 ϕ-side SVX hits in different layers:

$$\epsilon_{\text{svx-svt}} = \mathcal{P}(\text{SVX}|\text{SVT,XFT,COT}). \tag{7.7}$$

The SVX efficiency for SVT-matched tracks is measured using Level-1 auto-accept data and is found to be close to unity ($\geq$ 98%). No strong dependence on p_T, ϕ_0, $\cot\theta$, or z_0 is observed, as shown in Figure 7.7, except for a small drop at large track z_0 near the SVX edge. Similar to the XFT, the SVX efficiency for SVT-matched track is parameterized as:

$$\epsilon_{\text{svt-svx}}(p_T, \cot\theta, z_0, \phi_0) \approx \epsilon(p_T) \cdot \epsilon(z_0, \cot\theta)/\epsilon_0. \tag{7.8}$$

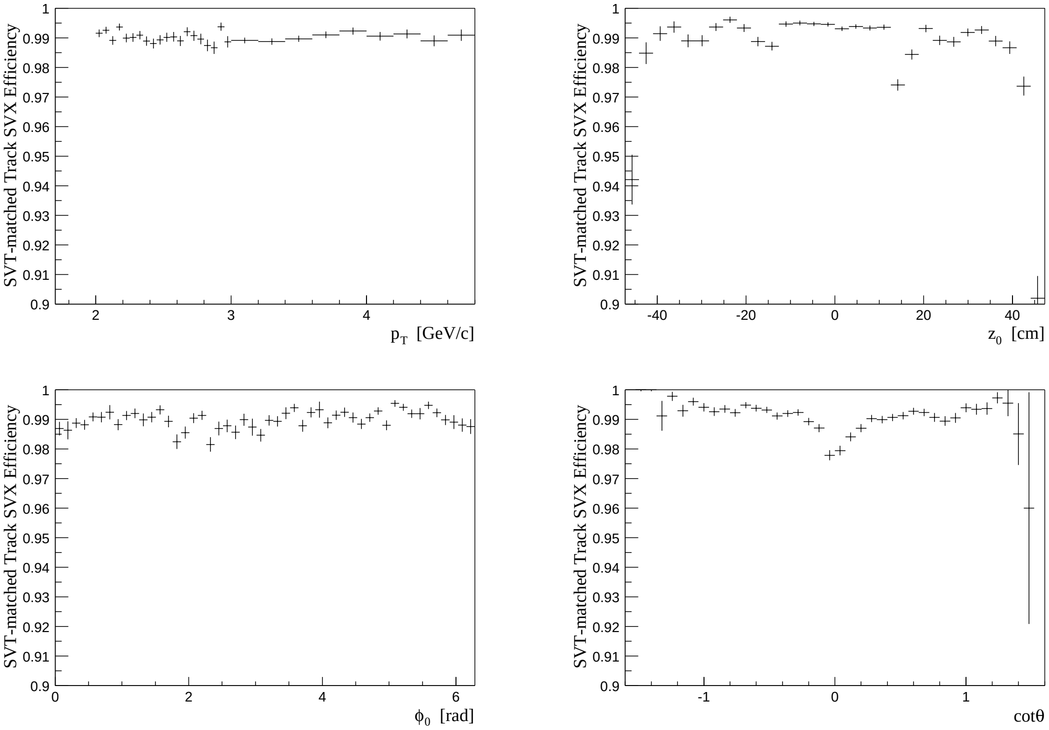

Figure 7.7: The efficiency for an offline track to have 3 or more SVX ϕ-side hits when the offline track is an SVT-matched track with $p_T(\mathrm{SVT}) \geq 2\,\mathrm{GeV}/c$.

7.6 SVX Efficiency for Single Tracks without the SVT Matching Requirement

The reconstructed D^+ and D_s^+ in the two-track trigger data sample have three tracks in the final state. At least two of the three daughters are required to be SVT-matched tracks and the third track is required to have SVX ϕ-side hits in at least 3 different layers. We measure the efficiency for this requirement as:

$$\epsilon_{\mathrm{SVX}} = \mathcal{P}(\mathrm{SVX}|\mathrm{COT}), \tag{7.9}$$

where the COT track satisfies the fiducial requirements listed at the beginning of Section 7. Similar to the single-track SVT efficiency, the SVX efficiency also has strong ϕ_0, $\cot\theta$, and z_0 dependences, and depends on changes in the SVX configuration. Since we only require hits in 3 different SVX layers, and the SVX configuration changes were fewer than for the SVT, smaller variations are observed, as shown in Figure 7.8. Nevertheless, we parameterized the SVX efficiency for single tracks in a similar approach as we did for the SVT using the minimum bias data on a store by store basis with the following parameterization:

$$\epsilon_{\mathrm{SVX}}(p_T, \cot\theta, z_0, \phi_0) \approx \epsilon(p_T) \cdot (\epsilon(z_0, \phi_0)/\epsilon_0) \cdot (\epsilon(\cot\theta)/\epsilon_0). \tag{7.10}$$

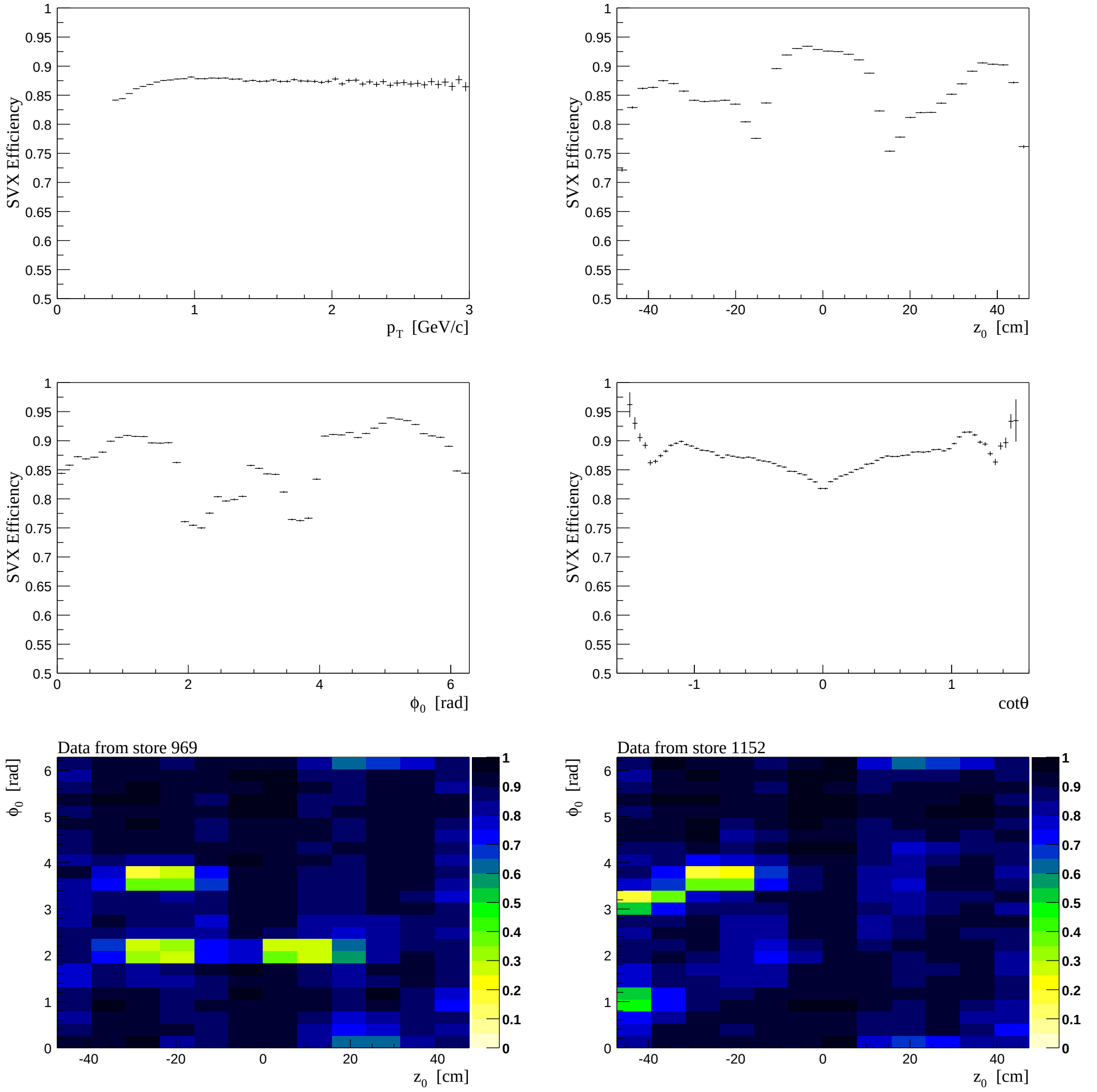

Figure 7.8: Single-track SVX efficiency as a function of p_T, z_0, ϕ_0, and $\cot\theta$. The last two plots are the SVX efficiency as a function of z_0 and ϕ_0 together for the data from two different beam stores, which shows the difference between their SVX configurations.

7.7 Effect of Track Multiplicity on Single-Track Efficiencies

We measured single-track efficiencies in minimum-bias and Level-1 auto-accept data that have low track multiplicities. When we use these efficiencies for charm events, we need to take into account that charm events tend to have higher track multiplicities and correspondingly smaller efficiencies [89].

Part of this effect will be covered in Sections 10.2 and 10.3, where we consider the possibility that the XFT track corresponding to one charm daughter may obscure the XFT track of another charm daughter. However, we also need to take into account the additional track multiplicity from fragmentation tracks.

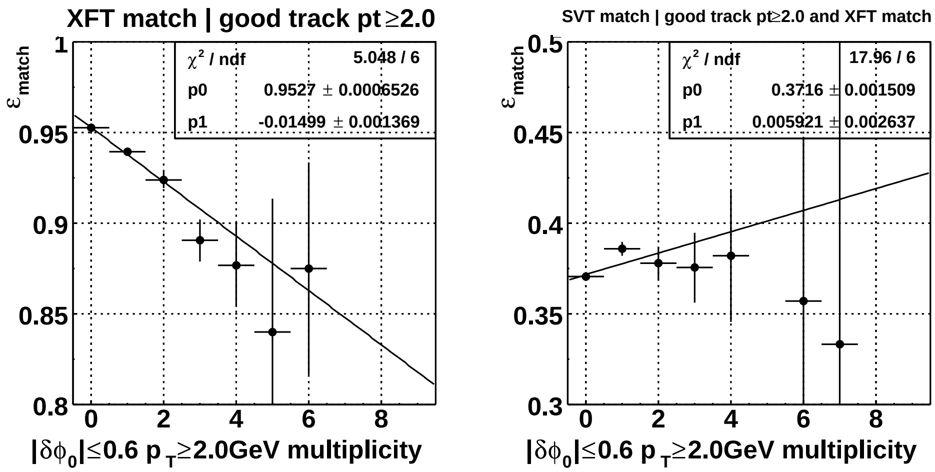

Figure 7.9: XFT and SVT efficiency dependence on the number of tracks with $p_T \geq 2\,\mathrm{GeV}/c$ and $|\Delta\phi_0| \leq 0.6$; both efficiencies are measured using minimum bias data.

The effect of the track multiplicity on the XFT and SVT efficiency is shown in Figure 7.9, where we plot the efficiency as a function of the number of high p_T ($\geq$2 GeV/c) tracks within 0.6 radians of the evaluated track. There is a clear decrease of the XFT efficiency as a function of the multiplicity, with 1.5% per unit of multiplicity. No such effect is seen for the SVT (once an XFT track has been required). The small *increase* of the SVT efficiency for higher multiplicity is probably caused by the lower multiplicity for high-η tracks, which have a smaller SVT efficiency.

We compared the multiplicity around tracks between data and MC, as shown in Figure 7.10, and find that fragmentation tracks add on average 0.31 tracks with $p_T \geq 2\,\mathrm{GeV}/c$ within $|\Delta\phi_0| \leq 0.6$ of the charm daughters. We take this effect into account by reducing the measured XFT efficiency by $0.31 \times 1.5 = 0.47\%$ per track. We take the full size of this correction as a systematic uncertainty.

Our motivation for the counting tracks within 0.6 rad is as follows: if we would count in data the number of additional tracks very close to one of the charm daughters (say, within 1.25°), we would find very few in the charm sample – since these are the events that got lost. Therefore we count in a much larger window, under the assumption that the fragmentation tracks are distributed more or less homogeneously around the charm daughters. This is admittedly a strong assumption. That is why we attribute the full size of the correction as a systematic uncertainty.

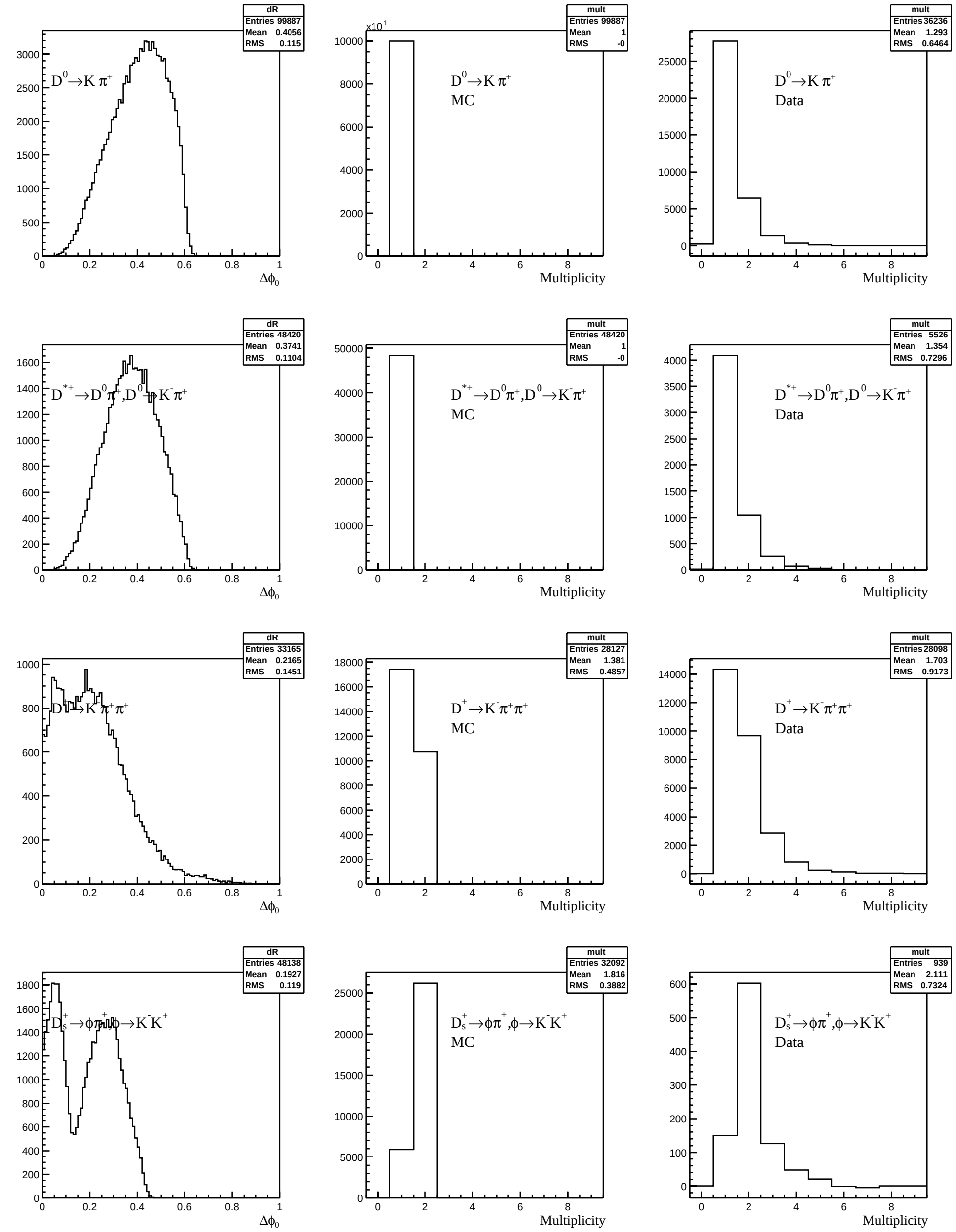

Figure 7.10: Left plots: The difference in angle between charm daughters with $p_T \geq 2\,\mathrm{GeV}/c$ (MC) after trigger and offline selection requirements. Middle plots: the MC multiplicity of tracks with $p_T \geq 2\mathrm{GeV}/c$ and $|\Delta\phi| \leq 0.6$. The generator used for the MC is HeavyQuarkGen: one charm meson per event is generated; no fragmentation tracks are simulated. Right plots: the same multiplicity distribution for data.

Chapter 8

Single-Track Detector Resolution

The p_T and d_0 resolutions of the XFT, SVT and offline, have a significant effect on the overall trigger and reconstruction efficiency. For example, the $p_T > 2\,\mathrm{GeV}/c$ requirement is applied on XFT tracks at Level-1, on SVT tracks at Level-2, on COT tracks at Level-3 and on SVX tracks in the offline analysis. In this section we measure these resolutions and study the correlation between them.

8.1 XFT and SVT Curvature Resolution

Since the offline track curvature is measured much more precisely than their online measurement, the XFT and SVT curvature resolution can be measured as $C - C(\mathrm{XFT})$ and $C - C(\mathrm{SVT})$ respectively, where C is the offline measured quality. The criteria used for matching and offline track selection here are the same as what we used for efficiency studies in section 7.3 and 7.4. The results are shown in Figure 8.1. Furthermore, no explicit correlation between the XFT and the SVT measurement are observed by examining the 2-D histogram of their curvature difference from offline quality.

A significant non-linearity of the SVT curvature measurement as a function of ϕ has been observed in other studies [81]. We evaluated the effect of this non-linearity by fitting it to a sinusoid and implementing it in the parameterization of the curvature reconstruction by the SVT. We found no measurable effect on the charm meson reconstruction efficiencies and decided to ignore the effect.

8.2 Impact Parameter Distribution for Offline Tracks

To study the impact parameter distribution for offline tracks, we use minimum bias events and examine the d_0 distribution of tracks in different p_T bins. In addition to the COT track selection criteria used in Section 7.6, the offline track is also required to have ϕ-side SVX hits in at least 3 different layers.

There are two contributions to the impact parameter distribution: one from the finite beam-spot size and the other from the detector resolution. The measurement of the beam-spot size and its z-dependence is described in Section 9.1. In this section

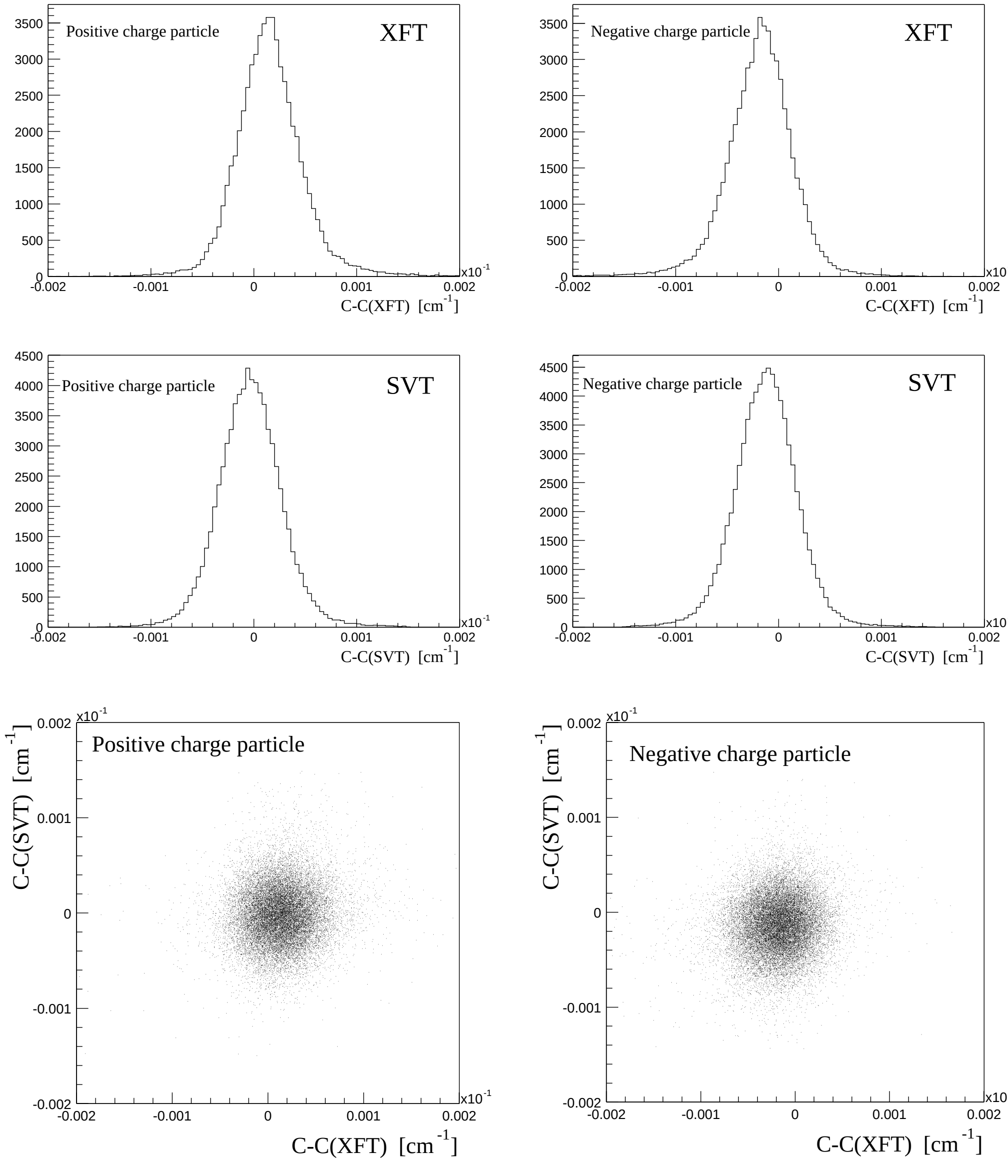

Figure 8.1: XFT and SVT curvature resolution and their correlation measured from minimum bias data. The XFT resolution is not centered at zero, due to the bias in the XFT system, which was introduced intentionally to increase the XFT efficiency at a given p_T(XFT) threshold.

we measure and parameterize the observed impact parameter distribution of tracks. When applying these parameterizations in the efficiency calculations (Section 9), we subtract the measured beam-spot size.

The d_0 distribution is fit with a double Gaussian function so that we can deconvolute it to get the detector contribution analytically.

$$f(d_0) = \frac{f_1}{\sqrt{2\pi}\sigma_{d1}} e^{-d_0^2/2\sigma_{d1}^2} + \frac{1-f_1}{\sqrt{2\pi}\sigma_{d2}} e^{-d_0^2/2\sigma_{d2}^2}, \tag{8.1}$$

The parameters f_1, σ_{d1}, and σ_{d2} are p_T dependent.

The width of the narrow Gaussian could be expected to be well described by a functional shape of type $\sqrt{a + b \cdot p_T^{-2}}$, but we found this gives a poor fit to the observed distributions. The curves are better described by an exponential function, as shown in Figure 8.2:

$$\begin{aligned} f_1(p_T) &= f_{10}(1 + \alpha_0 e^{\beta_0 p_T}); & (8.2)\\ \sigma_{d1}(p_T) &= \sigma_{10}(1 + \alpha_1 e^{\beta_1 p_T}); & (8.3)\\ \sigma_{d2}(p_T) &= \sigma_{20}(1 + \alpha_2 e^{\beta_2 p_T}). & (8.4) \end{aligned}$$

As expected, the track d_0 distribution narrows as the transverse momentum of the track increases, because of the relatively smaller multiple scattering effects.

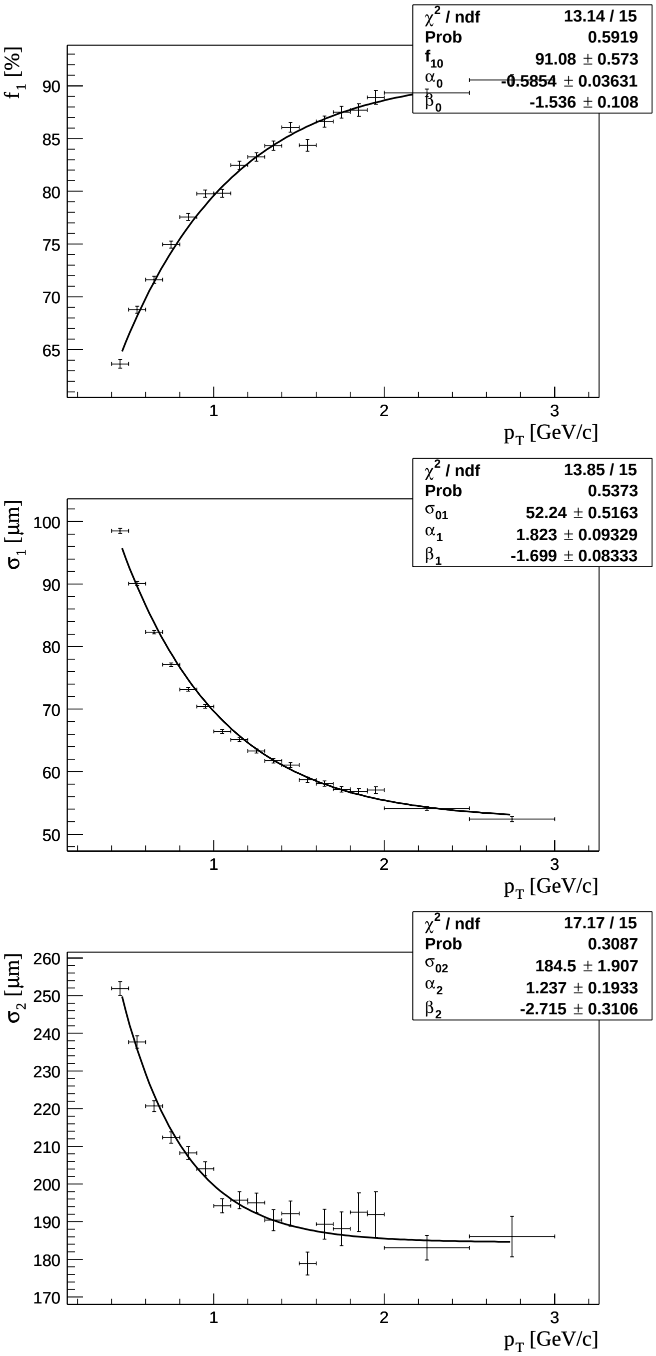

Figure 8.2: The results of the study of the d_0 distribution for offline tracks with 3 or more ϕ side SVX hits in minimum bias data (no XFT or SVT requirement). The quantities f_1, σ_1, and σ_2, and their corresponding parameterizations are described in the text.

8.3 Impact Parameter Resolution for SVT-matched Tracks

In principle, both online and offline measurement use the same silicon hit information, therefore their measurement results are expected to be highly correlated. Since the two-track trigger requires a minimum d_0(SVT) at Level-2 and the offline measured d_0 is used for reconstruction and analysis, a good understanding of the correlation between offline d_0 and online d_0(SVT) is essential for any analysis involving Monte Carlo, especially the efficiency and acceptance studies.

For an SVT-matched track, its offline d_0 and corresponding d_0(SVT) distribution are fit with a double Gaussian functions in different p_T bins. The results are shown in Figure 8.3. The correlation between the SVT and the offline measurement of the impact parameter distribution is illustrated in Figure 8.4.

We expect that the offline d_0 distribution can be described by a double Gaussian function for a given d_0(SVT) and vice versa. We parameterize the combined SVT and offline d_0 probability density function as a correlated double Gaussian function

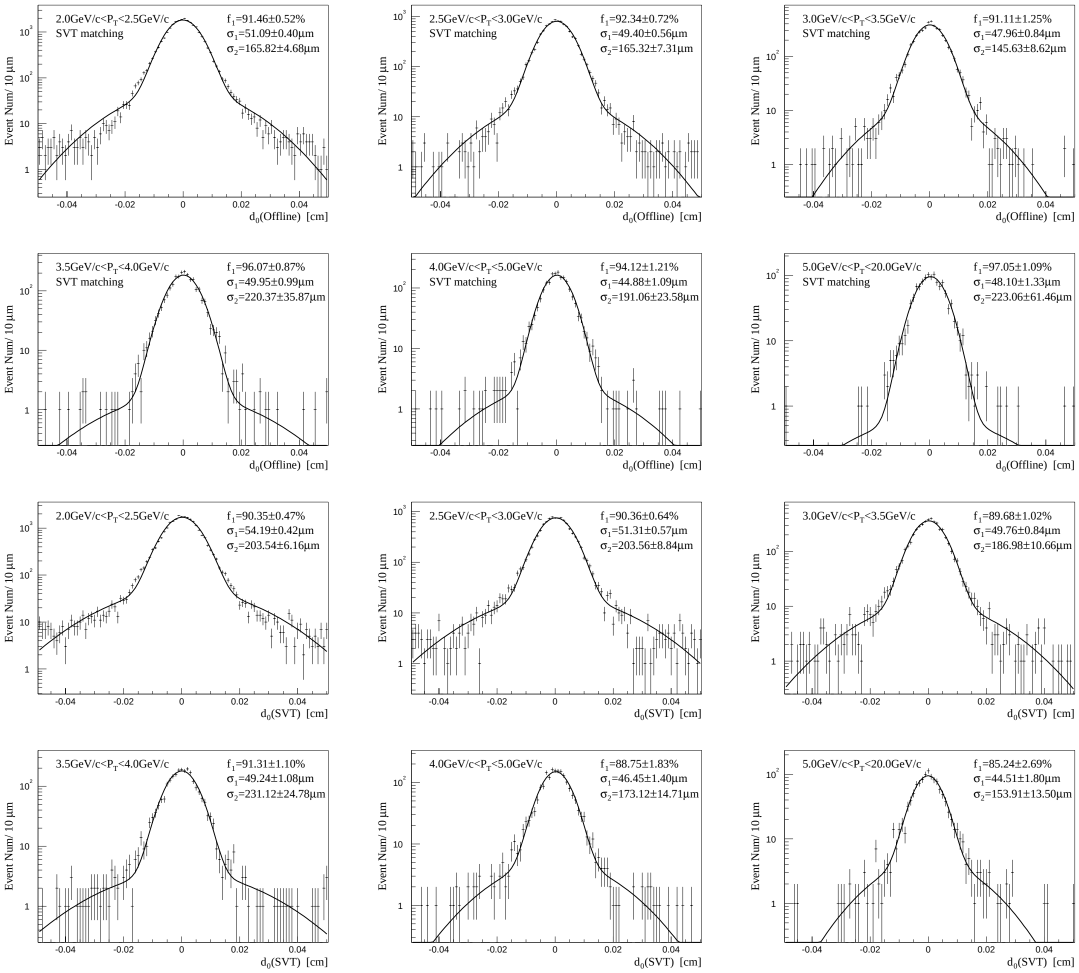

Figure 8.3: SVT-matched track offline d_0 and online d_0(SVT) distributions in different p_T bins. The quantities f_1, σ_1, and σ_2 are described in the text.

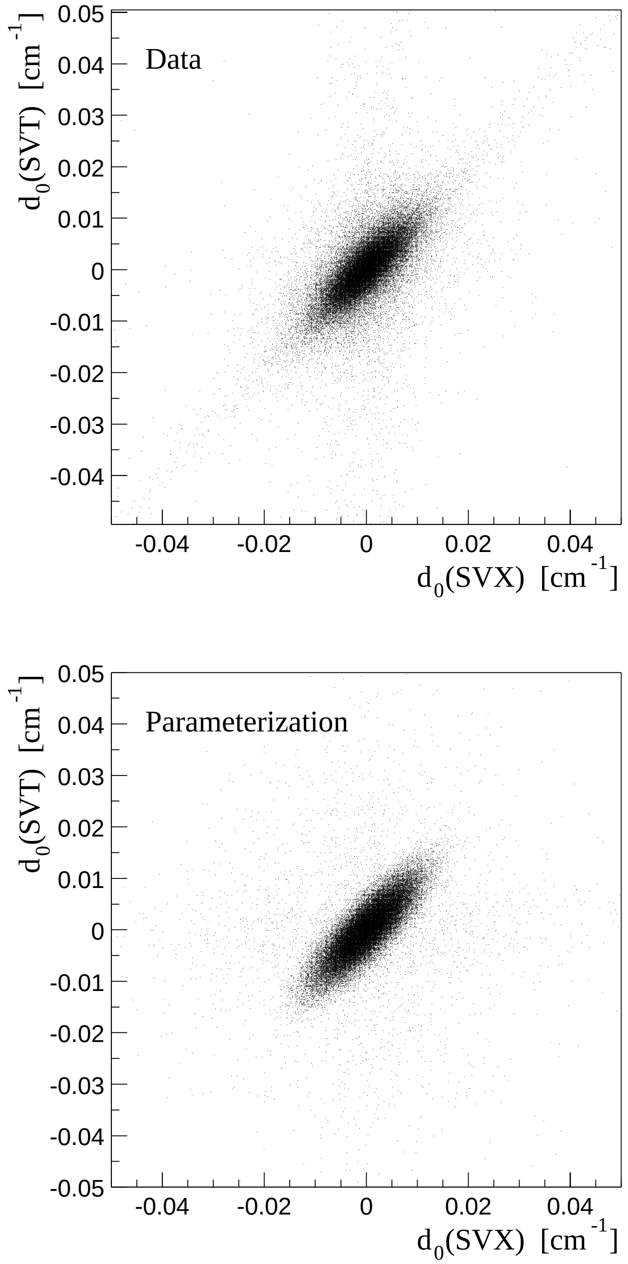

Figure 8.4: The correlation of track impact parameters measured by SVT and offline SVX from data (minimum bias) and parameterization.

in two dimensions:

$$\begin{aligned} G(d_0, d_0^{svt}) &= A \cdot g(d_0^{svt}, d_0; f_1^{svt}, \sigma_1^{svt}, f_1, \sigma_1, \rho_1) + \\ & B \cdot g(d_0^{svt}, d_0; f_1^{svt}, \sigma_1^{svt}, 1 - f_1, \sigma_2, \rho_2) + \\ & C \cdot g(d_0^{svt}, d_0; 1 - f_1^{svt}, \sigma_2^{svt}, f_1, \sigma_1, \rho_3) + \\ & D \cdot g(d_0^{svt}, d_0; 1 - f_1^{svt}, \sigma_2^{svt}, 1 - f_1, \sigma_2, \rho_4), \end{aligned} \tag{8.5}$$

and

$$\begin{aligned} B &= (1 - Af_1)/(1 - f_1), \\ C &= (1 - Af_1^{svt})/(1 - f_1^{svt}), \\ D &= [(1 - f_1^{svt}) - (f_1 - Af_1 f_1^{svt})]/[(1 - Af_1) \cdot (1 - Af_1^{svt})], \end{aligned} \tag{8.6}$$

were $g(d_0^{svt}; d_0; \rho)$ is the correlated Gaussian distribution between online and offline measured impact parameter values:

$$g(d_0^{svt}, f^{svt}, \sigma^{svt}; d_0, f, \sigma; \rho) = \frac{f^{svt} f}{2\pi\sigma^{svt}\sigma} \frac{1}{\sqrt{1-\rho^2}} \exp\{-\frac{1}{2(1-\rho^2)}(\frac{d_0^{svt2}}{\sigma^{svt2}} + \frac{d_0^2}{\sigma^2} - \frac{2\rho d_0^{svt} d_0}{\sigma^{svt}\sigma})\}; \tag{8.7}$$

$f_1^{svt}, f_1, \sigma_1^{svt}, \sigma_1, \sigma_2^{svt}, \sigma_2$ are the parameters of the double Gaussian function that describe the online and offline track impact parameter distribution. To extract the correlation ρ_1, ρ_2, ρ_3, ρ_4 and the normalization coefficient A, a binned chi-square likelihood fit is constructed to fit the two-dimensional distribution $G(d_0, d_0^{svt})$ in which the values of $f_1^{svt}, f_1, \sigma_1^{svt}, \sigma_1, \sigma_2^{svt}, \sigma_2$ are fixed from previous measurements shown in Figure 8.3. The returned values for ρ_2, ρ_3, and ρ_4 are consistent with zero. A slight p_T dependence was observed for $\rho_1 \sim 0.75$ and $A \sim 1.0$. For simplicity, we assume that $\rho_2 = \rho_3 = \rho_4 = 0$. We vary ρ_1 by ±0.1 in our evaluation of the systematic uncertainty.

Chapter 9

Detector Monte Carlo Simulation

To study the trigger and reconstruction efficiency, one approach is to rely on the full GEANT detector simulation. However, the current Monte Carlo GEANT simulation is still under development and it tends to overestimate the detector efficiency. A realistic projection of the direct charm meson efficiency may not be available from GEANT simulation without more detail studies. Instead of the GEANT simulation, a parameterized detector Monte Carlo simulation is used to calculate the trigger and reconstruction efficiency for charm mesons. Contrary to a GEANT-type MC, all correlations between efficiencies and resolutions have to be modeled explicitly. Therefore, we emphasize the importance of correlation studies and make an effort to use measured correlations whenever possible, and otherwise absorb the correlation uncertainties in the systematic uncertainty.

The flow diagram for the applied parameterized detector Monte Carlo simulation is shown in Figure 9.1. For MC generated particles, the tracking parameters are calculated from their true HEPG information, they are then smeared based on the corresponding resolution measured from data; single-track efficiencies are applied and the possible correlation between the two-track combination are evaluated and tuned based on comparisons between the MC and the data. Since we measured detector efficiency and resolution as a function of track offline quantities, in the actual simulation, the offline parameter smearing is done first.

9.1 Transverse Beam Spot Size

CDF note 4189 [90] describes an elegant method to measure the size of the beam spot, without bias from the detector resolution of the track impact parameter. The size of the beam spot is obtained from the correlation between the product of the impact parameters of pairs of tracks and their opening angle:

$$\sigma^2 = \left\langle \frac{d_1 d_2}{\cos(\Delta\phi)} \right\rangle \tag{9.1}$$

We use track pairs from the minimum-bias sample to measure the beam spot size. We require that the tracks have at least 25 axial and 25 stereo COT hits, have $p_T \geq 0.5\,\mathrm{GeV}/c$, traverse all COT superlayers, have SVX $r\phi$ hits in at least three different layers, and an impact parameter of less than 1 mm. We require that the tracks are

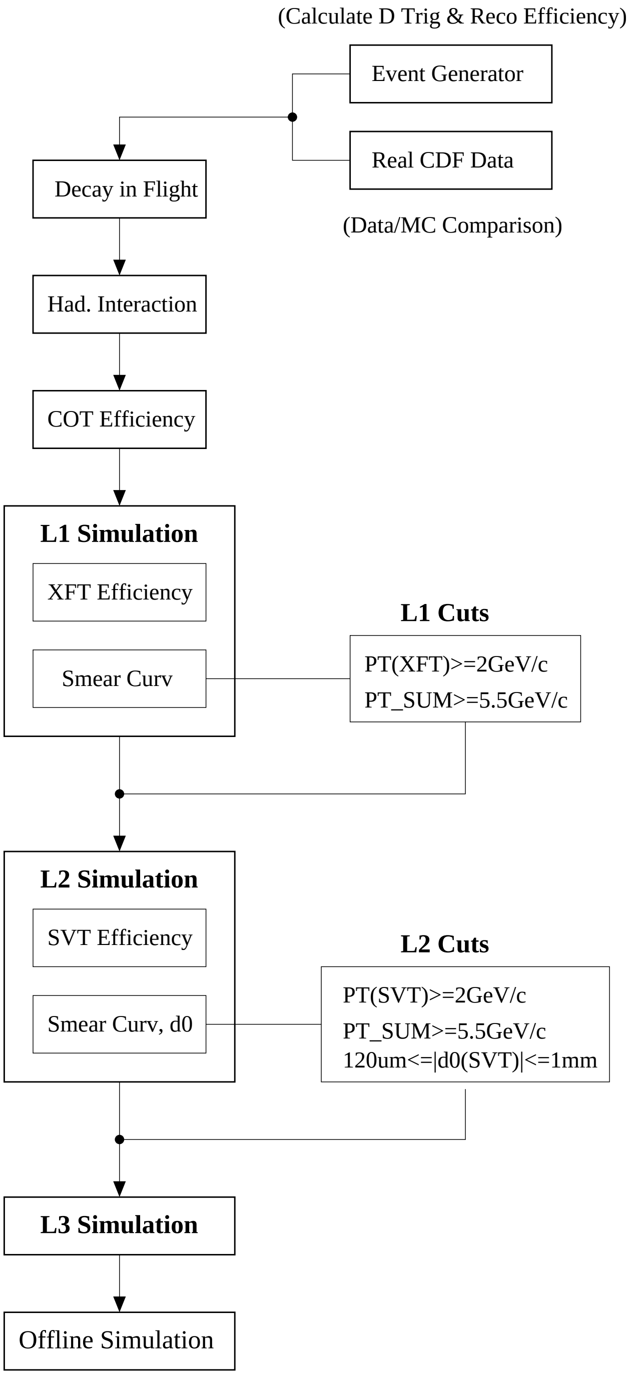

Figure 9.1: The block diagram of the detector Monte Carlo Simulation.

compatible with coming from the same vertex by demanding $|z_1 - z_2| \leq 5\,\mathrm{cm}$. We find an average beam spot size of $29.4 \pm 0.3\mu\mathrm{m}$ (see Figure 9.2).

We repeated the analysis with the track pairs binned in $z = \frac{z_1+z_2}{2}$. The effect of a widening of the beam spot for larger values of $|z|$ is clearly seen[1]. We fit the measured values to the expected functional shape:

$$\sigma(z) = \sigma_0 \sqrt{1 + \frac{(z - z_f)^2}{\beta^{*2}}}. \tag{9.2}$$

We find the value of the accelerator focusing parameter $\beta^* \approx 38\,\mathrm{cm}$, close to the nominal value of 35 cm [92], and optimal focus at $z \approx 5\,\mathrm{cm}$, where the beamspot is σ_0=26.2 μm. When we apply the same method with a higher p_T threshold of 2.0 GeV/c per track, using the Level-1 auto-accept data of the two-track trigger, we find a somewhat smaller value beam spot size, namely σ_0=24.5 μm. It is not clear what is the origin of this difference, but it may be due to the higher content of real heavy flavor in the high-p_T sample[2].

For the MC generation of the transverse beam spot size, we use the values obtained from the minimum bias sample: σ_0=26.2 μm, $z_f = 5.2\,\mathrm{cm}$ and $\beta^* = 38.6\,\mathrm{cm}$ and vary the value of σ_0 by $\pm 2\,\mu\mathrm{m}$ to account for the systematic uncertainty.

---

[1] This effect has been seen in Run II data before, see *e.g.* [91].

[2] Real lifetime tends to create particles with opposite sign impact parameter, and thus with a negative impact parameter product. We expect most real lifetime (*e.g.* K^0_S) to have a small opening angle ($< 90°$), which gives a bias to the beamspot measurement.

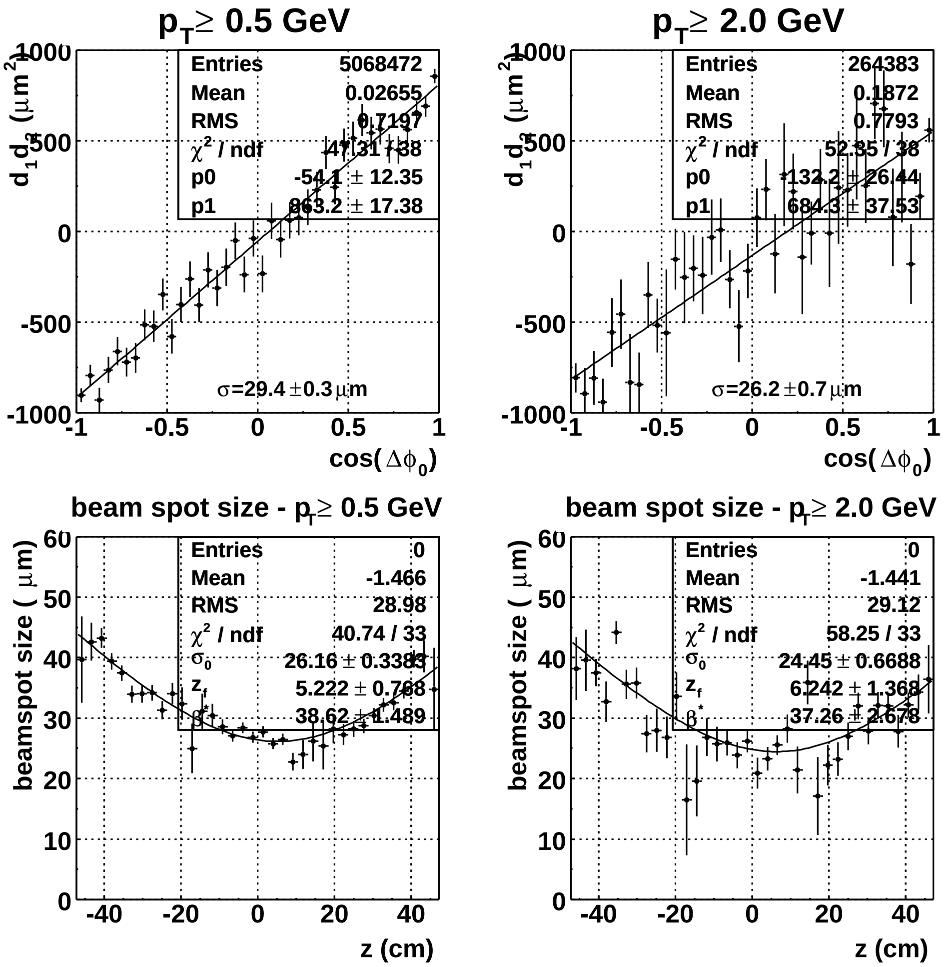

Figure 9.2: Upper plots: Using the correlation between the average impact parameter product of track pairs and their opening angle to determine the beam spot size. Lower plots: Beam spot size dependence on z. The low p_T threshold plots on the left are from minimum-bias data, the right-hand plots with the higher p_T threshold are from Level-1 accepts of the two-track trigger.

9.2 Shape of the Luminous Region

The silicon detector covers only part of the luminous region, while the measured luminosity of our sample refers to the full luminous region. Therefore, a detailed understanding of the shape of the luminous region is required to calculate the efficiency of the $|z| \leq 47.25\,\text{cm}$ requirement used in the analysis.

Figure 9.3 shows the z distribution of tracks in the minimum-bias sample. The track requirements are the same as the requirements used in Section 7.3, except no selection criteria are applied on z. The upper left plot has been fit to a Gaussian, which gives a poor description of the luminous region. The upper right plot has been fit to the product of a Gaussian and a factor that accounts for the reduced luminosity away from $z = z_0$, where the focusing is poorer:

$$n(z) \propto \frac{1}{1 + \frac{(z-z_0)^2}{\beta^{*2}}} \cdot e^{\frac{(z-z_0)^2}{2\sigma_z^2}} \tag{9.3}$$

this gives a much better description of the luminous region. Integrating between $\pm 47.25\,\text{cm}$ yields an efficiency of 89.9%. The parameters obtained from this fit will be used as the default for the generation of MC events.

We evaluate two systematic uncertainties associated with the shape of the luminous region. First we repeat the measurement lowering the p_T threshold to $0.5\,\text{GeV}/c$. This results in a wider spread, as shown in the lower-left plot of Figure 9.3, and an efficiency for $|z| \leq 47.25\,\text{cm}$ that is 1.0% lower. Second, we look for

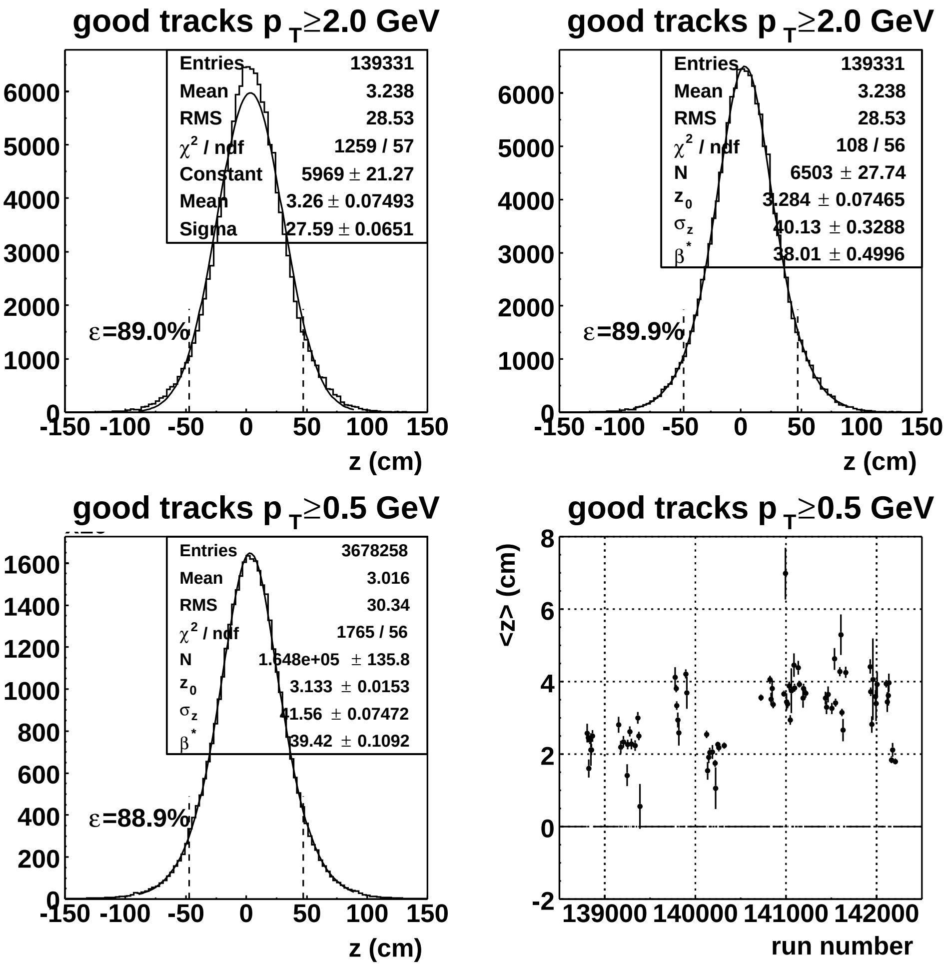

Figure 9.3: Shape of the luminous z-profile from minimum-bias data; the dashed lines indicate the size of the SVX detector, and the quoted efficiency refers to the $|z| \leq 47.25\,\mathrm{cm}$ requirement. The lower-right plot shows the run-dependence of the average z-position.

a run-dependence of the average z, and find that it moved by about ± 1 cm during the run-period considered, consistent with what was observed in [81]. Run-by-run variations cancel to first order in the efficiency calculation, but even the effect of a full $\pm 1\,\mathrm{cm}$ shift was found to give a deviation of only 0.13% on the efficiency of the $|z| \leq 47.25\,\mathrm{cm}$ requirement. However, a $\pm 1\,\mathrm{cm}$ shift may also change the SVX and SVT acceptance, so we do evaluate the overall effect of a $\pm 1\,\mathrm{cm}$ shift as a systematic uncertainty.

9.3 Level-1 Simulation

At Level-1, the eXtremely Fast Tracker (XFT) measures the track p_T and ϕ_6 values, which are used for the Level-1 trigger decision. We simulate the XFT by throwing a random number between 0 and 1, and if the number is smaller than the parameterized efficiency of Equation 7.2, the particle has an XFT track associated with it. The XFT curvature is simulated by smearing the offline curvature value according to the measured histogram in Figure 8.1. Although the XFT also measures track ϕ_6, at Level-1 the two-track trigger only requires that the two trigger tracks satisfy $\Delta\phi_6 \leq 135^\circ$. Since the Level-3 trigger requires $\Delta\phi_0 \leq 90^\circ$, no smearing of track ϕ_0 is necessary here. An event satisfies the Level-1 condition if it has a pair of tracks that satisfy:

- the two tracks have opposite charge;
- each track has $p_T(\text{XFT}) \geq 2.0\,\text{GeV}/c$;
- $p_{T1}(\text{XFT}) + p_{T2}(\text{XFT}) \geq 5.5\,\text{GeV}/c$.

When two of the charm daughters are within 1.25° of each other at SL6, only the one with the highest p_T is used for the trigger decision. For multi-body charm decays, we also take into account that the XTRP sends a maximum of two XFT tracks with $p_T \geq 2\,\text{GeV}/c$ per 15° wedge to the two-track trigger board. In case three of more $p_T \geq 2\,\text{GeV}/c$ XFT tracks are present in a single 15° wedge, only the outer two are used in the trigger decision.

9.4 Level-2 Simulation

At the second level of the trigger system, tracking information from the SVX silicon detector is measured by the Silicon Vertex Trigger (SVT). For the track pairs that satisfy the Level-1 requirements, their offline curvature measurement are smeared with the measured SVT resolution in Figure 8.1. The true impact parameter of the track is smeared using Equation 8.5 with $\rho = 0.75$. The efficiency is thrown according to the measured efficiency, using the parameterization of Equation 7.6.

Like for Level-1, no azimuthal angle smearing is performed due to much stricter selection criteria applied in Level-3 and offline reconstruction. An event is consider to pass Level-2 only if its Level-1 trigger track pair also satisfies:

- repeat the Level-1 event selection criteria using new SVT track information;
- each track has $120\,\mu\text{m} \leq |d_0(\text{SVT})| \leq 1\text{mm}$.

9.5 Level-3 Simulation

At Level-3, the SVT tracks are matched with COT tracks, which have much better resolutions: $\sigma(p_T)/p_T^2 = 0.0013\,[\text{GeV}/c]^{-1}$ and $\sigma(\phi_0) = 1.5\,\text{mrad}$. The Level-1 selection criteria are repeated on the SVT track pair as well as the opening angle requirement $2^\circ \leq \Delta\phi_0 \leq 90^\circ$. For the central value of the efficiency calculation, we assume that the L3 and offline measurement of p_T and ϕ_0 are 100% correlated. To evaluate the systematic uncertainty, we evaluate the difference when we model the offline and L3 measurement to be fully uncorrelated.

9.6 Energy Loss Simulation

Ionization energy loss in the detector material needs to be taken into account, since it results in the migration of events from high-p_T bins to low-p_T bins. Energy loss has been calibrated in detail on the J/Ψ in ref [93]. We have not applied the track-by-track energy correction — it was not available when the ntuples for this analysis we produced. Instead we model the energy loss in the simulating by reducing the track-p_T with $10\,\mathrm{MeV}/c$ per track. We evaluate systematic uncertainty by varying the energy loss with $\pm\,10\mathrm{MeV}/c$.

9.7 Offline Reconstruction

Better transverse momentum and azimuthal angle resolution are expected for offline tracks. We assume that $\sigma(p_T)/p_T^2 = 0.001\,[\mathrm{GeV}/c]^{-1}$ and $\sigma(\phi_0) = 1.5\,\mathrm{mrad}$. Since the offline p_T measurement are highly correlated with the COT only p_T measurement due to sharing of the same COT hits, we assume that the corresponding correlation efficiency is equal to 1. For the tracks without trigger requirement, the impact parameter is smeared according to a double Gaussian resolution function, using the measured values of $f_1, (p_T), \sigma_{d1}(p_T)$ and $\sigma_{d2}(p_T)$ as described in Section 8.2. The same event selection criteria and 2-D vertex reconstruction code used in the real data analysis are applied on the smeared offline track parameters.

9.8 Decay and Hadronic Interaction

The decay in the flight probabilities of kaons and pions can be calculated analytically. However, not all the kaons and pions that decay inside COT get lost during offline reconstruction. Based on a full detector GEANT detector simulation it has been shown in Figure 9.4 that a significant part of the particles decayed far away from the interaction point can be successfully reconstructed by the COT. For simplicity, we parameterize such reconstruction probability as

$$\begin{aligned}
\mathcal{P}_{\text{decay\_Reco}}(\pi) &= \begin{cases} 0.2 \quad R \leq 90\,\text{cm} \\ (R-90)/(131-90) \quad R > 90\,\text{cm} \end{cases} \\
\mathcal{P}_{\text{decay\_Reco}}(K) &= \begin{cases} 0 \quad R \leq 100\,\text{cm} \\ 0.8 \quad 100 < R \leq 120\,\text{cm} \\ 1.0 \quad R > 120\,\text{cm} \end{cases}
\end{aligned} \tag{9.4}$$

For evaluation systematic uncertainties, we take the difference between this model, with partial reconstruction for decay-in-flight hadrons, and the other extreme, where decay-in-flight hadrons have 0% probability to be reconstructed.

To understand the size and effect of the hadronic interaction, we generated 10^6 each of K^+, K^-, π^+ and π^- by FakeEvent with flat p_T and pseudo-rapidity $|\eta| \leq 1.5$. The hadronic interaction was simulated through a full GEANT detector simulation while the decay in flight was turned off. By looking at the OBSV bank we

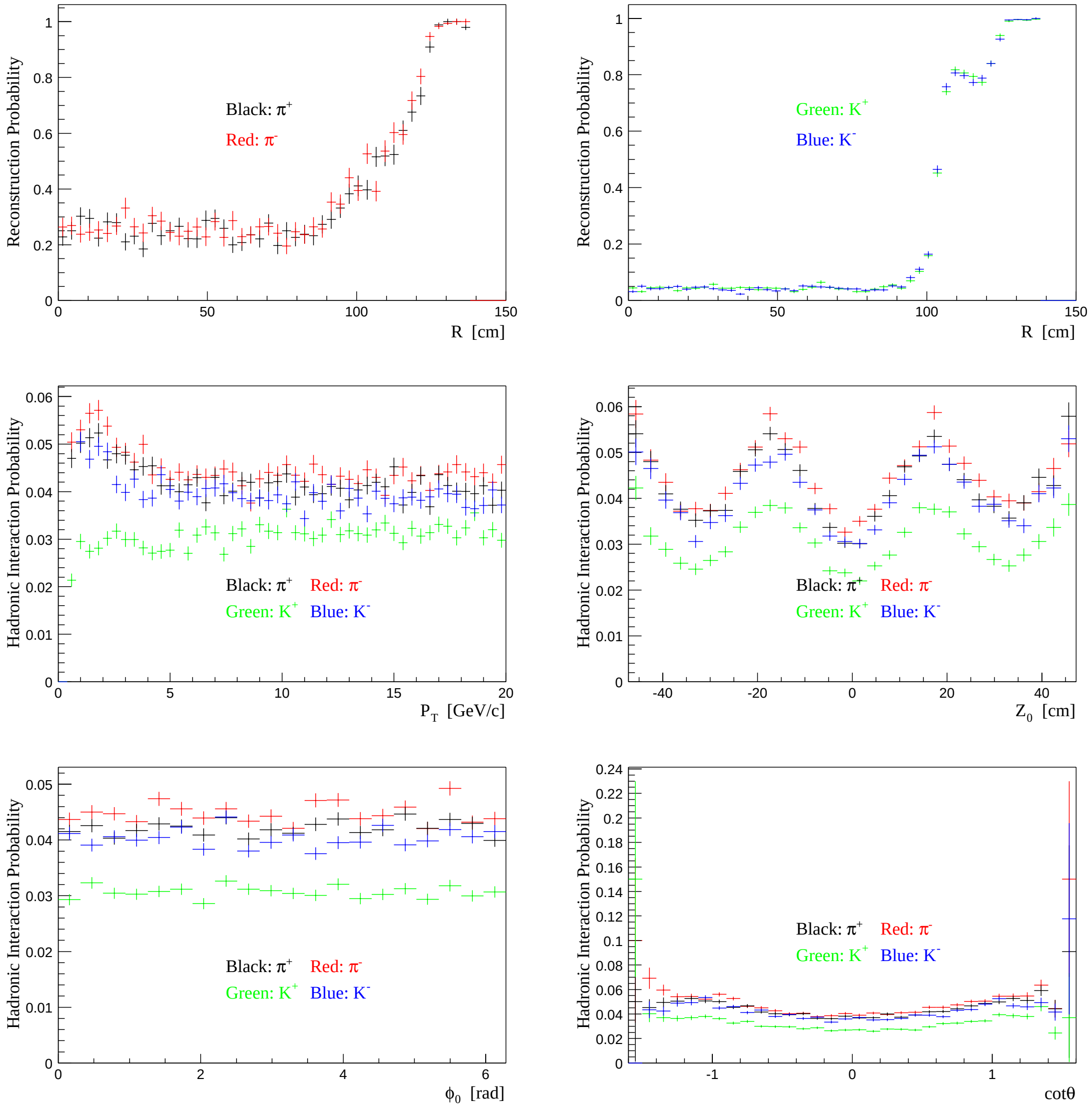

Figure 9.4: The top two plots are the COT reconstruction probabilities of kaons and pions that decay at the radius R inside COT. The other four plots are the hadronic interaction probabilities of kaons and pions as a function of various track parameters.

determined the probability for a given type of particle to undergo a strong interaction and subsequently get lost during the offline COT reconstruction. Similar to the efficiency measurement, the parameterized hadronic interaction has been derived from the GEANT simulation as

$$\epsilon(K^{\pm}, \pi^{\pm}) = \epsilon(p_T) \cdot (\epsilon(\phi_0)/\epsilon_0) \cdot (\epsilon(z_0, \cot\theta)/\epsilon_0). \tag{9.5}$$

where $\epsilon(p_T)$, $\epsilon(\phi_0)$ are the GEANT-predicted hadronic interaction probability as a function of p_T and ϕ_0, $\epsilon(z_0, \cot\theta)$ is the probability as a function of z_0 and $\cot\theta$ together, while ϵ_0 is the normalization factor.

The projections of the hadronic interaction probability versus p_T, z_0, ϕ_0 and $\cot\theta$ are shown in Figure 9.4. We find a typical interaction probability of about 4% for π^+, π^- and $K-$, and about 1% less for K^+.

Since there are indications that the GEANT simulation underestimates the amount of passive material in the the silicon region by about 20% [93], we attribute a 20% systematic uncertainty to the hadronic interaction probability.

We also attribute a 20% uncertainty to the hadronic interaction cross section from the model in GEANT, resulting in a total relative uncertainty of 28% on the hadronic interaction probability.

Chapter 10

Data and Monte Carlo Comparison for the Detector Simulation

In this section, the parameterized detector Monte Carlo simulation is used to predict some physical observables that can be compared with the data. One of the advantage of the parameterized detector simulation is that we can feed real CDF data as the input, in which some measurable qualities can be directly compared against the MC prediction on a statistical basis. This is a powerful way to cross-check whether correlations in the parameterized detector simulation have been well modeled. The accuracy of the model and its possible systematic biases can thus be evaluated explicitly. In following sections, several parts of the MC modules listed in the flow diagram have been carefully studied and technical details involved in the actual simulation are also elaborated.

10.1 MC and Data Comparison for XFT and SVT Curvature Resolution Effects

The XFT measured track momentum is used for the Level-1 decision of the two-track trigger. In our detector Monte Carlo, it is simulated by smearing the offline track curvature according to the measured XFT curvature resolution, as shown in Figure 8.1. Thus for a COT track in a minimum bias event that has been matched with an XFT track, whether it passes the p_T(XFT) requirement can be simulated by applying such a requirement on its smeared offline p_T. Although such prediction may not agree with on an event-by-event basis with the actual decision as read from the TL2D bank[1], their agreement can be validated statistically. As shown in Figure 10.5, they do agree well except the MC prediction is slightly lower near the p_T threshold.

We account for this discrepancy by evaluating the effect of an additional $\pm 5\,\mathrm{MeV}/c$ bias in the XFT and $\pm 20\,\mathrm{MeV}/c$ in the SVT momentum measurement, and treat

---

[1] The XFT track information can be obtained from XFLD or XTRD banks as well.

the difference as a systematic uncertainty.

10.2 Two-Track XFT Efficiency

Although the single-track XFT efficiency has been measured and modeled in detail, it is not obvious that the two-track efficiency can be expressed simply as a product of two single-track efficiencies, because of possible correlations associated with the two-track properties such as opening angle, mean z_0, p_T summation etc. To do so, similar techniques developed in section 10.1 have been applied to the COT track pairs collected by the minimum bias trigger. Our MC-calculated efficiency for both COT tracks to be matched with XFT tracks is then compared with the measured results in terms of various two-track quantities. Note that the track parameter distributions depend on the physics process and trigger selection criteria, therefore a good agreement between MC and data for all kinematic variables of the two-track pair is mandatory to validate the efficiency parameterization before applying it to the D meson system.

The XFT can reconstruct at most one track per 1.25° bin in ϕ_6. In case of more than one candidate per 1.25° bin, the highest p_T track will be reported. We compared two different ways to account for this. In the literal implementation, we extrapolate tracks to SL6, and digitize the value of ϕ_6 in bins of 1.25°. In case of multiple entries per bin we reject the XFT track with the lowest p_T. However, when comparing the MC prediction with data measurement, it was found that the MC tends to give a somewhat higher two-track efficiency for small values of $\Delta\phi_6$. This is likely due to the fact that this model does not account for all possible interferences between two COT tracks at small $\Delta\phi_6$. We find better agreement by setting to zero the two-track efficiency if two tracks have $|\Delta\phi_6| \leq 1.25^\circ$, as shown in Figure 10.1. We treat the difference between the two models as a systematic uncertainty.

The XFT track informations then reported to the Level-1 trigger system by the eXTRaPolator board (XTRP). The XTRP divides the COT into 15° bins and reports only the two outermost XFT tracks with respect ϕ_6 that pass $2\,\mathrm{GeV/c}$ threshold in each bin.

10.3 Two-Track SVT Efficiency

Unlike the XFT, which has a uniform efficiency in ϕ, the SVT efficiency is a complicated function of the detector geometry. As a consequence, the efficiency for two tracks to be both reconstructed by the SVT depends strongly on the kinematics and geometry of the two-track pair. For example, if the opening angle is large, the two tracks go through different SVT wedges, and the efficiencies have little correlation. For small opening angles, the two tracks have a higher probability to go through

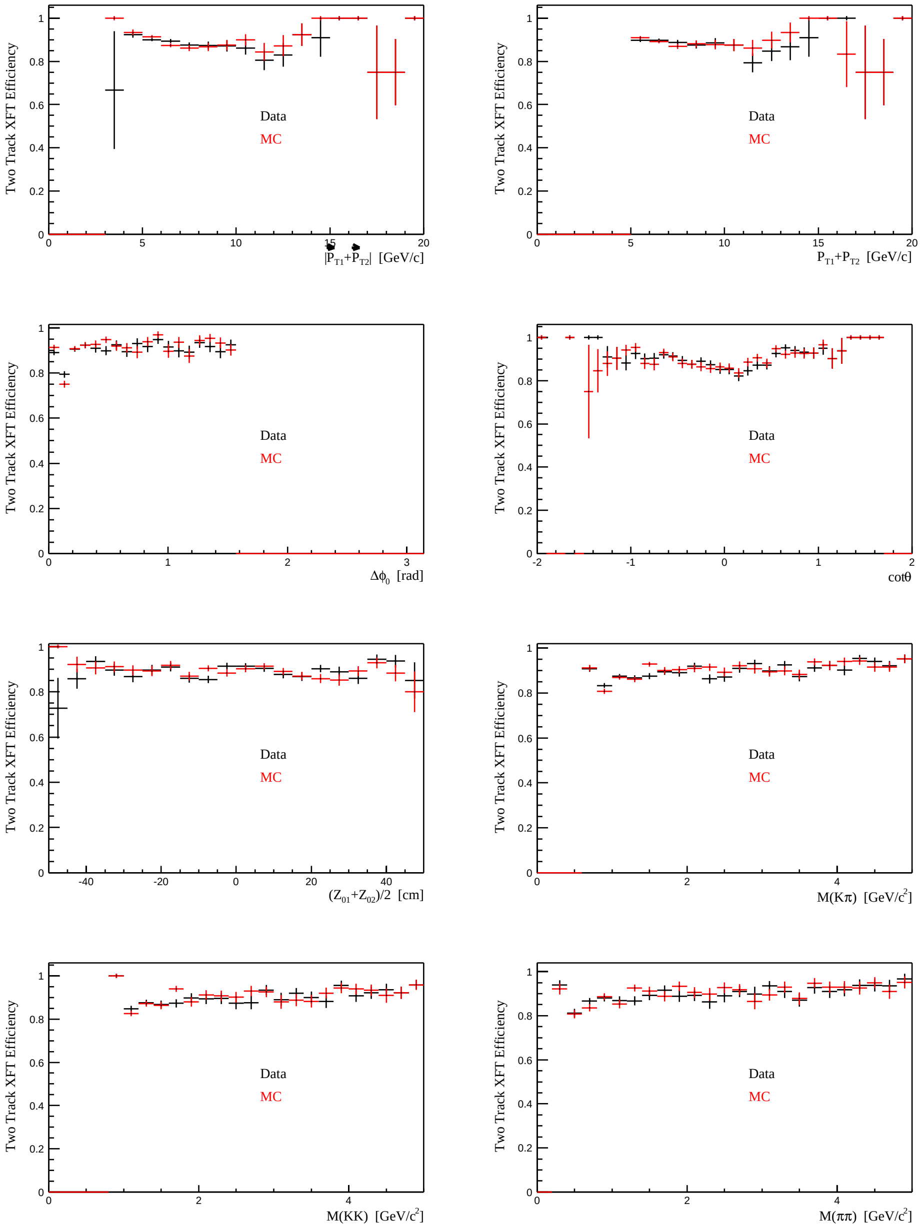

Figure 10.1: Comparison between measured two-track XFT efficiency and the Monte Carlo simulation, where we specifically require that both tracks to have opposite charge, and their offline qualities satisfy $p_{T1} \geq 2\,\mathrm{GeV}/c$, $p_{T2} \geq 2\,\mathrm{GeV}/c$, $p_{T1}+p_{T2} \geq 5.5\,\mathrm{GeV}/c$, and $2^\circ \leq |\Delta\phi_0| \leq 90^\circ$.

the same wedge, and the efficiencies are strongly correlated, typically resulting in a higher two-track efficiency. This correlation can be completely described if the single-track SVT efficiency is known as a function of all track parameters. In reality a few simplifying assumptions had to be made and the binning of each variable can not be too fine because of the limited available statistics. Therefore, we expect to underestimate the correlation of the SVT efficiency of two-track combinations.

Two-track combinations from the Level-1 auto-accept data are used as input to the parameterized SVT efficiency, and we compare the calculated two-track efficiency with the measured two-track efficiency. For track pairs with a large opening angle, the calculated two-track SVT efficiency shows good agreement with the measurement as shown in Figure 10.2. For small-angle track pairs the two-track efficiency is underestimated by about 10%. The reason for this discrepancy is that our single-track SVT efficiency does not fully describe the detailed geometric substructure due to the finite bin size used. In order to correct for the this effect, we artificially introduce an additional correlation of 0.10 for the efficiency of two tracks if they pass through the same SVX wedge. After introducing this additional correlation, the two-track efficiency calculated from the parameterized SVT efficiency agrees better with the direct measurement, as shown in Figure 10.2. We treat the full size of this correction as a systematic uncertainty.

If the (z,$\cot\theta$) correlation would not be taken into account, using the parameterization of Equation 7.5, a good description of the two-track efficiency can be obtained, but a somewhat larger additional correlation of 0.13 is required.

Since we use the parameterized SVT efficiency for calculating charm meson efficiencies, we show in Figure 10.2 that the calculated two-track efficiency reproduces the measurement as a function of many kinematic variables of the two-track combination. As an additional cross-check, we compare the measured two-track efficiency with the two-track efficiency of MC-generated D^0's as shown in Figure 10.3.

10.4 SVX Efficiency of the Third Track in Three-Track Systems

For the reconstruction of three-body D^+ and D_s^+ decays, we require that two tracks are SVT-matched and the third to have ϕ-side hits in at least 3 different SVX layers. Although the SVX efficiency is higher and more uniform than the SVT efficiency, simply applying the measured SVX efficiency may not fully take into account the correlation between the efficiency of the third track and the two SVT-matched tracks.

Similar to the two-track SVT efficiency study, three-track combinations from the Level-1 auto-accept data are used to calculate the SVX efficiency of the third

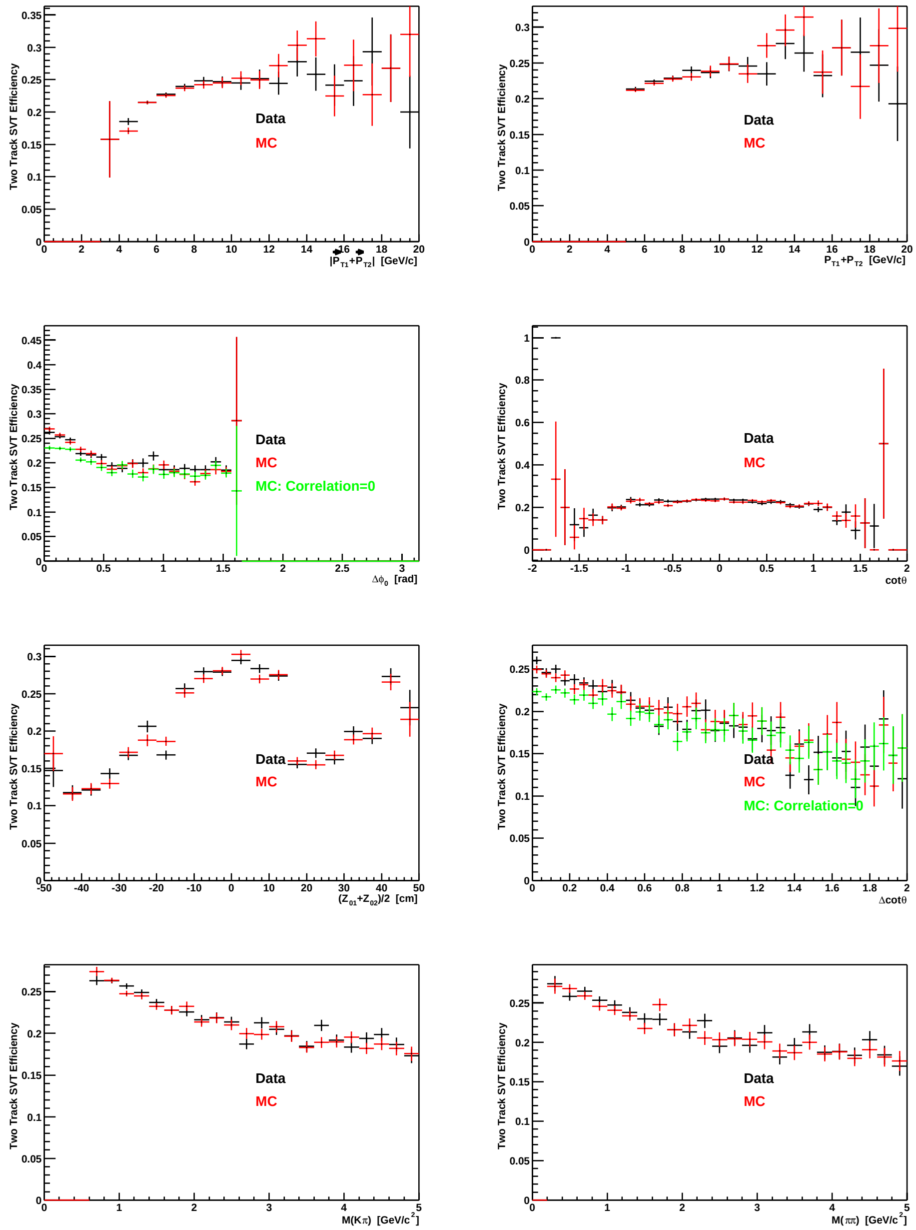

Figure 10.2: Comparison between measured two-track SVT efficiency from Level-1 auto-accepts of the two-track trigger and the parameterized two-track efficiency using the data as input. The tracks are required to have opposite charge, with $p_{T1} \geq 2\,\mathrm{GeV}/c$, $p_{T2} \geq 2\,\mathrm{GeV}/c$, $p_{T1} + p_{T2} \geq 5.5\,\mathrm{GeV}/c$, $2^\circ \leq |\Delta\phi_0| \leq 90^\circ$. Shown in green is the two-track efficiency without the additional 0.10 correlation for tracks in the same SVT wedge.

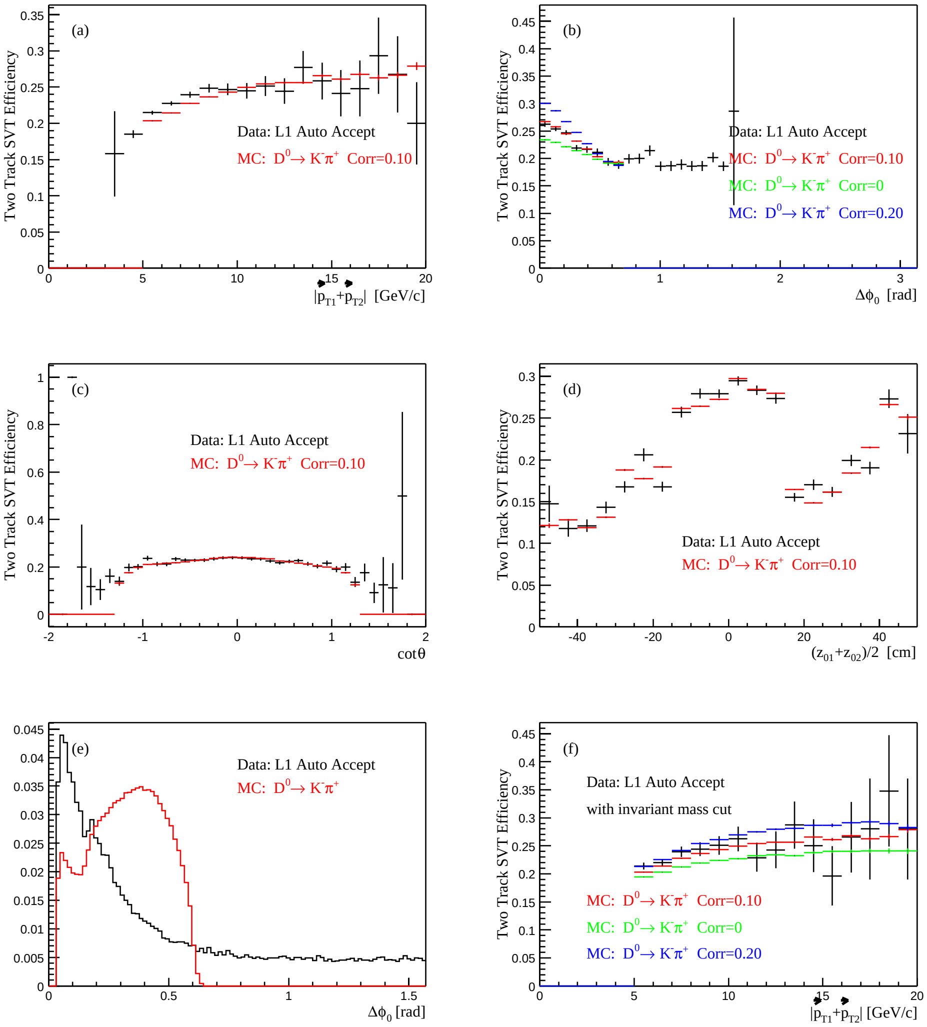

Figure 10.3: Plots (a),(b),(c) and (d) are comparisons between measured two-track SVT efficiency from Level-1 auto-accepts of the two-track trigger and the parameterized two-track efficiency of D^0 events from MC. The tracks are required to have opposite charge, with $p_{T1} \geq 2\,\mathrm{GeV}/c$, $p_{T2} \geq 2\,\mathrm{GeV}/c$, $p_{T1} + p_{T2} \geq 5.5\,\mathrm{GeV}/c$, $2^\circ \leq |\Delta\phi_0| \leq 90^\circ$. The deviation of the two track efficiencies between data and D^0 MC at low p_T bins is due to the different opening angle distribution between the two tracks, as illustrated in plot (e). In plot (f), the two tracks in Level-1 auto-accept data are required to have $K\pi$ invariant mass $|m(K\pi) - m(D^0)| \leq 400\,\mathrm{MeV}/c^2$, the deviation becomes less and is well covered by the systematic uncertainties.

track, and we compare to the measured efficiency. For the two SVT-matched tracks we require $p_{T1} \geq 2\,\mathrm{GeV}/c$, $p_{T2} \geq 2\,\mathrm{GeV}/c$, $p_{T1} + p_{T2} \geq 5.5\,\mathrm{GeV}/c$, and $2^\circ \leq |\Delta\phi_0| \leq 90^\circ$. A COT track is added to form a three-track system. The calculated SVX efficiency for the third track agrees with the measurement at large $\Delta\cot\theta = \cot\theta_3 - \cot\theta_{12}$, where θ_{12} is the polar angle of the vector-sum of the two SVT-matched tracks. At small $\Delta\cot\theta$ the SVX efficiency is underestimated by a few percent. Therefore, the calculated efficiency is systematically lower by the same amount compared to data with respect to the other geometrical variables. We correct for this discrepancy by adding a correlation of 0.05 to the SVX efficiency when the third track and the vector-sum of the SVT-matched tracks pass through the same SVX half-barrel. With this correction, the calculated third track SVX efficiency agrees with the measurement as shown in Figure 10.4. We treat the full size of this correction as a systematic uncertainty.

10.5 K_S^0 Impact Parameter Distribution

One of the direct application of the parameterized detector Monte Carlo simulation is to study the reconstructed prompt D meson impact parameter resolution, especially for 3 body D^+ and D_s^+ decays, which are crucial for secondary D fraction measurement [21]. Since the reconstructed D meson impact parameter resolution is dominated by the single-track d_0 resolution, one good way to check the track

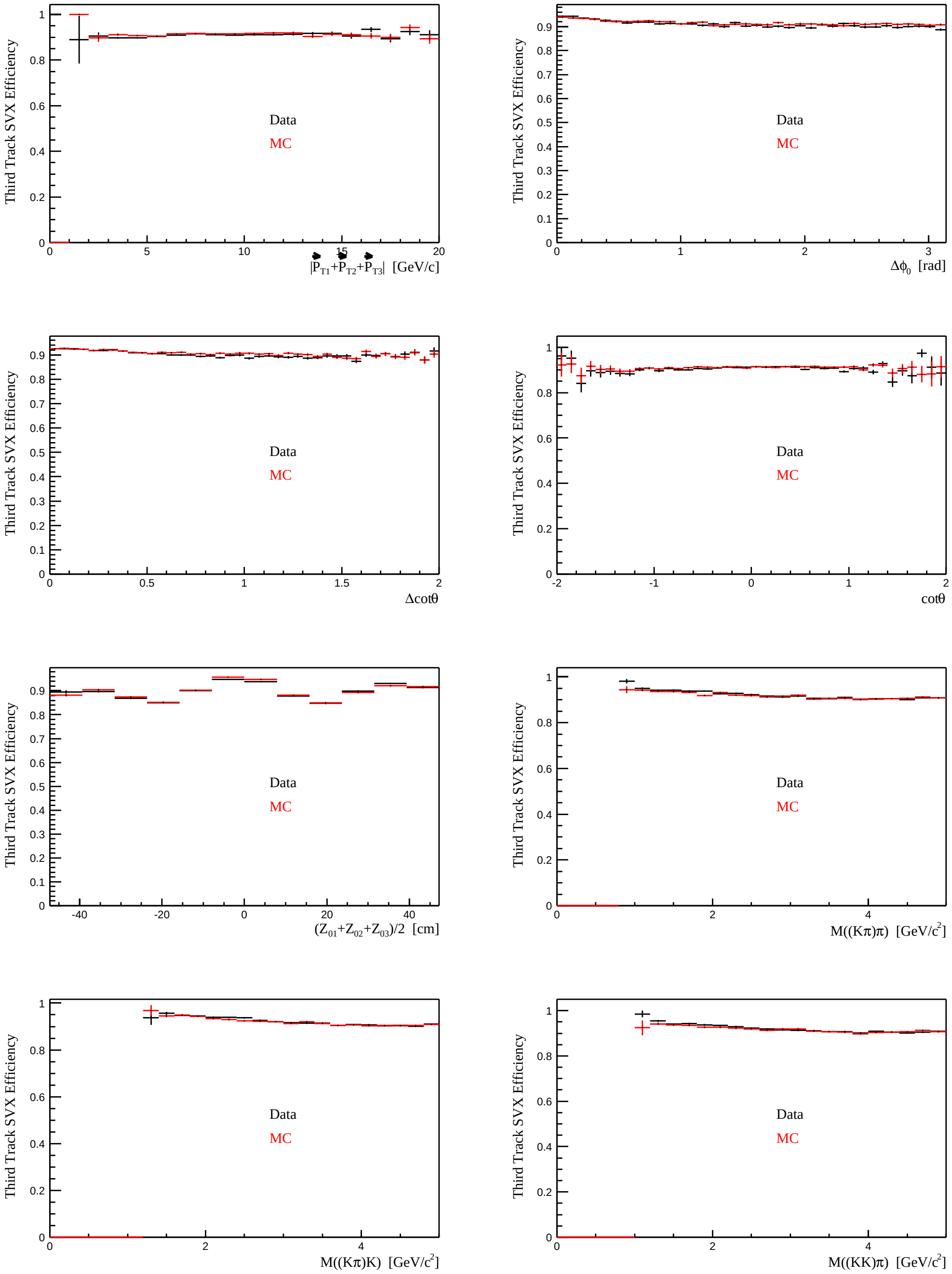

Figure 10.4: Comparison between measured SVX efficiency for the third track and the Monte Carlo simulation.

impact parameter smearing of our detector simulation is to compare measured and MC-predicted K_S^0 impact parameter in the two-track trigger sample since only a few percent of them are secondary [21]. The same K_S^0 reconstruction selection criteria used in section 6.4.1 are applied here.

The $\pi^+\pi^-$ invariant mass distribution for K_S^0 candidates is fit with a Gaussian to describe the signal and a linear term to describe the combinatorial background. No corrections have been made for energy loss. We define the signal region as $|m(\pi^+\pi^-) - m(K_\mathrm{S}^0)| \leq 2\sigma(m(K_\mathrm{S}^0))$, where $m(K_\mathrm{S}^0)$ and $\sigma(m(K_\mathrm{S}^0))$ are the measured K_S^0 mass and width. The side-band is defined as $3\sigma(m(K_\mathrm{S}^0)) \leq |m(\pi^+\pi^-) - m(K_\mathrm{S}^0)| \leq 5\sigma(m(K_\mathrm{S}^0))$.

After correcting the signal distribution for background using sideband subtraction, the resulting K_S^0 impact parameter distributions in different p_T and L_{xy} bins are modeled with the combination of a Gaussian distribution and an exponential distribution:

$$F_{K_s}(d_0) = \frac{1-\alpha_0}{2\lambda_{K_s}} e^{-|d_0|/\lambda_{K_s}} + \frac{\alpha_0}{\sqrt{2\pi}\sigma_{K_s}} e^{-d_0^2/2\sigma_{K_s}^2}. \tag{10.1}$$

To study the expected K_S^0 impact parameter resolution in MC, we generate K_S^0 with the FAKE_EVENT Generator with $5.0\,\mathrm{GeV}/c \leq p_T(K_S^0) \leq 20\,\mathrm{GeV}/c$. We assume that the $p_T(K_S^0)$ distribution follows p_T^{-4} and a flat pseudo-rapidity distribution $-2 < |\eta| < 2$. The average p_T and L_{xy} spectrums of K_S^0 from MC are higher than the K_S^0's from data, as shown in Figure 10.6. The K_S^0 is forced to decayed into $\pi^-\pi^+$, which are subsequently passed to the trigger and offline reconstruction simulation.

The same event selection criteria for K_S^0 reconstruction in the data are used here. The K_S^0 impact parameter distributions are also fit with Equation 10.1 in different p_T and L_{xy} bins. As shown in Figure 10.7, the central distributions for MC-predicted K_S^0 impact parameter agree very well with those measured from the two-track data, but with relatively longer tails.

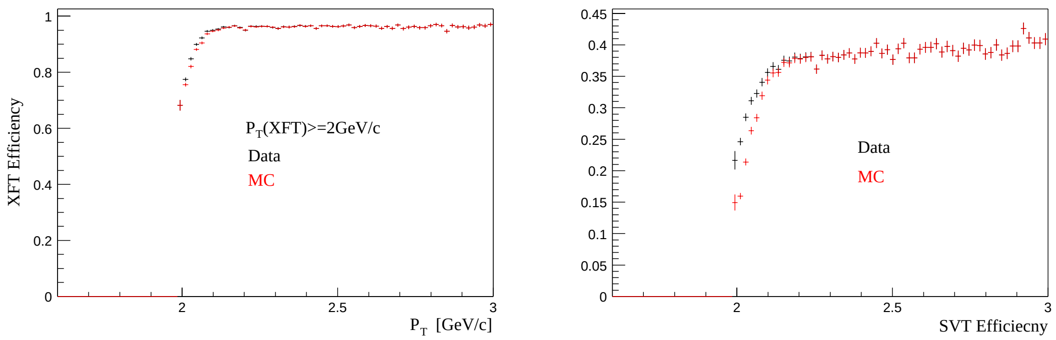

Figure 10.5: Comparison between measured and simulated single-track XFT and SVT efficiency with minimum p_T requirement.

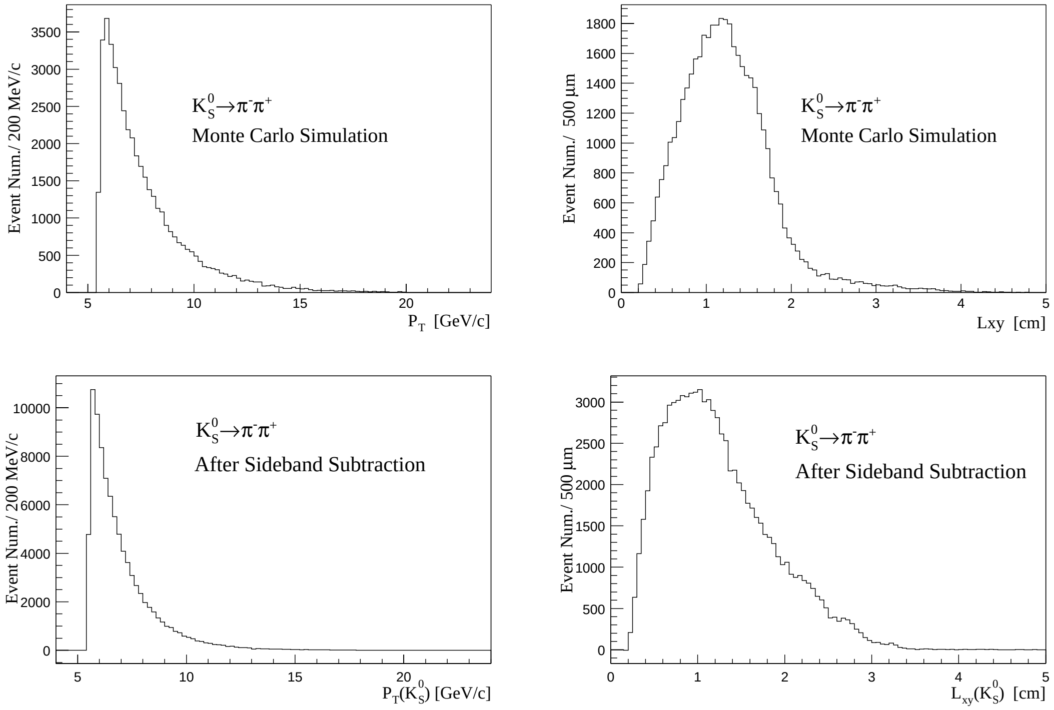

Figure 10.6: The p_T and L_{xy} distribution of K_S^0 after trigger and analysis requirements from Monte Carlo simulation and data.

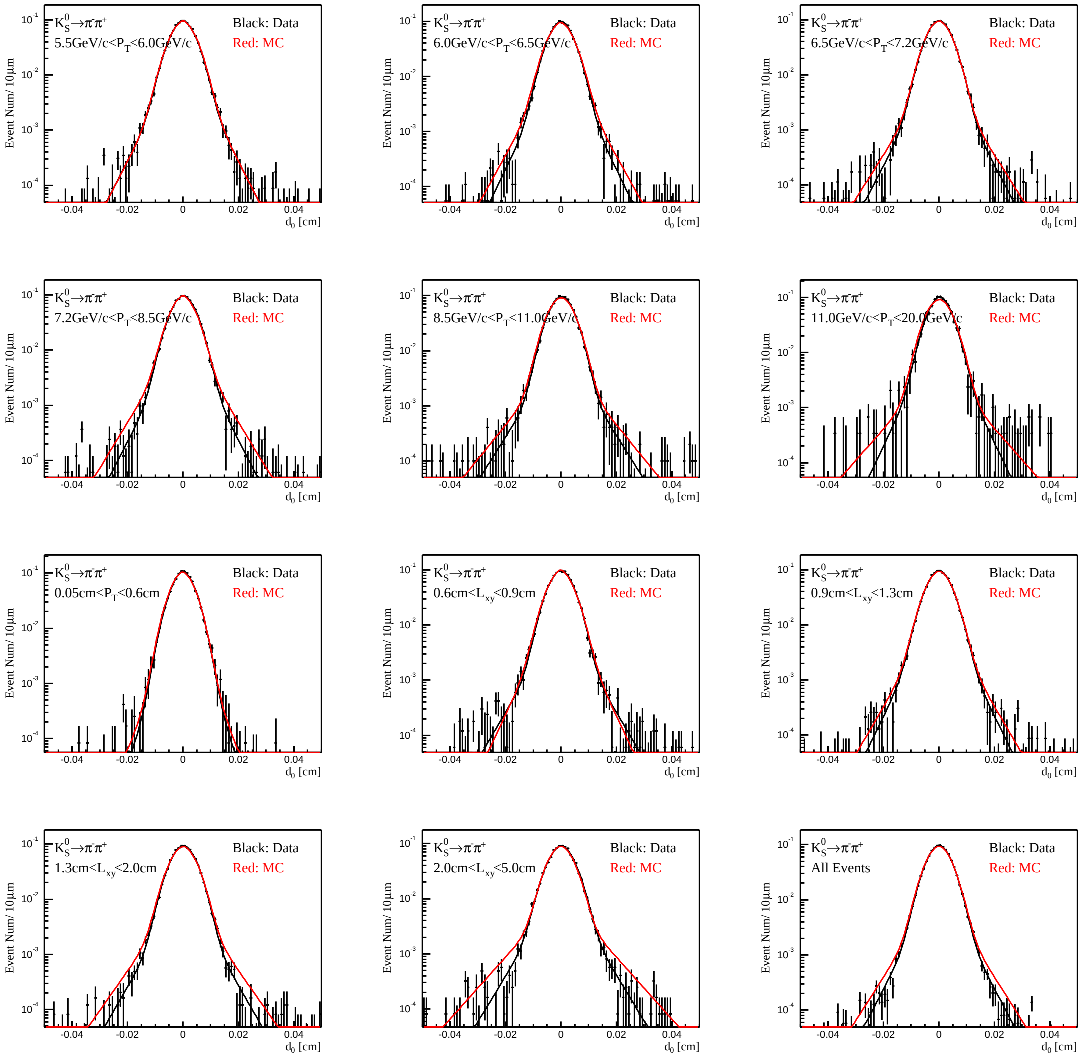

Figure 10.7: Comparison between the K_s impact parameter distribution measured from two-track data and the Monte Carlo simulation. The black and red curve are the fit results of the K_S^0 impact parameter from data and MC respectively. The histogram is the d_0 distribution from data. All of them are normalized to one.

Chapter 11

Charm Meson Trigger and Reconstruction Efficiency

11.1 Monte Carlo Generation of Prompt Charm Mesons

1×10^8 single D^0, D^{*+}, D^+, and D_s^+ mesons are generated with HeavyQuarkGen [94] respectively.

We do not explicitly generate $\overline{D}$ mesons, but instead flip the charge of all charm daughters for half the events. Therefore the calculated efficiencies are the average for D and $\overline{D}$. The difference in efficiency between D and $\overline{D}$ is expected to be at the

$O(1\%)$ level, from differences in the hadronic interaction cross section of and the COT efficiency for low-p_T tracks.

The following set of Monte Carlo parameters is chosen:

- the ϵ parameter in the Peterson fragmentation is set equal to 0.02 with the NLO charm quark p_T spectrum [18];
- the charm mass is set equal to $1.5\,\mathrm{GeV}/c$;
- the scale factor is set equal to 1;
- MRST is chosen as the parton distribution function;

The D mesons are forced to decay to the mode we are interested in via QQ package.

Since we apply selection criteria on the impact parameter of the charm daughters, the lifetime and its uncertainty directly affect the reconstruction efficiency. We use the PDG2002 [26] values for the charm lifetimes, and vary them with $\pm 1\sigma$ to evaluate the systematic uncertainty:

$$c\tau(D^0) = 123.4 \pm 0.8\mu\mathrm{m}(0.7\%); \tag{11.1}$$

$$c\tau(D^+) = 315 \pm 4\mu\mathrm{m}(1.2\%); \tag{11.2}$$

$$c\tau(D_s^+) = 147.0 \pm 2.7\mu\mathrm{m}(1.8\%). \tag{11.3}$$

11.2 Monte Carlo Generation of Secondary Charm Mesons

The production and fragmentation of b quarks is simulated with the Monte Carlo generator BGENERATOR, and the resulting B hadrons are decayed using the QQ package. The decays of the B mesons are inclusive, but the secondary charm mesons are forced to decay in the following modes:

- $D^0 \to K^-\pi^+$;
- $D^+ \to K^-\pi^+\pi^+$;
- $D_s^+ \to \phi\pi^+, \phi \to K^+K^-$.

More than 5×10^8 $b\bar{b}$ events are generated,

11.3 Dalitz Structure of the $D^+ \to K^-\pi^+\pi^+$ Decay

QQ has decayed $D^+ \to K^-\pi^+\pi^+$ according to phase-space, which corresponds to a uniform distribution in the kinematically allowed space of m_{12}^2, m_{13}^2, the mass squared of the two $K^-\pi^+$ combinations. However, we expect the efficiency to vary with m_{12}^2, m_{13}^2, and need a more detailed description of the D^+ decay. Therefore,

Resonance	mass	width	spin	amplitude	phase
non-resonant				1.0	0°
$K^*(892)^0$	0.8961	0.0507	1	0.78 ± 0.02	-60±3°
$K_0^*(1430)^0$	1.412	0.294	0	0.53 ± 0.02	132±2°
$K^*(1680)^0$	1.717	0.322	1	0.47 ± 0.03	-51±4°

Table 11.1: Resonances contributing to the $D^+ \to K^-\pi^+\pi^+$ decay from E691.

we reweight the generated events to make them correspond to the measured Dalitz-structure from E691 [95]. This parameterization includes a non-resonant fraction and contributions from the $K^*(892)^0$, $K_0^*(1430)^0$ and the $K^*(1680)^0$.

$$\frac{d^2\Gamma}{dm_{12}^2 dm_{13}^2} \propto \left| 1 + \sum_{k=1}^{n} A_k e^{i\delta_k} \left[\frac{1}{\sqrt{2}} BW_k(m_{12}) D_k(\cos\theta_{23}|_{12}) + \frac{1}{\sqrt{2}} BW_k(m_{13}) D_k(\cos\theta_{23}|_{13}) \right] \right|^2 \tag{11.4}$$

where A_k is the amplitude and δ_k is the relative phase of the contributing resonance, as listed in Table 11.1. To evaluate the systematic uncertainty, we varied the amplitude and phase parameter values with $\pm\sigma$ and added the corresponding uncertainties in quadrature.

$BW_k(E)$ is the normalized non-relativistic Breit-Wigner function:

$$BW_k(E) = \frac{-i\sqrt{\frac{\Gamma_k}{2\pi}}}{m_k - E - i\frac{\Gamma_k}{2}} \tag{11.5}$$

and D_k is an angular factor, which is 1 for spin-0 resonances and $-\cos\theta$ for spin-1 resonances, where θ is the angle between the two pions in the rest-frame of the resonance.

Figure 11.1 shows the resulting distribution, and the amplitudes of the individual resonances.

11.4 Correction of the D Meson p_T Distribution in the MC Simulation

The D meson trigger and reconstruction efficiency varies strongly as a function of the charm meson transverse momentum. Due to the finite size of the p_T bins, the D meson p_T distribution from the Monte Carlo simulation needs to match well the actual p_T distribution. We do not expect that the p_T spectrum from MC is a priori correct, since large discrepancies in the p_T spectrum are typical for heavy flavor production models, and were seen in particular in the Run I measurement of the D^{*+} cross section [18]. In this section we compare the p_T distribution of charm mesons in data and MC, and make a parameterization of the data/MC ratio. After applying this ratio as a reweight factor to the MC events, the p_T spectrum of the MC matches well the data, as shown in Section 11.8, and no second iteration is needed.

The same D meson reconstruction selection criteria used in section 5 are applied here. The D meson p_T spectra from data and MC are compared in Figure 11.2 and 11.3. We used sideband subtraction to obtain the distributions from data.

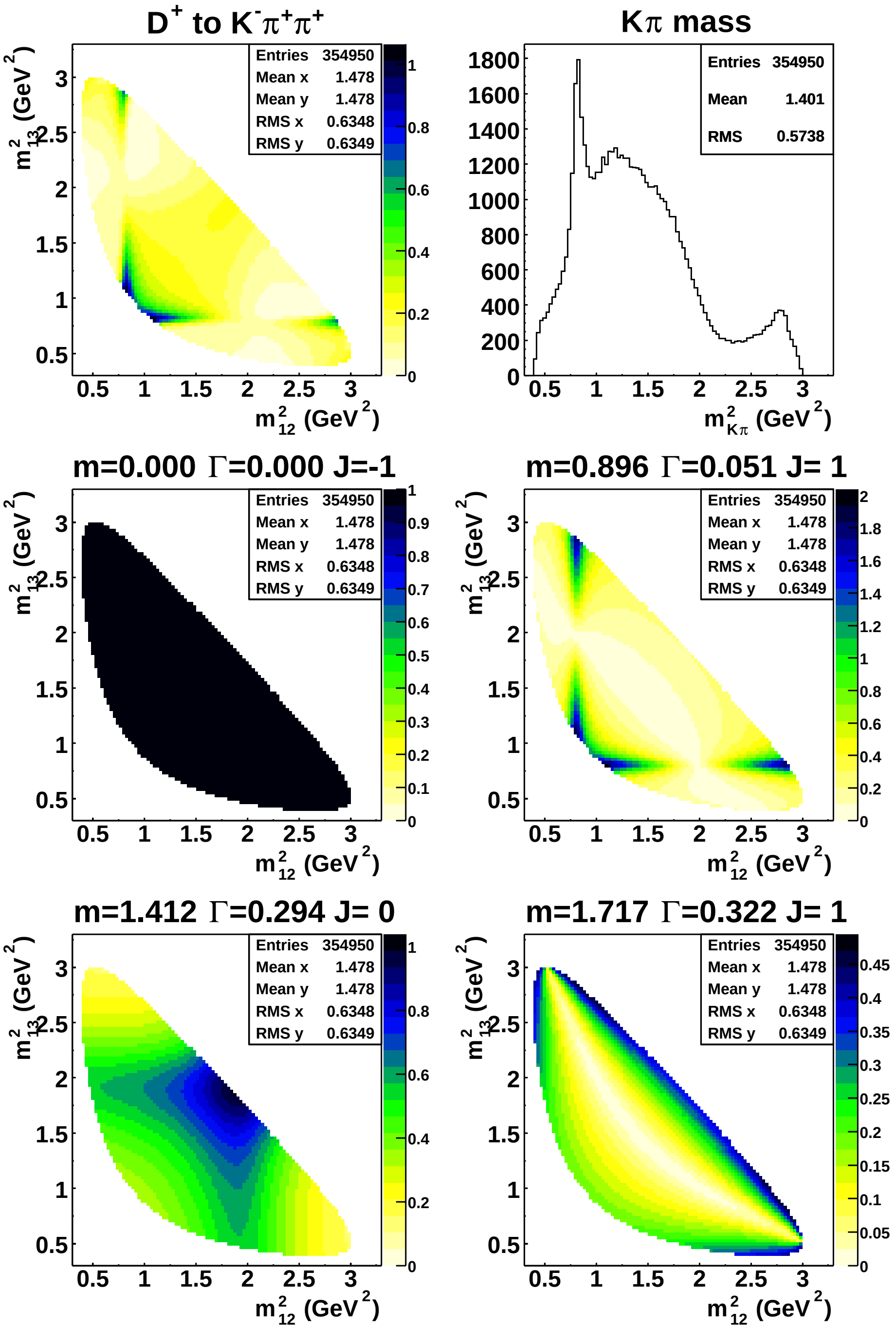

Figure 11.1: Dalitz distribution for $D^+ \to K^-\pi^+\pi^+$ with the amplitudes of the contributing resonances.

We use a $\pm 2\sigma$ region for the signal and the -5σ to -3σ and 3σ to 5σ regions as sidebands. The signal width has been determined in p_T bins, as described in section 5.

Sideband subtraction for the D^0 needs special attention, since the sidebands are dominated by the autoreflection of the signal, and do not represent the background under the signal peak. Therefore we generate the autoreflection sidebands for the MC sample and apply the same sideband subtraction in MC as in data.

The data are significantly softer than those of the either prompt or secondary D mesons from Monte Carlo simulation. We find that the ratio between data and MC can be well described by an exponential function:

$$p_T(D)_{DATA} = A\exp(Bp_T) \cdot p_T(D)_{MC}. \tag{11.6}$$

The slope parameters B for each type of D mesons are fit with or without secondary D meson contribution, which results in a slight change of its value, as shown in Figure 11.2 and 11.3. Since the difference is small, we choose the values fit with secondary D contributions, then correct the p_T spectrum of D mesons in the MC with the function $\exp(Bp_T)$, and use the reweighted MC for efficiency estimates. To evaluate the systematic uncertainty, we varied the slope parameters with $\pm 1\sigma$.

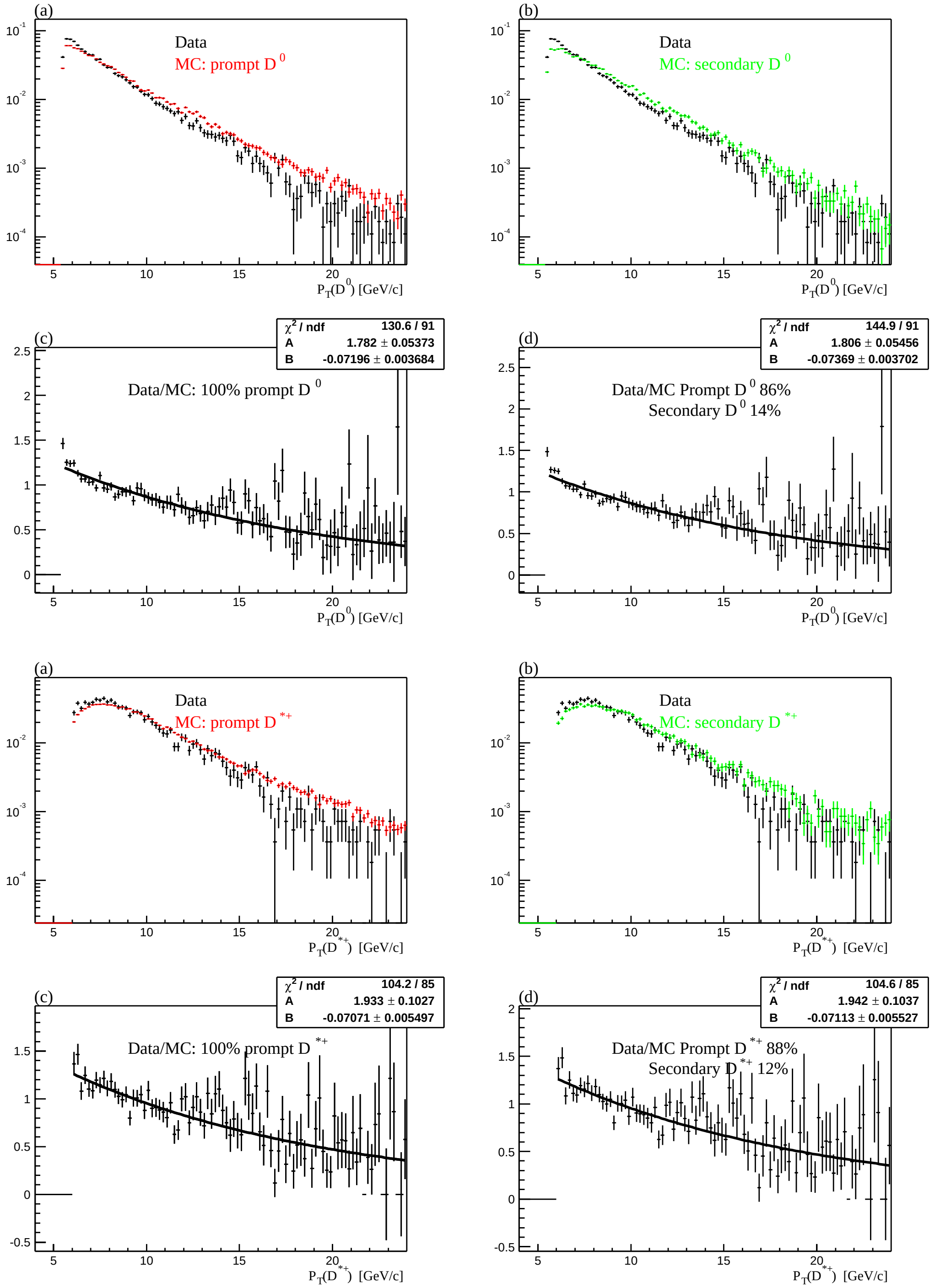

Figure 11.2: Comparison of normalized D^0, D^{*+} p_T distribution from data and Monte Carlo, and their ratios.

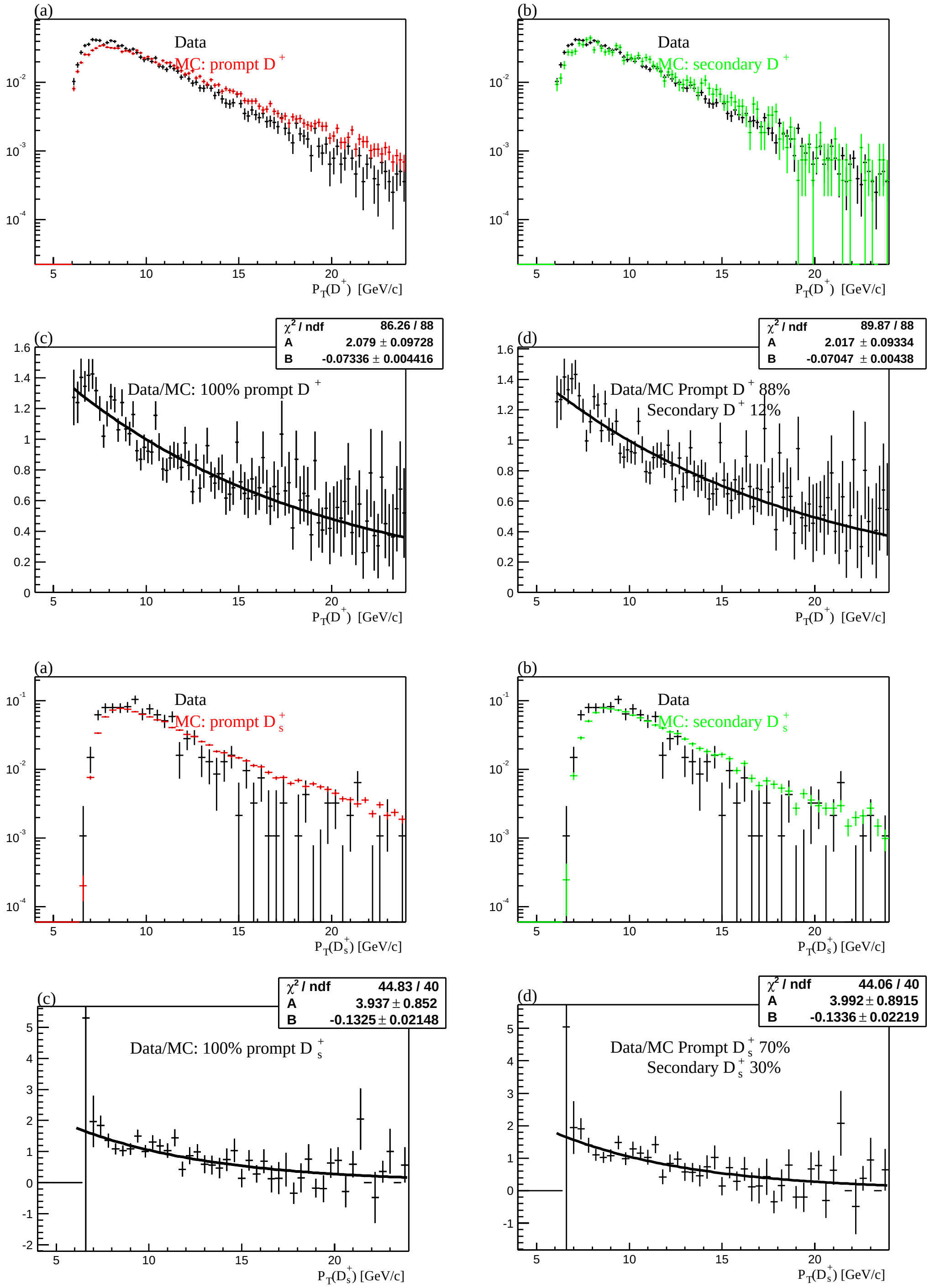

Figure 11.3: Comparison of normalized D^+, D_s^+ p_T distribution from data and Monte Carlo, and their ratios.

11.5 Correction of the D Meson Rapidity Distribution in the MC Simulation

Since we measure the differential and inclusive cross section for particles inside certain rapidity range, a good agreement of rapidity distributions between data and Monte Carlo are essential. Similar to the p_T distribution, we examine the D meson rapidity distribution from data with sideband subtraction and those of the MC-predicted prompt and secondary D mesons. As shown is Figure 11.4 and 11.5, they agree very well. Therefore in our analysis, no rapidity correction is done for Monte Carlo event generation.

11.6 D Meson Trigger and Reconstruction Efficiency

The definition of the D meson trigger and reconstruction efficiency is defined as the probability to pass the trigger and reconstruction simulation and offline selection criteria:

$$\epsilon(D) = \frac{\text{Num. of } D \text{ pass Trig \& Reco MC}}{\text{Num. of Generated } D \text{ Events}}, \tag{11.7}$$

where the D meson rapidity is required to be less than one. To estimate the efficiency, we generate prompt D mesons proportional to each individual run's offline

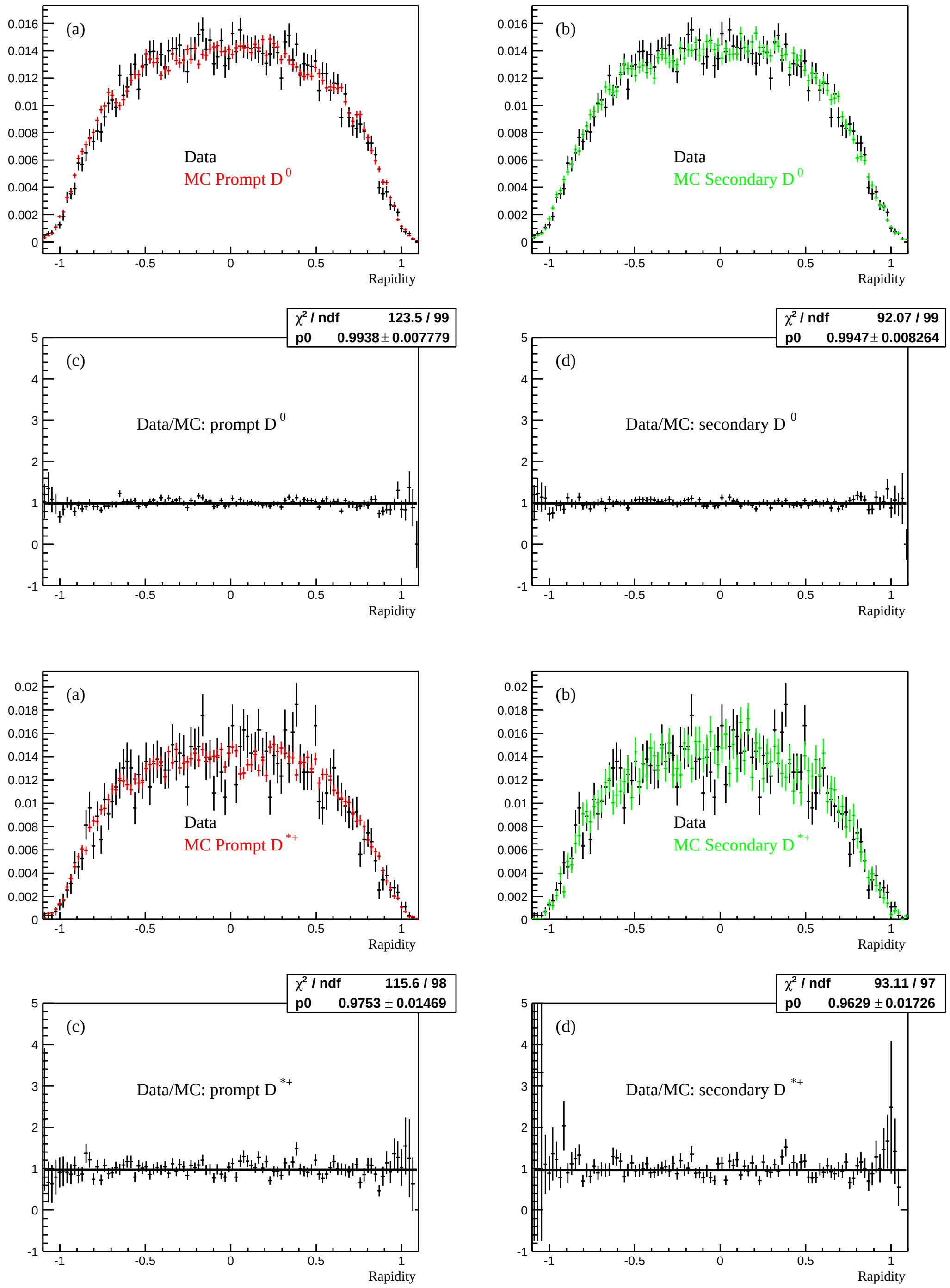

Figure 11.4: Comparison of normalized D^0, D^{*+} rapidity distribution from data and Monte Carlo, and their ratios.

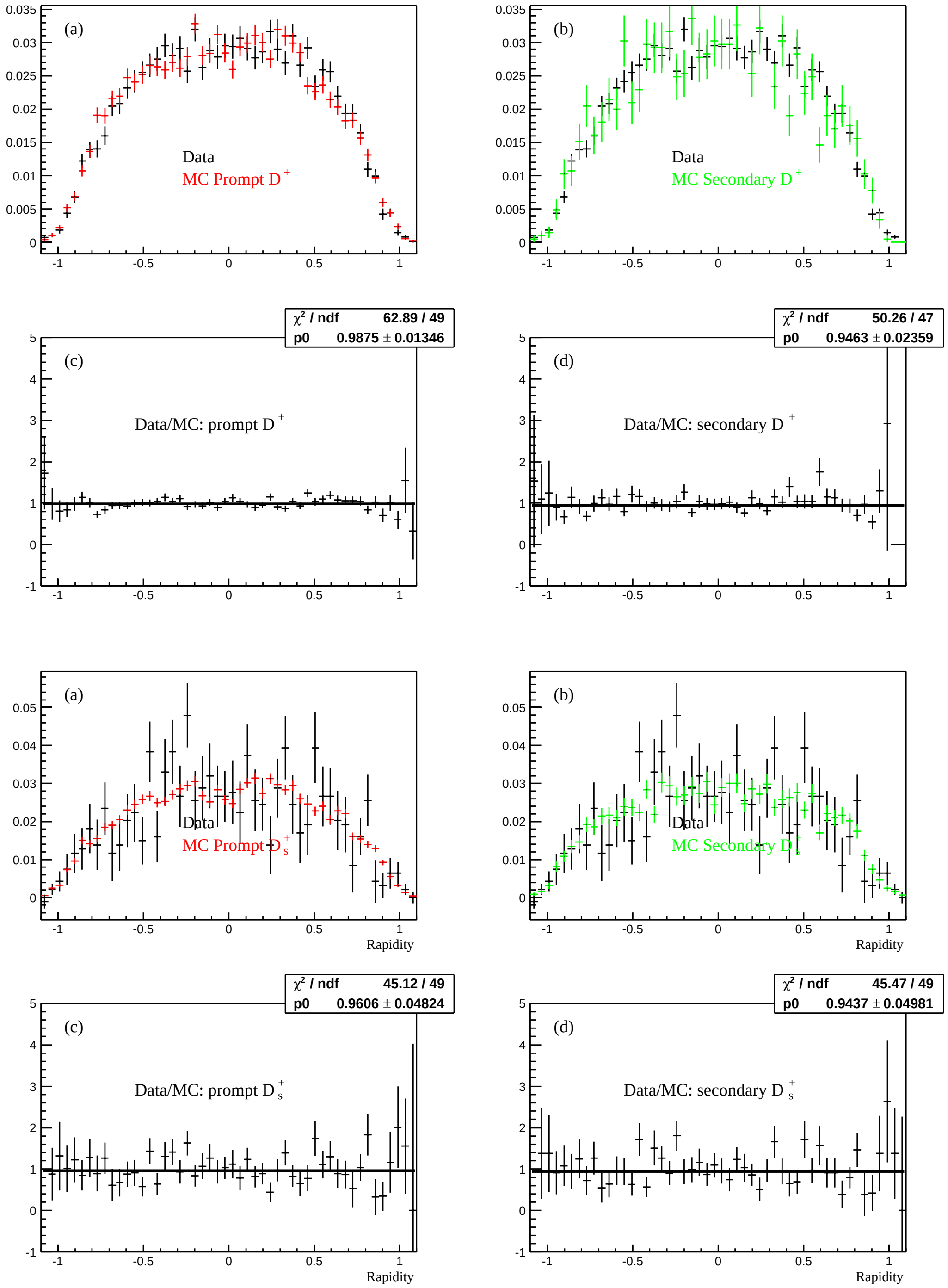

Figure 11.5: Comparison of normalized D^+, D_s^+ rapidity distribution from data and Monte Carlo, and their ratios.

luminosity that has been used for signal reconstruction, and subsequently pass them to the detector simulation with the corresponding SVT, SVX parameters. The results are listed in Table 11.2 to 11.9.

11.7 Discussion

Given the predicted D meson efficiencies, a natural question is whether the values are consistent with the expectation. The D meson efficiencies after various additional selection criteria and detector simulation are shown in Figure 11.6, 11.7, 11.8 and 11.9, the corresponding efficiency reduction after each step agrees well with the studies in previous sections. An more intuitive approach is to compare the results with the prediction based on the perfect detector model. Take $D^0 \to K^-\pi^+$ as an example, if we assume the detector has perfect efficiency and resolution, with only COT, decay and hadronic interaction simulation, the predicted D meson trigger and reconstruction efficiencies are roughly 8 times of the value from realistic simulation in the low $p_T(D^0)$ bins, and 5 times in the high $p_T(D^0)$ region. Given the two-track XFT efficiency is roughly about 80%, the two-track SVT efficiency is around 18% at low p_T, while about $20-25\%$ for high p_T due to the smaller opening angle, which results in higher probability to pass through the same SVX wedge. The naive estimate then gives 4.5 to 7 times efficiency drop just because of the XFT and SVT efficiency, which is well consistent with our prediction.

$D^0 \to K^-\pi^+$					
p_T [GeV/c]		5.5-6.0	6.0-7.0	7.0-8.0	8.0-10
$\epsilon(D^0)$ [10^{-3}]		3.53	4.93	6.30	7.30
Relative statistical error [%]		±0.8	±0.6	±0.7	±0.7
Systematic sources	Section	relative uncertainty [%]			
D^0 lifetime $\pm 1\sigma$	11.1	±1.1	±1.1	±1.1	±1.1
Transverse beam spot size $\pm 2\,\mu$m	9.1	-	-	-	-
Lum. region $p_{T,min} = 0.5/2.0\,$GeV/c	9.2	±1.4	±1.4	±1.4	±1.4
Luminous region ±1 cm	9.2	±0.5	±0.5	±0.5	±0.5
p_T reweight $\pm 1\sigma$	11.4	-	-	-	-
Decay inside COT	9.8	±1.1	±1.1	±1.1	±1.1
Hadronic interaction ±28%	9.8	±2.1	±2.1	±2.1	±2.1
COT efficiency stat	7.2	±0.4	±0.3	±0.5	±0.4
COT efficiency merge	7.2	±0.7	±0.7	±0.7	±0.7
COT efficiency ΔR	7.2	±1.2	±1.2	±1.2	±1.2
COT efficiency hits	7.2	±1.4	±1.4	±1.4	±1.4
XFT efficiency vs multiplicity	7.7	±1.0	±1.0	±1.0	±1.0
XFT efficiency wide/default match	7.3	±0.6	±0.6	±0.6	±0.6
XFT two-track efficiency	10.2	-	-	-	-
XFT p_T resolution ±5 MeV/c	10.1	-	-	-	-
SVT efficiency correction	7.4	±4.0	±4.0	±4.0	±4.0
SVT efficiency vs d_0	7.4	±1.5	±1.5	±1.5	±1.5
SVT efficiency wide/default match	7.4	±1.0	±1.0	±1.0	±1.0
SVT p_T resolution ±20 MeV/c	10.1	±1.0	-	-	-
SVT two-track correlation ±10%	10.3	±1.9	±3.1	±4.0	±6.3
SVX/SVT d_0 correlation ±10%	8.3	±2.5	±2.5	±2.5	±2.5
L3/offline correlation	9.5	-	-	-	-
Energy loss ±10 MeV/c	9.6	±4.1	±1.3	-	-
Total systematic uncertainty		±7.8	±7.2	±7.5	±8.9

Table 11.2: The D^0 meson trigger and reconstruction efficiencies and systematic uncertainties. The total systematic error is calculated by adding all individual components in quadrature.

$D^0 \to K^-\pi^+$				
p_T [GeV/c]		10-12	12-20	≥ 20
$\epsilon(D^0)$ [10^{-3}]		8.54	9.56	9.66
Relative statistical error [%]		±1.1	±1.3	±1.2
Systematic sources	Section	relative uncertainty [%]		
D^0 lifetime $\pm 1\sigma$	11.1	±1.1	±1.1	±1.1
Transverse beam spot size $\pm 2\,\mu$m	9.1	-	-	-
Lum. region $p_{T,min} = 0.5/2.0\,$GeV/c	9.2	±1.4	±1.4	±1.4
Luminous region $\pm 1\,$cm	9.2	±0.5	±0.5	±0.5
p_T reweight $\pm 1\sigma$	11.4	-	-	-
Decay inside COT	9.8	±1.1	±1.1	±1.1
Hadronic interaction ±28%	9.8	±2.1	±2.1	±2.1
COT efficiency stat	7.2	±0.6	±0.7	±0.7
COT efficiency merge	7.2	±0.7	±0.7	±0.7
COT efficiency ΔR	7.2	±1.2	±1.2	±1.2
COT efficiency hits	7.2	±1.4	±1.4	±1.4
XFT efficiency vs multiplicity	7.7	±1.0	±1.0	±1.0
XFT efficiency wide/default match	7.3	±0.6	±0.6	±0.6
XFT two-track efficiency	10.2	-	-	-
XFT p_T resolution $\pm 5\,$MeV/c	10.1	-	-	-
SVT efficiency correction	7.4	±4.0	±4.0	±4.0
SVT efficiency vs d_0	7.4	±1.5	±1.5	±1.5
SVT efficiency wide/default match	7.4	±1.0	±1.0	±1.0
SVT p_T resolution $\pm 20\,$MeV/c	10.1	-	-	-
SVT two-track correlation ±10%	10.3	±7.3	±8.5	±8.8
SVX/SVT d_0 correlation ±10%	8.3	±2.5	±2.5	±2.5
L3/offline correlation	9.5	-	-	-
Energy loss $\pm 10\,$MeV/c	9.6	-	-	-
Total systematic uncertainty		±9.7	±10.6	±10.8

Table 11.3: The D^0 meson trigger and reconstruction efficiencies and systematic uncertainties. The total systematic error is calculated by adding all individual components in quadrature.

$D^{*+} \to D^0\pi^+, D^0 \to K^-\pi^+$				
p_T [GeV/c]		6.0-7.0	7.0-8.0	8.0-10
$\epsilon(D^{*+})$ [10^{-3}]		1.18	2.98	5.48
Relative statistical error [%]		±1.2	±1.0	±0.8
Systematic sources	Section	relative uncertainty [%]		
D^0 lifetime $\pm 1\sigma$	11.1	±0.7	±0.7	±0.7
Transverse beam spot size $\pm 2\,\mu$m	9.1	-	-	-
Luminous region $p_{T,min} = 0.5/2.0\,$GeV/c	9.2	±2.2	±2.2	±2.2
Luminous region ±1 cm	9.2	±0.4	±0.4	±0.4
p_T reweight $\pm 1\sigma$	11.4	-	-	-
Decay inside COT	9.8	±1.5	±1.5	±1.5
Hadronic interaction ±28%	9.8	±2.5	±2.5	±2.5
COT efficiency stat	7.2	±0.5	±0.5	±0.4
COT efficiency merge	7.2	±0.9	±0.9	±0.9
COT efficiency ΔR	7.2	±1.3	±1.3	±1.3
COT efficiency hits	7.2	±2.1	±2.1	±2.1
XFT efficiency vs multiplicity	7.7	±1.0	±1.0	±1.0
XFT efficiency wide/default match	7.3	±0.6	±0.6	±0.6
XFT two-track efficiency	10.2	-	-	-
XFT p_T resolution $\pm 5\,$MeV/c	10.1	-	-	-
SVT efficiency correction	7.4	±4.0	±4.0	±4.0
SVT efficiency vs d_0	7.4	±0.9	±0.9	±0.9
SVT efficiency wide/default match	7.4	±1.0	±1.0	±1.0
SVT p_T resolution $\pm 20\,$MeV/c	10.1	±2.0	-	-
SVT two-track correlation ±10%	10.3	±1.5	±3.1	±5.9
SVX/SVT d_0 correlation ±10%	8.3	±2.1	±2.1	±2.1
L3/offline correlation	9.5	-	-	-
Energy loss $\pm 10\,$MeV/c	9.6	±13.9	±6.6	±4.2
Total systematic uncertainty		±15.6	±9.9	±9.9

Table 11.4: The D^{*+} meson trigger and reconstruction efficiencies and systematic uncertainties. The total systematic error is calculated by adding all individual components in quadrature.

$D^{*+} \to D^0\pi^+, D^0 \to K^-\pi^+$				
p_T [GeV/c]		10-12	12-20	≥ 12
$\epsilon(D^{*+})$ [10^{-3}]		7.66	8.37	8.51
Relative statistical error [%]		±1.1	±1.3	±1.2
Systematic sources	Section	relative uncertainty [%]		
D^0 lifetime $\pm 1\sigma$	11.1	±0.7	±0.7	±0.7
Transverse beam spot size $\pm 2\,\mu$m	9.1	-	-	-
Luminous region $p_{T,min} = 0.5/2.0\,$GeV/c	9.2	±2.2	±2.2	±2.2
Luminous region $\pm 1\,$cm	9.2	±0.4	±0.4	±0.4
p_T reweight $\pm 1\sigma$	11.4	-	-	-
Decay inside COT	9.8	±1.5	±1.5	±1.5
Hadronic interaction ±28%	9.8	±2.5	±2.5	±2.5
COT efficiency stat	7.2	±0.5	±0.6	±0.6
COT efficiency merge	7.2	±0.9	±0.9	±0.9
COT efficiency ΔR	7.2	±1.3	±1.3	±1.3
COT efficiency hits	7.2	±2.1	±2.1	±2.1
XFT efficiency vs multiplicity	7.7	±1.0	±1.0	±1.0
XFT efficiency wide/default match	7.3	±0.6	±0.6	±0.6
XFT two-track efficiency	10.2	-	-	-
XFT p_T resolution $\pm 5\,$MeV/c	10.1	-	-	-
SVT efficiency correction	7.4	±4.0	±4.0	±4.0
SVT efficiency vs d_0	7.4	±0.9	±0.9	±0.9
SVT efficiency wide/default match	7.4	±1.0	±1.0	±1.0
SVT p_T resolution $\pm 20\,$MeV/c	10.1	-	-	-
SVT two-track correlation ±10%	10.3	±6.8	±8.4	±8.4
SVX/SVT d_0 correlation ±10%	8.3	±2.1	±2.1	±2.1
L3/offline correlation	9.5	-	-	-
Energy loss $\pm 10\,$MeV/c	9.6	-	-	-
Total systematic uncertainty		±9.5	±10.7	±10.7

Table 11.5: The D^{*+} meson trigger and reconstruction efficiencies and systematic uncertainties. The total systematic error is calculated by adding all individual components in quadrature.

$D^+ \to K^-\pi^+\pi^+$				
p_T [GeV/c]		6.0-7.0	7.0-8.0	8.0-10
$\epsilon(D^+)$ [10^{-3}]		1.46	4.83	9.33
Relative statistical error [%]		±1.9	±1.4	±1.1
Systematic sources	Section	relative uncertainty [%]		
D^+ lifetime $\pm 1\sigma$	11.1	±1.7	±1.7	±1.7
Transverse beam spot size $\pm 2\,\mu$m	9.1	-	-	-
Luminous region $p_{T,min} = 0.5/2.0\,$GeV/c	9.2	±3.4	±3.4	±3.4
Luminous region ±1 cm	9.2	±1.7	±1.7	±1.7
p_T reweight $\pm 1\sigma$	11.4	-	-	-
Decay inside COT	9.8	±1.3	±1.3	±1.3
Hadronic interaction ±28%	9.8	±3.8	±3.8	±3.8
COT efficiency stat	7.2	±0.7	±0.5	±0.4
COT efficiency merge	7.2	±1.2	±1.2	±1.2
COT efficiency ΔR	7.2	±0.9	±0.9	±0.9
COT efficiency hits	7.2	±2.1	±2.1	±2.1
XFT efficiency vs multiplicity	7.7	±1.0	±1.0	±1.0
XFT efficiency wide/default match	7.3	±0.6	±0.6	±0.6
XFT two-track efficiency	10.2	±1.8	±1.8	±1.8
XFT p_T resolution ±5 MeV/c	10.1	-	-	-
SVT efficiency correction	7.4	±4.0	±4.0	±4.0
SVT efficiency vs d_0	7.4	±1.9	±1.9	±1.9
SVT efficiency wide/default match	7.4	±1.0	±1.0	±1.0
SVT p_T resolution ±20 MeV/c	10.1	±3.8	-	-
SVT two-track correlation ±10%	10.3	±5.1	±5.9	±8.1
SVX three-track correlation ±5%	10.4	±2.9	±2.9	±2.9
SVX/SVT d_0 correlation ±10%	8.3	±1.5	±1.5	±1.5
L3/offline correlation	9.5	-	-	-
Energy loss ±10 MeV/c	9.6	±6.4	±3.1	-
Dalitz Decay	11.3	±0.6	±0.6	±0.6
Total systematic uncertainty		±12.6	±11.0	±11.9

Table 11.6: The D^+ meson trigger and reconstruction efficiencies and systematic uncertainties. The total systematic error is calculated by adding all individual components in quadrature.

$D^+ \to K^-\pi^+\pi^+$				
p_T [GeV/c]		10-12	12-20	≥ 20
$\epsilon(D^+)$ [10^{-3}]		14.2	18.7	18.8
Relative statistical error [%]		±1.5	±1.5	±1.4
Systematic sources	Section	relative uncertainty [%]		
D^+ lifetime $\pm 1\sigma$	11.1	±1.7	±1.7	±1.7
Transverse beam spot size $\pm 2\,\mu$m	9.1	-	-	-
Luminous region $p_{T,min} = 0.5/2.0\,$GeV/c	9.2	±3.4	±3.4	±3.4
Luminous region ±1 cm	9.2	±1.7	±1.7	±1.7
p_T reweight $\pm 1\sigma$	11.4	-	-	-
Decay inside COT	9.8	±1.3	±1.3	±1.3
Hadronic interaction ±28%	9.8	±3.8	±3.8	±3.8
COT efficiency stat	7.2	±0.5	±0.6	±0.6
COT efficiency merge	7.2	±1.2	±1.2	±1.2
COT efficiency ΔR	7.2	±0.9	±0.9	±0.9
COT efficiency hits	7.2	±2.1	±2.1	±2.1
XFT efficiency vs multiplicity	7.7	±1.0	±1.0	±1.0
XFT efficiency wide/default match	7.3	±0.6	±0.6	±0.6
XFT two-track efficiency	10.2	±1.8	±1.8	±1.8
XFT p_T resolution ±5 MeV/c	10.1	-	-	-
SVT efficiency correction	7.4	±4.0	±4.0	±4.0
SVT efficiency vs d_0	7.4	±1.9	±1.9	±1.9
SVT efficiency wide/default match	7.4	±1.0	±1.0	±1.0
SVT p_T resolution ±20 MeV/c	10.1	-	-	-
SVT two-track correlation ±10%	10.3	±9.8	±9.3	±9.6
SVX three-track correlation ±5%	10.4	±2.9	±2.9	±2.9
SVX/SVT d_0 correlation ±10%	8.3	±1.5	±1.5	±1.5
L3/offline correlation	9.5	-	-	-
Energy loss ±10 MeV/c	9.6	-	-	-
Dalitz Decay	11.3	±0.6	±0.6	±0.6
Total systematic uncertainty		±13.1	±12.8	±13.0

Table 11.7: The D^+ meson trigger and reconstruction efficiencies and systematic uncertainties. The total systematic error is calculated by adding all individual components in quadrature.

$D_s^+ \to \phi\pi^+, \phi \to K^-\pi^+$				
p_T [GeV/c]		6.0-8.0	8.0-10	10-12
$\epsilon(D_s^+)$ [10^{-3}]		0.31	3.35	5.67
Relative statistical error [%]		±2.1	±1.1	±1.6
Systematic source	Section	relative uncertainty [%]		
D_s^+ lifetime $\pm1\sigma$	11.1	±2.3	±2.3	±2.3
Transverse beam spot size $\pm2\,\mu$m	9.1	-	-	-
Luminous region $p_{T,min} = 0.5/2.0\,$GeV/c	9.2	±3.0	±3.0	±3.0
Luminous region ±1 cm	9.2	±0.2	±0.2	±0.2
p_T reweight $\pm1\sigma$	11.4	-	-	-
Decay inside COT	9.8	±1.9	±1.9	±1.9
Hadronic interaction ±28%	9.8	±3.2	±3.2	±3.2
COT efficiency stat	7.2	±0.5	±0.3	±0.5
COT efficiency merge	7.2	±0.9	±0.9	±0.9
COT efficiency ΔR	7.2	±1.2	±1.2	±1.2
COT efficiency hits	7.2	±2.1	±2.1	±2.1
XFT efficiency vs multiplicity	7.7	±1.0	±1.0	±1.0
XFT efficiency wide/default match	7.3	±0.6	±0.6	±0.6
XFT two-track efficiency	10.2	±2.2	±2.2	±2.2
XFT p_T resolution ±5 MeV/c	10.1	-	-	-
SVT efficiency correction	7.4	±4.0	±4.0	±4.0
SVT efficiency vs d_0	7.4	±2.2	±2.2	±2.2
SVT efficiency wide/default match	7.4	±1.0	±1.0	±1.0
SVT p_T resolution ±20 MeV/c	10.1	±1.4	±1.4	±1.4
SVT two-track correlation ±10%	10.3	±6.9	±6.7	±10.4
SVX three-track correlation ±5%	10.4	±3.1	±3.1	±3.1
SVX/SVT d_0 correlation ±10%	8.3	±3.5	±3.5	±3.5
L3/offline correlation	9.5	-	-	-
Energy loss ±10 MeV/c	9.6	±6.4	±2.4	-
Total systematic uncertainty		±13.2	±11.7	±14.0

Table 11.8: The D_s^+ meson trigger and reconstruction efficiencies and systematic uncertainties. The total systematic error is calculated by adding all individual components in quadrature.

$D_s^+ \to \phi\pi^+, \phi \to K^-\pi^+$			
p_T [GeV/c]		12-20	≥ 12
$\epsilon(D_s^+)$ [10^{-3}]		6.61	6.69
Relative statistical error [%]		±1.9	±1.8
Systematic source	Section	relative uncertainty [%]	
D_s^+ lifetime $\pm 1\sigma$	11.1	±2.3	±2.3
Transverse beam spot size $\pm 2\,\mu$m	9.1	-	-
Luminous region $p_{T,min} = 0.5/2.0\,$GeV/c	9.2	±3.0	±3.0
Luminous region ±1 cm	9.2	±0.2	±0.2
p_T reweight $\pm 1\sigma$	11.4	-	-
Decay inside COT	9.8	±1.9	±1.9
Hadronic interaction ±28%	9.8	±3.2	±3.2
COT efficiency stat	7.2	±0.9	±0.9
COT efficiency merge	7.2	±0.9	±0.9
COT efficiency ΔR	7.2	±1.2	±1.2
COT efficiency hits	7.2	±2.1	±2.1
XFT efficiency vs multiplicity	7.7	±1.0	±1.0
XFT efficiency wide/default match	7.3	±0.6	±0.6
XFT two-track efficiency	10.2	±2.2	±2.2
XFT p_T resolution ±5 MeV/c	10.1	-	-
SVT efficiency correction	7.4	±4.0	±4.0
SVT efficiency vs d_0	7.4	±2.2	±2.2
SVT efficiency wide/default match	7.4	±1.0	±1.0
SVT p_T resolution ±20 MeV/c	10.1	±1.4	±1.4
SVT two-track correlation ±10%	10.3	±10.7	±10.5
SVX three-track correlation ±5%	10.4	±3.1	±3.1
SVX/SVT d_0 correlation ±10%	8.3	±3.5	±3.5
L3/offline correlation	9.5	-	-
Energy loss ±10 MeV/c	9.6	-	-
Total systematic uncertainty		±14.2	±14.2

Table 11.9: The D_s^+ meson trigger and reconstruction efficiencies and systematic uncertainties. The total systematic error is calculated by adding all individual components in quadrature.

The efficiency for the $D^0 \to K^-\pi^+$ increases from about 3.2 to 9.3×10^{-3} between a p_T of 5.5 and 20 GeV/c. This increase is mostly due to the higher probability of the decay daughters to satisfy the 2 GeV/c SVT threshold.

The D^* has a significantly smaller efficiency than the D^0, especially for the low-p_T bins. This can be explained by the effect of the 500 MeV/c requirement on the slow pion, which causes a large loss of efficiency for D^{*+} with low p_T. In the highest-p_T bin the efficiency for D^{*+} is almost equal to the D^0 efficiency.

The efficiency for $D^+ \to K^-\pi^+\pi^+$ varies strongly with p_T: At low p_T, the efficiency is lower than for $D^0 \to K^-\pi^+$, since the energy is spread over three tracks instead of two. For the highest p_T bin, the long lifetime of the D^+ contributes to the high fraction of tracks with a significant impact parameter, and results in an efficiency that is twice as high as for D^0.

The $D_s \to \phi\pi^+$ decay has the lowest efficiency of all, since it is a three-body decay and suffers from a short lifetime. On top of that, we require that one pion and one kaon are SVT tracks, leaving only one possible track combination to trigger on. The 6-8 GeV/c p_T bin in Table 11.8 has such a low efficiency that we decide not to use it in the analysis.

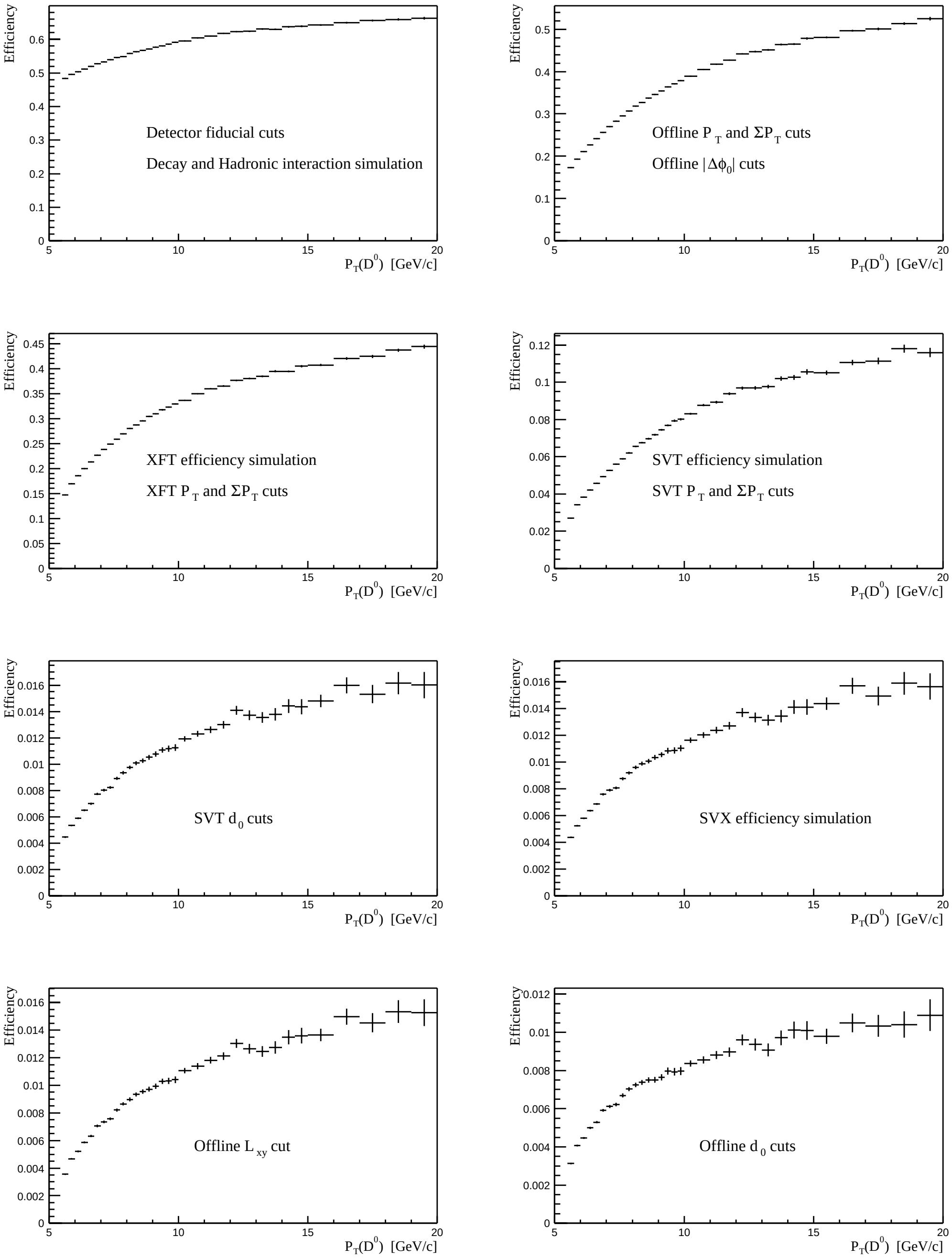

Figure 11.6: The D^0 trigger and reconstruction efficiency after various selections from Monte Carlo simulation.

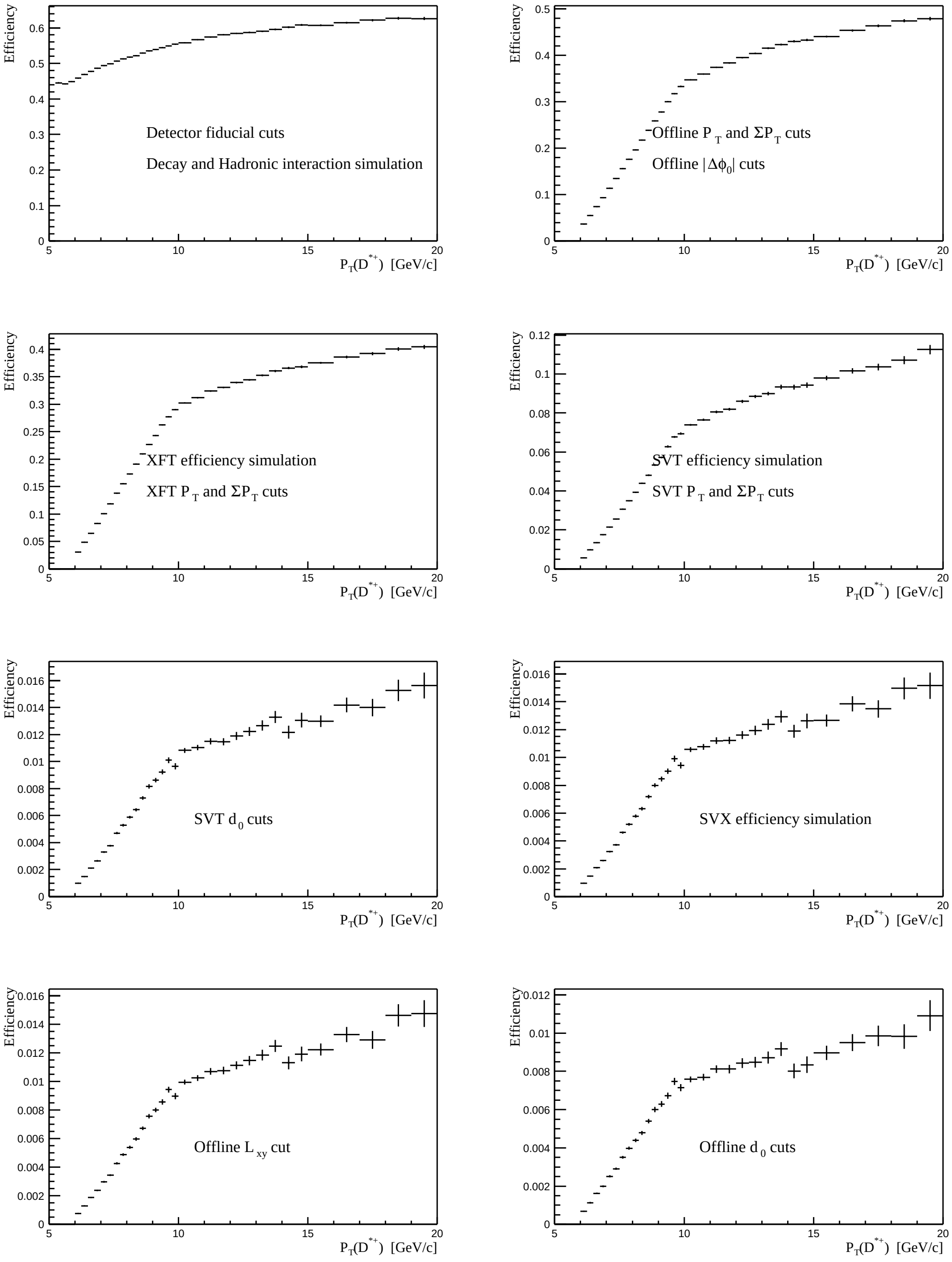

Figure 11.7: The D^{*+} trigger and reconstruction efficiency after various selections from Monte Carlo simulation.

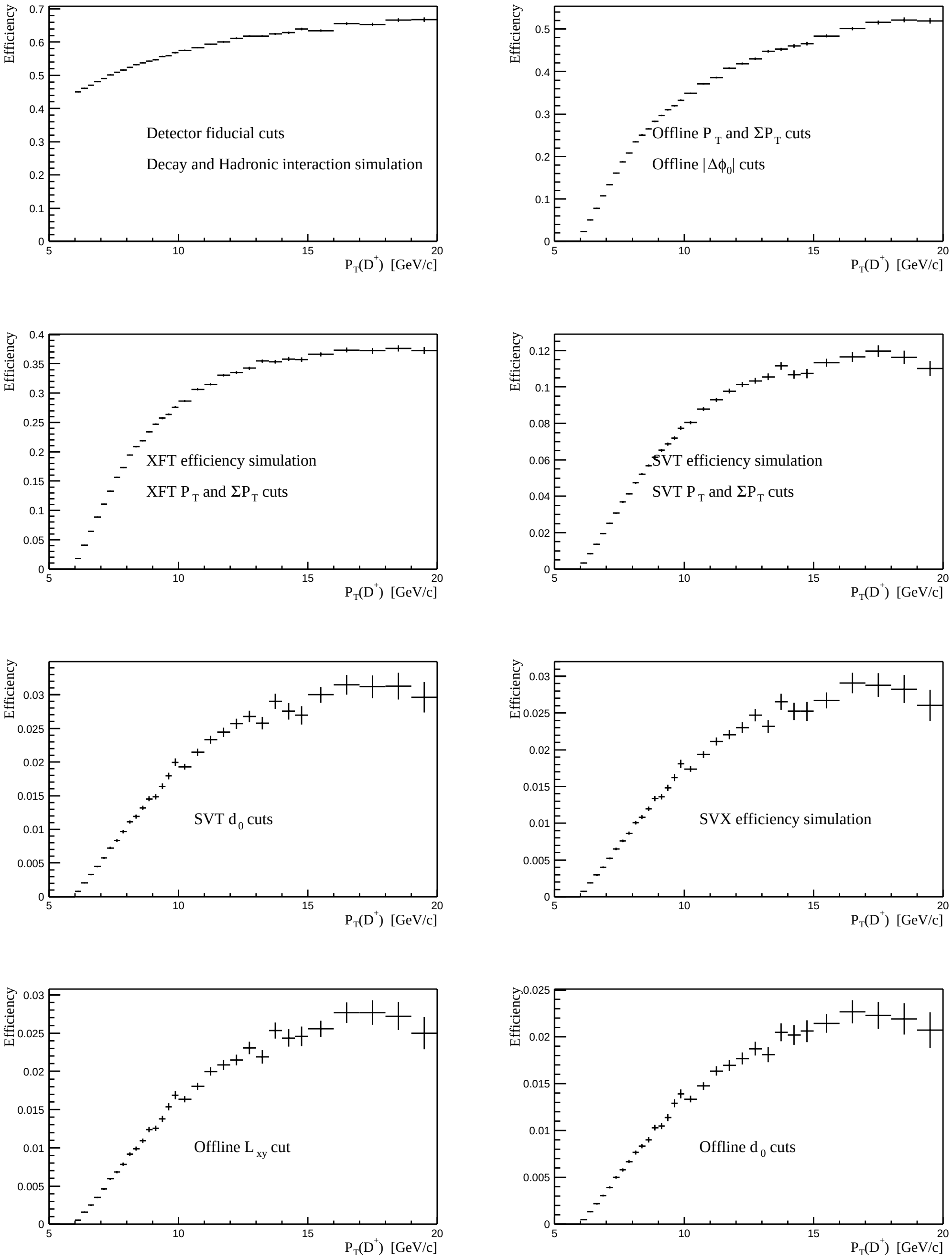

Figure 11.8: The D^+ trigger and reconstruction efficiency after various selections from Monte Carlo simulation.

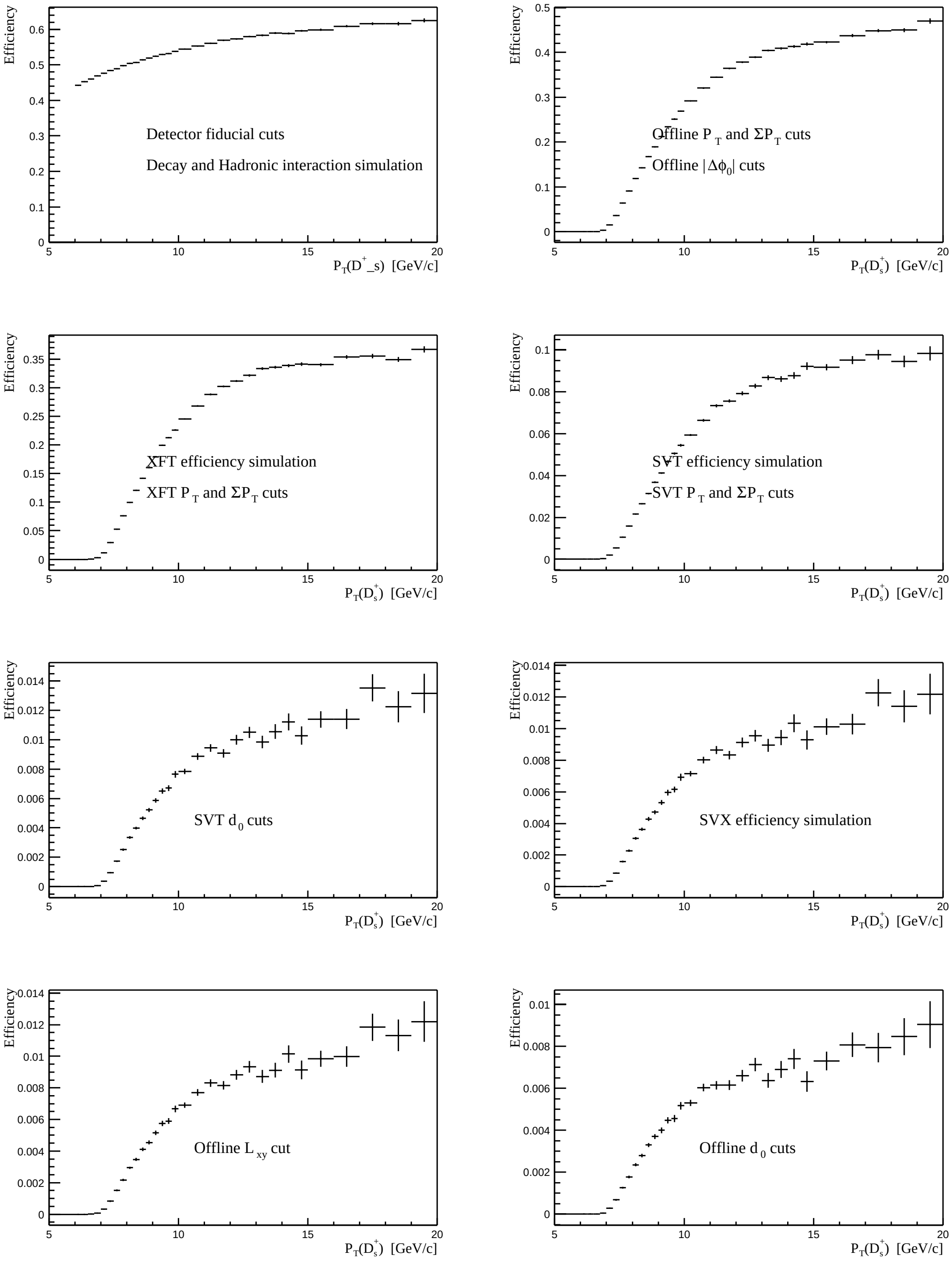

Figure 11.9: The D_s^+ trigger and reconstruction efficiency after various selections from Monte Carlo simulation.

11.8 Data and Monte Carlo Comparison

To further test our simulation, the sideband subtracted D meson p_T, z_0, L_{xy}, and ct distributions are compared with the corresponding Monte Carlo predictions. The definition of the signal and sideband region and the treatment of the autoreflection of the D^0 is the same as was used in Section 11.4 for determining the p_T reweight factors.

As shown in Figure 11.10 and 11.11, good agreement has been achieved. Note that the data/MC comparison of the p_T spectrum is not a test of the MC. Since we applied a reweight factor to the MC data and MC must agree by construction. The comparison does show, however, that no further iterations of the reweighting procedure are needed.

During our signal reconstruction, we apply track impact parameter requirements on both the online impact parameter measured with the SVT, and the offline impact parameter. Although they are correlated, we expect a significant inefficiency. In Figure 11.12, we compare the ratio of charm yields if we apply the default offline selection of 120 μm on d_0, compared to not applying offline requirements on d_0, and find no disagreement. This is a cross-check of our description of the resolution of the SVT impact parameter, and in particular its correlation with the SVX resolution. We further test this by tightening the offline requirements beyond the default values:

In Figures 11.13 we compare the charm yield for d_0 requirements of $150\,\mu$m and $200\,\mu$m to no offline requirements. Note that for the D^0 the tighter d_0 selection has a stronger effect on data than on MC. This can be explained by the absence of secondary D^0 in the MC. The apparent lifetime of secondary D^0 is longer than for prompt D^0, as shown in Figure 6.8.

Another interesting distribution is the decay angle of the π_s^+ in the center of mass frame of the D^{*+}, shown in Figure 11.14. This distribution is very sensitive to the tracking efficiency close to the $500\,\mathrm{MeV}/c$ p_T threshold. We also do a data/MC comparison of the decay angle between the D^0 flight direction and the K^- in the center of mass frame of the D^0, as shown in Figure 11.15. For this comparison we use D^0's from D^{*+} decay; for the inclusive D^0 decays the auto reflection gives a strong bias to this distribution. Note the asymmetry in Figure 11.15: the trigger efficiency for kaons boosted backward is higher than for pions.

In Figure 11.16 we compare the Dalitz-plot for $D^+ \to K^-\pi^+\pi^+$ observed in data and MC. Sideband subtraction is non-trivial for Dalitz-plots (the sidebands have a different size of the kinematically allowed space in the Dalitz-plot), so we won't make a quantitative comparison here, but do note that the MC reproduces the main features seen in data. Also shown is the reconstruction and trigger efficiency over the Dalitz-space. It is clearly non-uniform and tends to be low right where the decay probability is highest (compare with Figure 11.1).

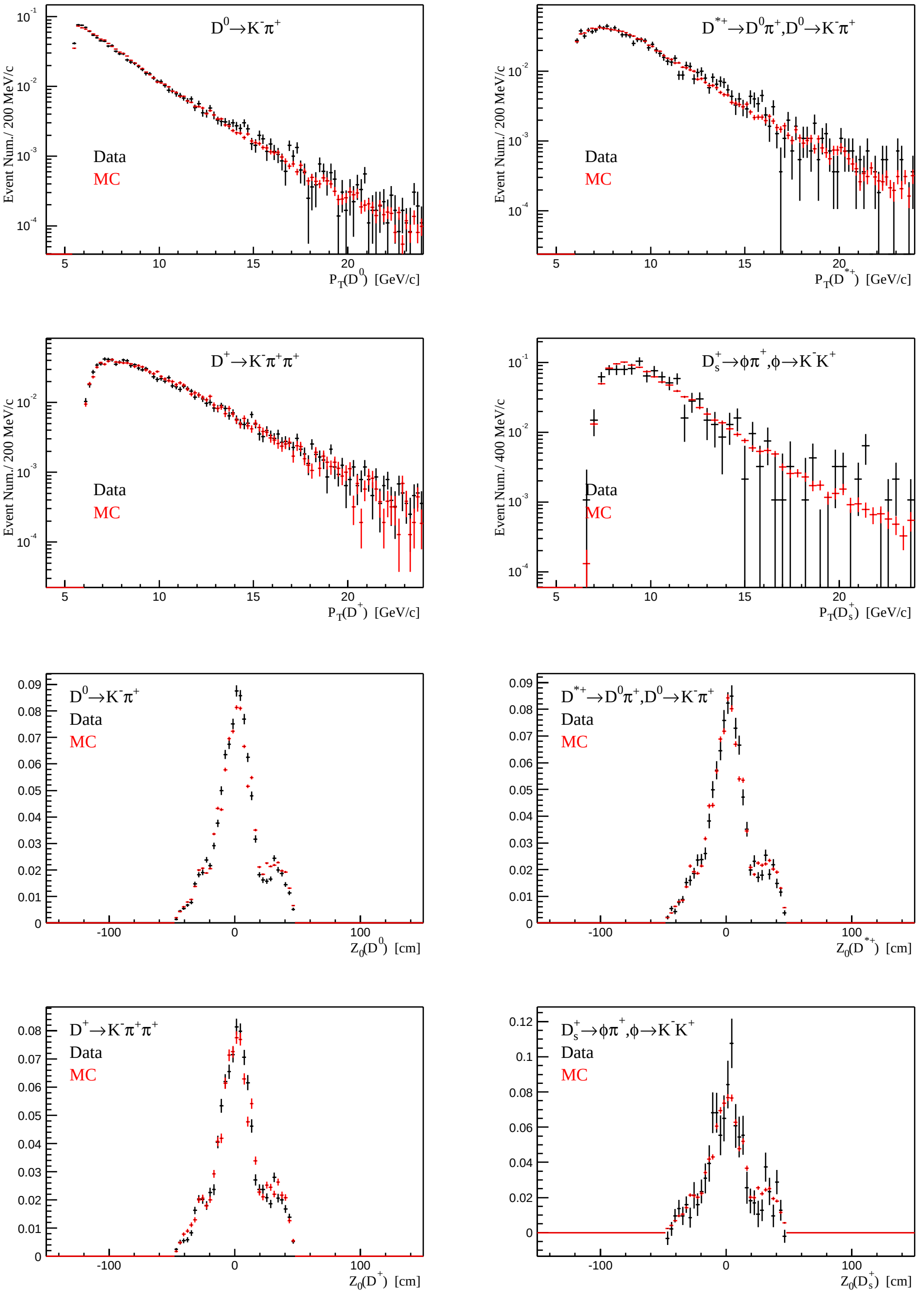

Figure 11.10: Comparison of normalized D meson p_T and z_0 distribution from data and Monte Carlo simulation, where we assume that the secondary D fractions are: $f_B(D^0) = 14\%$, $f_B(D^{*+}) = 12\%$, $f_B(D^+) = 12\%$, and $f_B(D_s^+) = 30\%$.

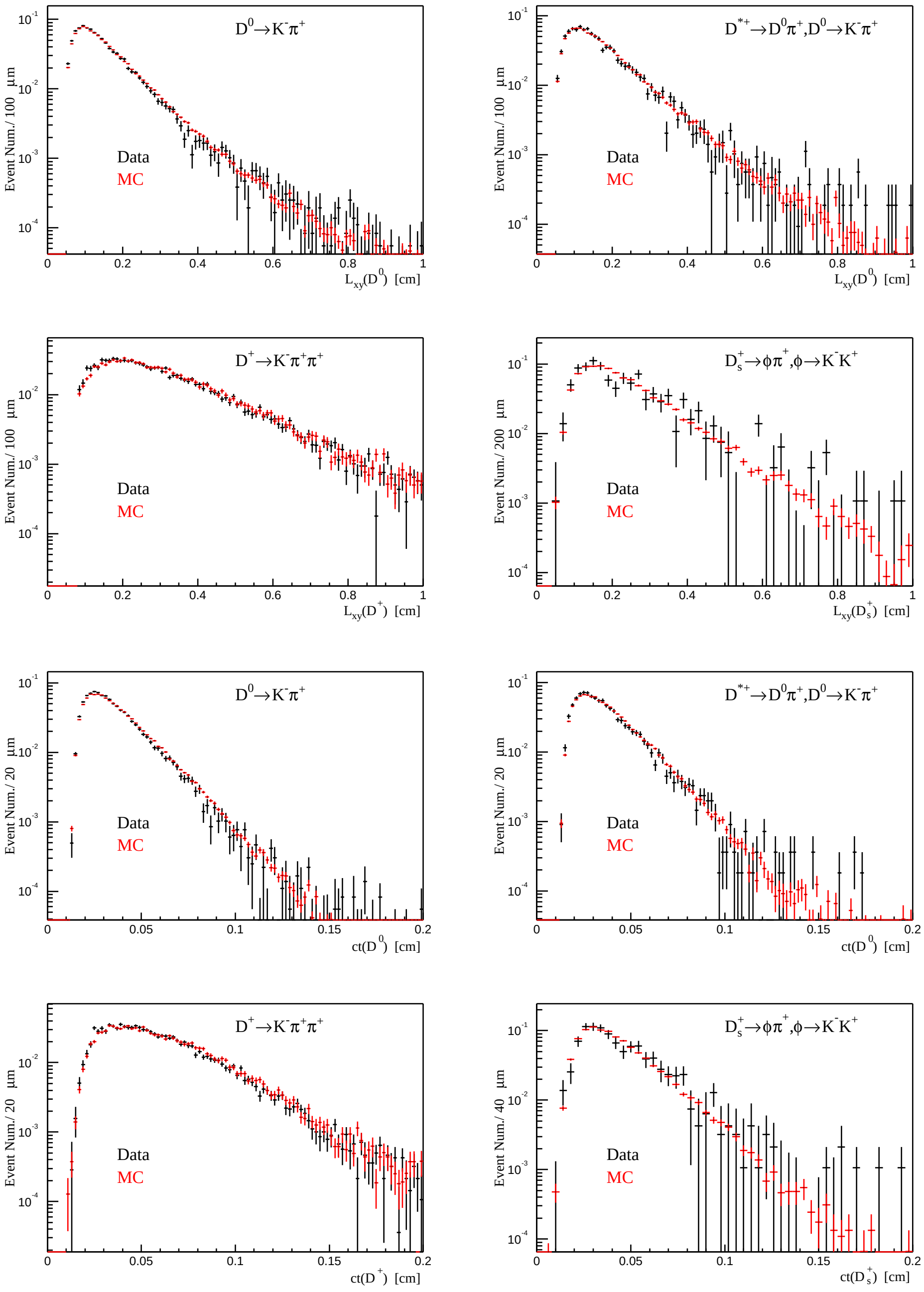

Figure 11.11: Comparison of normalized D meson L_{xy} and ct distribution from data and Monte Carlo simulation, where we assume that the secondary D fractions are: $f_B(D^0) = 14\%$, $f_B(D^{*+}) = 12\%$, $f_B(D^+) = 12\%$, and $f_B(D_s^+) = 30\%$.

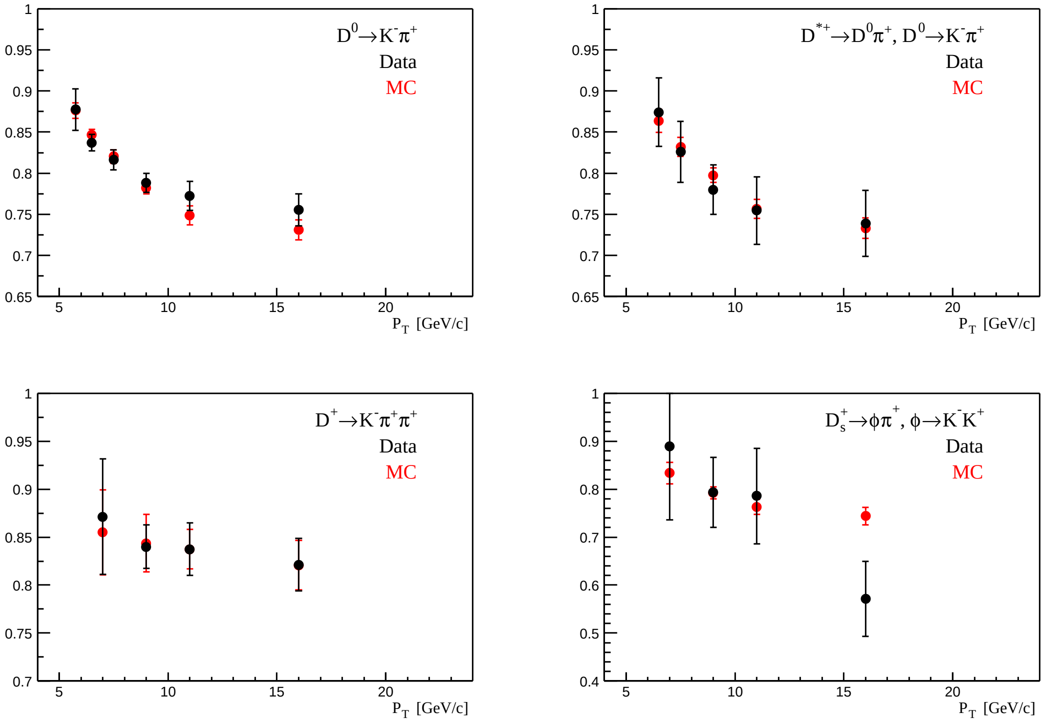

Figure 11.12: The ratio between the D meson yields with and without offline d_0 requirements from Monte Carlo simulation (prompt D only) and data.

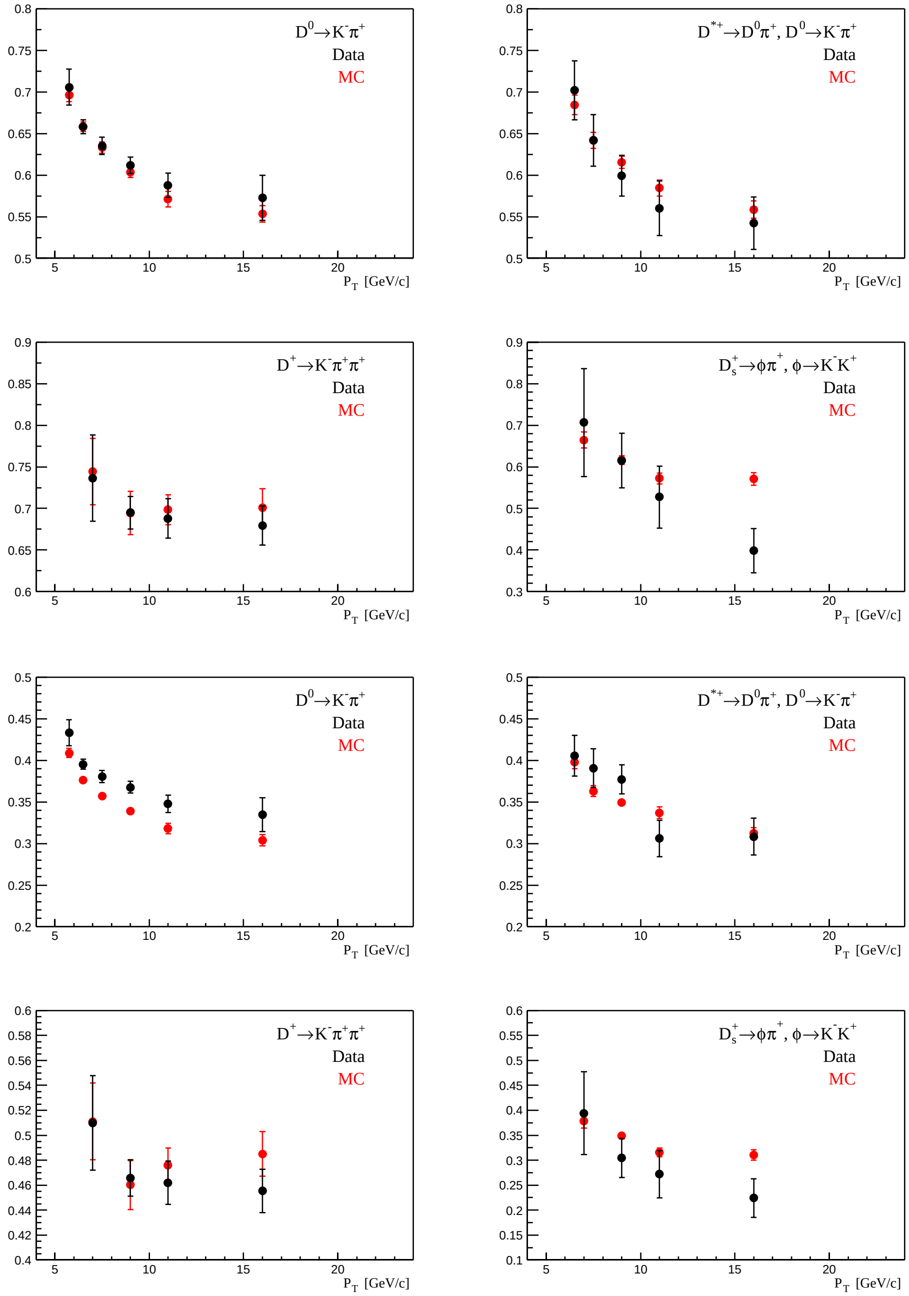

Figure 11.13: The ratio between the D meson yields with tight offline impact parameter requirements (150 μm in the upper four plots and 200 μm in the lower four plots) and no offline impact parameter requirement for MC (prompt D only) and data.

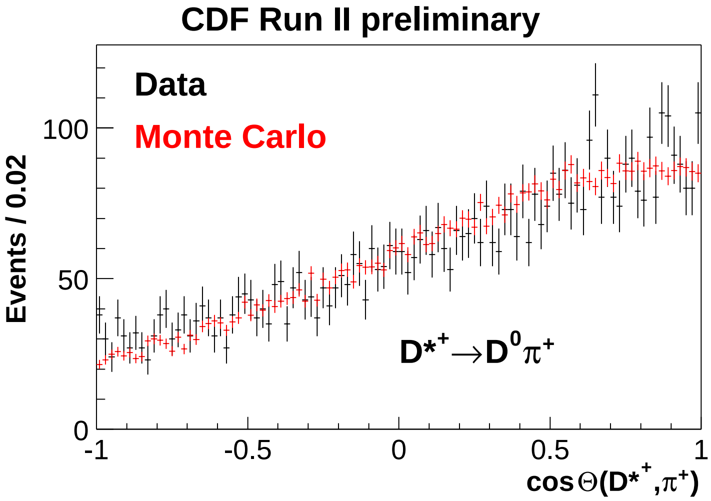

Figure 11.14: Data/MC comparison of the angle between the D^{*+} flight direction and the direction of the π_s^+ in the D^{*+} center of mass frame. Here we assume the secondary D^{*+} fraction is $f_B(D^{*+}) = 12\%$.

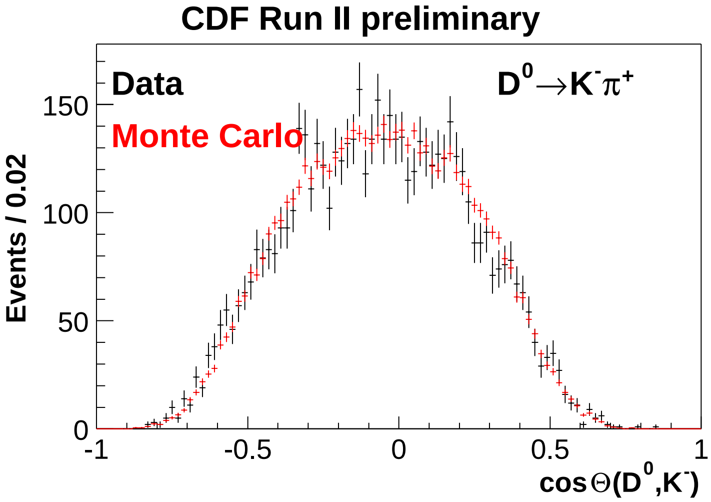

Figure 11.15: Data/MC comparison of the angle between the D^0 flight direction and the direction of the K^- in the D^0 center of mass frame. For this plot we only used D^0's from D^{*+} decay for which there is no ambiguity of the mass assignment. Here we assume the secondary D^{*+} fraction is $f_B(D^{*+}) = 12\%$.

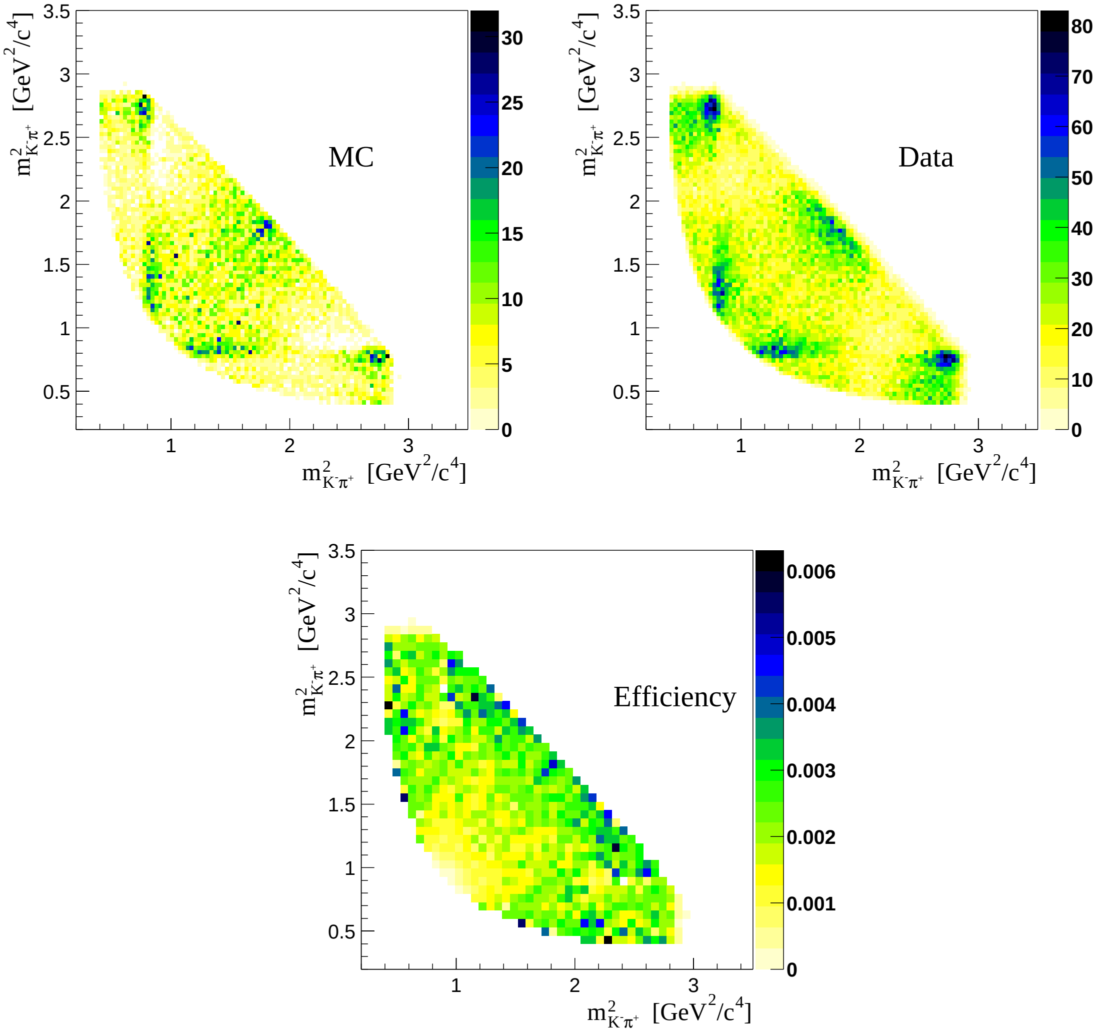

Figure 11.16: Dalitz-plot of the $D^+ \rightarrow K^-\pi^+\pi^+$ decay in MC (left) and data (right). No background subtraction has been applied to data. The lower plot shows the non-uniformity of the trigger and reconstruction efficiency over the allowed Dalitz-space.

11.9 Systematic Uncertainties

Systematic uncertainties have been evaluated by repeating the efficiency calculation with different assumptions, and evaluating the difference with the central efficiency calculation. Whenever possible, we averaged the effect of a 1σ 'up' shift and a one σ 'down' shift. Since the calculation is based on a large but finite MC sample, the systematic uncertainty calculation is somewhat affected by the statistical uncertainty of the MC sample. Therefore, some systematic uncertainties that are expected to be equal for all charm types may differ in practice by several permille, since they have been calculated on independent samples.

The systematic uncertainties from different contributions for D meson efficiency are summarized in Tables 11.2 to 11.8. For those systematic uncertainties where we expect and observe little variation with p_T, we use the averaged variation over all the p_T bins as the systematic error. We also ignore the systematic uncertainties that are at least 10 times smaller than the largest systematic contribution, since their contribution to the total systematic uncertainty is negligible, and their calculation is affected by the statistical uncertainty if the MC sample.

The sources of systematic uncertainties have already been described in previous sections are not repeated here. Tables 11.2 to 11.8 contain a column for each source of systematic uncertainty that refers to the section where it has been discussed.

The largest sources of systematic uncertainty are the COT tracking efficiency and the two-track correlation of the SVT efficiency. Also we find the systematic uncertainties on 3-track modes larger than on two-track modes. The systematic uncertainty due to the track ionization energy is significant only in the low-p_T bins.

Chapter 12

Cross Section Results

12.1 Integrated Cross Section

The integrated cross section σ_i in each p_T bin i is calculated using the following equation:

$$\sigma_i = \frac{N_i/2 \cdot f_{D,i}}{\mathcal{L} \cdot \epsilon_i \cdot \mathrm{Br}} \tag{12.1}$$

where N_i is the number of charm mesons obtained from the mass distribution in each p_T bin, $f_{D,i}$ is the fraction of the direct charm in that bin, and ϵ_i is the trigger and reconstruction efficiency per bin. The (offline) integrated luminosity of the data sample we used is $5.801\,\mathrm{pb}^{-1}$. The systematic uncertainty on the CDF luminosity is ±6.0% [96, 97] (4.4% from the CLC acceptance, 4% from the total inelastic cross section). The factor of 1/2 is included because we count both D and $\overline{D}$ mesons while we report the cross section for D mesons and not for the sum of D and $\overline{D}$. What is actually measured is the averaged cross section for D and $\overline{D}$ mesons, and we assume charge invariance in the production process. We use the following world averaged [26] values of the decay branching ratios:

$$\begin{aligned}
\mathrm{Br}(D^0 \to K^-\pi^+) &= 3.80 \pm 0.09\% \\
\mathrm{Br}(D^0 \to K^+\pi^-) &= (1.48 \pm 0.21) \times 10^{-4} \\
\mathrm{Br}(D^{*+} \to D^0\pi^+) &= 67.7 \pm 0.5\% \\
\mathrm{Br}(D^+ \to K^-\pi^+\pi^+) &= 9.1 \pm 0.6\% \\
\mathrm{Br}(D_s^+ \to \phi\pi^+) &= 3.6 \pm 0.9\% \\
\mathrm{Br}(\phi \to K^-K^+) &= 49.2^{+0.6}_{-0.7}\%
\end{aligned} \tag{12.2}$$

Since no particle ID is used in our signal reconstruction, when we reconstruct $D^0 \to K^-\pi^+$, we also select the double Cabibbo suppressed decay $\bar{D}^0 \to K^-\pi^+$. In the D^0 cross section calculation, the branching ratio is therefore the sum of both decay channels. The integrated charm meson cross sections are listed in Table 12.1. The corresponding rapidity range is $|y| \leq 1$.

We report two versions of the highest p_T bin: one that has an upper limit on p_T, which is used for the differential cross section, and one that is open ended, for the integrated cross section.

The integrated cross section for charm mesons with minimum transverse momentum p_T^{min} and $|y| \leq 1.0$ is given by:

$$\sigma(p_T(D) \geq \; p_T^{min}, |y| \leq 1) = \sum_{p_T \geq p_T^{min}} \sigma_i, \tag{12.3}$$

where the open ended version of the highest p_T bin is used. The total statistical uncertainty is the sum in quadrature of the statistical error in each bin, and the systematic uncertainties have been summed linearly, since they are fully correlated between the different p_T bins. The results are listed in Table 12.1.

12.2 Differential Cross Section

We choose to report the differential cross section $\frac{d\sigma}{dp_T}$ at the center of each bin. Since in general the second derivative of the differential cross section is non-zero, the average differential cross section in a bin $\sigma_i/\Delta p_T$ differs from the value at the center of the bin. We correct for this using a bin center correction, which is calculated as follows:

$$\frac{d\sigma}{dp_T} = \frac{\sigma((p_T^{max} + p_T^{min})/2)}{\frac{1}{p_{max} - p_{min}} \int_{p_T^{min}}^{p_T^{max}} \sigma(p_T) dp_T} \cdot \frac{\sigma_i}{p_T^{max} - p_T^{min}}, \tag{12.4}$$

where p_T^{max} and p_T^{min} are the bin boundaries. For calculating the integral we use the charm meson p_T spectrum from MC, reweighted to give a better description of the data. This reweighting procedure has been described in [84]. The calculated values of the bin center correction are shown in Tables 12.3. The bin center correction is smaller than 5%, except for the highest p_T bin, where the correction is typically

35%. To evaluate the systematic uncertainty due to the charm meson p_T spectrum, we vary the p_T spectrum shape parameter by $\pm 1\sigma$. The observed variations are negligible except for the highest p_T bin, where the bin center correction varies by about 1% for D^0, D^{*+}, D^+, and 5% for D_s^+. The measured differential cross sections at the center of each p_T bin are listed in the Table 12.2 and Figures 12.1, 12.2, 12.3 and 12.4.

12.3 Comparison with the Theory

12.3.1 D meson Production Ratio

It is possible to interpret the ratios of D^0, D^{*+}, D^+ cross-sections in terms of the ratio of vector (V) to pseudo-scalar (P) production, taking into account the feeddown from vector states to pseudoscalar states.

Under mild model assumptions, two independent measurements $\varepsilon \equiv \frac{V}{V+P}$ can be extracted from the measured ratios, and the comparison can serve as a consistency check.

Assuming that the direct production of D^0 and D^+ are equal and the D^{*0} production is equal to the D^{*+} cross section, which are expected valid under SU(2) flavor symmetry at high energies, the naive spin counting predicts that $\varepsilon = 0.75$.

p_T [GeV/c]	σ [nb]	$\sigma(p_T(D^0) \geq p_T^{min}, \lvert y\rvert \leq 1)$ [nb]
$5.5-6.0$	$3943 \pm 111 \pm 445$	$13250 \pm 172 \pm 1508$
$6.0-7.0$	$4146 \pm 95 \pm 451$	$9307 \pm 131 \pm 1064$
$7.0-8.0$	$2090 \pm 59 \pm 231$	$5161 \pm 90 \pm 613$
$8.0-10.0$	$1886 \pm 54 \pm 227$	$3071 \pm 68 \pm 382$
$10.0-12.0$	$682 \pm 32 \pm 86$	$1186 \pm 42 \pm 154$
$12.0-20.0$	$472 \pm 27 \pm 63$	$503 \pm 28 \pm 68$

p_T [GeV/c]	σ [nb]	$\sigma(p_T(D^{*+}) \geq p_T^{min}, \lvert y\rvert \leq 1)$ [nb]
$6.0-7.0$	$2477 \pm 110 \pm 434$	$5159 \pm 127 \pm 774$
$7.0-8.0$	$1169 \pm 48 \pm 148$	$2682 \pm 63 \pm 341$
$8.0-10.0$	$905 \pm 33 \pm 115$	$1513 \pm 41 \pm 193$
$10.0-12.0$	$309 \pm 17 \pm 38$	$608 \pm 23 \pm 78$
$12.0-20.0$	$282 \pm 15 \pm 38$	$299 \pm 16 \pm 40$

p_T [GeV/c]	σ [nb]	$\sigma(p_T(D^{+}) \geq p_T^{min}, \lvert y\rvert \leq 1)$ [nb]
$6.0-7.0$	$2005 \pm 71 \pm 340$	$4338 \pm 79 \pm 721$
$7.0-8.0$	$1005 \pm 29 \pm 159$	$2334 \pm 36 \pm 381$
$8.0-10.0$	$795 \pm 18 \pm 131$	$1329 \pm 21 \pm 223$
$10.0-12.0$	$284 \pm 9 \pm 49$	$534 \pm 11 \pm 92$
$12.0-20.0$	$222 \pm 7 \pm 38$	$250 \pm 7 \pm 43$

p_T [GeV/c]	σ [nb]	$\sigma(p_T(D_s^{+}) \geq p_T^{min}, \lvert y\rvert \leq 1)$ [nb]
$8.0-10.0$	$505 \pm 43 \pm 143$	$751 \pm 50 \pm 216$
$10.0-12.0$	$134 \pm 19 \pm 40$	$246 \pm 25 \pm 72$
$12.0-20.0$	$117 \pm 15 \pm 35$	$112 \pm 16 \pm 33$

Table 12.1: Summary of the measured direct charm meson cross sections and their uncertainties in different p_T bins. The first error is statistical and the second systematic.

p_T [GeV/c]	$d\sigma(D^0, \|y\| \leq 1)/dp_T$ [nb/(GeV/c)]
5.75	$7837 \pm 220 \pm 884$
6.5	$4056 \pm 93 \pm 441$
7.5	$2052 \pm 58 \pm 227$
9.0	$890 \pm 25 \pm 107$
11.0	$327 \pm 15 \pm 41$
16.0	$39.9 \pm 2.3 \pm 5.3$

p_T [GeV/c]	$d\sigma(D^{*+}, \|y\| \leq 1)/dp_T$ [nb/(GeV/c)]
6.5	$2421 \pm 108 \pm 424$
7.5	$1147 \pm 48 \pm 145$
9.0	$427 \pm 16 \pm 54$
11.0	$148 \pm 8 \pm 18$
16.0	$23.8 \pm 1.3 \pm 3.2$

p_T [GeV/c]	$d\sigma(D^+, \|y\| \leq 1)/dp_T$ [nb/(GeV/c)]
6.5	$1961 \pm 69 \pm 332$
7.5	$986 \pm 28 \pm 156$
9.0	$375 \pm 9 \pm 62$
11.0	$136 \pm 4 \pm 24$
16.0	$19.0 \pm 0.6 \pm 3.2$

p_T [GeV/c]	$d\sigma(D_s^+, \|y\| \leq 1)/dp_T$ [nb/(GeV/c)]
9.0	$236 \pm 20 \pm 67$
11.0	$64 \pm 9 \pm 19$
16.0	$9.0 \pm 1.2 \pm 2.7$

Table 12.2: Summary of the measured direct charm meson differential cross sections and their uncertainties at the center of each p_T bin. The first error is statistical and the second systematic.

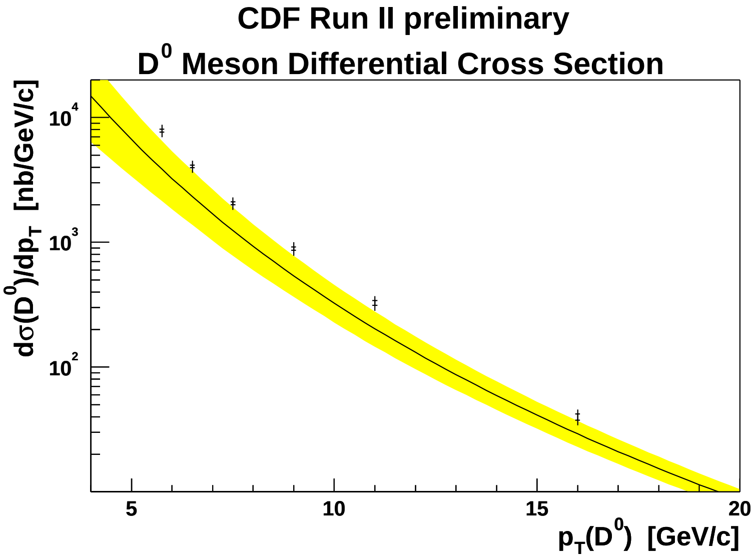

Figure 12.1: D^0 meson differential cross section. The inner error bar represents the statistical uncertainty, the outer error bar the quadratic sum of the statistical and systematic uncertainty.

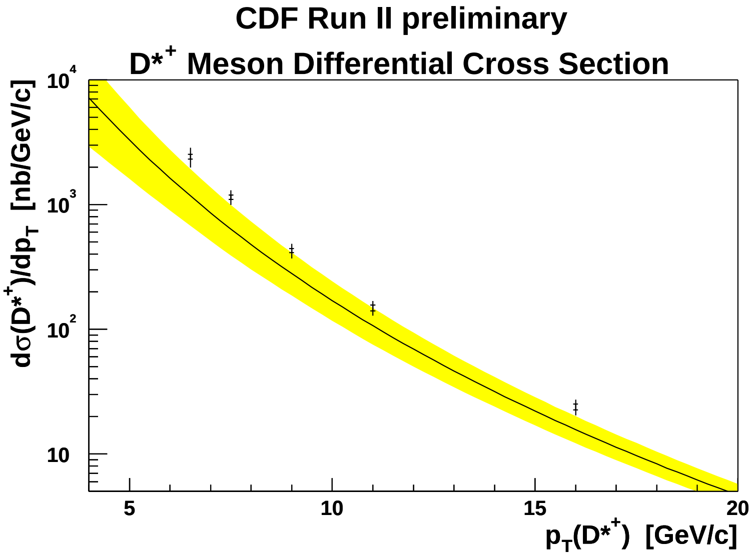

Figure 12.2: D^{*+} meson differential cross section. The inner error bar represents the statistical uncertainty, the outer error bar the quadratic sum of the statistical and systematic uncertainty.

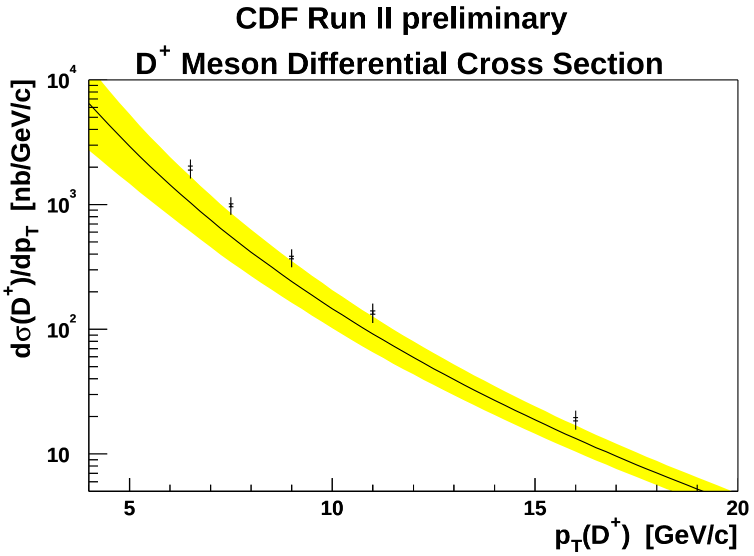

Figure 12.3: D^+ meson differential cross section. The inner error bar represents the statistical uncertainty, the outer error bar the quadratic sum of the statistical and systematic uncertainty.

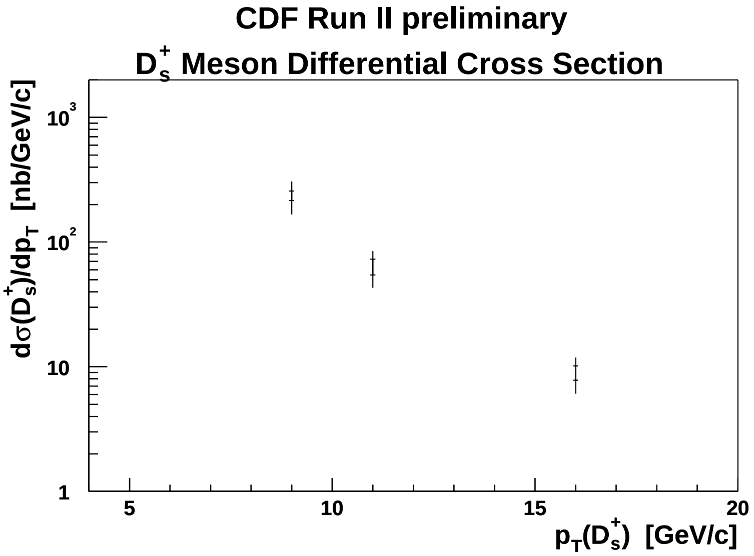

Figure 12.4: D_s^+ meson differential cross section. The inner error bar represents the statistical uncertainty, the outer error bar the quadratic sum of the statistical and systematic uncertainty.

<table>
<tr><td colspan="7">$D^0 \to K^-\pi^+$</td></tr>
<tr><td>p_T [GeV]</td><td>5.5- 6.0</td><td>6.0- 7.0</td><td>7.0- 8.0</td><td>8.0-10.0</td><td>10.0-12.0</td><td>12.0-20.0</td></tr>
<tr><td>$c_{bin}(\%)$</td><td>99.4</td><td>97.8</td><td>98.2</td><td>94.4</td><td>95.8</td><td>67.7</td></tr>
<tr><td>δc_{bin} - stat</td><td>-</td><td>-</td><td>-</td><td>-</td><td>-</td><td>0.5(0.7)</td></tr>
<tr><td colspan="7">$D^{*+} \to D^0(K^-\pi^+)\pi^+$</td></tr>
<tr><td>p_T [GeV]</td><td>6.0- 7.0</td><td>7.0- 8.0</td><td>8.0-10.0</td><td>10.0-12.0</td><td>12.0-20.0</td><td></td></tr>
<tr><td>$c_{bin}(\%)$</td><td>97.8</td><td>98.1</td><td>94.3</td><td>95.8</td><td>67.6</td><td></td></tr>
<tr><td>δc_{bin} - stat</td><td>-</td><td>-</td><td>-</td><td>-</td><td>0.7(1.1)</td><td></td></tr>
<tr><td colspan="7">$D^+ \to K^-\pi^+\pi^+$</td></tr>
<tr><td>p_T [GeV]</td><td>6.0- 7.0</td><td>7.0- 8.0</td><td>8.0-10.0</td><td>10.0-12.0</td><td>12.0-20.0</td><td></td></tr>
<tr><td>$c_{bin}(\%)$</td><td>97.8</td><td>98.2</td><td>94.4</td><td>95.9</td><td>68.2</td><td></td></tr>
<tr><td>δc_{bin} - stat</td><td>-</td><td>-</td><td>-</td><td>-</td><td>0.6(0.9)</td><td></td></tr>
<tr><td colspan="7">$D_s^+ \to \phi(K^-K^+)\pi^+$</td></tr>
<tr><td>p_T [GeV]</td><td>8.0-10.0</td><td>10.0-12.0</td><td>12.0-20.0</td><td></td><td></td><td></td></tr>
<tr><td>$c_{bin}(\%)$</td><td>93.6</td><td>94.8</td><td>61.4</td><td></td><td></td><td></td></tr>
<tr><td>δc_{bin} - stat</td><td>-</td><td>-</td><td>2.9(4.7)</td><td></td><td></td><td></td></tr>
</table>

Table 12.3: calculated values of the bin center correction for D mesons in different p_T bins. For the uncertainties, the number between parentheses is the relative uncertainty in %.

More detail theoretical calculations based on the string fragmentation approach [98] and the thermodynamical approach [99] yield the value 0.66 for ε. The experimental measurement from LEP [100] results in a value close to 0.6.

The D^{*+} and D^{*0} branching ratios to D^0 and D^+ are well known: $B(D^{*0} \to D^0 X) = 100\%$, $B(D^{*+} \to D^0 X) = 67.7\%$ and $B(D^{*+} \to D^+ X) = 32.3\%$. To simplify the equations, we use here $B(D^{*+} \to D^0 X) = 2/3$ and $B(D^{*+} \to D^+ X) = 1/3$. It then follows that

$$\varepsilon_0 = \left(\frac{\sigma(D^0)}{\sigma(D^{*+})} - \frac{2}{3}\right)^{-1}, \tag{12.5}$$

$$\varepsilon_+ = \left(\frac{\sigma(D^+)}{\sigma(D^{*+})} + \frac{2}{3}\right)^{-1}. \tag{12.6}$$

A caveat here is that these equations only hold for the total cross-sections, while we measure the cross-section at some p_T cut-off. In particular the vector states do not transfer all transverse momentum to the pseudoscalar particles, and Equations 12.5 and 12.6 need to be corrected to perform a measurement of ε.

Since we are more interested in a cross-check of the ratios than in the actual determination of ε, we use a generator-level Pythia $c\bar{c}$ MC to estimate the bias on ε when not correcting for the p_T cutoff. By default, Pythia generates 3 vector mesons for every pseudoscalar meson ($\varepsilon = 0.75$). We removed half the vector mesons, resulting in an effective value of 0.6 for ε. When applying Equations 12.5 and 12.6 on the Pythia MC, with a p_T cutoff of 6 GeV, we find $\varepsilon_0 = 0.88$ and $\varepsilon_+ = 0.66$.

We thus conclude that using a fixed p_T cutoff gives a significant upward bias to the determination on ε.

When we use Equations 12.5 and 12.6 with the measured cross sections for $p_T \geq 6\,\text{GeV}$, we find $\varepsilon_0 = 0.83$ and $\varepsilon_+ = 0.67$. These values are very close to the Pythia MC generated with $\varepsilon = 0.6$, and indicate that the measured ratio's of D^0, D^{*+} and D^+ behave as expected.

12.3.2 Differential Cross Section

In Figures 12.1 to 12.4 we compare the measured cross-section to calculations from Cacciari and Nason [101].

The predictions consist of a resummed perturbative calculation, called Fixed Order Next-to-Leading-Log (FONLL) [102]. The CTEQ6M [103] parton distribution set has been used and the value of Λ_{QCD} has been fixed at 0.226 GeV. The charm quark mass has been set to 1.5 GeV. The charm quark cross-section is convoluted with fragmentation functions that have been extracted from D^* measurements from the ALEPH collaboration [100]. For the central value calculation the renormalizaton and factorization scale have been set to $m_T = \sqrt{m_c^2 + p_T^2}$. The uncertainty has been evaluated by varying both scales to $0.5m_T$ and $2m_T$.

We find that the measured cross-sections are higher than the central value of the calculations, but the difference is not incompatible with the quoted theoretical and experimental uncertainties. For a more detailed comparison we plot the ratio of the measured to the calculated cross-section in Figure 12.5. We find similar trends for all three mesons that we have been given predictions for: at low p_T the measurements are higher than theory by 70-90%, while at high p_T the difference decreases to 30-40%.

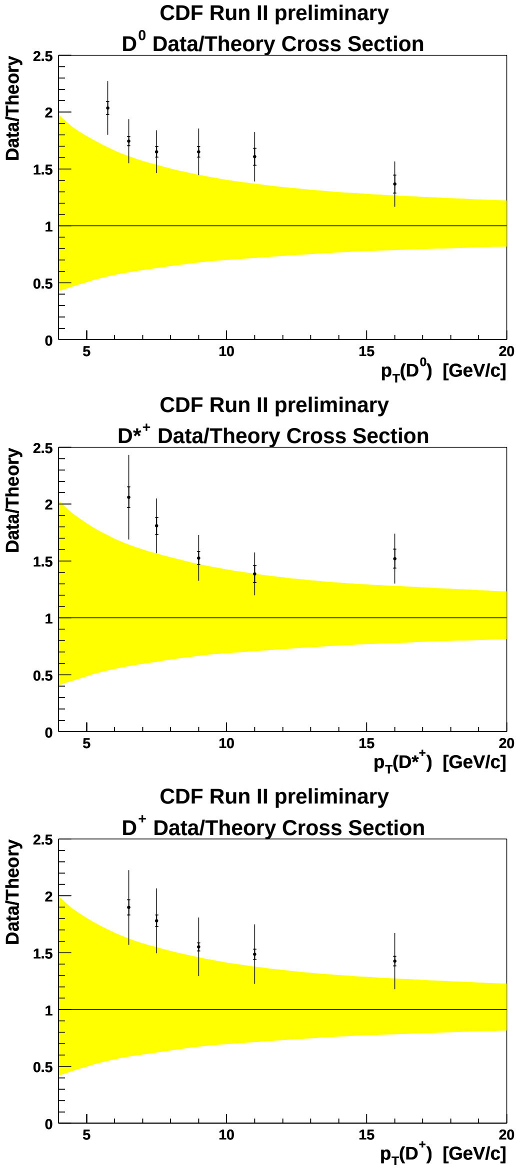

Figure 12.5: Ratio of the measured cross sections to the theoretical calculation from Cacciari and Nason. The inner error bar represents the statistical uncertainty, the outer error bar the quadratic sum of the statistical and systematic uncertainty. The yellow line represents the uncertainty from varying the renormalization and factorization scale.

Chapter 13

Conclusion

The direct charm meson production cross sections in $p\bar{p}$ collisions at $\sqrt{s} = 1.96\,\mathrm{TeV}$ have been measured at CDF using fully reconstructed decay modes: $D^0 \to K^-\pi^+$, $D^{*+} \to D^0(K^-\pi^+)\pi^+$, $D^+ \to K^-\pi^+\pi^+$, and $D_s^+ \to \phi(K^+K^-)\pi^+$ collected by the silicon vertex trigger. We present the cross section results for the rapidity range $|y| \leq 1.0$, both integrated over p_T and differential $d\sigma/dp_T$. We find that

$$\begin{array}{rcl} \sigma(D^0, p_T \geq 5.5\,\mathrm{GeV}/c) & = & 13.3 \pm 0.2 \pm 1.5\,\mu\mathrm{b}, \\ \sigma(D^{*+}, p_T \geq 6.0\,\mathrm{GeV}/c) & = & 5.2 \pm 0.1 \pm 0.8\,\mu\mathrm{b}, \\ \sigma(D^+, p_T \geq 6.0\,\mathrm{GeV}/c) & = & 4.0 \pm 0.1 \pm 0.7\,\mu\mathrm{b}, \\ \sigma(D_s^+, p_T \geq 8.0\,\mathrm{GeV}/c) & = & 0.75 \pm 0.05 \pm 0.22\,\mu\mathrm{b}, \end{array} \tag{13.1}$$

where the first error is statistical and the second systematic. Although the measured direct charm production cross sections are compatible with the theoretical calculation within less than two standard deviations, the experimental results of all four D mesons are consistently higher than the predictions by $80 - 90\,\%$ at low p_T, and $30 - 40\,\%$ at high p_T.

Using the silicon vertex trigger, CDF expects to have a date sample that contains an order of 10^7 fully reconstructed charm hadrons, as well as large amounts of hadronic B decays by the end of Run II. These statistics will push our heavy flavor program into the regime of precision physics. During this analysis, we performed detail studies of trigger and tracking systems that are crucial for the heavy flavor measurements. The knowledge and experience we gained through the charm meson cross section measurement will be a valuable foundation for future heavy flavor analysis at CDF.

Appendix A

Run List

```
run    start      store trigger luminosity: ini.  int.
                                         (10^30)(nb^-1)
138809 02/09 11:30  969 PHYSICS_0_04[5,260]  6.9  23.7
138811 02/09 12:59  969 PHYSICS_0_04[5,260]  6.4   8.8
138812 02/09 13:33  969 PHYSICS_0_04[5,260]  6.1   1.8
138815 02/09 14:23  969 PHYSICS_0_04[5,260]  6.0  14.3
138816 02/09 15:16  969 PHYSICS_0_04[5,260]  5.7   2.0
138818 02/09 15:35  969 PHYSICS_0_04[5,260]  5.6   6.0
138819 02/09 16:05  969 PHYSICS_0_04[5,260]  5.5  35.4
138820 02/09 18:24  969 PHYSICS_0_04[5,260]  4.8  17.3
138821 02/09 19:44  969 PHYSICS_0_04[5,260]  4.4   3.0
138822 02/09 20:03  969 PHYSICS_0_04[5,260]  4.4  19.8
138838 02/10 05:34  971 PHYSICS_0_04[5,260]  8.1  88.3
138839 02/10 09:31  971 PHYSICS_0_04[5,260]  6.1  49.8
138842 02/10 12:36  971 PHYSICS_0_04[5,260]  5.1   7.7
138860 02/10 18:31  973 PHYSICS_0_04[5,260]  8.5  76.1
138861 02/10 21:44  973 PHYSICS_0_04[5,260]  6.8  22.6
138863 02/10 23:09  973 PHYSICS_0_04[5,260]  6.1  29.7
138865 02/11 03:03  973 PHYSICS_0_04[5,260]  4.7   9.3
138868 02/11 04:22  973 PHYSICS_0_04[5,260]  4.5   1.3
139157 02/14 08:46  990 PHYSICS_0_04[5,260]  5.0  24.9
139177 02/14 15:58  990 PHYSICS_0_04[7,263]  3.5  27.1
```

```
139207 02/15 09:20  992 PHYSICS_0_04[7,263]  4.4  42.1
139248 02/15 21:12  994 PHYSICS_0_04[7,263] 12.0  28.1
139253 02/16 03:08  994 PHYSICS_0_04[7,263]  7.6 123.8
139278 02/16 23:24  996 PHYSICS_0_04[7,263]  6.4  81.1
139298 02/17 12:16  998 PHYSICS_0_04[7,263]  6.2  28.5
139299 02/17 14:03  998 PHYSICS_0_04[7,263]  5.5  37.4
139335 02/18 01:37 1000 PHYSICS_0_04[7,263]  8.6  11.0
139338 02/18 05:38 1000 PHYSICS_0_04[7,263]  6.7  60.0
139339 02/18 08:42 1000 PHYSICS_0_04[7,263]  6.0   8.3
139368 02/18 19:41 1002 PHYSICS_1_01[1,265]  8.2  16.4
139369 02/18 20:24 1002 PHYSICS_0_04[7,263]  8.3  30.3
139370 02/18 21:52 1002 PHYSICS_1_01[1,265]  7.5  19.5
139371 02/18 22:53 1002 PHYSICS_1_01[1,265]  7.2  23.4
139375 02/19 01:38 1002 PHYSICS_1_01[1,265]  6.0  78.3
139383 02/19 07:39 1002 PHYSICS_1_01[1,265]  4.7   3.2
139775 02/24 07:47 1018 PHYSICS_1_01[1,266]  7.6   6.4
139776 02/24 08:22 1018 PHYSICS_1_01[1,266]  7.2   2.7
139778 02/24 09:08 1018 PHYSICS_1_01[1,266]  6.3   7.4
139780 02/24 09:44 1018 PHYSICS_1_01[1,266]  6.3   1.5
139781 02/24 09:54 1018 PHYSICS_1_01[1,266]  6.2  11.0
139782 02/24 10:36 1018 PHYSICS_1_01[1,266]  5.9   3.7
139783 02/24 11:04 1018 PHYSICS_1_01[1,266]  5.8  39.3
139785 02/24 13:40 1018 PHYSICS_1_01[1,266]  4.8   5.6
139786 02/24 14:20 1018 PHYSICS_1_01[1,266]  4.6  24.2
139787 02/24 16:02 1018 PHYSICS_1_01[1,266]  4.2  17.7
139788 02/24 17:23 1018 PHYSICS_1_01[1,266]  3.9  13.2
139798 02/24 23:37 1020 PHYSICS_1_01[1,266]  5.9  24.6
139799 02/25 01:36 1020 PHYSICS_1_01[1,266]  4.3  56.9
139800 02/25 06:52 1020 PHYSICS_1_01[1,266]  3.2   0.9
139801 02/25 07:42 1020 PHYSICS_1_01[1,266]  3.0  18.8
139815 02/25 12:03 1020 PHYSICS_1_01[1,266]  2.3   1.3
139817 02/25 12:19 1020 PHYSICS_1_01[1,266]  2.3   4.0
139891 02/26 02:13 1023 PHYSICS_1_01[1,266]  7.9  27.9
139892 02/26 03:37 1023 PHYSICS_1_01[1,266]  7.1   5.5
139893 02/26 05:10 1023 PHYSICS_1_01[1,266]  6.1   7.1
139894 02/26 05:38 1023 PHYSICS_1_01[1,266]  6.2  14.6
139897 02/26 07:05 1023 PHYSICS_1_01[1,266]  5.7  50.6
139901 02/26 10:36 1023 PHYSICS_1_01[1,266]  4.8   6.4
140127 02/28 18:40 1036 PHYSICS_1_01[1,266] 12.0  77.9
140129 02/28 21:11 1036 PHYSICS_1_01[1,266]  9.4 175.9
140131 03/01 04:32 1036 PHYSICS_1_01[1,266]  6.1  23.7
```

```
140148 03/01 11:12 1038 PHYSICS_1_01[1,266] 10.7  44.3
140149 03/01 12:47 1038 PHYSICS_1_01[1,266]  9.2  19.4
140150 03/01 13:30 1038 PHYSICS_1_01[1,266]  8.5  21.7
140151 03/01 14:23 1038 PHYSICS_1_01[1,266]  8.0   6.7
140155 03/01 14:59 1038 PHYSICS_1_01[1,266]  7.8  39.8
140156 03/01 16:44 1038 PHYSICS_1_01[1,266]  6.7  99.6
140157 03/01 22:17 1038 PHYSICS_1_01[1,266]  4.9  39.7
140160 03/02 01:14 1038 PHYSICS_1_01[1,266]  4.3   7.9
140187 03/02 05:58 1040 PHYSICS_1_01[1,266]  8.8  44.3
140215 03/02 19:11 1043 PHYSICS_1_01[1,266] 10.7   8.6
140219 03/02 23:22 1043 PHYSICS_1_01[1,266]  6.6  11.4
140220 03/03 00:07 1043 PHYSICS_1_01[1,266]  6.4 123.9
140223 03/03 07:31 1043 PHYSICS_1_01[1,266]  4.2   3.2
140240 03/03 10:33 1045 PHYSICS_1_01[1,266]  0.5   6.1
140241 03/03 11:20 1045 PHYSICS_1_01[1,266] 10.2 123.1
140242 03/03 16:23 1045 PHYSICS_1_01[1,266]  6.4 119.0
140247 03/03 23:37 1045 PHYSICS_1_01[1,266]  4.3   6.0
140257 03/04 04:32 1047 PHYSICS_1_01[1,266]  4.4  88.5
140315 03/04 22:25 1048 PHYSICS_1_01[1,266]  4.8 110.3
140722 03/10 06:18 1063 PHYSICS_1_01[1,267]  6.6  44.5
140723 03/10 08:34 1063 PHYSICS_1_01[1,267]  5.1  61.3
140725 03/10 13:12 1063 PHYSICS_1_01[1,267]  3.5  21.9
140729 03/10 17:01 1063 PHYSICS_1_01[1,267]  2.9   9.2
140819 03/12 14:41 1070 PHYSICS_1_01[1,267]  7.1   4.9
140825 03/12 15:37 1070 PHYSICS_1_01[1,267]  6.2   2.7
140826 03/12 16:09 1070 PHYSICS_1_01[1,267]  6.0  63.0
140828 03/12 19:55 1070 PHYSICS_1_01[1,267]  4.6  22.1
140829 03/12 21:28 1070 PHYSICS_1_01[1,267]  4.1  10.5
140832 03/12 22:48 1070 PHYSICS_1_01[1,267]  3.7  29.8
140836 03/13 01:37 1070 PHYSICS_1_01[1,267]  3.2   2.0
140848 03/13 05:08 1072 PHYSICS_1_01[1,267]  7.4   1.5
140850 03/13 05:24 1072 PHYSICS_1_01[1,267]  7.3  23.4
140851 03/13 06:42 1072 PHYSICS_1_01[1,267]  6.1  43.4
140852 03/13 09:01 1072 PHYSICS_1_01[1,267]  5.0  74.3
140857 03/13 15:33 1072 PHYSICS_1_01[1,267]  3.4   3.3
140971 03/15 02:09 1080 PHYSICS_1_01[2,270]  9.5   9.5
140973 03/15 02:35 1080 PHYSICS_1_01[2,270]  8.8 206.9
141000 03/15 17:03 1082 PHYSICS_1_01[2,270]  9.1   3.7
141002 03/15 17:23 1082 PHYSICS_1_01[2,270]  9.0  27.3
141004 03/15 18:55 1082 PHYSICS_1_01[2,270]  7.6   3.8
141007 03/15 19:26 1082 PHYSICS_1_01[2,270]  7.2   4.2
```

```
141013 03/15 21:35 1082 PHYSICS_1_01[2,270]  6.1  90.0
141017 03/16 02:49 1082 PHYSICS_1_01[2,270]  4.6   2.3
141038 03/16 06:39 1084 PHYSICS_1_01[2,270]  8.4  20.6
141039 03/16 07:28 1084 PHYSICS_1_01[2,270]  7.8  99.5
141041 03/16 12:16 1084 PHYSICS_1_01[2,270]  5.6   2.8
141042 03/16 12:36 1084 PHYSICS_1_01[2,270]  5.5  16.4
141044 03/16 13:41 1084 PHYSICS_1_01[2,270]  5.0  26.5
141045 03/16 15:23 1084 PHYSICS_1_01[2,270]  4.7   4.2
141046 03/16 15:56 1084 PHYSICS_1_01[2,270]  4.5  18.7
141048 03/16 17:48 1084 PHYSICS_1_01[2,270]  4.1   8.6
141055 03/16 19:32 1084 PHYSICS_1_01[2,270]  3.9   2.5
141088 03/17 08:45 1089 PHYSICS_1_01[2,270]  6.3  12.4
141090 03/17 09:26 1089 PHYSICS_1_01[2,270]  5.8   1.7
141092 03/17 09:44 1089 PHYSICS_1_01[2,270]  5.8  36.7
141093 03/17 11:57 1089 PHYSICS_1_01[2,270]  5.1   5.4
141094 03/17 12:27 1089 PHYSICS_1_01[2,270]  4.9  11.3
141096 03/17 13:25 1089 PHYSICS_1_01[2,270]  4.6   4.1
141097 03/17 13:53 1089 PHYSICS_1_01[2,270]  4.7  18.6
141098 03/17 15:21 1089 PHYSICS_1_01[2,270]  4.3   6.1
141099 03/17 15:59 1089 PHYSICS_1_01[2,270]  4.2   1.4
141100 03/17 16:26 1089 PHYSICS_1_01[2,270]  4.2  10.6
141101 03/17 17:19 1089 PHYSICS_1_01[2,270]  4.0   3.0
141140 03/17 23:11 1091 PHYSICS_1_01[2,270]  8.2  51.2
141141 03/18 01:19 1091 PHYSICS_1_01[2,270]  6.6  89.1
141143 03/18 06:00 1091 PHYSICS_1_01[2,270]  4.7  20.0
141144 03/18 07:18 1091 PHYSICS_1_01[2,270]  4.5  16.6
141146 03/18 08:36 1091 PHYSICS_1_01[2,270]  4.1  18.7
141189 03/18 14:07 1093 PHYSICS_1_01[2,270]  9.8  14.0
141190 03/18 14:36 1093 PHYSICS_1_01[2,270]  9.3  19.7
141191 03/18 15:56 1093 PHYSICS_1_01[2,270]  8.2  40.8
141192 03/18 17:48 1093 PHYSICS_1_01[2,270]  7.1  50.7
141197 03/18 20:26 1093 PHYSICS_1_01[2,270]  6.0   1.5
141199 03/18 20:48 1093 PHYSICS_1_01[2,270]  6.0   2.1
141212 03/19 00:34 1095 PHYSICS_1_01[2,270] 10.4   5.5
141213 03/19 00:51 1095 PHYSICS_1_01[2,270] 10.2  63.4
141215 03/19 03:22 1095 PHYSICS_1_01[2,270]  7.9   2.7
141216 03/19 03:38 1095 PHYSICS_1_01[2,270]  7.7  41.6
141218 03/19 05:31 1095 PHYSICS_1_01[2,270]  6.8  23.3
141433 03/21 12:36 1113 PHYSICS_1_01[2,270]  6.6   8.4
141434 03/21 13:09 1113 PHYSICS_1_01[2,270]  6.0  20.5
141435 03/21 14:22 1113 PHYSICS_1_01[3,271]  5.0   1.1
```

```
141436 03/21 14:32 1113 PHYSICS_1_01[3,271]  4.8   6.4
141437 03/21 15:03 1113 PHYSICS_1_01[2,270]  4.6   4.4
141438 03/21 15:27 1113 PHYSICS_1_01[3,271]  4.3  18.5
141442 03/21 18:22 1113 PHYSICS_1_01[3,271]  3.1   9.3
141445 03/21 19:21 1113 PHYSICS_1_01[2,270]  2.8   3.6
141446 03/21 19:52 1113 PHYSICS_1_01[3,271]  2.6  11.7
141461 03/21 22:26 1113 PHYSICS_1_01[3,271]  2.0  12.4
141508 03/22 12:42 1116 PHYSICS_1_01[3,271]  6.8  12.4
141509 03/22 13:37 1116 PHYSICS_1_01[3,271]  5.7  36.8
141540 03/23 10:02 1120 PHYSICS_1_01[4,275]  7.0  18.2
141541 03/23 11:02 1120 PHYSICS_1_01[4,275]  6.5   6.9
141542 03/23 12:23 1120 PHYSICS_1_01[4,275]  5.3  50.2
141543 03/23 15:07 1120 PHYSICS_1_01[3,271]  5.0  13.4
141544 03/23 15:58 1120 PHYSICS_1_01[4,275]  4.8  33.2
141546 03/23 18:33 1120 PHYSICS_1_01[4,275]  4.1   6.8
141549 03/23 19:32 1120 PHYSICS_1_01[4,275]  3.8   4.2
141598 03/24 21:47 1124 PHYSICS_1_01[4,275]  6.4  97.8
141601 03/25 03:34 1124 PHYSICS_1_01[4,275]  4.1   4.5
141613 03/25 05:44 1126 PHYSICS_1_01[4,275]  0.0   4.2
141618 03/25 07:08 1126 PHYSICS_1_01[4,275]  9.4 103.7
141619 03/25 10:48 1126 PHYSICS_1_01[4,275]  7.1  82.5
141621 03/25 14:21 1126 PHYSICS_1_01[4,275]  6.2  17.4
141660 03/25 19:16 1128 PHYSICS_1_01[4,275]  7.7  65.5
141926 03/28 07:59 1137 PHYSICS_1_01[4,275]  9.2   2.9
141927 03/28 08:27 1137 PHYSICS_1_01[4,275]  9.0   1.6
141928 03/28 08:55 1137 PHYSICS_1_01[4,275]  8.7  48.3
141931 03/28 11:04 1137 PHYSICS_1_01[4,275]  7.8 139.8
141948 03/28 17:08 1137 PHYSICS_1_01[4,275]  5.7  12.8
141950 03/28 18:03 1137 PHYSICS_1_01[4,275]  5.6  20.4
141954 03/28 19:39 1137 PHYSICS_1_01[4,275]  5.2   1.2
141984 03/29 01:39 1140 PHYSICS_1_01[4,275] 12.3  89.6
141999 03/29 09:06 1140 PHYSICS_1_01[4,275]  6.9   7.2
142005 03/29 11:44 1140 PHYSICS_1_01[4,275]  6.2  15.8
142105 03/29 20:57 1142 PHYSICS_1_01[4,275] 12.2  34.7
142107 03/30 00:23 1142 PHYSICS_1_01[4,275]  8.3  15.3
142108 03/30 01:02 1142 PHYSICS_1_01[4,275]  8.3  21.3
142109 03/30 02:02 1142 PHYSICS_1_01[4,275]  7.6  14.9
142110 03/30 02:40 1142 PHYSICS_1_01[4,275]  7.3 127.4
142111 03/30 08:30 1142 PHYSICS_1_01[4,275]  5.4  19.3
142130 03/30 13:18 1144 PHYSICS_1_01[4,275] 13.8  33.3
142131 03/30 14:10 1144 PHYSICS_1_01[4,275] 11.9  36.7
```

```
142168 03/31 08:12 1150 PHYSICS_1_01[4,275] 10.5 156.3
142170 03/31 14:22 1150 PHYSICS_1_01[4,275]  5.7  33.2
142177 03/31 17:11 1150 PHYSICS_1_01[4,275]  4.9  34.4
142202 03/31 23:05 1152 PHYSICS_1_01[4,275] 10.9 181.2
142203 04/01 09:05 1152 PHYSICS_1_01[4,275]  3.3   2.0
142204 04/01 09:22 1152 PHYSICS_1_01[4,275]  3.3   3.3
142205 04/01 09:48 1152 PHYSICS_1_01[4,275]  3.2   2.7
142206 04/01 10:10 1152 PHYSICS_1_01[4,275]  3.2   3.5
```

Appendix B

General Relations of Helix Parameter

The trajectory of a charged particle inside the COT is defined by the following equation:

$$\begin{aligned}
x &= r\sin\phi - (r+d_0)\sin\phi_0, \\
y &= -r\cos\phi + (r+d_0)\cos\phi_0, \\
z &= z_0 + s\lambda, \\
r &= 1/2C, \\
\phi &= \phi(s) = 2Cs + \phi_0.
\end{aligned} \tag{B.1}$$

Where s is the arc length along the track. The pseudorapidity can be calculated as $\eta = -\ln(\tan\frac{\theta}{2})$. If we know a charged particle has momentum (P_x, P_y, P_z) at the vertex position $\vec{x} = (x_v, y_v, z_v)$. We can calculate the transverse momentum:

$$P_T = \sqrt{P_x^2 + P_y^2} \tag{B.2}$$

In a homogeneous magnetic field B, the particle track follows a helix, and the curvature is:

$$C = Q\frac{1.49896 \cdot 10^{-4} \cdot B[\text{kG}]}{P_T[\text{GeV}/c]} = Q\frac{\eta}{P_T}. \tag{B.3}$$

At CDF, the constant $\eta = 0.00211592$. Subsequently we have:

$$\begin{aligned}
\lambda &= \cot\theta = \tfrac{P_z}{P_T} \quad r = \tfrac{Q}{2C}, \\
s &= \tfrac{1}{2C}\sin^{-1}[2C(x_v\cos\phi_0 + y_v\sin\phi_0)] \\
d_0 &= y_v\cos\phi_0 - x_v\sin\phi_0 - \tfrac{1}{C}\sin^2 Cs, \\
z_0 &= z_v - s\lambda, \\
\phi_0 &= \tan^{-1}\left(\tfrac{y_0}{x_0}\right) - Q\tfrac{\pi}{2} \approx \tan^{-1}\left(\tfrac{P_y}{P_x}\right),
\end{aligned} \tag{B.4}$$

where x_0 and y_0 are the coordinates of the helix center:

$$\begin{aligned}
x_0 &= x_v - r\sin\alpha &&= x_v - rP_y/P_T, \\
y_0 &= y_v + r\cos\alpha &&= y_v + rP_x/P_T.
\end{aligned} \tag{B.5}$$

When $s \ll r$, it is often valid to apply straight line approximation ($C \to 0$) to simplify the calculation. Then the impact parameter d_0 can be simply computed at any point (x_v, y_v) on the track as follows:

$$d_0 = -x_v\sin\phi_0 + y_v\cos\phi_0. \tag{B.6}$$

The arc length along the track from the point of closest approach to the point (x_v, y_v) is then given by

$$s_0 = x_v \cos\phi_0 + y_v \sin\phi_0. \tag{B.7}$$

At CDF, the track parameters is calculated with respect to the detector geometric origin. However the interaction position is often slightly off. Assuming the event primary vertex is at (x_p, y_p), as long as it is not too far away from the detector geometric origin, the impact parameter with respect to the event primary vertex is

$$d_0^{'} \approx d_0 + x_p \sin\phi_0 - y_p \cos\phi_0. \tag{B.8}$$

Under the straight line approximation, the intersection point of two tracks can be simply expressed as

$$\begin{aligned} x &= -d_0^1 \sin\phi_0^1 + d\cos\phi_0^1, \\ y &= d_0^1 \cos\phi_0^1 + d\sin\phi_0^1, \\ d &= (d_0^2 - d_0^1 \cos(\Delta\phi_0))/\sin(\Delta\phi_0), \end{aligned} \tag{B.9}$$

where $\Delta\phi_0 = \phi_0^1 - \phi_0^2$ is the angle between two tracks.

Appendix C

Vertex Fit Package and Two Dimensional Vertex Constraints

The resolution of a reconstructed vertex can be improved by applying a vertex fit with various geometric and kinematic constraints. In CDF a commonly used vertex fitting package is CTVMFT [83], which allows us to fit vertices in three dimensions. At this time, the SVX z information is not as well understood as the $r - \phi$ information, therefore, we developed a similar vertex fitting program that allows us to fit vertices to in either two or three dimensions. In this analysis, we restrict ourselves to two dimensional vertex fits.

To check the fitting program, $D^+ \to K^-\pi^+\pi^+$ decays were generated with Monte Carlo, and the track parameters were smeared about their generated values using a Gaussian function with the expected CDF resolution. The "pull" distributions of the fitted parameters are shown in Fig. C.1. The results of the vertex fit program are reasonable and the uncertainties on the fitted parameters are calculated correctly. The vertex χ^2 probability distribution is flat. These observations support that our vertex fitting program is working correctly.

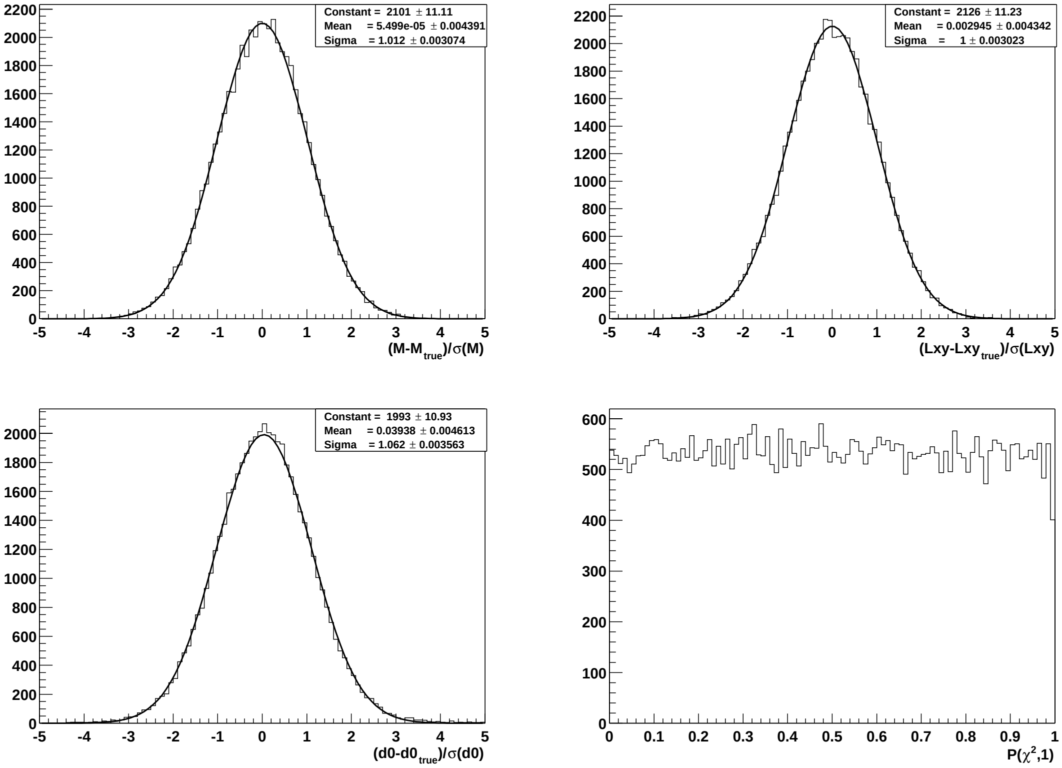

Figure C.1: The pull distributions for the invariant mass (upper left), the decay length (upper right), and the impact parameter (lower left) for Monte Carlo generated $D^+ \to K^-\pi^+\pi^+$ decays. The lower right plot shows the probability distribution of the vertex χ^2.

Appendix D

Test of the B Fraction Fit Procedure

A binned likelihood technique is used to fit the charm impact parameter distribution from data. We generated a set of toy Monte Carlo experiments and we used these toy data to evaluate the performance of the fitting procedure.

We generate the toy data sets using the following procedure. We assume we have a signal of N D mesons. We use four values of N, 2000, 5000, 10000, and 30000, which provides us a range that covers the amount of signal observed so far in the four D meson decays considered in this analysis. The fraction of these D mesons coming from secondary B decay is f_B, so the number of directly produced D mesons is $(1 - f_B)N$. We use three values of f_B: 10%, 15%, and 20%. We generate an impact parameter distribution by randomly assigning an impact parameter to each of the $(1 - f_B)N$ prompt D mesons using the probability distribution described by Eq. 6.5. We fix $\alpha_0 = 70\%$, $\sigma_D = 40\mu$m and the ratio $\lambda_D/\sigma_D = 1.13$. For each of the f_bN secondary D mesons, we randomly assign an impact parameter according to the probability distribution described by Eq. 6.3. We use $\epsilon_1 = 90\%$, $\lambda = 100\mu m$ and $\lambda_2 = 20\mu m$. We then smear this impact parameter using the same resolution function used to smear the impact parameters of the direct charm decays.

For the each of the twelve total combinations of our four values of N and three values of f_B, we generate 100 toy data sets. The results of the fit for f_B for these twelve sets of 100 toy experiments are shown in Fig. D.1. For each value of f_B, the average value of the distribution of fitted values of f_B from the 100 toy experiments agrees with the generated value: no significant bias on this parameter is observed, and the distribution is described by a Gaussian. The corresponding "pull" distributions, that is the distribution of the difference of the measured value of f_B from the true value of f_B divided by the estimated error on the measured value of f_B, are shown in Fig. D.2. Although these distributions look reasonable, the width of some of these distributions is less than one, indicating that the statistical error on f_B is overestimated by the fit. Since systematic errors on f_B will dominate the small statistical uncertainty, this possible overestimate is unimportant.

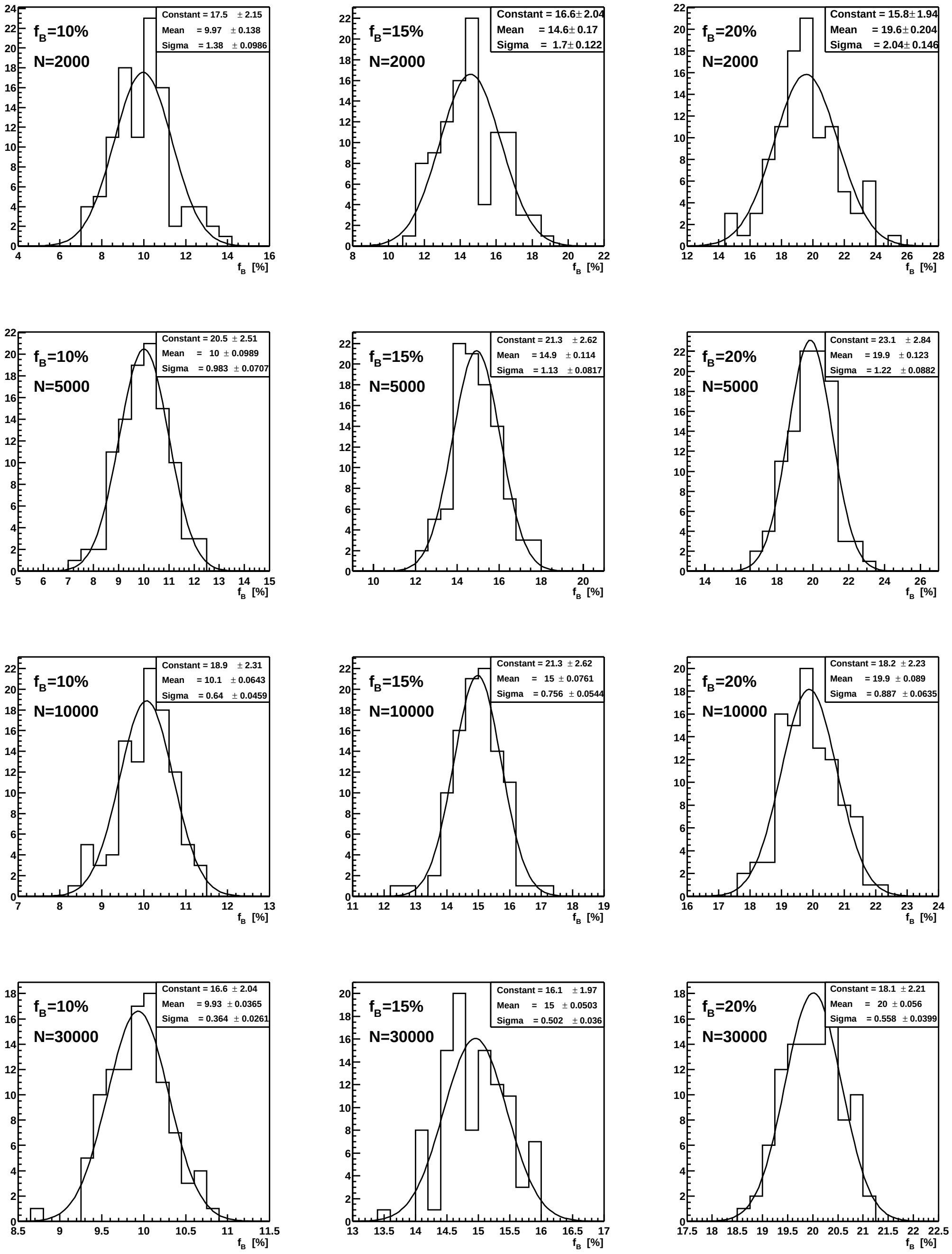

Figure D.1: The distributions of B fraction f_B determined by the fit for 100 toy experiments for each of the various f_b and signal N.

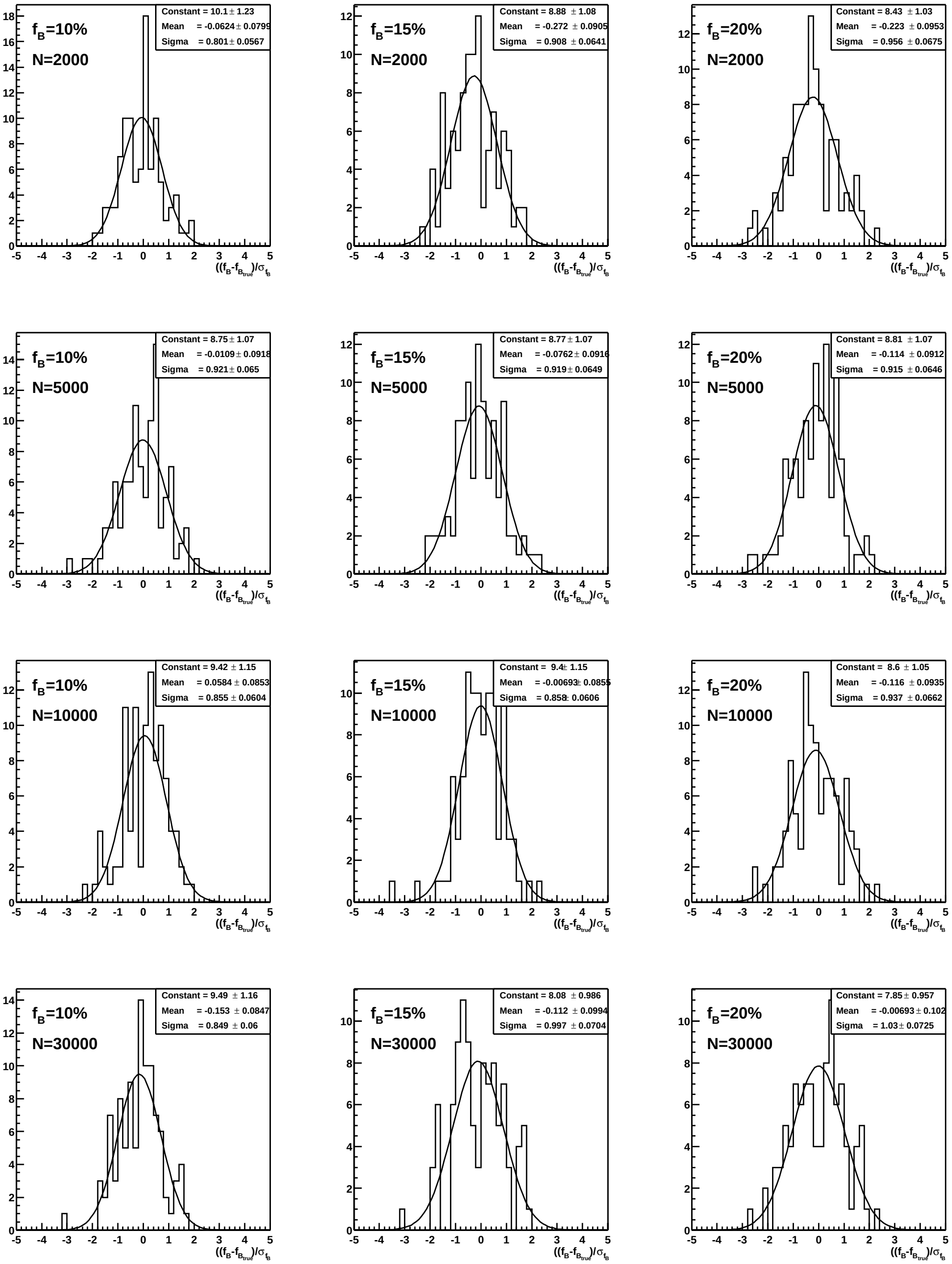

Figure D.2: The pull distribution of B fraction f_B determined by the fit for 100 toy experiments for each of the various f_b and signal N.

Bibliography

[1] S. L. Glashow. Partial symmetries of weak interactions. *Nucl. Phys.*, 22:579–588, 1961.

[2] S. Weinberg. A model of leptons. *Phys. Rev. Lett.*, 19:1264–1266, 1967.

[3] Eugene D. Commins and Philip H. Bucksbaum. *Weak Interactions of Leptons and Quarks*. Cambridge University Press, 1983.

[4] N. Cabibbo. Unitary symmetry and leptonic decays. *Phys. Rev. Lett.*, 10:531–532, 1963.

[5] M. Kobayashi and T. Maskawa. CP violation in the renormalizable theory of weak interaction. *Prog. Theor. Phys.*, 49:652–657, 1973.

[6] F. Abe et al. Measurement of bottom quark production in 1.8-tev p anti-p collisions using semileptonic decay muons. *Phys. Rev. Lett.*, 71:2396–2400, 1993.

[7] F. Abe et al. Measurement of the bottom quark production cross-section using semileptonic decay electrons in p anti-p collisions at s**(1/2) = 1.8-TeV. *Phys. Rev. Lett.*, 71:500–504, 1993.

[8] F. Abe et al. Measurement of the b meson differential cross-section, d sigma / d p(t), in p anti-p collisions at s**(1/2) = 1.8- tev. *Phys. Rev. Lett.*, 75:1451–1455, 1995.

[9] B. Abbott et al. The b anti-b production cross section and angular correlations in p anti-p collisions at s**(1/2) = 1.8- tev. *Phys. Lett.*, B487:264–272, 2000.

[10] P. Nason, S. Dawson, and R. K. Ellis. The total cross-section for the production of heavy quarks in hadronic collisions. *Nucl. Phys.*, B303:607, 1988.

[11] W. Beenakker, H. Kuijf, W. L. van Neerven, and J. Smith. QCD corrections to heavy quark production in p anti-p collisions. *Phys. Rev.*, D40:54–82, 1989.

[12] P. Nason, S. Dawson, and R. K. Ellis. The one particle inclusive differential cross-section for heavy quark production in hadronic collisions. *Nucl. Phys.*, B327:49–92, 1989.

[13] W. Beenakker, W. L. van Neerven, R. Meng, G. A. Schuler, and J. Smith. QCD corrections to heavy quark production in hadron-hadron collisions. *Nucl. Phys.*, B351:507–560, 1991.

[14] Michelangelo L. Mangano, Paolo Nason, and Giovanni Ridolfi. Heavy quark correlations in hadron collisions at next-to- leading order. *Nucl. Phys.*, B373:295–345, 1992.

[15] D. Acosta et al. Measurement of the b+ total cross section and b+ differential cross section dsigma/dp(t) in p anti-p collisions at s**(1/2) = 1.8-tev. *Phys. Rev.*, D65:052005, 2002.

[16] Matteo Cacciari and Paolo Nason. Is there a significant excess in bottom hadroproduction at the tevatron? *Phys. Rev. Lett.*, 89:122003, 2002.

[17] C. Peterson, D. Schlatter, I. Schmitt, and Peter M. Zerwas. Scaling violations in inclusive e+ e- annihilation spectra. *Phys. Rev.*, D27:105, 1983.

[18] T. Nakaya. Measurement of the $D^{*+}(2010)$ production cross section in $p\bar{p}$ collisions at $\sqrt{s} = 1.8\,\mathrm{TeV}$. CDFNOTE 5025, 1999.

[19] M. Cacciari, M. Greco, S. Rolli, and A. Tanzini. Charmed mesons fragmentation functions. *Phys. Rev.*, D55:2736–2740, 1997.

[20] CDF II Collaboration. The CDF Run II Technical Design Report. FERMILAB-Pub-96-390-E.

[21] Chunhui Chen, Rolf Oldeman, and Joseph Kroll. A Method to Measure the Direct and Secondary Charm Fraction in Two Track Data. CDFNOTE 5996, 2002.

[22] A. J. Buras, W. Slominski, and H. Steger. B0 anti-b0 mixing, cp violation and the b meson decay. *Nucl. Phys.*, B245:369, 1984.

[23] Yosef Nir. CP violation in and beyond the standard model. *hep-ph/9911321*, 1999.

[24] K. Anikeev et al. B physics at the Tevatron: Run II and beyond. *hep-ph/0201071*, 2001.

[25] Andrzej J. Buras and Robert Fleischer. Quark mixing, CP violation and rare decays after the top quark discovery. *hep-ph/9704376*, 1997.

[26] K. Hagiwara et al. Review of particle physics. *Phys. Rev.*, D66:010001, 2002.

[27] Colin Gay. B Mixing. *Ann. Rev. Nucl. Part. Sci.*, 50:577–641, 2000.

[28] F. Parodi, P. Roudeau, and A. Stocchi. Constraints on the Parameters of the CKM Matrix by End 1998. *Nuovo Cim.*, A112:833–854, 1999.

[29] T. Affolder et al. A Measurement of $\sin 2\beta$ from $B_d^0 \to J/\psi K_S^0$ with the CDF Detector. *Phys. Rev.*, D61:072005, 2000.

[30] K. Abe et al. An improved measurement of mixing-induced cp violation in the neutral b meson system. *Phys. Rev.*, D66:071102, 2002.

[31] B. Aubert et al. Measurement of the cp-violating asymmetry amplitude sin 2beta. *Phys. Rev. Lett.*, 89:201802, 2002.

[32] Monika Grothe. Mixing in the d0 system: Results from collider experiments. *Mod. Phys. Lett.*, A18:1–22, 2003.

[33] Chunhui Chen, Rolf Oldeman, and Joseph Kroll. Opportunities for Charm Physics at CDF. CDFNOTE 5859, 2002.

[34] Ikaros I. Y. Bigi. Charm physics - like Botticelli in the Sistine chapel. hep-ph/0107102, 2001.

[35] E. M. Aitala et al. Measurements of lifetimes and a limit on the lifetime difference in the neutral D meson system. *Phys. Rev. Lett.*, 83:32, 1999.

[36] J. M. Link et al. A measurement of lifetime differences in the neutral D meson system. *Phys. Lett.*, B485:62–70, 2000.

[37] S. E. Csorna et al. Lifetime differences, direct cp violation and partial widths in d0 meson decays to k+ k- and pi+ pi-. *Phys. Rev.*, D65:092001, 2002.

[38] Monika Grothe. Results on mixing in the D0 system from BaBar. *AIP Conf. Proc.*, 618:285–292, 2002.

[39] K. Abe et al. A measurement of lifetime difference in d0 meson decays. *Phys. Rev. Lett.*, 88:162001, 2002.

[40] G. Blaylock, A. Seiden, and Y. Nir. The Role of CP violation in $D^0\overline{D^0}$ mixing. *Phys. Lett.*, B355:555–560, 1995.

[41] E. M. Aitala et al. A search for $D^0\overline{D^0}$ mixing and doubly-Cabibbo- suppressed decays of the D^0 in hadronic final states. *Phys. Rev.*, D57:13–27, 1998.

[42] J. M. Link et al. A study of the decay $D^0 \to K^+\pi^-$. *Phys. Rev. Lett.*, 86:2955–2958, 2001.

[43] R. Godang et al. Search for $D^0\overline{D^0}$ mixing. *Phys. Rev. Lett.*, 84:5038–5042, 2000.

[44] Ulrik Egede. Mixing in the d0 anti-d0 system at babar. *hep-ex/0210060*, 2002.

[45] K. Abe et al. A measurement of the rate of wrong-sign decays $D^0 \to K^+\pi^-$. *hep-ex/0208051*, 2002.

[46] E. M. Aitala et al. Branching fractions for $D^0 \to K^+K^-$ and $D^0 \to \pi^+\pi^-$, and a search for CP violation in D^0 decays. *Phys. Lett.*, B421:405–411, 1998.

[47] J. M. Link et al. Search for CP violation in D^0 and D^+ decays. *Phys. Lett.*, B491:232–239, 2000.

[48] E. M. Aitala et al. Search for CP violation in charged D meson decays. *Phys. Lett.*, B403:377–382, 1997.

[49] S. Fajfer, S. Prelovsek, and P. Singer. Rare charm meson decays $D \to P\ell^+\ell^-$ and $c \to u\ell^+\ell^-$ in SM and MSSM. *Phys. Rev.*, D64:114009, 2001.

[50] E. M. Aitala et al. Search for rare and forbidden dilepton decays of the D^+, D_s^+, and D^0 charmed mesons. *Phys. Lett.*, B462:401–409, 1999.

[51] E. M. Aitala et al. Search for rare and forbidden charm meson decays $D^0 \rightarrow V\ell^+\ell^-$ and $hh\ell\ell$. *Phys. Rev. Lett.*, 86:3969–3972, 2001.

[52] Michael E. Peskin and Daniel V. Schroeder. *An Introduction to Quantum Field Theory.* Addison Wesley, 1995.

[53] Chris Quigg. *Gauge Theories of the Strong, Weak, and Electromagnetic Interactions.* Addison Wesley, 1997.

[54] Francis Halzen and Alan D. Martin. *Quarks & Leptons.* John Wiley & Sons, 1984.

[55] Gordon Kane. *Modern Elementary Particle Physics.* Addison Wesley, 1993.

[56] Lincoln Wolfenstein. Parametrization of the kobayashi-maskawa matrix. *Phys. Rev. Lett.*, 51:1945, 1983.

[57] E.K. Ellis, W.J. Sterling, and B.R. Webber. *QCD and Collider Physics.* Cambridge University Press, 1996.

[58] Michelangelo L. Mangano. Heavy-quark production in hadronic collisions. *hep-ph/9711337*, 1997.

[59] Stefano Frixione, Michelangelo L. Mangano, Paolo Nason, and Giovanni Ridolfi. Heavy-quark production. *Adv. Ser. Direct. High Energy Phys.*, 15:609–706, 1998.

[60] Paolo Nason. Heavy flavour production. *hep-ph/0207362*, 2002.

[61] O. Biebel, P. Nason, and B. R. Webber. Jet Fragmentation in e^+e^- Annihilation. *hep-ph/0109282*, 2001.

[62] Stanley J. Brodsky, C. Peterson, and N. Sakai. Intrinsic heavy quark states. *Phys. Rev.*, D23:2745, 1981.

[63] Hans Wenzel. Tracking in the SVX. CDFNOTE 1790, 1998.

[64] A Mukherjee, R. Wagner, et al. CDF Central Outer Tracker. CDFNOTE 6227, 2002.

[65] A. Sill. CDF Run II Silicon Tracking Projects. *Nucl. Instrum. Meth.*, A447:1–8, 2000.

[66] CDF II Collaboration. Proposal for Enhancement of the CDF II Detector: An Inner Silicon Layer and a Time of Flight Detector. Proposal P-909 submitted to the Fermi lab Director and PAC, October 23, 1998.

[67] CDF II Collaboration. Update to Proposal P-909: Physics Performance of the CDF II with An Inner Silicon Layer and a Time of Flight Detector. Submitted to the Fermi lab Director and PAC, January 5, 1999.

[68] Chen Chunhui et al. Front End Electronics for the CDF-II Time-of-Flight System. Presented at 2001 IEEE NSS/MIC conference, San Diego, U.S.A. Nov 4-10, 2001.

[69] F. Abe et al. Measurement of the anti-proton proton total cross-section at s**(1/2) = 546-GeV and 1800-GeV. *Phys. Rev.*, D50:5550–5561, 1994.

[70] J. Elias et al. Luminosity monitor based on cherenkov counters for p anti-p colliders. *Nucl. Instrum. Meth.*, A441:366–373, 2000.

[71] D. Acosta et al. The cdf cherenkov luminosity monitor. *Nucl. Instrum. Meth.*, A461:540–544, 2001.

[72] D. Acosta et al. The performance of the cdf luminosity monitor. *Nucl. Instrum. Meth.*, A494:57–62, 2002.

[73] W. Ashmanskas et al. The CDF Silicon Vertex Tracker. FERMILAB-CONF-00-238-E.

[74] W. Ashmanskas et al. Performance of the CDF Online Silicon Vertex Tracker. *IEEE Trans. Nucl. Sci.*, 49:1177–1184, 2002.

[75] S. Donati. All hadronic B decay trigger with the CDF silicon vertex tracker. Presented at 8th International Symposium on Heavy Flavor Physics (Heavy Flavors 8), Southampton, England, 25-29 Jul 1999.

[76] S. Donati and G. Punzi. Two Track Trigger with full SVT Simulation. CDFNOTE 3780, 1998.

[77] Intae Yu and Jonathan Lewis. Two Track Trigger for Run II and Efficiencies for B Hadronic Decays. CDFNOTE 4095, 1997.

[78] The Trigger and Datasets Working Groups. CDF Run-II Trigger Table and Datasets Plan. CDFNOTE 4718, 2001.

[79] Manfred Paulini and Barry Wicklund. Summary of Proposals for B Physics Trigger in Run II. CDFNOTE 5483, 2000.

[80] D. Acosta et al. The CLC Minimum Bias Trigger. CDFNOTE 5861, 2002.

[81] S. De Cecco, S. Giagu, M. Rescigno, and A. Cerri. A Measurement of the Relative Branhing fractions $\Gamma(D^0 \to K^+K^-)/\Gamma(D^0 \to K\pi)$ and $\Gamma(D^0 \to \pi^+\pi^-)/\Gamma(D^0 \to K\pi)$. CDFNOTE 6018, 2002.

[82] K.Anikeev et.al. Measurement of the Mass Difference $m(D_s^\pm) - m(D^\pm)$ in the $\phi\pi$ Decay Channel. CDFNOTE 6021, 2002.

[83] John Marriner. Secondary Vertex Fit with Mass and Pointing Constraints. CDFNOTE 1996, 1993.

[84] Chunhui Chen, Rolf Oldeman, and Joseph Kroll. Trigger and Reconstruction Efficiency for Direct Charm Meson in the Two-Track Hadronic Data Sample. CDFNOTE 6165, 2002.

[85] D. Glenzinski et al. Determination of the Run IIa COT Tracking Efficiency Using the W-No-Track Sample. CDFNOTE 5973, 2002.

[86] C. Chen, I. Cho, C. Hays, M. Herndon, J. Kraus, J. Kroll, T. Miao, P. Murat, R. Oldeman, and J.C Yun. Measurement of the Track Reconstruction Efficiency in the COT Using a MC Track Embedding Technique. CDFNOTE 6394, 2003.

[87] R. Oldeman. Estimate of hadronic B-trigger rates from special SVT runs before the Fall 2001 shutdown. CDFNOTE 5786, 2001.

[88] Roberto Carosi for the SVT group. Report from SVT Workshop. *Talk on B meeting Sept 27, 2002.*

[89] Daniel Jeans. A decrease of the XFT efficiency at high multiplicity was observed in a HW/Z MC study of the SVT efficiency. *Private communication.*

[90] S. Donati and L. Ristori. Measuring beam width and SVX impact parameter resolution. CDFNOTE 4189, 1997.

[91] Isamu Nakamura. Talk on B-tagging meeting Sept 27, 2002.

[92] Run II handbook. *http://www-bd.fnal.gov/lug/runII_handbook/RunII_index.html.*

[93] K.Anikeev et.al. Calibration of Energy Loss and Magnetic Field using J/psi Events in Run II. CDFNOTE 5958, 2002.

[94] S. Gromoll and Ch. Paus. A Heavy Quark Generator. CDFNOTE 5985, 2002.

[95] J. C. Anjos et al. A Dalitz plot analysis of $D \to K\pi\pi$ decays. *Phys. Rev.*, D48:56–62, 1993.

[96] D. Acosta et al. A first look at the CLC Luminosity Measurements. CDFNOTE 6052, 2002.

[97] S Klimenko, J Konigsberg, and T Liss. Average cross-section of the inelastic PPbar scattering at 1800 TeV. CDFNOTE 6314, 2003.

[98] Yi-Jin Pei. A Simple approach to describe hadron production rates in e^+e^- annihilation. *Z. Phys.*, C72:39–46, 1996.

[99] Francesco Becattini. A Thermodynamical approach to hadron production in e^+e^- collisions. *Z. Phys.*, C69:485–492, 1996.

[100] R. Barate et al. Study of charm production in Z decays. *Eur. Phys. J.*, C16:597–611, 2000.

[101] P. Nason M. Cacciari. *private communication.*

[102] Matteo Cacciari, Mario Greco, and Paolo Nason. The p(T) spectrum in heavy-flavour hadroproduction. *JHEP*, 05:007, 1998.

[103] J. Pumplin et al. New generation of parton distributions with uncertainties from global QCD analysis. *JHEP*, 07:012, 2002.